

IRE Transactions



on ANTENNAS and PROPAGATION

Volume AP-9

JULY, 1961

Number 4

Published Bimonthly

In This Issue

The Traveling-Wave Linear Antenna

Resonance Characteristics of a Corrugated Cylinder

New Circularly-Polarized Frequency-Independent Antennas

Arbitrary Polarization from Annular Slot Planar Antennas

Lossless Multiple Beams in Linear Arrays

Two-Dimensional Luneberg Lenses

Evaluation of Radiation Integrals

An Iris-Excited Slot Radiator

Reflection from a Stratified Inhomogeneity

Discontinuities in an Electromagnetic Field

Elevated Duct Propagation

Over-the-Horizon Tropospheric Propagation

Simultaneous Scintillation Observations

Studies of Meteor Propagation

Computing Ionospheric Focusing

PUBLISHED BY THE
Professional Group on Antennas and Propagation

Administrative Committee

Harry Fine, *Chairman*

Sidney Bowhill, *Vice Chairman*

K. S. Kelleher, *Secretary-Treasurer*

R. J. Adams

A. B. Crawford

R. C. Hansen

D. Adcock

N. J. Gamara

E. K. Smith, Jr.

R. N. Bracewell

W. E. Gordon

T. E. Tice

H. V. Cottony

L. G. Trolese

Ex-Officio Members

J. I. Bohnert

E. C. Jordan

K. M. Siegel

A. Dorne

R. Justice

P. H. Smith

V. R. Eshleman

R. L. Mattingly

L. C. Van Atta

J. W. Findlay

D. C. Ports

A. T. Waterman, Jr.

Chapter Chairmen

Akron

Dayton

Philadelphia

J. R. Shoemaker

C. G. Conrad

F. Klawnsnick

Albuquerque-Los Alamos

Denver-Boulder

San Diego

D. Thorn

W. C. Coombs

H. Dickstein

Boston

Los Angeles

San Francisco

J. Ruze

L. A. Kurtz

R. C. Honey

Chicago

Orange Belt

Syracuse

H. L. Woodbury

D. S. Sabih

E. B. Mullen

Columbus

Washington, D. C.

H. B. Querido

R. J. Adams

S. A. Bowhill, *Editor*

H. V. Cottony, *Associate Editor (Antennas)*

A. T. Waterman, Jr., *Associate Editor (Propagation)*

K. M. Siegel, *Associate Editor (Electromagnetic Theory)*

J. W. Findlay, *Associate Editor (Radio Astronomy)*

IRE TRANSACTIONS® PGAP IS A PUBLICATION DEVOTED TO
EXPERIMENTAL AND THEORETICAL PAPERS ON RADIO ANTENNAS,
ON GUIDED OR UNGUIDED PROPAGATION OF RADIO WAVES, AND
ON ALLIED FIELDS OF RADIO PHYSICS SUCH AS RADIO ASTRONOMY

MANUSCRIPTS should be submitted to Sidney A. Bowhill, *Editor*, 222 Electrical Engineering, Pennsylvania State University, University Park, Pa. Manuscripts should be original typewritten copy, double-spaced, plus one carbon copy and two sets of copies of illustrations. Original illustrations will be called for if the paper is accepted. References should appear as footnotes and include author's name, title, journal, volume, initial and final page numbers, and date.

CONTRIBUTIONS, which should average 15 double-spaced typewritten pages in length, are subjected to review by the *Associate Editors* and their readers. Each paper must have a summary of less than 200 words.

COMMUNICATIONS should not exceed five double-spaced typewritten pages in length, together with not more than three illustrations. Accepted at the Editor's discretion, they appear in the first available issue.

NEWS ITEMS concerning PGAP members and group activities should be sent to the *News Editor*, R. C. Hansen, Aerospace Corp., Box 95085, Los Angeles 45, Calif.

ORIGINAL ILLUSTRATIONS should be submitted as follows: All line drawings (graphs, charts, block diagrams, cutaways, etc.) should be inked uniformly and ready for reproduction. If commercially printed grids are used in graph drawings, author should be sure printer's ink is of a color that will reproduce. Photographs should be glossy prints. Call-outs or labels should be marked on a registered tissue overlay, not on the illustration itself. No illustration should be larger than 8 x 10 inches. Lettering on illustrations must have height at least two per cent of the illustration width.

Copies can be purchased from the INSTITUTE OF RADIO ENGINEERS, 1 East 79 St., New York 21, N.Y. Individual copies of this issue, and all available back issues, except Vols. AP-5, No. 1; AP-6, No. 1; AP-7, Special Supplement, may be purchased at the following prices: IRE members (one copy) \$2.25, libraries and colleges \$3.25, all others \$4.50. Yearly subscription rate: non-members \$17.00; colleges and public libraries \$10.00. IRE TRANSACTIONS ON ANTENNAS AND PROPAGATION. Copyright © 1961, by The Institute of Radio Engineers, Inc. Printed in U.S.A. Printed by George Banta Co., Inc., Curtis Reed Plaza, Menasha, Wisconsin.

Second-class postage paid at MENASHA, WISCONSIN, and additional mailing offices under the act of August 24, 1912. Acceptance for mailing at a special rate of postage is provided for in the act of February 28, 1925, embodied in Paragraph 4, Section 412, P. L. & R., authorized October 26, 1927.

ANTENNAS REVIEWERS

Adams, R. J.
Andreasen, M. G.
Bailin, L. L.
Blacksmith, P., Jr.
Bouche, E. L.
Brown, R. M., Jr.
Brueckmann, H.
Carter, P. S., Jr.
Deschamps, G. A.
DuHamel, R. H.
Duncan, J. W.
Goodrich, R.
Hansen, R. C.
Harris, J. H.
Hessel, A.
Hiatt, R. E.
Holt, F. S.
Honey, R. C.
Hyneman, R. F.
Jones, E. M. T.
Jordan, E. C.
Justice, R.
Kelleher, K. S.
Lo, Y. T.
Marston, A. E.
Mattingly, R. L.
Moore, R. K.
Morgan, S. P.
Morita, T.
Phillips, C. E.
Rotman, W.
Rumsey, V. H.
Ruze, J.
Shmoys, J.
Sinclair, G.
Swenson, G. W., Jr.
Tanner, R. L.
Villeneuve, A. T.
Wait, J. R.
Yen, J. L.
Zucker, F. J.

PROPAGATION REVIEWERS

Abel, W. G.
Beard, C. I.
Bolgiano, R.
Booker, H. G.
Bracewell, R. N.
Bullington, K.
Carroll, T. J.
Chisholm, J. H.
de Bettencourt, J. T.
Dyce, R. B.
Eshleman, V. R.
Gautier, T. N.
Gordon, W. E.
Lowenthal, M.
Manning, L. A.
Morita, T.
Norton, K. A.
Pfister, W.
Rogers, T. F.
Rumsey, V. H.
Straiton, A. W.
Twersky, V.
Trolese, L. G.
Wheelon, A. D.
Yabroff, I.

ELECTROMAGNETIC THEORY REVIEWERS

Chen, K-M.
Chu, C-M.
Crispin, J. W.
Diamond, H.
Goodrich, R. F.
Heins, A. E.
Hiatt, R. E.
Kleinman, R. E.
Marcuvitz, N.
Meltz, G.
Olte, A.
Raybin, D. M.
Ritt, R. K.
Sengupta, D. L.
Senior, T. B. A.
Silver, S.
Weil, H.
Weston, V. H.
Wren, A. W., Jr.
Vivian, W. E.

IRE Transactions on Antennas and Propagation

Volume AP-9

JULY, 1961

Published Bimonthly

Number 4

TABLE OF CONTENTS

CONTRIBUTIONS

The Traveling-Wave Linear Antenna.....	Edward E. Altshuler	324
Resonance Characteristics of a Corrugated Cylinder Excited by a Magnetic Dipole.....	J. R. Wait and A. M. Conda	330
New Circularly-Polarized Frequency-Independent Antennas with Conical Beam or Omnidirectional Patterns.....	J. D. Dyson and P. E. Mayes	334
Arbitrary Polarization from Annular Slot Planar Antennas..	F. J. Goebels, Jr. and K. C. Kelly	342
A Theoretical Limitation on the Formation of Lossless Multiple Beams in Linear Arrays..	J. L. Allen	350
A General Analysis of Nonplanar, Two-Dimensional Luneberg Lenses.....	S. Adachi, R. C. Rudduck, and C. H. Walter	353
The Numerical Evaluation of Radiation Integrals.....	J. H. Richmond	358
An Iris-Excited Slot Radiator in the Narrow Wall of Rectangular Waveguide.....	D. G. Dudley, Jr.	361
Reflection of Electromagnetic Waves from a Stratified Inhomogeneity.....	R. Yamada	364
On Propagating Discontinuities in an Electromagnetic Field.....	Kent R. Johnson	370
Elevated Duct Propagation in the Tradewinds.....	D. L. Ringwalt and F. C. Macdonald	377
Frequency Variations Due to Over-the-Horizon Tropospheric Propagation.....	J. H. Chisholm, S. J. Goodman, J. M. Kennedy, L. B. Lambert, L. P. Rainville, and J. F. Roche	384
Simultaneous Scintillation Observations on 1300-Mc and 3000-Mc Signals Received During the Solar Eclipse of October 2, 1959.....	J. Aarons and J. P. Castelli	390
Studies of Meteor Propagation at 49 and 74 Mc.....	J. B. Berry, Jr., J. C. James, and M. L. Meeks	395
A Method for Computing Ionospheric Focusing of Radio Waves, Using Vertical Incidence Ionograms.....	E. Warren and D. Muldrew	403
Corrections to:		
"The Stanford Microwave Spectroheliograph Antenna, a Microsteradian Pencil Beam Interferometer"		
"Tolerance Theory of Large Antennas"		
"Interferometry and the Spectral Sensitivity Island Diagram".....		R. N. Bracewell 409

COMMUNICATIONS

Graphical Construction of Rays in an Ideal Luneburg Lens.....	H. E. Schrank	410
Backscattering from a Finite Cone—Comparison of Theory and Experiment.....	Joseph B. Keller	411
Focal Length of a Cassegrain Reflector.....	W. D. White and L. K. DeSize	412
Reply to Comments by White and DeSize	E. J. Wilkinson and A. J. Appelbaum	412
Phase Correction by Dielectric Slabs in Sectoral Horn Antennas.....	M. A. Quddus and J. P. German	413
Comparison of Observed Tropospheric Refraction with Values Computed from the Surface Refractivity.....	B. R. Bean	415
The Excitation of a Dielectric-Rod Antenna by a Helix.....	T. S. Chu and N. R. Kilcoyne	416
Contributors.....		418
Papers to be Published in Future Issues.....	Inside Back Cover	

contributions

The Traveling-Wave Linear Antenna*

EDWARD E. ALTSHULER†, MEMBER, IRE

Summary—It is shown experimentally that an essentially traveling-wave distribution of current can be produced on a linear antenna by inserting a resistance of suitable magnitude one-quarter wavelength from the end of the antenna. A theory for the resistively-loaded dipole antenna is formulated on the basis that the inserted resistors (one in each arm) can be replaced by equivalent generators and that the resulting triply-driven antenna can be solved by the superposition of singly- and doubly-driven dipoles. Approximately 50 per cent of the power is dissipated in these resistors.

With a traveling-wave distribution of current on an antenna available, the properties of this antenna are then investigated and compared with those of the conventional linear antenna. It is found that the input impedance of the traveling-wave antenna remains essentially constant as a function of antenna length, whereas that of the conventional linear antenna varies considerably. It is also shown that the input impedance of the traveling-wave antenna varies only slightly over a 2 to 1 frequency band. The directional properties of the traveling-wave and conventional dipole are compared, and it is shown that a minor lobe does not appear in the radiation pattern of the traveling-wave dipole until it is much longer than the conventional dipole. Also, it is shown that where the directional properties of the conventional dipole are quite sensitive to a change in frequency, those of the traveling-wave dipole are not.

* Received by the PGAP, June 30, 1960; revised manuscripts received, October 3, 1960, and January 1, 1961. This research was made possible by support extended to Harvard Univ. by AFCL under Contract No. AF19(604)4118.

† Electromagnetic Rad. Lab., AF Cambridge Res. Labs., Laurence G. Hanscom Field, Bedford, Mass. Formerly with Cruft Lab., Harvard University, Cambridge, Mass.

INTRODUCTION

THE properties of the linear antenna have been investigated in considerable detail by King.¹ It has been shown theoretically and verified experimentally that an essentially standing-wave distribution of current exists on short antennas of this type. This report deals with a linear antenna very much like the conventional one, except that it has been modified so that a traveling-wave distribution of current exists on all but its end quarter-wavelength, which has a standing-wave. The traveling wave is produced on the antenna very much as a traveling wave is produced on a transmission line. According to transmission-line theory, a pure traveling wave can be created by terminating the line in its characteristic impedance. If the line is assumed lossless, its characteristic impedance is a pure resistance. If the line were terminated in an open circuit, one could produce a traveling wave by placing a resistor equal to the characteristic resistance of the line in series with the line one-quarter wavelength from its end.

¹ R. W. P. King, "The Theory of Linear Antennas," Harvard University Press, Cambridge, Mass.; 1956.

A linear antenna is in two ways similar to an open-ended transmission line. First, it ends in an open circuit since the boundary conditions state that the axial current must go to zero at the end of the antenna. Secondly, a standing-wave distribution of current exists on the antenna. It seems reasonable that it may therefore be possible to create a traveling wave on a linear antenna by placing a resistor one-quarter wavelength from the end.

Unfortunately, the antenna does not have a characteristic resistance associated with it in the TEM sense of the transmission line. Therefore, the correct value of resistance is not immediately obvious. However, by considering simple antenna theory, it can be shown that a relation exists between the characteristic resistance R_c of a transmission line and the expansion parameter ψ of an antenna. The input impedance of an ideal, open-circuited transmission line is

$$Z_{in} = -jR_c \cot \beta_0 h,$$

where h is the length of the line and β_0 is the free space phase constant. The zeroth-order input impedance of a dipole is

$$Z_{in} = -j \frac{\zeta_0}{2\pi} \psi \cot \beta_0 h,$$

where h is the half-length of the dipole and ζ_0 is the free-space characteristic impedance. Therefore, R_c corresponds to $\zeta_0/2\pi \psi$.

The expansion parameter is a somewhat arbitrarily defined quantity which is related to the ratio of the vector potential at any cross section on the outside surface of the antenna to the total axial current in the conductor at that cross section. It can be shown that this ratio is reasonably constant over all parts of the antenna, except where the current is very small or zero. It can be shown further that $\psi \doteq \Omega - 2$, where $\Omega \doteq 2 \ln 2h/a$, where h is the half-length of a dipole, and a is its radius.² Since the expansion parameter is a function of the length of the antenna, while the characteristic resistance is independent of the length of the transmission line, it is obvious that this correspondence is not precise. It does suggest, however, an order of magnitude of the resistance required to approximate a traveling-wave distribution on the antenna, namely 60ψ ohms. Since the quantity $\Omega - 2$ has a value in the range of 9 to 15 for reasonably thin dipoles, a resistance of the order of magnitude 6×10^2 ohms might be expected, for example, when $\Omega = 12$.

The theoretical distribution of current on the resistive-loaded antenna is calculated as follows. The resistor is first replaced by a constant-voltage generator. This is made possible by applying the compensation

theorem of network theory, which states that an impedance in which a current I is flowing can be replaced by a potential difference equal to $-IZ$, without changing the electrical behavior of the network. In replacing each resistor by a constant-voltage generator, one obtains a dipole driven by three separate generators. Due to the linearity of Maxwell's equations, one can simplify the problem still further by applying the superposition theorem, which states that if several sources are present in a linear electrical network, the network may be solved by finding the currents or voltages in the network resulting from the presence of one source at a time, and then superimposing the results. The voltage generators omitted are replaced by connections of zero resistance. This enables one to treat the three-generator antenna as the superposition of two symmetrically-driven antennas; one driven by a single generator at the center, the other driven by two generators, each located one-quarter wavelength from the end. In order to analyze the doubly-driven dipole, superposition may be applied again. This time it is the superposition of two asymmetric dipoles. The asymmetric dipole can be solved approximately by treating its top and bottom parts separately, as if each were a base-driven antenna over an infinite, perfectly conducting plane. The current distribution has been calculated for a loaded antenna of half-length $h = 3\lambda/4$.³

Once a sound experimental setup is available, it is possible to produce a traveling-wave distribution of current on a linear antenna by inserting a series resistance one-quarter wavelength from the end of the antenna. The input impedance, current distribution and radiation field of this antenna then can be measured. From these data, the behavior of the traveling-wave linear antenna can be completely described. It is found that it differs significantly from the corresponding standing-wave antenna. In order to show these differences, numerous comparisons are made between the results obtained from the two antennas.

EXPERIMENTAL RESULTS

Impedance and Admittance

The first experimental task was to determine which value of resistance, when placed one-quarter wavelength from the end of the antenna, produced a distribution of current which most closely resembled a traveling wave. Carbofilm resistors having dc values ranging from 3 ohms to 1 megohm were selected. The impedances of these resistors were measured at 600 Mc, and it was found that as the value of resistance increased, the dc and RF values began to differ. For resistances greater than 500 ohms, the correlation was very poor. The microwave impedance of the resistor was measured

² *Ibid.*, p. 77.

³ E. E. Altshuler, "The Traveling Wave Linear Antenna," Cruft Lab., Harvard University, Cambridge, Mass. Sci. Rep. No. 7; 1960.

by locating the resistor at the end of the center conductor of a coaxial line in series with a short circuit, and then measuring the input impedance.

As has been previously mentioned, the input impedance of a traveling-wave transmission line is independent of the line length. It therefore seems reasonable to assume that the input impedance of a traveling-wave antenna is also essentially independent of its length. Therefore, by measuring the input impedance of a traveling-wave antenna as a function of its length, it is possible to determine which value of resistance, when placed one-quarter wavelength from the end of the antenna, changes the distribution of current so that it most closely resembles a traveling wave, without having to actually measure the distribution of current that exists for each resistor. After extensive measurements which involved the use of numerous resistors, it was found that the insertion of a resistor having a dc resistance of 240 ohms produced an antenna that had an input impedance which was almost independent of length. The RF value of the resistance differed by less than a few per cent from the dc value. It was also discovered that the impedance characteristics of this antenna were not sensitive to a small change from the optimum resistance.

With a 240-ohm resistor fixed at a distance of one-quarter wavelength from the end of the antenna, the input impedance of the antenna was measured at 600 Mc as the half-length h was changed from 0.5λ to

1.5λ in 0.05λ increments. The normalized input impedance of the monopole above an image screen is plotted in Fig. 1. For the purpose of comparison, the measured impedance of the corresponding standing-wave antenna is also plotted on the same graph. The actual measured impedance of the monopole can be obtained by multiplying the normalized value by 123.6 ohms. The impedance of the corresponding dipole is simply twice that of the monopole. It is interesting to note that the impedance of the traveling-wave dipole has a value of approximately $(320 + j110)$ ohms. Therefore, it seems reasonable to assume that the input impedance of the unloaded dipole should approach this value as the dipole length approaches infinity.

In order to investigate the broad-band properties of the traveling-wave antenna, the input impedance of an antenna of half-length, $h = 31.25$ cm, was measured over a frequency range from 300 Mc to 900 Mc in 100 Mc increments. The result is shown in Fig. 2. The 240-ohm resistor was located 12.50 cm from the end of the antenna which corresponded to one-quarter λ at 600 Mc. Once again, the impedance of the corresponding standing-wave antenna is plotted on the same graph.

Distribution of Current

The distribution of current on the 240-ohm loaded antenna was measured for half-lengths ranging from $h = \lambda/2$ to $h = 11 \lambda/4$.³ The relative amplitude $|I|/V_0$,

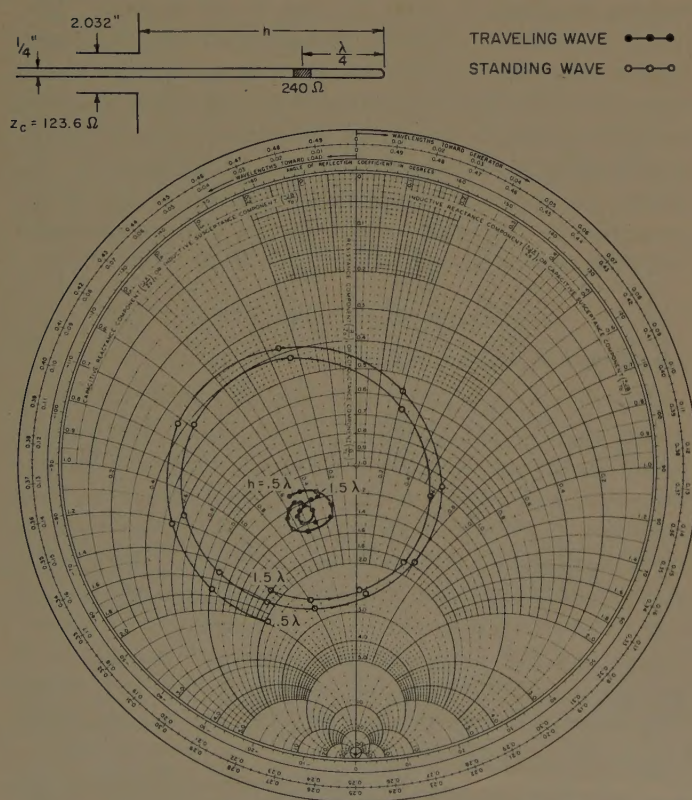


Fig. 1—Measured normalized impedances of traveling- and standing-wave linear antennas at 600 Mc.

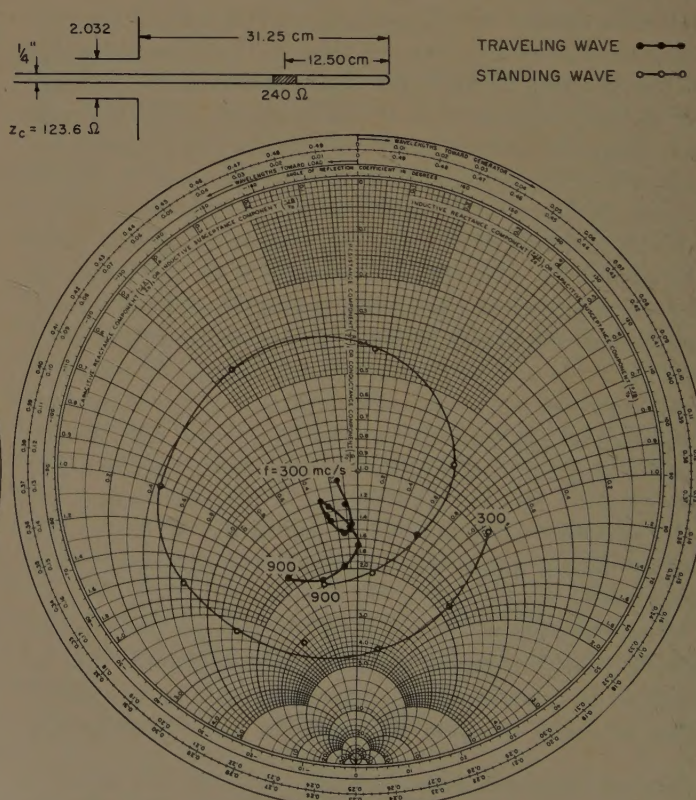


Fig. 2—Measured normalized impedances of traveling- and standing-wave linear antennas ($h = 31.25$ cm).

phase $\theta = \tan^{-1} I'/I''$, and real and imaginary components I''/V_0^e and I'/V_0^e are plotted for antennas of half-length $h = 5\lambda/8$ and $11\lambda/4$ in Figs. 3 and 4 along with θ_T , which is a reference phase that varies linearly with distance along the antenna and thereby corresponds to the phase of a pure traveling wave.

Since the relative amplitude decreases almost exponentially with distance, and since the phase varies almost linearly with distance, the resultant distribution of

current up to the resistor can be approximated by an exponentially attenuated traveling wave. At the resistor, the current amplitude remains continuous and then decreases nearly cosinusoidally to zero at the end of the antenna. The phase undergoes a change in slope at the resistor, since it changes from a linear variation with distance along the antenna to an almost constant value which is independent of distance. Therefore, the distribution of current on the end quarter-wavelength of the loaded antenna behaves very much like that on the unloaded antenna.

It is interesting to observe the behavior of the current in its transition from a standing wave to a traveling wave. This is illustrated in Fig. 5 for $h = 7\lambda/4$. As the inserted resistance is increased from zero ohms to 240 ohms, the standing-wave pattern of the relative current amplitude tends toward a standing-wave ratio of unity. As the resistance is increased above 240 ohms, the standing-wave ratio begins to increase. For the limiting case of $R = \infty$, one would expect the current distribution to resemble that of an antenna of half-length $h = 3\lambda/2$. It is for this reason that the standing-wave pattern shifts by 90° as the resistance is increased from below 240 ohms to above 240 ohms. The phase of the unloaded antenna oscillates somewhat sinusoidally about the linear traveling-wave phase. As the resistance is increased, the amplitude of the sinusoidal oscillation decreases until at 240 ohms it is essentially zero. As the resistance is increased above 240 ohms, the amplitude begins to increase. The shift that the sinusoidal-phase pattern undergoes when the resistance is increased from below 240 ohms to above 240 ohms is 180° . This corresponds to the shift that the phase pattern of an un-

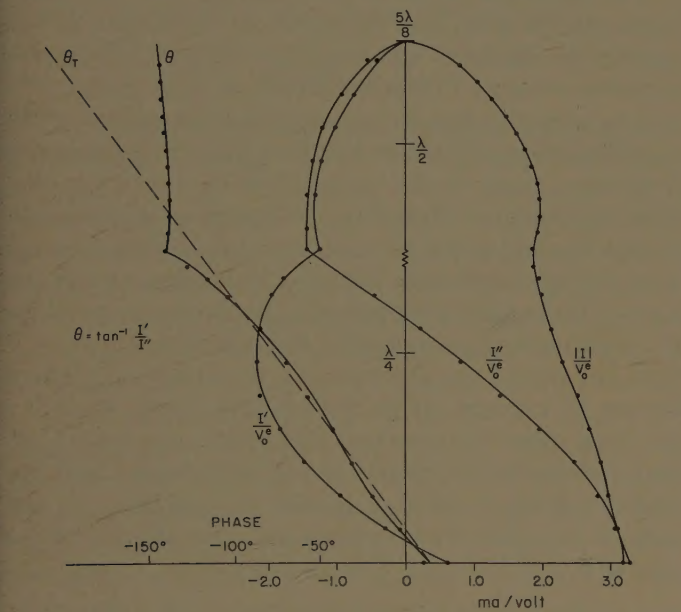


Fig. 3—Distribution of current for $h = 5\lambda/8$.

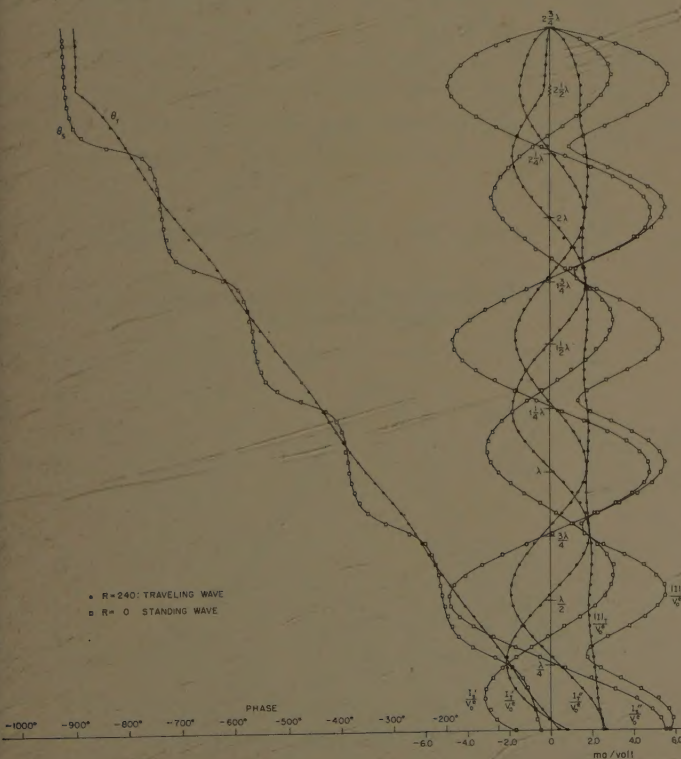


Fig. 4—Distribution of current for $h = 2\frac{3}{4}\lambda$.

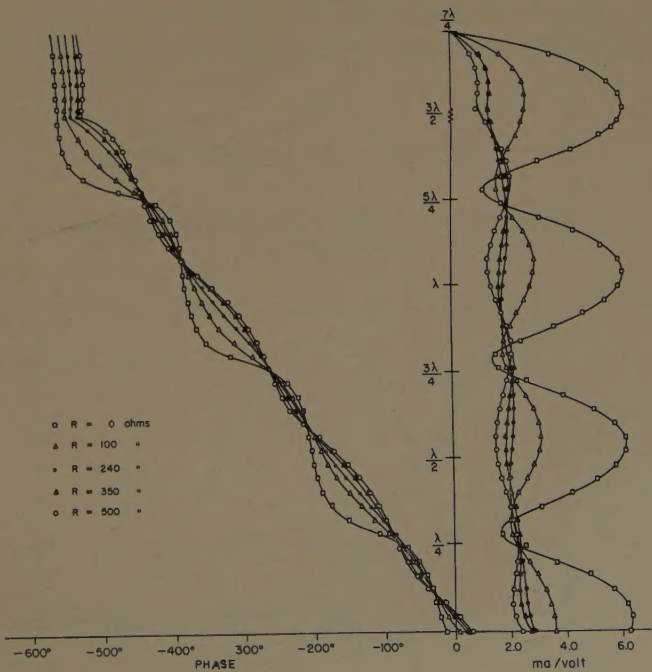


Fig. 5—Distribution of current for $h = 7\lambda/4$.

loaded antenna undergoes when it is reduced in length from $h = 7\lambda/4$ to $h = 3\lambda/2$.

It is expected that the standing-wave distribution of current on the unloaded antenna eventually approaches that of a traveling wave, as the antenna is made longer and longer. The current distributions of the unloaded and 240-ohm loaded antennas of half-length $h = 11\lambda/4$ (the longest antenna that could be measured with the available equipment) are shown in Fig. 4. As can be seen, there is little indication that the unloaded antenna is beginning to approach a traveling-wave distribution. Therefore, it seems reasonable to assume that, as in the case of the open-circuited transmission line, the antenna must be extremely long before a traveling-wave distribution comparable to that obtained by the insertion of a 240-ohm resistor is produced.

Radiation Field

The relative power patterns of traveling- and standing-wave dipoles are shown in Figs. 6 and 7. As is expected, the directional properties do not differ very much for short dipoles, since the current distributions are somewhat alike. However, as the dipole becomes longer, a significant difference arises in the respective patterns. A minor lobe does not appear in the radiation pattern of the traveling-wave dipole until it is much longer than the corresponding standing-wave dipole. This behavior is in agreement with the power patterns

which were calculated earlier.³ It seems that the null, which ordinarily appears in the radiation pattern of the conventional dipole, is essentially filled in for the traveling-wave case. Therefore, the sidelobe in the conventional dipole pattern becomes part of the main lobe in the corresponding traveling-wave dipole pattern. It is interesting to note that some traveling-wave dipoles have half-power beamwidths of approximately 100° which is considerably larger than the beamwidths that can be obtained with conventional dipoles.

The radiation patterns of traveling- and standing-wave dipoles were also measured as a function of frequency for dipoles of half-length $h = 32.6$ cm. The power patterns of these dipoles are shown in Figs. 8 and 9. It can be seen that where the directional properties of the standing-wave dipole are quite sensitive to a change in frequency, those of the traveling-wave dipole are relatively insensitive. Therefore, the traveling-wave dipole, in addition to having a broad-band impedance, also has a broad-band radiation pattern. Naturally, as the frequency is changed from 600 Mc, the frequency at which the resistor is at an optimum distance of one-quarter λ from the end of the antenna, the traveling-wave distribution of current up to the resistor tends toward a standing-wave distribution. Therefore, one would expect the directional properties of both loaded and unloaded dipoles to be very similar at 1200 Mc, the frequency at which the resistor is $\frac{1}{2}\lambda$ from the end of the antenna.

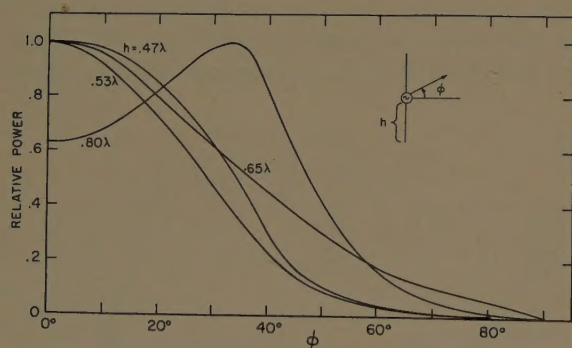


Fig. 6—Measured power pattern of traveling-wave dipole at 600 Mc.

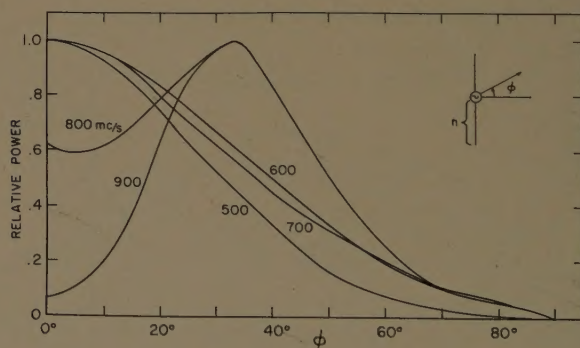


Fig. 8—Measured power pattern of traveling-wave dipole ($h = 32.6$ cm).

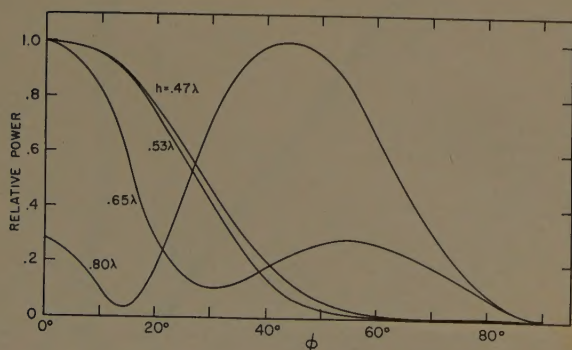
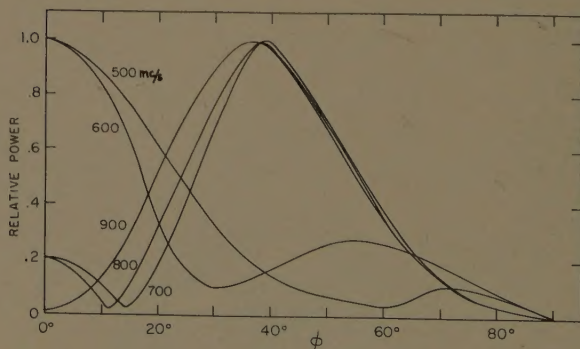


Fig. 7—Measured power pattern of standing-wave dipole at 600 Mc.



MEASURED POWER PATTERN OF
STANDING-WAVE DIPOLE ($h = 32.6$ cm)

Fig. 9—Measured power pattern of standing-wave dipole ($h = 32.6$ cm).

Efficiency

Let the efficiency of an antenna be defined as the ratio of the power radiated by the antenna to the power supplied to the antenna. The real power that is delivered to the antenna and is not radiated is usually dissipated in the form of heat. In general, the conventional linear antenna has a radiating efficiency of close to 100 per cent. The only losses which are present are those due to the finite conductivity of the antenna and the insulators which may be used to support it. The 240-ohm loaded antenna is approximately 50 per cent efficient.³

CONCLUSIONS

The results which have been reported here represent an extensive investigation of the traveling-wave linear antenna and its comparison with the conventional linear antenna. It has been shown experimentally that an essentially traveling-wave distribution of current can be produced on a linear antenna of $\Omega \approx 10$, by inserting a resistance of approximately 240 ohms one-quarter wavelength from the end of the antenna. The radiation resistance of the traveling-wave monopole above an image plane is approximately 160 ohms. Therefore, the amplitude of the current at the resistor must always be less than the amplitude at the input of the antenna, since more power must be delivered to the antenna than can be dissipated in the resistor. For this reason, the current amplitude on the traveling-wave antenna is always attenuated. As the resistance is increased from its optimum value of 240 ohms toward infinity or decreased toward zero, the current distribution changes from an attenuated traveling wave to a standing wave. This transition is quite gradual. It is expected that the current distribution would undergo a similar transition when the resistor is moved, for example, from its optimum position of one-quarter wavelength from the end of the antenna to $\frac{1}{2}$ wavelength from the end.

The input impedance of the traveling-wave antenna has been shown to remain essentially constant as a function of antenna length. It is for this reason that this antenna is very broad-band compared to the conventional linear antenna. A broad-band antenna is in practice very desirable since it allows a good impedance match to be obtained over a wide band of frequencies. As has been pointed out earlier, the bandwidth limitation results from the fact that upon changing frequency, the electrical distance of the resistor from the end of the antenna is changed from its optimum length. Therefore, the essentially constant input impedance of the traveling-wave antenna as a function of length tends to the variable input impedance of the standing-wave antenna.

The directional properties of the traveling-wave dipole have been shown to be quite different from those of the corresponding standing-wave dipole. Whether they are more useful depends on the particular application for the antenna. The radiation properties of the traveling-wave dipoles are superior to those of the conventional dipole in two respects. First, the traveling-wave dipole can be operated over a relatively wide frequency range with only a small variation in its directional properties. Secondly, it can be designed to have a half-power beamwidth which is over 20° larger than that which can be obtained with a conventional dipole.

An investigation directed toward improving the efficiency of this antenna is presently being conducted. It may be possible to replace the carbon resistor by a more useful resistive element, for example, a resonant antenna with the appropriate radiation resistance. Therefore, energy ordinarily dissipated in ohmic losses will instead be radiated by the second antenna.

ACKNOWLEDGMENT

The author is indebted to Professor R. W. P. King for his very helpful guidance and encouragement during the course of this research.

Resonance Characteristics of a Corrugated Cylinder Excited by a Magnetic Dipole*

J. R. WAIT†, SENIOR MEMBER, IRE, AND A. M. CONDA†, MEMBER, IRE

Summary—Radiation from an axial magnetic-current element in the presence of a corrugated cylinder is considered. It is indicated that the power radiated in a given mode depends on the surface reactance, the circumference of the cylinder and the elevation angle. For certain values of the parameters, particular modes are strongly excited in a manner corresponding to the resonance condition of the circumferential (or spiral) surface waves.

INTRODUCTION

THE nature of surface waves on curved boundaries has been receiving considerable attention recently.¹ Of particular interest is the situation where the supporting structure is closed,² in which case the structure may be resonant by virtue of the circulating nature of the waves.³ Such resonant effects have been discussed previously for circular and elliptical cylinders with assumed reactive boundary conditions and line-source excitation.⁴ It was demonstrated that when the dimensions of the circular cylinder and its surface reactance were chosen in a certain way, the radiated energy was confined to a single mode which had a radiation pattern of the form $\cos m\phi$, where m is an integer. A similar situation existed for elliptical cylinders but then it was necessary for the surface reactance to vary in a prescribed manner.⁴

These results mentioned above are applicable only to a purely two-dimensional situation. Of somewhat greater practical interest is the situation where a cylindrical structure is excited by a dipole located in its neighborhood. This problem is investigated in the present paper.

FORMAL SOLUTION

The model chosen is a circular cylinder of radius a and of infinite length which is corrugated by shallow grooves parallel to the axis. Choosing a cylindrical coordinate system (ρ, ϕ, z) , the magnetic dipole of moment Kdz_0 is located at ρ_0, ϕ_0, z_0 and is oriented in the z (axial) direction. The situation is illustrated in Fig. 1.

* Received by the PGAP, August 1, 1960; revised manuscript received, December 21, 1960. The research reported here was sponsored by the Electronics Res. Directorate, AF Cambridge Res. Labs., AF Res. Div., Air Res. and Dev. Command, Cambridge, Mass.

† Natl. Bureau of Standards, Boulder, Colo.
¹ See, for example, section on Surface Waves in the Special Supplement of IRE TRANS. ON ANTENNAS AND PROPAGATION, vol. AP-7, pp. S132-S288; December, 1959.

² J. R. Wait and A. M. Conda, "Radiation from slots on dielectric-clad and corrugated cylinders," *J. Res. N.B.S.*, vol. 59, pp. 307-316; November, 1957.

³ A. L. Cullen, "Surface wave resonance effect in a reactive cylindrical structure excited by an axial line source," *J. Res. N.B.S.*, vol. 64D, pp. 13-20; January-February, 1960.

⁴ J. R. Wait and A. M. Conda, "On the resonance excitation of a corrugated cylinder antenna," Monograph No. 386E, IEE; June, 1960.

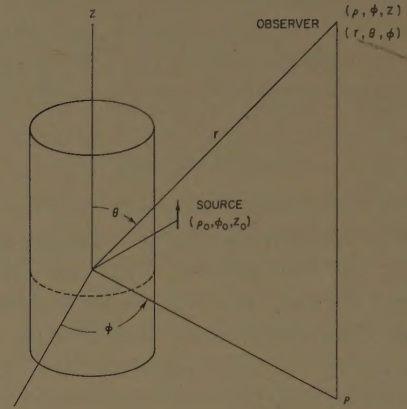


Fig. 1—The longitudinally-corrugated cylinder and an axial-magnetic dipole in its vicinity.

The boundary conditions at the surface of the cylinder (*i.e.*, $\rho = a$) are $E_\phi = -iXH_z$ and $E_z = 0$ where X is the average surface reactance. If the grooves are rectangular in cross section, with periodicity d , width w , and depth l , it is known that, approximately²

$$X \cong \eta_0 \frac{w}{d} \tan kl$$

where $\eta_0 \cong 120 \pi$ and $k = 2 \pi / \text{wavelength}$. This formula for X is valid provided that $kd \ll 1$ and kl is not near an odd multiple of $\pi/2$.

For the presently formulated problem, it is possible to derive the fields from a magnetic Hertz vector which has only a z component, Π^* . Thus

$$\begin{aligned} E_\rho &= \frac{k^2}{i\epsilon\omega} \frac{\partial \Pi^*}{\partial \phi}, & H_\phi &= \frac{\partial^2 \Pi^*}{\rho \partial \phi \partial z} \\ E_\phi &= -\frac{k^2}{i\epsilon\omega} \frac{\partial \Pi^*}{\partial \rho}, & H_\rho &= \frac{\partial^2 \Pi^*}{\partial \rho \partial z} \\ E_z &= 0, & H_z &= \left(k^2 + \frac{\partial^2}{\partial z^2} \right) \Pi^*, \end{aligned} \quad (1)$$

when ϵ is the dielectric constant of free space. A suitable integral form for Π^* is suggested immediately by the nature of the solution for an axial magnetic dipole in the neighborhood of a perfectly conducting cylinder.⁵ It is given by

$$\begin{aligned} \Pi^* &= -\frac{Kdz_0}{8\pi\mu\omega} \sum_{m=0}^{\infty} \epsilon_m \cos m(\phi - \phi_0) \int_{-\infty}^{+\infty} H_m^{(2)}(v\rho_0) \\ &\quad \times [J_m(v\rho) - H_m^{(2)}(v\rho) A_m] e^{-ih(z-z_0)} dh \end{aligned} \quad (2)$$

⁵ J. R. Wait, "Electromagnetic Radiation from Cylindrical Structures," Pergamon Press, New York, N. Y., p. 28, ff.; 1959.

for $\rho < \rho_0$. In this equation the symbols have the following meaning:

- μ = permeability of free space
 K = magnetic current of source element
 dz_0 = infinitesimal length of source element
 $\epsilon_0 = 1, \epsilon_m = 2$ ($m = 1, 2, 3 \dots$)
 ρ, ϕ, z = cylindrical coordinates of observer
 ρ_0, ϕ_0, z_0 = cylindrical coordinates of source
 $v = (k^2 - h^2)^{1/2}$
 $J_m(x)$ = Bessel function of first type of order m
 $H_m^{(2)}(x)$ = Hankel function of second kind of order m .

It is readily seen that the boundary conditions at $\rho = a$ are satisfied if

$$A_m(v) = \frac{J_m'(va) + \bar{G}J_m(va)}{H_m^{(2)'}(va) + \bar{G}H_m^{(2)}(va)} \quad (3)$$

and

$$\bar{G} = \frac{X}{\eta_0} \frac{v}{k} = G \frac{(k^2 - h^2)^{1/2}}{k},$$

where $G = X/\eta_0$. When X is set equal to zero, the earlier solution for the perfectly-conducting cylinder is recovered.⁶

THE RADIATION FIELDS

In the far field (*i.e.*, $k\rho \gg 1$), the infinite integral in (2) may be evaluated by a saddle-point method. Following the earlier work⁵ that deals with the perfectly-conducting cylinder, it easily follows, in terms of spherical coordinates, that

$$E_\phi \cong \frac{e^{-ikr}}{r} dS(\theta) M^*(\phi) \quad (4)$$

when

$$dS(\theta) = -\frac{ik \sin \theta}{2\pi} K e^{ikz_0 \cos \theta} dz_0 \quad (5)$$

and

$$M^*(\phi) = \frac{1}{2} \sum_{m=0}^{\infty} \epsilon_m \cos m(\phi - \phi_0) e^{im\pi/2} \times [J_m(k\rho_0 \sin \theta) - A_m(k \sin \theta) H_m^{(2)}(k\rho_0 \sin \theta)]. \quad (6)$$

The result is easily extended to a magnetic current $K(z_0)$ extending from z_1 to z_2 by simply integrating over z_0 . Thus, $dS(\theta)$ is replaced by $S(\theta)$ where

$$S(\theta) = \frac{-ik \sin \theta}{2\pi} \int_{z_1}^{z_2} K(z_0) e^{ikz_0 \cos \theta} dz_0. \quad (7)$$

To simulate an axial slot on the cylinder, the source element is now allowed to approach the cylinder. Thus, setting $\rho_0 = a$, it follows that

$$M^*(\phi) = \frac{1}{i\pi x} \sum_{m=0}^{\infty} \frac{\epsilon_m \cos m(\phi - \phi_0) e^{im\pi/2}}{H_m^{(2)'}(x) + \bar{G}H_m^{(2)}(x)}, \quad (8)$$

where $\bar{G} = G \sin \theta$ and $x = ka \sin \theta$. Then, further specializing the magnetic current element to be a half wave in length with a sinusoidal variation, it is a simple matter to arrive at

$$E_\phi \cong -\frac{e^{-ikr} K_0 \cos\left(\frac{\pi}{2} \cos \theta\right)}{xr\pi^2 \sin \theta} \sum_{m=0}^{\infty} \frac{\epsilon_m e^{im\pi/2} \cos m\phi}{H_m^{(2)'}(x) + \bar{G}H_m^{(2)}(x)}, \quad (9)$$

which is valid in the far field.

In the equatorial plane (*i.e.*, $\theta = \pi/2$ or $z = 0$), the radiation field may be written

$$E_\phi \cong -\frac{e^{-ikr} K_0}{\pi^2 r} Q(\phi), \quad (10)$$

where

$$Q(\phi) = \frac{1}{x} \sum_{m=0}^{\infty} \frac{\epsilon_m e^{im\pi/2} \cos m\phi}{H_m^{(2)'}(x) + \bar{G}H_m^{(2)}(x)} \quad (11)$$

where $x = ka$.

Numerical values of $Q(\phi)$ were given by Wait and Conda² for ϕ from 0 to 180°, $x = 2, 3$ and 8 and several values of G in the range between 0 and 0.3. It was observed that in several cases the function $Q(\phi)$ varied in an oscillatory manner with ϕ . This is not surprising since a term in the summand becomes large when $H_m^{(2)'}(x) + \bar{G}H_m^{(2)}(x)$ is small. In fact, since G is real, the magnitude of this quantity has a minimum when

$$G \cong -\frac{Y_m'(x)}{Y_m(x)}, \quad (12)$$

where $Y_m(x)$ is the Neumann function of order m . For example, if $x = 3$, then the term corresponding to $m = 6$ is predominant if

$$G = 1.65,$$

which corresponds to an inductive surface reactance,

$$X = 120\pi = 622 \text{ ohms.}$$

In this case the pattern can be expected to be almost proportional to $\cos 6\phi$ since the other terms in the series expansion are relatively small. To confirm this statement, the magnitude $|Q(\phi)|$ is plotted in Fig. 2 as a function of ϕ from 0 to 180°, for $ka = 3$ and $G = \bar{G} = 1.65$. Indeed, it is seen that the pattern behaves in a manner similar to the function $|\cos m\phi|$.

The above-mentioned pattern is applicable only to the equatorial plane (*i.e.*, $\theta = 90^\circ$) if $ka = 3$ and $G = 1.65$.

For other values of θ , the structure is no longer resonant. However, if $x = ka \sin \theta = 3$ and $\bar{G} = 1.65$ or $G = 1.65/\sin \theta$, resonance is again achieved. Thus the pattern plotted in Fig. 2 is applicable to other angles if the size of the cylinder and the surface reactance are readjusted.

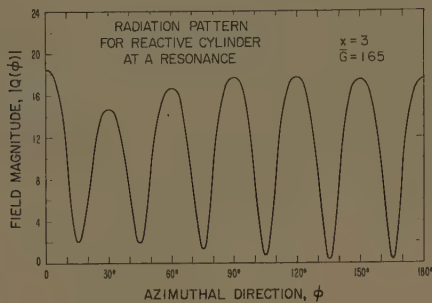


Fig. 2—The azimuthal radiation pattern of a magnetic-current element on the surface of a corrugated cylinder. The surface reactance of the cylinder is chosen so that the $\cos \phi$ term is predominant.

POWER CONSIDERATIONS

The power radiated from the magnetic current in the presence of the cylinder is now considered. The total power P is obtained by integrating the radial component of the Poynting vector over an infinite sphere. Thus,

$$P = \lim_{r \rightarrow \infty} \int_{\theta=0}^{\pi} \int_{\phi=0}^{2\pi} S_r r^2 \sin \theta d\theta d\phi \quad (13)$$

where

$$S_r = -\frac{E_\phi H_\theta^*}{2} \cong \frac{E_\phi E_\phi^*}{2\eta_0}. \quad (14)$$

Since K_0 is by nature a voltage, it is convenient to define a radiation conductance g by

$$P = K_0^2 g / 2. \quad (15)$$

Because of the orthogonality of the series expansions for E_ϕ , the integration with respect to ϕ is easily carried out.⁶ Then, for the half-wave magnetic-current element, the final expression for g may be written

$$\eta_0^2 g = \sum_{m=0}^{\infty} \int_0^{\pi/2} I_m(\theta) d\theta, \quad (16)$$

where

$$I_m(\theta) = \frac{480}{\pi^2} \frac{\cos^2 \left[\frac{\pi}{2} \cos \theta \right]}{(ka)^2 \sin^3 \theta} \frac{1}{|H_m^{(2)'}(ka \sin \theta) + G \sin \theta H_m^{(2)}(ka \sin \theta)|^2}. \quad (17)$$

⁶ *Ibid.*, p. 48,

The quantity $I_m(\theta)$ can be interpreted as the power flowing through a conical segment from θ to $\theta + d\theta$ for the m th mode. To illustrate the nature of the power flow, $\sqrt{I_m(\theta)}$ is plotted as a function of θ from 0 to 90° for $ka = 3$ and $G = 1.65$ in Fig. 3. It is immediately noticed that at $\theta = 90^\circ$, the 6th mode is highly resonant as expected. At $\theta = 63^\circ$, however, the 5th mode is predominant. This corresponds to a quasi-resonance. Further quasi-resonances occur at smaller angles when the successively lower order modes, in turn, become predominant.

The effect of changing the surface reactance to a larger value is illustrated in Fig. 4 where $G = 2.00$. The lower-order modes are now more predominant.

The integrations with respect to θ , indicated in (16), were carried out by a graphical method which involved replotting $I_m(\theta)$ on a linear scale and using a planimeter to obtain the area under the curves. This approach was supplemented by a semi-analytical method which consisted essentially of matching a Gaussian function $\exp(-\alpha(\theta - \theta_0)^2)$ to the resonant peaks at $\theta = \theta_0$. By a judicious combination of these two methods, a reason-

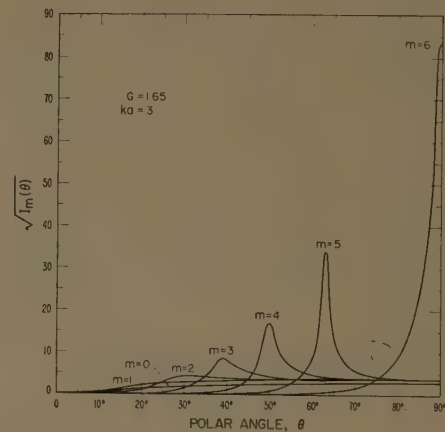


Fig. 3—The quantity $I_m(\theta)$ is proportional to the power flux at angle θ . The surface reactance is chosen so that the $m=6$ mode is resonant in the equatorial plane (*i.e.*, at $\theta = 90^\circ$).

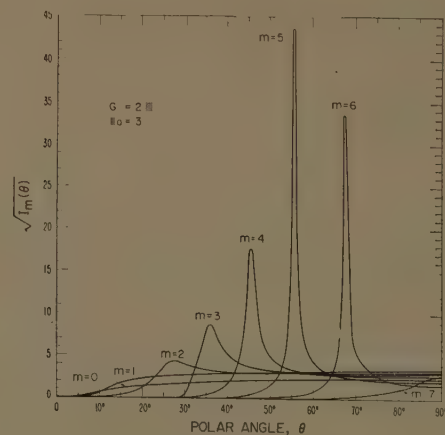


Fig. 4—Same as Fig. 3 but with a larger value of the surface reactance.

able estimate of the power going into each individual mode was obtained. For $ka=3$, the results are given in Table I.

TABLE I
Tabulation of $\int_0^{\pi/2} I_m(\theta) d\theta$

m	$G=1.65$	$G=2.00$
0	7.3	5.7
1	15.3	11.8
2	17.2	12.9
3	20.8	15.6
4	30.6	22.7
5	67.0	40.1
6	217.4	28.9
7	0.04	0.82
8	0.00 . . .	0.00 . . .
\sum_m	376.0	139.0

The summation of these entries indicated in Table I is proportional to the total power supplied by the source. The corresponding values of the conductance g are 2.67 and 0.98 mmhos, respectively, for $G=1.65$ and 2.00, respectively. From previous work, it is known that the corresponding value of G is 0.92 mmho for $ka=3$. The presence of axial corrugations is thus seen to increase the total radiation conductance somewhat.

AN EQUIVALENT ELECTRICAL PROBLEM

The foregoing analysis has been specially developed for a magnetic-current element parallel to an axially-corrugated cylinder. The results, however, are also formally applicable to an electric current element parallel to a cylinder which has the following boundary conditions: $E_z = -iX_e H_\phi$ and $H_z = 0$ at $\rho = a$, where X_e is the (average) surface reactance of the cylinder. The condition that H_z vanish on the cylinder requires that it be effectively a perfect magnetic conductor in the axial direction. The changes in the formulas developed above are listed as follows:

In (2), left-hand side, Π^* is replaced by Π , the z components of the electric Hertz vector,

In (2), right-hand side, $-Kdz_0/(8\pi\mu\omega)$ is replaced

by $-Idz_0/8\pi\epsilon\omega$ when I is the electric current of the dipole element.

In (3), right-hand side, $A_m(v)$ has the same form, but now

$$\bar{G} = \frac{\eta_0}{X_e} \frac{v}{k} = \frac{\eta_0}{X_e} \frac{(k^2 - h^2)^{1/2}}{k} \quad (18)$$

and

$$G = \eta_0/X_e.$$

In spherical coordinates the radiation pattern is then given by

$$E_\theta = -\frac{\eta_0 e^{-ikr}}{r} S(\theta) M(\phi), \quad (19)$$

where $M(\phi)$ has exactly the same form as $M^*(\phi)$, given by (16), but of course $A_m(k \sin \theta)$ is to be modified as mentioned above. Also, in this case,

$$S(\theta) = -\frac{ik \sin \theta}{2\pi} \int_{z_0}^{z_2} I(z_0) e^{ikz_0 \cos \theta} dz_0. \quad (20)$$

The remainder of the analysis may be carried over directly so that the results of the power calculation apply also to a half-wave electric antenna with sinusoidal current. In fact, the radiation resistance r is given explicitly by

$$r = \sum_{m=0}^{\infty} \int_0^{\pi/2} I_m(\theta) d\theta \quad (21)$$

when $I_m(\theta)$ is given by (17), remembering only that G is now to be identified with η_0/X_e where X_e is a capacitive reactance.

This equivalent electric problem is probably only of pure academic interest since the boundary conditions are somewhat unrealistic. Nevertheless, it seems worth mentioning since the results may have some similarity with related problems requiring more sophisticated approaches.⁷

⁷ J. R. Wait, "Radiation from an electric dipole in the presence of a corrugated cylinder," *Appl. Sci. Res.*, vol. 6, Section B, pp. 117-123; 1955.

New Circularly-Polarized Frequency-Independent Antennas with Conical Beam or Omnidirectional Patterns*

J. D. DYSON†, MEMBER, IRE, AND P. E. MAYES†, MEMBER, IRE

Summary—A conical beam may be obtained from balanced equiangular spiral antennas by constructing an antenna with more than two spiral arms and symmetrically connecting these arms to provide a suppression of the radiated fields on the axis of the antenna. The angle of this conical beam can be controlled and, with proper choice of parameters, confined to the immediate vicinity of the azimuthal ($\theta = 90^\circ$) plane.

An antenna with four symmetrically spaced arms can provide a radiation pattern that is within 3 db of omnidirectional circularly polarized coverage in the azimuthal plane. The standing-wave ratio of this antenna referred to a 50-ohm coaxial cable is less than 2-to-1 over the pattern bandwidth.

This four-arm version retains the wide frequency bandwidths of the basic conical log-spiral antenna, and it provides a coverage which heretofore has been difficult to obtain even with narrow-band antennas.

I. INTRODUCTION

THE balanced planar and conical equiangular spiral antennas have been demonstrated to have essentially frequency-independent radiation and impedance characteristics over bandwidths which are at the discretion of the design engineer.^{1,2} These antennas, based upon the equiangular or log-spiral³ curve, have the property that the highest and lowest usable frequencies are independent. The highest usable frequency is determined by the diameter of the truncated region at the origin, which must remain small in terms of the operating wavelength, and the lowest usable frequency by the arm length and hence the maximum diameter of the antenna.

The two-arm planar antenna provides circularly-polarized, single-lobe, bidirectional radiation on the axis of the antenna. An orthogonal projection of the two-arm planar antenna on a conical surface forms an antenna which, over a suitable range of parameters, confines the radiation to a single lobe along the axis of the cone in the direction of its apex.

* Received by the PGAP, August 7, 1960; revised manuscript received, January 23, 1960. A condensed version of this paper was presented at the URSI-IRE Spring Meeting, Washington, D. C., May 3, 1960, under the title "The Log-Spiral Omnidirectional Circularly Polarized Antenna." This work was supported by Wright Air Dev. Div. under contract AF33(616)-6079, and is covered in University of Illinois Antenna Lab. Tech. Rept. No. 46; June 20, 1960.

† Antenna Lab., Dept. of Elec. Engr., University of Illinois, Urbana, Ill.

¹ J. D. Dyson, "The equiangular spiral antenna," IRE TRANS. ON ANTENNAS AND PROPAGATION, vol. AP-7, pp. 181-187; April, 1959. Also University of Illinois, Antenna Lab., Urbana, Tech. Rept. No. 21; September 15, 1957.

² J. D. Dyson, "The unidirectional equiangular spiral antenna," IRE TRANS. ON ANTENNAS AND PROPAGATION, vol. AP-7, pp. 329-334; October, 1959. Also University of Illinois, Antenna Lab., Urbana, Tech. Rept. No. 33; July 10, 1958.

³ A convenient abbreviation for logarithmic spiral, a synonym for equiangular spiral.

It is possible to devise a multitude of structures by using the log-spiral arm as a basic element. Many different excitations may be used when several log-spiral arms with a common origin are placed on a cone or plane. Some configurations and excitations produce radiation patterns which are distinctly different from those obtained heretofore. It is the purpose of this paper to introduce a simple theory relating the excitation and the radiation fields (insofar as now possible), and to present data showing the performance of the four-arm conical log-spiral antenna with one particular excitation.

II. THE CONICAL LOG-SPIRAL ANTENNA

A. The Basic Structure

The conical log-spiral antenna with its associated coordinate system is shown in Fig. 1. On a plane surface, the edges of one arm of a logarithmic spiral antenna may be defined by

$$\rho_1' = \rho_0' e^{a\phi}$$

and

$$\rho_2' = \rho_0' e^{a(\phi-\delta)}$$

and since

$$\tan \alpha = \frac{\rho'}{d\rho'/d\phi} = \frac{1}{a}$$

$$\rho_1' = \rho_0' e^{(1/\tan \alpha)\phi},$$

The orthogonal projection of ρ_1' and ρ_2' on the surface of revolution $\pi - \theta = \theta_0$ is defined by

$$\rho_1 = \rho_0 e^{(\sin \theta_0 / \tan \alpha)\phi}$$

and

$$\begin{aligned} \rho_2 &= \rho_0 e^{(\sin \theta_0 / \tan \alpha)(\phi-\delta)} \\ &= K\rho_1, \end{aligned}$$

where

$$K = e^{(-\sin \theta_0 / \tan \alpha)\delta},$$

ρ_0 is the radius vector from the origin to the truncation of the spiral at the apex region, and ρ_1 and ρ_2 are the radius vectors to the inner and outer edges of the exponentially expanding arm at a given angle ϕ . The angle δ is a constant and of such value that if the curve traced by ρ_1 is rotated about the axis through the angle δ , it will coincide with the curve traced out by ρ_2 . The angle α , a constant, is the angle between the radius vector and a tangent to the log-spiral curve at point of intersection.

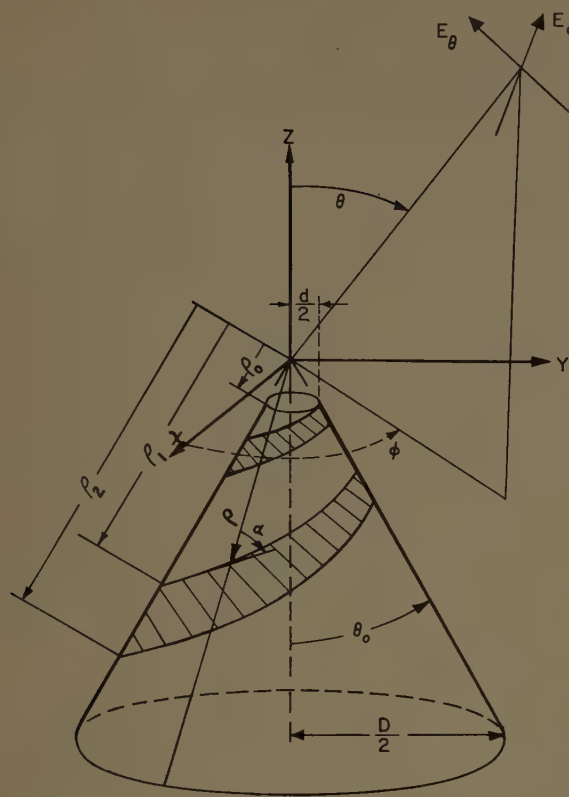


Fig. 1—A conical log-spiral antenna with associated coordinate system.

The second arm of the balanced structure is defined by rotating curves 1 and 2 through π radians. Hence the defining parameters are: the included cone angle $2\theta_0$; the arm width determined by δ , or K ; the rate of spiral α ; the base diameter D ; and the apex diameter d .

B. THE RADIATION PATTERN BEAMWIDTH

The beamwidth of the two-arm conical antenna can be controlled over a limited range by a suitable choice in the rate of spiral. Fig. 2 shows typical electric field radiation patterns for balanced two-arm antennas constructed on a 20° cone with an α of 73° , 60° , and 45° . Typical half-power beamwidths range from 60° – 70° for an α of 82° , 70° – 80° for an α of 73° , and 160° – 180° for an α of 60° . As the angle α is decreased to 45° the beamwidth increases to 180° – 200° . Pattern cuts through the axis and perpendicular to the axis of the antenna [Fig. 2(c)] indicate that this latter case provides essentially circularly polarized coverage in one hemisphere and omnidirectional coverage on the $\theta = 90^\circ$ plane.

It has been pointed out that a modified version of the balanced conical antenna is obtained when the width of the arm is made constant rather than tapered.² This form of the antenna is readily constructed of wire or cable. However, it is only an approximation to the true equiangular spiral structure. The approximation is good for relatively tightly spiraled antennas, *i.e.*, α greater than 60° , and results in only minor pattern changes. As

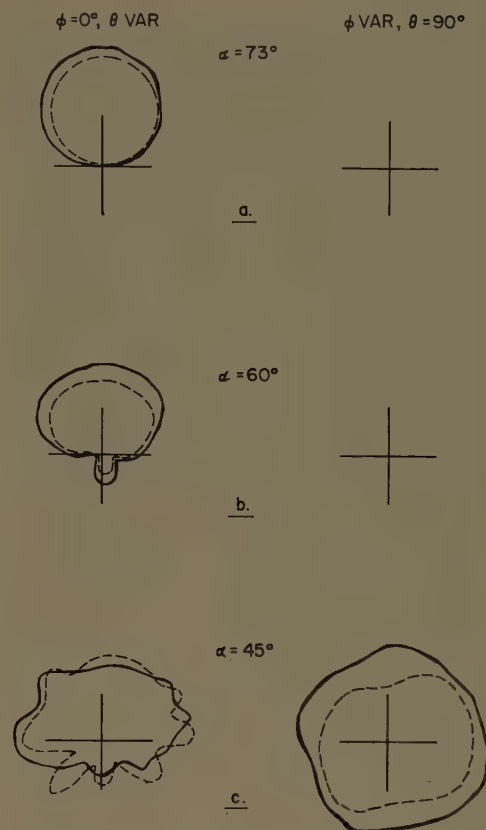


Fig. 2—Variation in electric field pattern of typical balanced two-arm conical equiangular spiral antenna $\theta_0 = 10^\circ$. — E_ϕ , --- E_θ , polarization.

the angle α is decreased to the neighborhood of 45° to 50° , marked pattern changes occur for the wire approximation, including a multilobing of the main beam and large radiation off the base of the cone. Thus, to realize patterns such as the ones shown in Fig. 2(c), the decrease in the rate of spiral must be accompanied by an increase in the arm width, *i.e.*, increase in δ (or K). The patterns shown in Fig. 2(c) were for an antenna constructed with the following parameters: $2\theta_0 = 20^\circ$, $\alpha = 45^\circ$, and $K = 0.75$ ($\delta \cong 94^\circ$).

III. THE CONICAL BEAM ANTENNA

A. The Principle

When using multiple-arm structures the number of choices of feeding systems increases.⁴ There are basic excitations of multi-terminal antennas which are simply related to the azimuthal variations of fields of the form $e^{\pm im\phi}$ associated with solutions of Maxwell's equations. The parameter m must be an integer to make the field single-valued.

Excitations of the spiral arms which correspond to groups of the radiation "modes" associated with integral values of the exponent m are readily apparent. The

⁴ G. A. Deschamps, "Impedance properties of complementary multiterminal planar structures," IRE TRANS. ON ANTENNAS AND PROPAGATION, vol. AP-7, pp. S371–S378, December, 1959. Also University of Illinois, Antenna Lab., Urbana, Tech. Rept. No. 43; November 11, 1959.

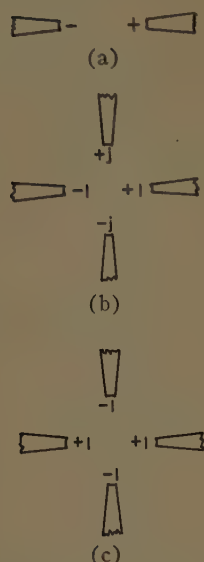


Fig. 3—Possible feeding arrangements for multiarm structures.

customary excitation of the two-arm spirals, as shown in Fig. 3(a), will produce only modes with odd integer values of m , since a rotation of 180° is equivalent to a 180° phase shift:

$$e^{\pm jm\phi} = -e^{\pm jm(\phi+\pi)}, \quad m = \pm 1, \pm 3, \pm 5, \text{ etc.}$$

The low axial ratio measured in the fields produced by log-spiral antennas indicates that this configuration produces very little cross-polarized field. The sense of rotation of the circularly polarized field is determined by the direction of winding of the spiral arms. The assumption of a traveling wave of current along the antenna arms with phase progression away from the feed point at the apex leads to a direction of phase delay in the fields produced by these currents. The sense of the polarization can be determined from the hand used when pointing the fingers in the direction of the phase delay of the currents and the thumb in the direction of the radiated beam. This definition corresponds to the IRE Standard. Thus the antenna wound as shown in Fig. 1 will produce a left-hand circularly-polarized beam. For right-hand circular polarization in the positive-half-space the phase must be delayed in the direction of increasing ϕ ; for the left-hand sense, the phase must be advanced in the increasing ϕ direction. Thus the spirals wound in the right-hand sense will produce primarily fields which have a phase variation of the form $e^{-jm\phi}$; those wound in the left-hand sense, $e^{+jm\phi}$.

The remarkable property of the conical log-spiral antennas is the purity with which they produce the lowest-order fields consistent with the sense of winding and excitation. An experimental investigation of several conical log-spiral antennas indicates excellent agreement between the phase variation of the lowest-order mode and measured values. Fig. 4 shows the relative phase of

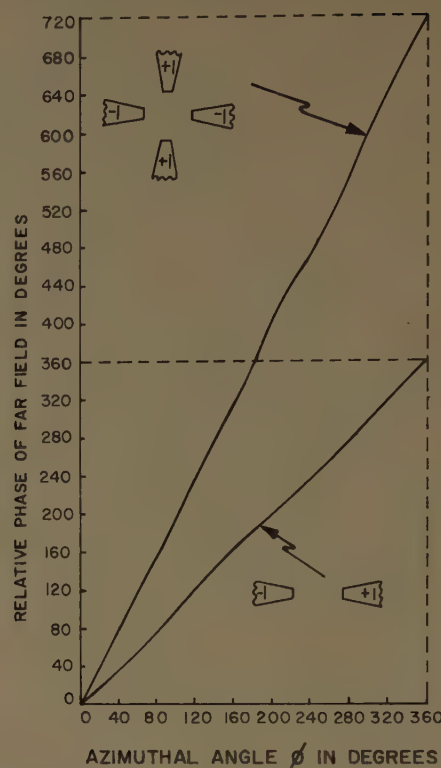


Fig. 4—Measured phase of radiated field as a function of the azimuthal angle, ϕ , for two antennas $\alpha=45^\circ$, $\theta=90^\circ$.

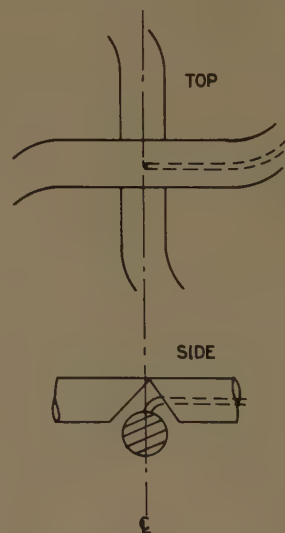


Fig. 5—"Infinite balun" feed used on a four-arm conical beam antenna.

the radiated electric field (in the $\theta=90^\circ$ plane) as a function of the azimuthal angle for two antennas, a two-arm left-hand circular-polarized antenna excited to produce fields varying as $e^{+j\phi}$, and a four-arm left-hand polarized antenna excited to produce fields varying as $e^{+j2\phi}$. These curves exhibit a nearly straight line relationship.

Examination of the solutions of Maxwell's equations in spherical coordinates shows that values of m different from unity are always accompanied by a null along the

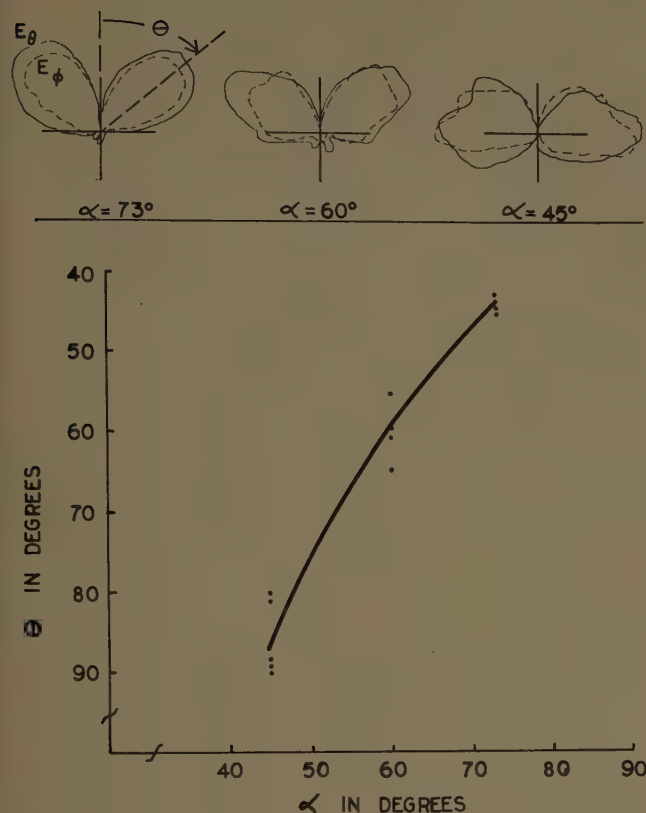


Fig. 6—Typical electric field patterns and orientation of the conical beam as a function of the rate of spiral ($7.5^\circ \leq \theta_0 \leq 10^\circ$).

polar, or $\theta=0$ axis.⁵ Therefore we expect an excitation which corresponds to any $m \neq \pm 1$ to produce a conical beam. The excitation of four arms corresponding to $m=2$, as shown in Fig. 3(c), is the simplest case.

This lowest-order conical beam excitation is readily achieved by connecting opposite arms together and feeding one pair against the other, *i.e.*, 180° out of phase. It is apparent also from the symmetry of the input currents in this case that there will be zero field along the antenna axis. The antenna can be fed by a balanced feed line, or a coaxial line and balun, placed on the axis of symmetry. It may also be fed by carrying the feed cable along one of the arms as outlined in the previous paper.² Details of this latter method are shown in Fig. 5. The balance and symmetry of the feed is important if symmetrical patterns are desired.

B. Radiation Patterns

Fig. 6 shows typical radiation patterns of symmetrical four-arm antennas fed in the manner shown in Fig. 3(c). As indicated, the rate of spiral (the parameter α),

⁵ V. H. Rumsey, "A solution to the equiangular spiral antenna problem," IRE TRANS. ON ANTENNAS AND PROPAGATION, vol. AP-7, p. S117; December, 1959. Rumsey's derivation considers the fields produced by an infinite number of planar log-spiral filaments. The more general result here is achieved simply by considering the properties of the associated Legendre functions and their derivatives. The idea of producing the conical beam with a four-arm spiral was originally conceived by considering the symmetry of the antenna currents.

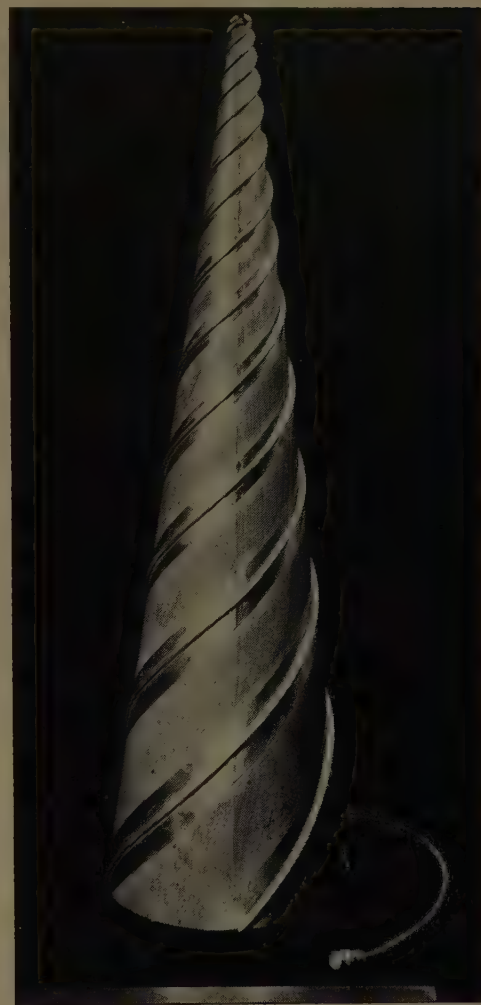


Fig. 7—Antenna 4C-15-45-9 etched from copper-clad teflon impregnated fiberglass with "infinite balun" feed. These antennas have also been fed with a conventional balun along the axis of the cone.

$$\alpha = 45^\circ$$

$$\theta_0 = 7.5^\circ$$

$$D = 20.5 \text{ cm}$$

$$d = 1.7 \text{ cm}$$

which was the primary factor in controlling the beam-width of the balanced two-arm antenna, determines the orientation of the conical beam of the balanced four-arm antenna. Conical antennas may be constructed to provide a conical beam with any angle of orientation from around 40° to more than 90° off the axis of the antenna. The case where the beam maximum is located at $\theta=90^\circ$ is of particular interest since it fills a need for a simple, very broad-band, circularly-polarized, omnidirectional source.

Fig. 7 shows a typical four-arm balanced equiangular spiral antenna constructed on a 15° cone. This antenna was etched from a flexible, copper-clad, teflon-impregnated, fiberglass material and then formed into a cone. The feed cable is RG 141/U. The energized cable is carried along one arm; dummy cables are placed on the other arms to maintain structural symmetry. To obtain the desired bandwidth, the arms on this particular antenna were later extended to a cone base diameter of

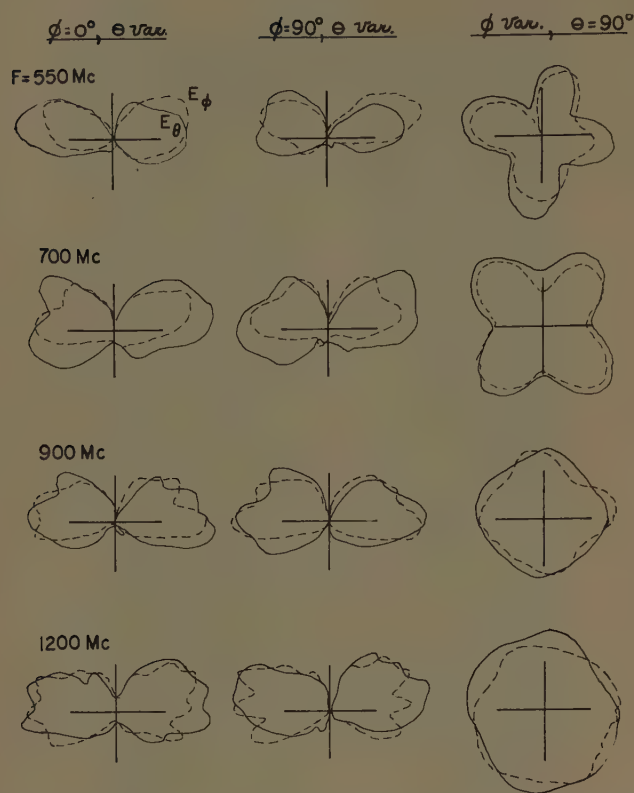


FIG. 8—Electric field patterns of a balanced symmetrical four-arm conical equiangular spiral antenna; $\theta_0=7.5^\circ$, $\alpha=45^\circ$, $K=0.925$, $D=31$ cm, $d=1.5$ cm.

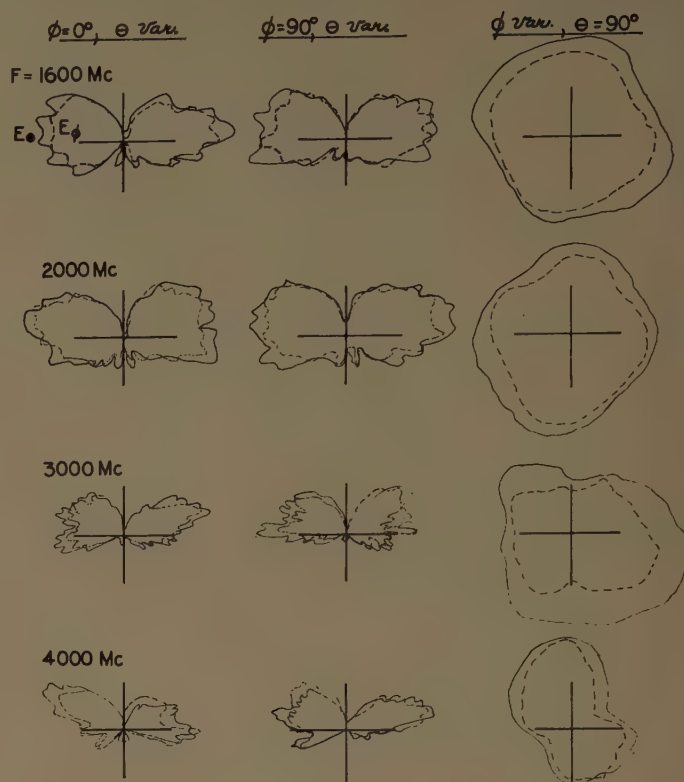


FIG. 9—Electric field patterns of a balanced symmetrical four-arm conical equiangular spiral antenna; $\theta_0=7.5^\circ$, $\alpha=45^\circ$, $K=0.925$, $D=31$ cm, $d=1.5$ cm.

31 centimeters. Radiation patterns of this antenna are shown in Figs. 8 and 9 from 550 Mc where the base is 0.57 wavelength in diameter up to 4000 Mc, where the diameter of truncated apex is approximately 0.2 wavelength. The patterns are for E_θ and E_ϕ polarized fields. The first two columns are pattern cuts through the axis of the antenna and the third column is for a cut perpendicular to the axis on the $\theta=90^\circ$ plane.

The azimuthal coverage shown in these patterns may be examined in greater detail in Fig. 10, where the total deviation in decibels from omnidirectional coverage is plotted for the orthogonal polarizations. The axial ratio in the $\theta=90^\circ$ plane varies somewhat with the angle ϕ . It is shown for one particular angle, which is a representative angle of orientation and not an optimum case. Over a considerable bandwidth the total amplitude deviation is less than 3 db and the axial ratio is 3 db or less.

Two pattern characteristics should be noted. For large α , the conical beam patterns are smooth and well formed and, if desired, the arms may be approximated by wire or cable. As the angle α decreases beyond 60° the radiation patterns exhibit minor irregularities and are not as symmetrical. In addition, these loosely spiraled antennas require wider exponentially expanding arms. These characteristics correspond to those noted for the two-arm axial beam antennas.

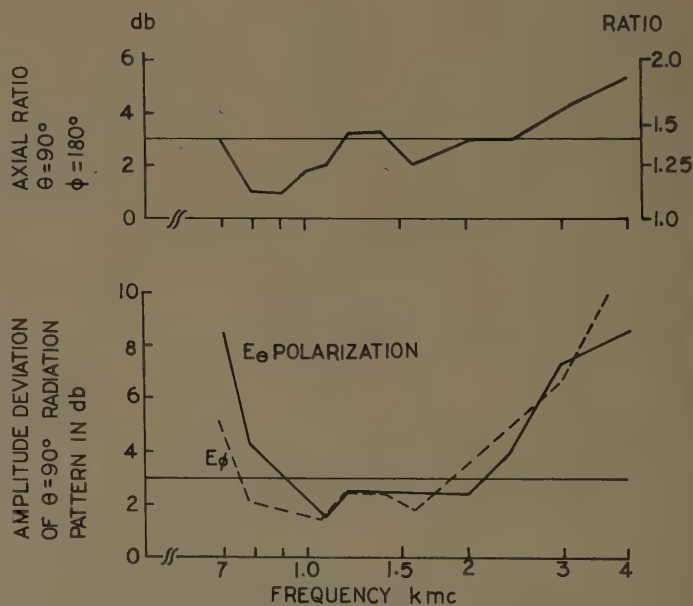


Fig. 10—Azimuthal coverage of the radiation patterns in Figs. 8 and 9.

C. Pattern Beamwidth

The beamwidth in a $\phi=\text{constant}$ plane is relatively insensitive to a change in antenna parameters. Antennas constructed with both 15° and 20° included cone

angles ($2\theta_0$), with $45^\circ \leq \alpha \leq 73^\circ$, and with cable arms or with exponentially expanding arms, had half-power beamwidths ranging from 35 to 55 degrees, with an average value of 45 degrees.

D. The Input Impedance

The input impedance of the four-arm antenna, fed in the manner of Fig. 3(c), rapidly converges to a characteristic value. Antennas, constructed with 15° or 20° included cone angles, typically have an input impedance of from 45 to 55 ohms for α ranging from 45° to 60° . As α is increased to 73° the impedance rises to the neighborhood of 70 ohms. These values are approximately one-half those noted for similar two-arm antennas.

The input voltage standing wave ratio of the antenna referred to in Figs. 8 and 9 is plotted in Fig. 11. Note that it is less than 1.5 to 1 referred to 50 ohms over most of the usable pattern bandwidth.

E. Operating Bandwidth as a Function of Antenna Size

The usable antenna bandwidth is fundamentally determined by the diameter of the truncated apex and the antenna arm length. As with the two-arm antennas, the radiation patterns tend to deteriorate as the apex region approaches $\frac{1}{2}$ wavelength in diameter. It was previously noted that the balanced two-arm antenna constructed on a 15° or 20° (total apex angle) cone, with an α of 73° could be operated to a frequency such that the cone base diameter is on the order of $\frac{1}{2}$ wavelength. As the rate of spiral is decreased, *i.e.*, α decreased to 45° , there is not sufficient radiating surface on this size cone to dissipate the energy without back radiation and hence the size of the cone must be increased to the order of 0.6 wavelength at the lowest frequency of operation. The four-arm structures exhibit very similar characteristics, and hence omnidirectional coverage on the $\theta = 90^\circ$ plane requires an antenna whose base diameter is on the order of 0.6 to $\frac{2}{3}$ wavelength at the lowest operating frequency.

IV. A MODIFIED VERSION

Thus far, we have considered only antennas constructed from the equiangular spiral curve. The pattern characteristics of these log-spiral antennas (such as the beamwidth of the two-arm antennas and the angle of orientation of the conical beam of the four-arm antennas) are relatively constant for a change in the frequency of operation. These characteristics are directly related to the constant parameter, α , which indicates the rate of spiraling of the arms.

It is possible to construct conical antennas from other curves. Planar Archimedean spiral curves, which describe a balanced antenna with well-formed bidirectional patterns, may be orthogonally projected onto a conical surface as shown in Fig. 12(b). For this curve the parameter α at any point on the curve is directly related to the angle ϕ at that point. Hence, as the frequency of operation is changed, the active aperture of

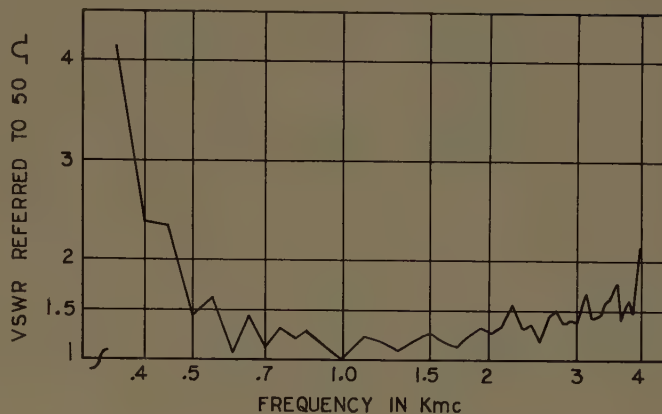


Fig. 11—VSWR of typical four-arm conical equiangular spiral; $\alpha = 45^\circ$, $\theta_0 = 7.5^\circ$, $D = 31$, $d = 1.5$ cm, $K = 0.925$.

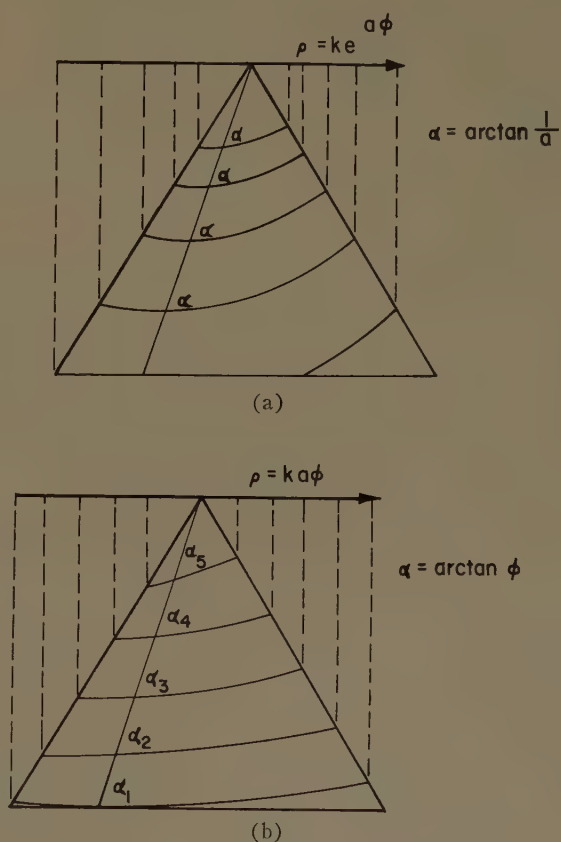


Fig. 12—Projection of equiangular spiral and Archimedes spiral curves on a conical surface.

the antenna is composed of a structure with a changing rate of spiral. This shows up as a definite widening of the beamwidth of the two-arm conical Archimedes spiral antenna as the operating frequency is increased. There is also a variation in the angle of orientation of the conical beam of the four-arm conical Archimedes spiral antenna with a change in frequency.

Radiation patterns for one particular four-arm conical Archimedes spiral antenna are shown in Fig. 13(a). This antenna was constructed to provide a range of α

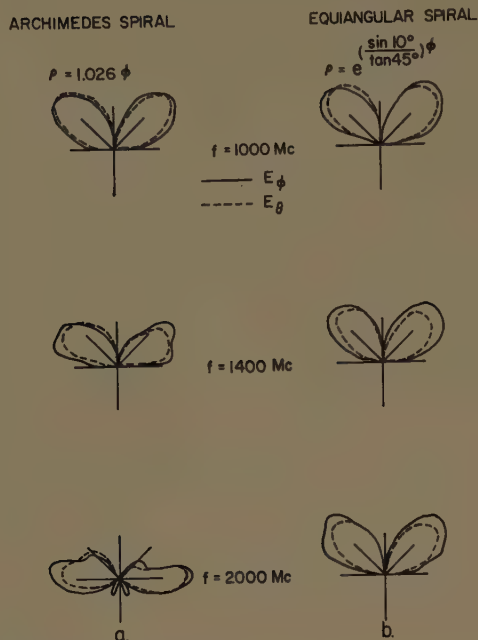


Fig. 13—Electric field patterns of symmetrical four-arm conical antennas; $\theta_0 = 10^\circ$, $D = 29.5$ cm, $d = 4.5$ cm ($\phi = 90^\circ$, θ var pattern).

from approximately 45° at the apex region to 85° at the base. As indicated in Fig. 13, the complete range of beam orientation from approximately 45° to 90° off axis is swept out as the frequency is varied from 1000 to 2000 Mc. Thus the conical beam may be frequency scanned in the polar angle. For comparison, patterns for an equiangular spiral antenna (with $\alpha = 85^\circ$) wound on the same cone are shown in Fig. 13(b).

V. CONCLUSIONS

It is possible to obtain a conical beam from the balanced equiangular spiral antenna by constructing the antenna with more than two arms and connecting these arms to provide a higher order ϕ -variation which is accompanied by an axial null. The angle of this conical beam can be controlled; in particular, it can be placed in the immediate vicinity of the $\theta = 90^\circ$ plane to provide an omnidirectional pattern.

An antenna with four symmetrically spaced arms can provide a radiation pattern that is within 3 db of omnidirectional coverage. The standing-wave ratio of this antenna, referred to a 50 ohm coaxial cable, is usually less than 1.5 to 1 over the pattern bandwidth.

This form of log-spiral retains the extremely wide frequency bandwidth and circular polarization properties of the basic conical log-spiral antenna and it provides a coverage which heretofore has been difficult to obtain even with narrow-band antennas.

Since the Archimedean spiral approximates a log-spiral with changing parameters, this version of the antenna may be constructed such that the conical beam may be frequency scanned in the polar angle.

APPENDIX

Consider a radiating system composed of a number of identical conductors on the surface of a cone. Assume that the structure has N -fold rotational symmetry as in Fig. 14; *i.e.*, a rotation about the cone axis through the angle $2\pi/N$ will leave the structure unchanged. Figs. 3(b) and 3(c) show examples of four-fold symmetry.



Fig. 14—Terminal region of structure having N -fold rotational symmetry.

The excitation of the conductors will be accomplished at the apex of the cone where the dimensions are small compared to the wavelength. There will be N terminals available in the excitation region, symmetrically spaced about a circle of small radius. Denoting the input current at the n th terminal by I_n , the excitation can be described by the current vector

$$I = (I_N, I_1, I_2, I_3, \dots, I_{N-1}).$$

Any index is defined modulo N . To satisfy the requirement of conservation of current, we note that

$$\sum_{n=1}^N I_n = 0. \quad (1)$$

This viewpoint, that each possible excitation is represented by a vector I , leads to the examination of the possible basis for the vectors of this space. Because of n -fold symmetry the choice of "symmetrical components" as base vectors proves more convenient than others.

Rotation of the excitation by one step,

$$I_A = (I_1, I_2, I_3, \dots, I_N), \quad (2)$$

would simply produce a field which is rotated in space by the angle $2\pi/N$. Hence the transformation of excitation,

$$I' = PI, \quad (3)$$

where P is the $n \times n$ permutation matrix:

$$P = \begin{bmatrix} 0 & 1 & 0 & 0 & \dots & 0 & 0 \\ 0 & 0 & 1 & 0 & \dots & 0 & 0 \\ 0 & 0 & 0 & 1 & \dots & 0 & 0 \\ \vdots & \vdots & \vdots & \vdots & \ddots & \vdots & \vdots \\ 1 & 0 & 0 & 0 & \dots & 0 & 0 \end{bmatrix}, \quad (4)$$

produces a simple change in the field. The matrix P is a special case of circulant matrices. The eigenvalues of P are $\exp(2\pi k/N)$ and the eigenvectors are

$$A_k = N^{-1/2}(1, e^{j(2\pi k/N)}, \dots, e^{j(2\pi k(N-1)/N)}, e^{j(2\pi k(N-1)/N)}). \quad (5)$$

From these eigenvectors we can obtain the basis of our vector space.

The eigenvectors of P for the case $N=4$ are

$$\begin{aligned} A_1 &= 1/2(1, j, -1, -j), \\ A_2 &= 1/2(1, -1, 1, -1), \\ A_3 &= 1/2(1, -j, -1, j), \\ A_4 &= 1/2(1, 1, 1, 1). \end{aligned} \quad (6)$$

Note that A_1 , A_2 , and A_3 satisfy the condition of (1), whereas A_4 does not. The former three vectors provide an orthonormal basis which spans the vector space of all possible excitations when $N=4$.

$$A_i \cdot A_j^* = \delta_{ij}, \quad i, j = 1, 2, 3. \quad (7)$$

Let us now examine the properties of these basic excitations. Excitation $I=A_1$ produces a field in which a rotation by $\pi/2$ is equivalent to a $\pi/2$ change in phase. Solutions of Maxwell's equations in spherical coordinates can be written with azimuthal variation of the form $e^{jm\phi}$ (m integer). Of these solutions only those with $m=4k+1$ ($k=0, \pm 1, \pm 2, \pm 3, \dots$) will satisfy the above relationship between rotation and change in phase. Hence the excitation $I=A_1$ will produce fields which can be expressed by

$$F_1 = \sum a_k \phi_{4k+1}, \quad (8)$$

where

$$\phi m = g_m(r, \theta) e^{jm\phi}.$$

Similarly, $I=A_2$ yields $m=4k+2$ and $I=A_3$ yields $m=4k+3$; each of these will produce fields

$$F_p = \sum a_k \phi_{4k+p}. \quad (9)$$

A similar argument can be carried through for arbitrary N .

Any excitation satisfying (1) can be expressed as a linear combination of A_1 , A_2 , and A_3 , and the fields produced thereby as a linear combination of F_1 , F_2 , and F_3 . Thus an excitation described by E_k will produce the fields

$$F = \sum (A_{j_i}^* E_k) F_{j_i}. \quad (10)$$

If the coefficients a_k above were known, the fields produced by any excitation would be completely determined. Unfortunately, this problem has not yet been solved for log-spiral elements.

Some useful observations can be made for the log-spiral, however, by interpreting the above results in terms of experimental data. Consider the case $N=2$ which has been extensively investigated. The eigen-

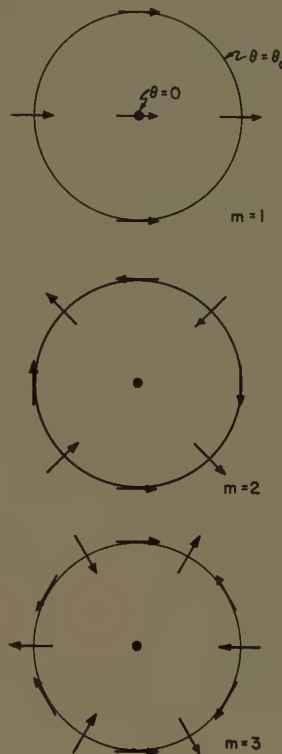


Fig. 15—Instantaneous electric vectors at $\theta=0$ and $\theta=\theta_0$ for three values of m .

vectors for the permutation matrix in this case are

$$\begin{aligned} A_1 &= \frac{1}{2}(1, -1), \\ A_2 &= \frac{1}{2}(1, 1), \end{aligned} \quad (11)$$

and only A_1 satisfies (1). This corresponds to the excitation of the two-arm spiral sketched in Fig. 3(a). The field F_1 for the case $N=2$ would be of the form

$$F_1 = \sum a_k \phi_{2k+1}, \quad (12)$$

and the possible ϕ -variations are

$$e^{j(2k+1)\phi}.$$

It has been observed that the radiation produced by two-arm log-spiral antennas is very nearly circularly-polarized over the major portion of the beam. Circular polarization with nonzero field on the axis requires that E_ϕ and E_θ vary as $\cos(\omega t + \phi)$ and $\sin(\omega t + \phi)$, respectively; the $m=1$ case. Functions with higher values of m would contribute to the off-axis fields. Fig. 15 shows a sketch of how the circularly polarized fields would appear instantaneously around the polar axis for a few of the small values of m . The values $m=1$ and 3 would predominate for the two-arm case. Note that these add alternately in and out of phase in orthogonal cross sections. Hence the rotational symmetry of the beam should provide an indication of the relative magnitude of these two fields, neglecting all others. A tightly-wound spiral produces more nearly rotationally-symmetric beams, hence predominantly the $m=1$ case.

The excitation of Fig. 3(c) used to produce the conical beams is one of the eigenvectors of (6), namely A_2 . This excitation produces fields

$$F_2 = \sum a_k \phi_{4k+2},$$

and the experimental results indicate that, for certain parameter choices, the lowest-order terms of this series predominate:

$$F_2 \approx a_0 \phi_2 + a_{-1} \phi_{-2}.$$

These two cases seem equally likely on the basis of the order of the functions involved. However, these two

cases correspond to circular polarized fields of opposite sense. One sense of polarization is favored over the other by the direction of the spiral winding. Hence it is reasonable that one of the coefficients a_0, a_{-1} be small, a conjecture which is again confirmed experimentally.

ACKNOWLEDGMENT

The authors are pleased to acknowledge the assistance of Prof. G. A. Deschamps in formulating the theory of excitation of multiarm antennas. Discussions with W. T. Patton were helpful. O. L. McClelland supervised the measurements program.

Arbitrary Polarization from Annular Slot Planar Antennas*

F. J. GOEBELS, JR.†, MEMBER, IRE AND K. C. KELLY†, MEMBER, IRE

Summary—This paper describes the analysis and design of a class of antennas which can radiate and receive constant-shape pencil beams with either circular sense, any linear or elliptical polarization by a simple adjustment in the feed circuit. Such radiators are called arbitrarily polarized antennas. The apertures described are located on upper plates of radial waveguides and are composed of annular slots, with each annulus consisting of a discrete number of crossed slots. The annular slots are positioned so that each arm of the crossed slots can couple by a constant factor with the radial or circumferential currents flowing over the aperture plate to produce a common instantaneous direction for the electric field in each slot pair. Both standing-wave and traveling-wave array types are employed. The standing-wave array requires only one radial waveguide mode for its operation. The traveling-wave array requires two modes and results in greater bandwidth and greater freedom in arraying many annuli. The methods used to excite the various radial waveguide modes are discussed; theoretical and experimental radiation patterns at X band are compared.

I. INTRODUCTION

THE two-dimensional planar array of slots has proven to be a most valuable adjunct to the antenna techniques available to the microwave antenna designer. Of the several types of waveguides which have been employed to excite the slots, the various forms of parallel-plate waveguides are usually easy to feed and to fabricate. The radial waveguide form is ideally suited for exciting slot systems which form a circular two-dimensional aperture. By the same token, annular slots suggest themselves as the basic radiating

element. General radiation-pattern synthesis with annular elements has been studied by several researchers,¹⁻³ but the attention of this paper is focused on pencil beam antennas.

Antennas whose pattern shapes are insensitive to changes in polarization of operation by virtue of a simple adjustment in the feed are of immediate value for improving radar performance as well as for countermeasure devices. The standing-wave and traveling-wave arbitrarily polarized radial-waveguide antennas to be discussed meet this requirement.

The apertures, located on the upper plates of radial waveguides, are composed of annular slots, with each annulus comprised of a discrete number of crossed slots (Fig. 1). In the following discussion, a cylindrical coordinate system (ρ, ψ, z) is used to denote the aperture variables, while the standard spherical coordinate system (R, θ, ϕ) denotes the far-field points of observation. The aperture is assumed to lie in the x, y plane, and the pencil beam formed has its maximum along the z axis (Fig. 2). The theoretical patterns take into consideration the annular slot width (w). Although discrete slots are used, the ability to predict their behavior from continuous annular-slot theory justifies their being called annular slots. All the radiation patterns pre-

* Received by the PGAP, August 30, 1960. This work has been supported in part by Wright Air Dev. Ctr. under Contract AF33(600)-31582. This paper was presented at the 1959 IRE National Convention, New York, N. Y., March 23-26.

† Antenna Dept., Hughes Aircraft Co., Culver City, Calif.

¹ R. W. Bickmore, "Radiation Pattern Synthesis with Annular Slots," University of California, Berkeley, ERL Rept. No. 112, Series 60; May, 1954.

² A. C. Schell and E. L. Bouche, "A concentric loop array," 1958 IRE WESCON CONVENTION RECORD, pt. 1, pp. 212-215.

³ K. C. Kelly, "Recent annular slot array experiments," 1957 IRE NATIONAL CONVENTION RECORD, pt. 1, pp. 144-151.

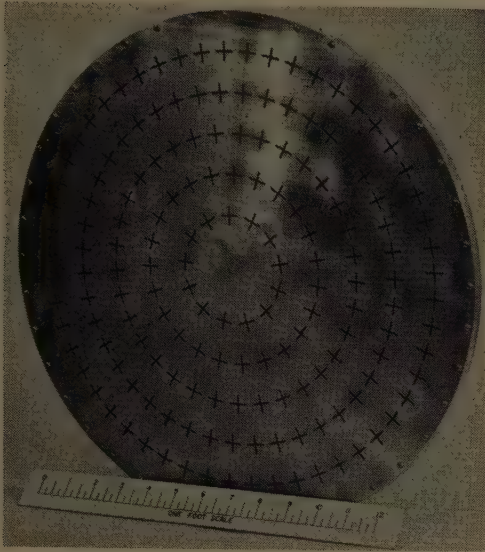


Fig. 1—A typical annular slot array.

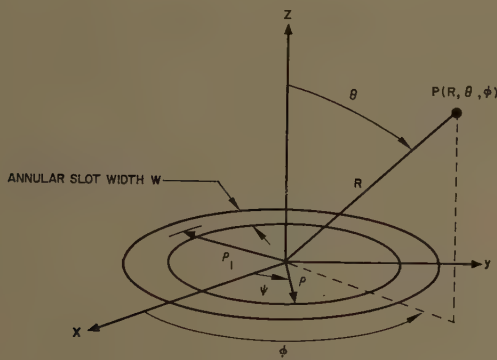


Fig. 2—Annular slot and space geometry.

sented were taken in a ϕ plane so that the angle variable on the abscissas is θ . The discussion is in terms of the transmitting operation but, since the antennas are reciprocal, the performance is the same on receive.

II. THEORETICAL ANALYSIS

Arbitrary polarization is achieved, for any polarization used, by exciting the aperture of the antenna in such a way that the electromagnetic field radiated into space by each of the crossed slots, in a given annular slot, is of equal magnitude and is polarized parallel to a common plane of polarization at any given instant of time. This condition is accomplished in the following manner:

1) By using the appropriate radial waveguide mode or modal pairs which induce in the plate of the aperture radial and circumferential currents having sine and cosine azimuthal dependencies, respectively. The modes used in this study have $H_\psi = \sin(\psi + \gamma) \sin \omega t$ and $H_\rho = \cos(\psi + \gamma) \sin \omega t$ azimuthal behaviors at the plane of the plates. This behavior is established by the feed when linear polarization, at any inclination γ , is desired. These structures also support $H_\psi = \sin(\psi \pm \omega t)$ and $H_\rho = \cos(\psi \pm \omega t)$ which the feed can create for cir-

cular polarization. Elliptical polarization results from any combination of these two limits of polarization conditions.

2) By positioning the concentric annuli of crossed slots at radii where the total current flowing has the form $\vec{I}_{\text{total}} = \hat{e}_\rho I_0 \sin(\psi + \gamma) + \hat{e}_\psi I_0 \cos(\psi + \gamma)$. Here I_0 is the current amplitude and \hat{e}_ρ and \hat{e}_ψ are unit vectors in the radial and circumferential directions, respectively. The radii at which this result is obtained are shown to be discrete for the standing-wave, and continuous for the traveling-wave array.

A. Standing-Wave Array

1) *Aperture Excitation:* The standing-wave radial waveguide antenna is a single-mode operated device. In particular, the E_{10} mode was used, although it is also possible to use any E_{1n} or H_{1n} type mode where $n=1, 2, 3, \dots$. The modal notation used is that of Marcuvitz.⁴

For the E_{10} mode, the magnetic fields in the radial waveguide are given by

$$H_\rho = j \frac{k\eta}{\rho} \{ A H_1^{(2)}(k\rho) + B H_1^{(1)}(k\rho) \} \cos \psi \quad (1)$$

$$H_\psi = -jk^2 \eta \{ A H_1^{(2)}(k\rho) + B H_1^{(1)}(k\rho) \} \sin \psi \quad (2)$$

where

H_ρ is the radial magnetic field,

H_ψ is the circumferential magnetic field,

$H_1^{(2)}(k\rho)$ is the Hankel function of order one and represents a radially outward traveling wave,

$H_1^{(1)}(k\rho)$ is the Hankel function of order one and represents a radially inward traveling wave,

k is the free-space propagation constant, $k = 2\pi/\lambda_0$

A and B are real constants,

η is the intrinsic admittance,

$e^{j\omega t}$ time dependence is assumed and omitted.

Assume that a perfect short terminates the waveguide structure, i.e., $A = B$. Using the relations

$$H_1^{(2)}(k\rho) = J_1(k\rho) - jN_1(k\rho)$$

$$K_1^{(1)}(k\rho) = J_1(k\rho) + jN_1(k\rho),$$

(1) and (2) reduce to

$$H_\rho = j2k\eta A \left\{ \frac{J_1(k\rho)}{\rho} \right\} \cos \psi \quad (3)$$

$$H_\psi = -j2k\eta A \{ kJ_1'(k\rho) \} \sin \psi. \quad (4)$$

Now consider the radii at which $|H_\rho(\rho)| = |H_\psi(\rho)|$. These positions are found to be discrete and are determined from the equation

$$J_2(k\rho) = 0. \quad (5)$$

⁴ N. Marcuvitz, ed., "Waveguide Handbook," McGraw-Hill Book Co., Inc., New York, N. Y., pp. 27-29; 1951.

At these radial positions corresponding to the roots of Bessel function $J_2(x)$, the total current flowing has the form,

$$\bar{I}_{\text{total}} = \hat{e}_\rho I_0 \sin(\psi + \gamma) + \hat{e}_\psi I_0 \cos(\psi + \gamma) \quad (6)$$

where

$$I_0 \propto k J_1'(k\rho) = \frac{J_1(k\rho)}{\rho}$$

and γ is the inclination of any desired linear polarization established by the feed.

Under these conditions, the resultant electric field in a given annular slot at a radius ρ_1 is polarized parallel to a common plane of polarization (Fig. 3) and can be represented by

$$\begin{aligned} \bar{E}_{\text{slot}}(\rho_1, \psi, t) = & \hat{e}_\rho [E_s(\rho_1) \sin(\psi + \gamma) \sin \omega t] \\ & + \hat{e}_\psi [E_s(\rho_1) \cos(\psi + \gamma) \sin \omega t]. \end{aligned} \quad (7)$$

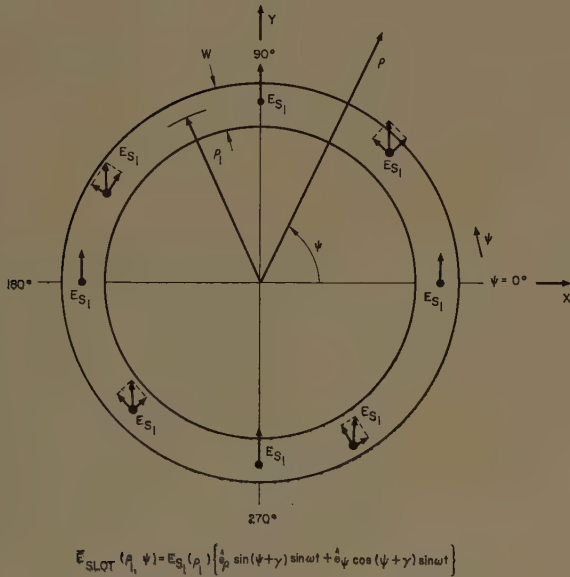


Fig. 3—The electric field in an annular slot excited with vertical polarization for $\gamma=0$.

To radiate arbitrary elliptical polarization or either circular sense polarization, two E_{10} modes of the appropriate amplitude and phase are required. The electric field in the annular slot for each case is

$$\begin{aligned} \bar{E}_{\text{slot}}(\rho_1, \psi, t) = & \hat{e}_\rho [E_{s1}(\rho_1) \sin \psi \sin \omega t + E_{s2}(\rho_1) \sin(\psi + \delta) \sin(\omega t + \delta)] \\ & + \hat{e}_\psi [E_{s1}(\rho_1) \cos \psi \sin \omega t \\ & + E_{s2}(\rho_1) \cos(\psi + \delta) \sin(\omega t + \delta)], \end{aligned} \quad (8)$$

$$\begin{aligned} \bar{E}_{\text{slot}}(\rho_1, \psi, t) = & \hat{e}_\rho [E_s(\rho_1) \cos(\psi \pm \omega t)] \\ & - \hat{e}_\psi [E_s(\rho_1) \sin(\psi \pm \omega t)], \end{aligned} \quad (9)$$

where

δ is the relative phase between the two modes, $E_{s1}(\rho_1)$ and $E_{s2}(\rho_1)$ are real and represent the electric field amplitudes of the two modes in the slot.

2) *The Radiation Fields:* From the integral solution of the vector wave equation, the far-zone radiation fields are given by⁵

$$E_\theta = -E_0(R) \int_{\text{aperture}} \{ \eta \bar{J}_m \cdot \hat{e}_\phi \} e^{jk\rho\hat{e}_\rho \cdot \hat{e}_R} dS \quad (10)$$

$$E_\phi = -E_0(R) \int_{\text{aperture}} \{ -\eta \bar{J}_m \cdot \hat{e}_\theta \} e^{jk\rho\hat{e}_\rho \cdot \hat{e}_R} dS \quad (11)$$

where

$\hat{e}_R, \hat{e}_\theta, \hat{e}_\phi$ are the unit vectors in the spherical coordinate system,

J_m is the magnetic current density in the aperture, η is the intrinsic admittance, and

$$E_0(R) = \frac{jw\mu}{4\pi R} e^{-jkR}.$$

Now consider the case where a linearly polarized radial waveguide mode of arbitrary inclination γ excites a given annular slot. Then, using Fig. 2 and (7), the radiation fields become⁶

$$E_{\theta 1} = E_{l1}(R, \theta, \rho_1, w) \sin(\phi + \gamma) \quad (12)$$

$$E_{\phi 1} = E_{l1}(R, \theta, \rho_1, w) \cos(\phi + \gamma) \cos \theta \quad (13)$$

where

$$\begin{aligned} E_{l1}(R, \theta, \rho_1, w) = & \frac{2\pi E_0(R) E_s(\rho_1)}{k \sin \theta} \left\{ \left(\rho_1 + \frac{w}{2} \right) J_1 \left[\left(\rho_1 + \frac{w}{2} \right) k \sin \theta \right] \right. \\ & \left. - \left(\rho_1 - \frac{w}{2} \right) J_1 \left[\left(\rho_1 - \frac{w}{2} \right) k \sin \theta \right] \right\}. \end{aligned} \quad (14)$$

Now the resultant far-field expression at any point in space is obtained by vector addition of (12) and (13) and is

$$\bar{E}_{T1}(R, \theta, \phi) = \hat{e}_T E_{l1}(R, \theta) \sqrt{1 - \sin^2 \theta \cos^2(\phi + \gamma)}. \quad (15)$$

To achieve arbitrary linear polarization, $|E_{T1}|$ should be independent of ϕ for each value of γ . However, it is clear from (12), (13), and (15) that this condition is only valid in the region of the main beam and near-in side-lobes ($\cos \theta \approx 1$). Therefore, it is within this region that arbitrary linear polarization or any type of polarization yields the same pattern in all ϕ planes. The effect of the $\cos \theta$ term will be evident in the theoretical and experimental patterns to be shown in the section on experimental results.

Next, consider the most general case where the electric field in the annular slot is elliptically polarized.

⁵ S. Silver, Ed., "Microwave Antenna Theory and Design," McGraw-Hill Book Co., Inc., New York, N. Y., p. 89; 1949.

⁶ Complete derivation can be found in Hughes Aircraft Co. Tech Memo. No. 592; July, 1959.

Then, using (8),

$$E_{\theta_1} = E_{e_1}(R, \theta, \rho_1, w) \cdot \{E_{s_1}(\rho_1) \sin \phi + E_{s_2}(\rho_1) \sin(\phi + \delta)\} \quad (16)$$

$$E_{\phi_1} = E_{e_1}(R, \theta, \rho_1, w) \cdot \{E_{s_1}(\rho_1) \cos \phi + E_{s_2}(\rho_1) \cos(\phi + \delta)\} \cos \theta \quad (17)$$

where

$$E_{e_1}(R, \theta, \rho_1, w) = \frac{2\pi E_0(R)}{k \sin \theta} \left\{ \left(\rho_1 + \frac{w}{2} \right) J_1 \left[\left(\rho_1 + \frac{w}{2} \right) k \sin \theta \right] - \left(\rho_1 - \frac{w}{2} \right) J_1 \left[\left(\rho_1 - \frac{w}{2} \right) k \sin \theta \right] \right\}, \quad (18)$$

and, if the $\cos \theta$ factor is ignored,

$$\bar{E}_{T_1}(R, \theta) = \hat{e}_T E_{e_1}(R, \theta) \sqrt{E_{s_1}^2 + E_{s_2}^2 + 2E_{s_1}E_{s_2} \cos \delta}. \quad (19)$$

Here again it is observed that $|E_{T_1}|$ is independent of ϕ , in the valid region, for each value of δ . Furthermore, from (19) it is evident that this pattern constancy with respect to ϕ is valid for all polarizations (various values of E_{s_1} , E_{s_2} , and δ) transmitted or received by the antenna.

Sidelobe reduction is obtained by arraying concentric annular slots (Fig. 1). Under these circumstances,

$$\begin{cases} E_{\theta_N} = \sum_{n=1}^N E_{\theta_{2n-1}} \\ E_{\phi_N} = \sum_{n=1}^N E_{\phi_{2n-1}} \end{cases} \quad (20)$$

where $(2n-1)$ corresponds to the annular slot position for odd roots of $J_2(x)$ and N is the total number of annuli, or

$$\begin{cases} E_{\theta_N} = \sum_{n=0}^N E_{\theta_{2n}} \\ E_{\phi_N} = \sum_{n=1}^N E_{\phi_{2n}} \end{cases} \quad (21)$$

where $(2n)$ corresponds to the annular slot position for even roots of $J_2(x)$ and N is the total number of annuli.

Thus, in order to have all annuli radiate in phase, they must be at either even or odd roots of J_2 , not both (Fig. 5). This condition necessitates using annular slot interelement spacings of greater than λ_0 , but the second order main beams are greatly reduced because of the high directivity of the element factor.

Tapering of the aperture distribution would require a reduction of the length and an increase in the spacing of the crossed slots composing the annular slot radiators.

B. Traveling-Wave Array

1) *Aperture Excitation*: The traveling-wave antenna is a dual-mode operated device. The E_{11} and H_{11} modal pairs were used, although it is possible to use any modal pairs E_{1n} and H_{1n} (where $n=1, 2, \dots$).

Again, for the radial and circumferential magnetic fields associated with both modes,⁴

$$\begin{cases} H_{\rho}^{e_{11}} = jA \frac{k\eta}{\rho} \cos\left(\frac{\pi}{b}z\right) H_1^{(2)}(K_1\rho) \cos \psi \\ H_{\psi}^{e_{11}} = -jA k K_1 \eta \cos\left(\frac{\pi}{b}z\right) H_1'^{(2)}(K_1\rho) \sin \psi \end{cases} \quad (22)$$

$$\begin{cases} H_{\rho}^{h_{11}} = B \frac{K_1\pi}{b} \cos\left(\frac{\pi}{b}z\right) H_1'^{(2)}(K_1\rho) \cos \psi \\ H_{\psi}^{h_{11}} = -B \frac{\pi}{\rho b} \cos\left(\frac{\pi}{b}z\right) H_1^{(2)}(K_1\rho) \sin \psi \end{cases} \quad (23)$$

where

A and B are the real amplitudes of the E_{11} and H_{11} radial waveguide modes, respectively, b is the height of the radial waveguide, and

$$K_1 = \sqrt{k^2 - \left(\frac{\pi}{b}\right)^2}.$$

Now consider feeding the H_{11} mode $\pi/2$ degrees out of phase with the E_{11} mode. One then equates the magnitudes of the linear combination of both orthogonal H fields to determine the condition that must be obeyed in order to have their magnitudes equal. The condition is

$$A = \left[\frac{\pi}{k\eta b} \right] B. \quad (24)$$

Hence, when the radial waveguide is excited by the E_{11} and H_{11} modal pair with the prescribed relative phase and amplitude, the total current flowing over the entire aperture is

$$\bar{I}_{\text{total}} = \hat{e}_{\rho} I_0 \sin(\psi + \gamma) + \hat{e}_{\psi} I_0 \cos(\psi + \gamma) \quad (25)$$

where

$$I_0 \propto H_0^{(2)}(K_1\rho).$$

Thus, an annular slot may be positioned at any radius on the aperture and not just at discrete points as was shown necessary for the standing-wave fed annulus. Sidelobe reduction is again achieved by arraying concentric annuli.

To achieve any desired linear polarization requires only a single modal pair. Two modal pairs are necessary for arbitrary elliptical or either sense circular polarizations.

2) *The Far Field*: The far-field derivations parallel those for the standing-wave array described above.

III. EXPERIMENTAL RESULTS

A. Standing-Wave Array

The radial waveguide required to support the E_{10} standing-wave mode consists of a radial waveguide "cavity" which is fed at its center from a circular waveguide. The annular slot aperture is located on the upper plate of the cavity with each annulus consisting of a discrete number of crossed slots so oriented that each arm of a given crossed slot is perpendicular to the current flow at that radius (Figs. 1 and 4). The dominant TE_{11} circular waveguide mode is used to excite the E_{10} radial waveguide mode. The polarization of the TE_{11} mode controls the polarization radiated by the antenna. The $J_2(x)$ slot current-coupling positions are nearly at a minimum for the radial current and nearly at a maximum for the circumferential current (Fig. 5). Nonresonant length crossed slots are used throughout. All experiments were at X band.

Pattern comparisons for one, two and five annular slot arrays in both principal planes ($\phi=0^\circ$, $\phi=90^\circ$) are given in Figs. 6-11 using linear and circular polarizations.



Fig. 4—Antenna and feed for a single annular slot radiator.

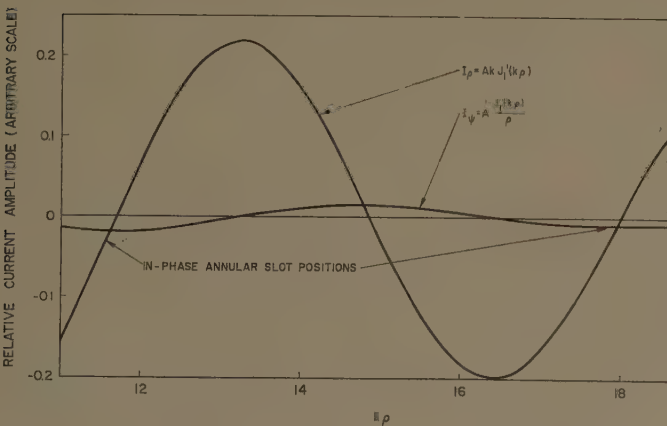


Fig. 5—Radial and circumferential current behavior in the aperture of a standing-wave array.

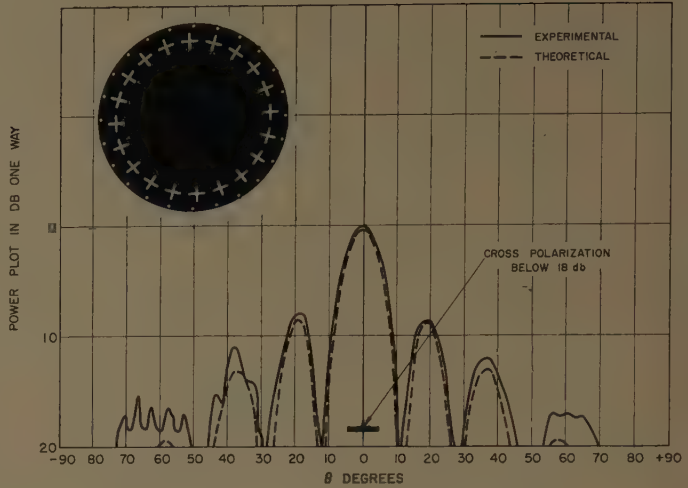


Fig. 6— $\phi=0^\circ$ plane pattern for E_θ polarization in a standing-wave antenna.

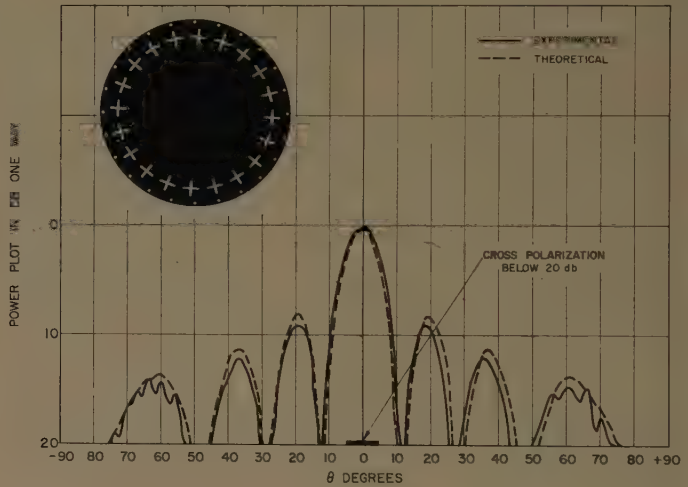


Fig. 7— $\phi=90^\circ$ plane pattern for E_θ polarization in a standing-wave antenna.

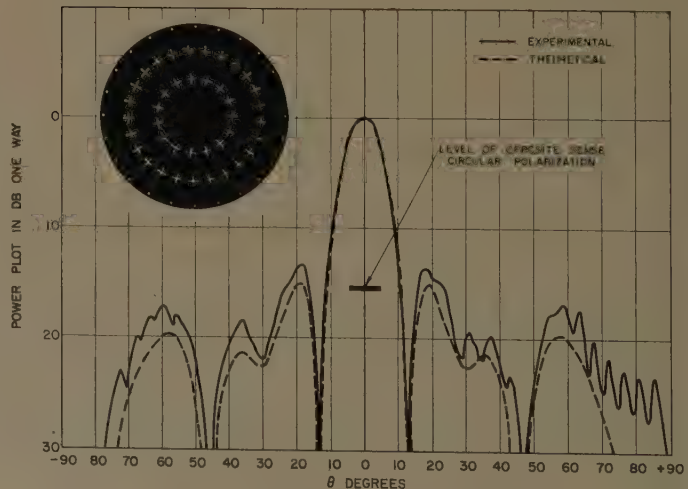


Fig. 8— $\phi=0^\circ$ plane pattern for circular polarization in a standing-wave antenna.

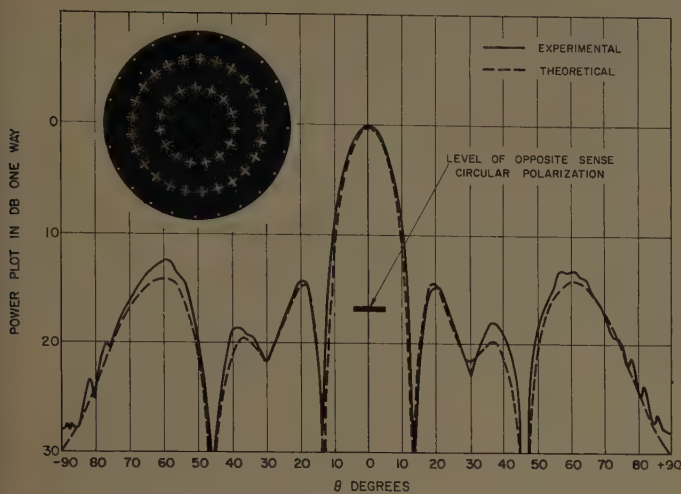


Fig. 9— $\phi = 90^\circ$ plane pattern for circular polarization in a standing-wave antenna.

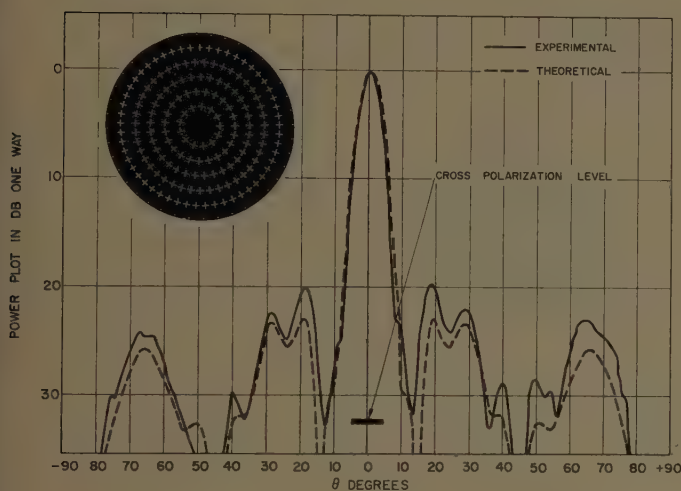


Fig. 10— $\phi = 0^\circ$ plane pattern for E_ϕ polarization in a standing-wave antenna.

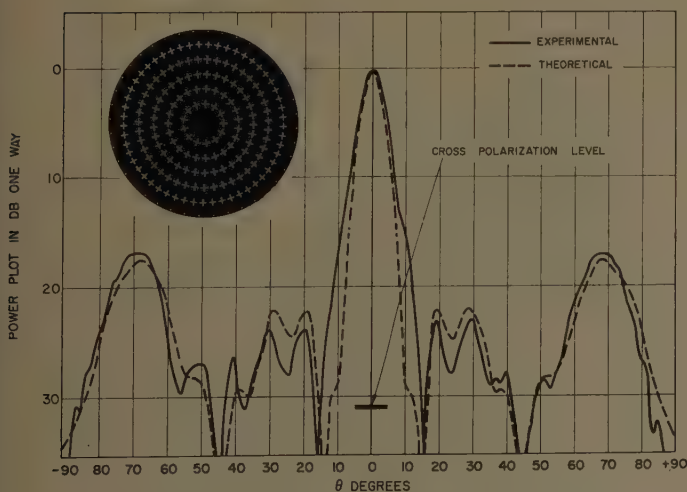


Fig. 11— $\phi = 90^\circ$ plane pattern for E_θ polarization in a standing-wave antenna.

The cross-polarization levels indicated in the figures are peak-intensity levels in the plane. These peaks occurred near broadside. At other angles, the cross-polarization intensity levels are greatly suppressed. The feed isolation between the rejected and transmitted senses of circular polarization was measured independently of the antenna and found to be 17 db. A greater feed isolation would lower the cross-polarization level or reception of the unwanted sense of circular polarization. In general, good pattern agreement was obtained. However, the pattern in Fig. 11 marks the beginning of the degradation of the aperture distribution for the innermost annular slot radiators. This disturbance of the characteristics of their excitation is fundamental for the standing-wave array. The outermost annular slots, because of their finite impedances, cause the innermost slots to see an impedance other than a short. This condition unbalances the amplitudes of the I_ρ and I_ψ current components in the slots by changing their behavior from that of a Bessel function dependency (which can be equalized) to that of a Hankel function dependency (which cannot be equalized). Furthermore, the bandwidth is observed to suffer as annular slots are positioned at larger radii. This characteristic is also fundamental, as can be seen from Fig. 5. For annular slots at large radii, it is observed that their positions, governed by the roots of $J_2(x)$, asymptotically approach those for the roots of $J_1'(x)$, which is the amplitude factor for the radial current. Hence, the larger the radius at which an annular slot is located, the less frequency change is necessary to distort the desired current distribution in the annular slot. For the annular slot in Fig. 4, the bandwidth was 3 per cent for a 2-db change in sidelobe level.

The irregularities in the patterns taken were predicted theoretically and are explained by the fact that an interelement spacing of greater than λ_0 had to be used in order to have the annular slot elements radiate in phase. All the annular slots contained crossed slots of equal length and interslot spacing. They were made to couple lightly to the E_{10} mode so that the desired aperture distribution was not appreciably disturbed. Consequently, in the operation of a standing-wave array of this type, optimum efficiency was sacrificed in order to achieve polarization versatility.

B. Traveling-Wave Arrays

Two traveling-wave antennas were designed, each utilizing a different feed structure in exciting the E_{11} and H_{11} radial waveguide modal pair. Both antennas were 28 inches in diameter and contained three annular slot radiators.

The first antenna used a dual feed which gave independent control over the amplitude and phase of each mode excited (Fig. 12). The E_{11} radial waveguide mode was excited by using a circular waveguide located at the

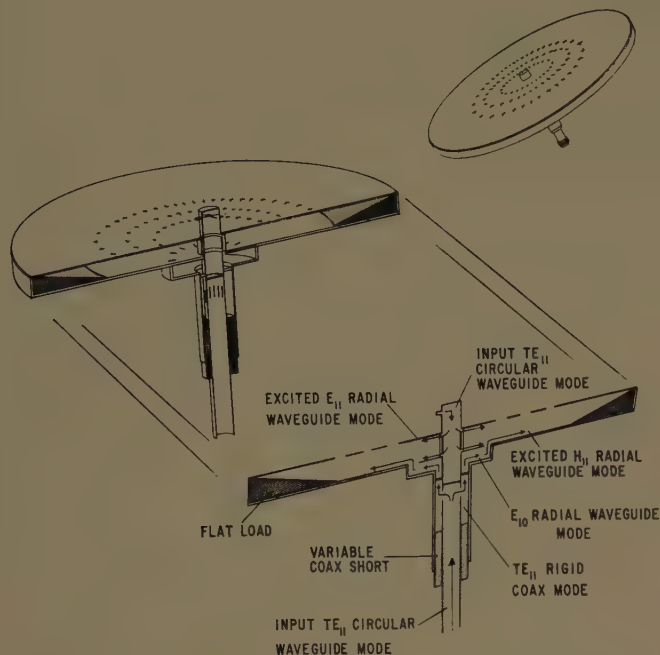


Fig. 12—Traveling-wave feed used to independently excite the E_{11} and H_{11} radial waveguide modal pair.

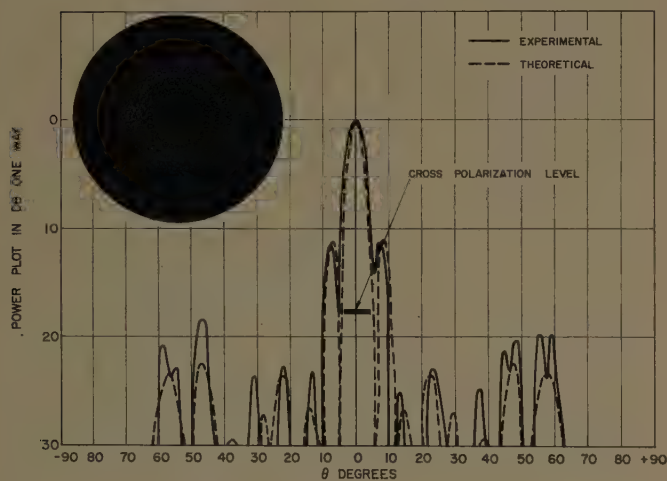


Fig. 13— $\phi = 0^\circ$ plane pattern for independent mode excited traveling-wave array using E_ϕ polarization.

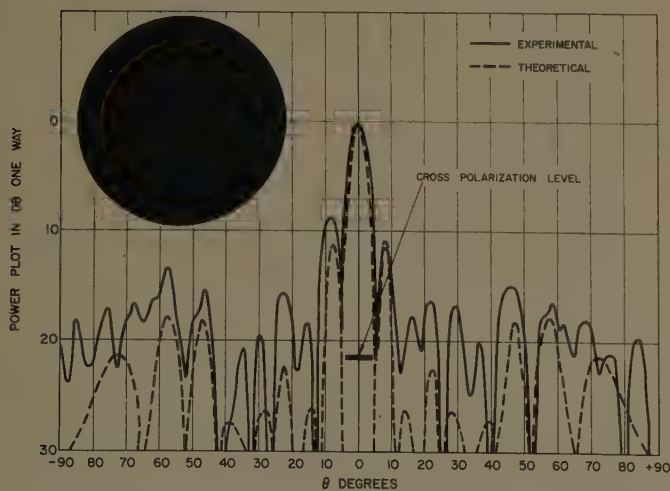


Fig. 14— $\phi = 90^\circ$ plane pattern for independent mode excited traveling-wave array using E_θ polarization.

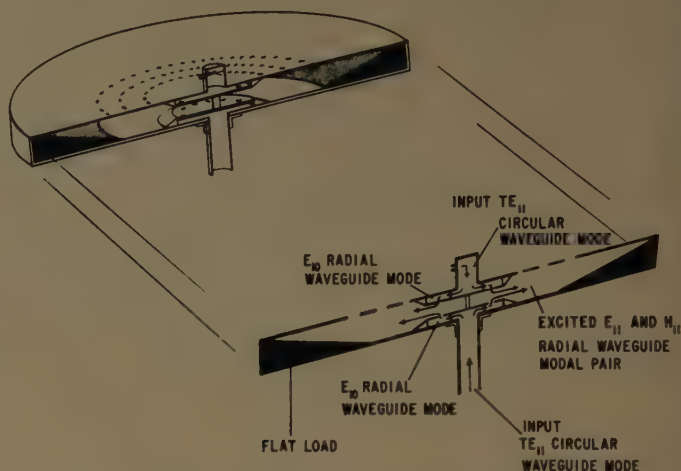


Fig. 15—Traveling-wave feed used to dependently excite the E_{11} and H_{11} radial waveguide modal pair.

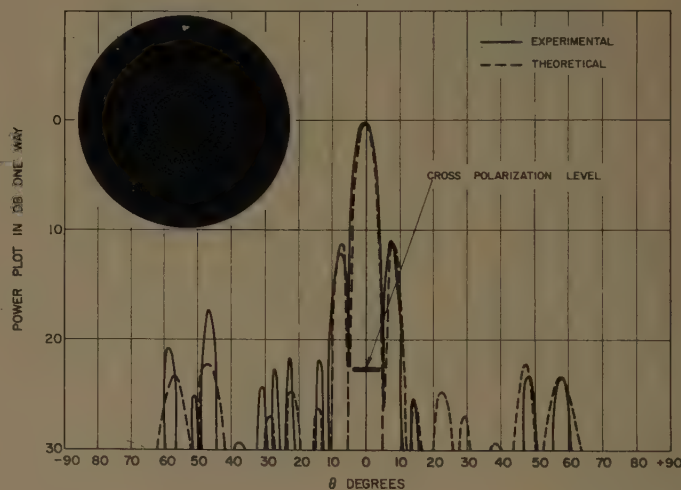


Fig. 16— $\phi = 0^\circ$ plane pattern for dependent mode excited traveling-wave array using E_ϕ polarization.

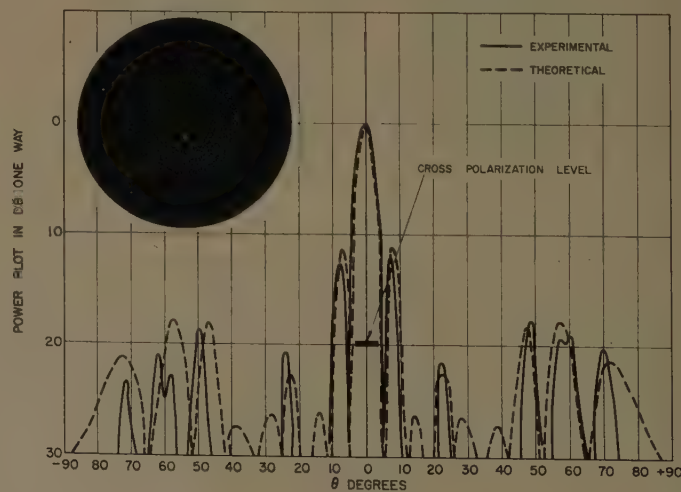


Fig. 17— $\phi = 90^\circ$ plane pattern for dependent mode excited traveling-wave array using E_θ polarization.

center of the antenna which propagated the TE_{11} mode. Two continuous transverse slots, spaced one-half guide wavelength apart on the circular waveguide wall, satisfied the required excitation for the E_{11} mode. The H_{11} mode was forced to propagate by use of a miniature radial waveguide exciter which contained the E_{10} mode. The exciter was located at the center of the antenna on its lower plate and caused the excitation of the H_{11} mode through an annular group of radially-oriented slots. Satisfactory amplitude and phase control over the two modes were achieved by this method. Patterns taken with this antenna were in good agreement with the theory (Fig. 13 and 14).

The second antenna utilized a feed which excites both modes simultaneously and with the proper phase and amplitude through a common pair of miniature radial waveguide cavities (Fig. 15). These exciters were also positioned at the center of the antenna, one on the upper plate and the other on the lower plate. Each contained an annulus of crossed slots which gave rise to equal radial and circumferential currents in the antenna aperture. Both cavity exciters were fed independently. Patterns taken with this antenna were also in good agreement with the theory (Figs. 16 and 17).

The polarization radiated or received for the traveling-wave antennas is governed by the polarization of the two input TE_{11} circular waveguide modes. Both exciters for these modes have to be commonly aligned to radiate a prescribed polarization. Several types of exciters can be used, one of which is the turnstile feed that was employed in these experiments.

The traveling-wave excited array overcomes the shortcomings associated with its standing-wave counterpart. Its improved antenna characteristics arise from the nature of its current distribution and the manner in which it is excited.

First, because the two orthogonal currents (25) display the same radial dependence over the entire aperture, greater bandwidth is achieved. A small change in frequency does not cause the radial and circumferential currents to become unbalanced, as occurs with the standing-wave version. Furthermore, it is easily possible to vary the spacing of the waveguide plate as frequency is changed in order to keep K_1 constant and thus eliminate the change in interannulus phase which would otherwise occur.

Second, because traveling-wave excitation is employed, no fundamental limitation exists on the number of annuli that can be arrayed or on the tightness of coupling of any annulus.

The measured bandwidth for an annular slot radiator at a radius $\rho = 5.5 \lambda_0$ was only about 5 per cent for a 2-db change in sidelobe level. However, it was limited because of the feed structure used. Where more bandwidth is required, alternate feeding methods would have to be employed. It should be noted here that the traveling-wave excited arrays can also be made to yield low sidelobes. The reason the three annular slot array displayed only 11-db sidelobes was due to some aperture blocking on the part of the feed structure. However, with the construction of a more compact feed, this problem can be obviated.

IV. CONCLUSIONS

It has been demonstrated that a class of arbitrarily polarized planar radiators can be obtained by use of the modal characteristics associated with radial-waveguide structures. Their basic radiating element was found to be an annular slot with a highly directive element pattern. Low sidelobe operation was shown to be an inherent feature with these antennas and good experimental agreement was observed. The standing-wave array was found to have fundamental weaknesses, namely, narrow bandwidth and a limited arraying potential. The traveling-wave arrays, however, did not possess these limitations and hence were more versatile.

Because this class of antennas can analyze and distinguish the polarization characteristics from desired targets, they might be used to improve radar performance or be incorporated into systems which must discern man-made targets from ground clutter. Also, they should find utility in countermeasure operation where the positive detection and jamming of a radar of unknown character is required. Furthermore, the single mode-operated array can be made arbitrarily thin, light in weight, and compact, and hence should prove useful in the seeker system of a small-diameter missile.

Finally, it should be emphasized that the primary objective of this study was to demonstrate the polarization versatility of radial-waveguide antennas. The fact that the apertures coupled lightly to the input energy is not indicative of their ultimate performance. On the contrary, the efficiency of the traveling-wave array can be made comparable to that of other antennas in use today. Furthermore, tight slot coupling may be used with a standing-wave antenna with a single annular element; it remains for further investigation to determine the optimum efficiency attainable using several annular slot radiators.

A Theoretical Limitation on the Formation of Lossless Multiple Beams in Linear Arrays*

J. L. ALLEN†, MEMBER, IRE

Summary—It is well known that through the use of lenses, several independent beams can be formed from a single antenna, with each beam having essentially the gain corresponding to the aperture of the lens. Recently, feed systems have been developed for linear arrays which achieve similar performance through the use of directional couplers.

In this paper it is shown that the shape of the beams which can be formed from an equispaced array by such a feed matrix is not arbitrary, unless one is willing to accept losses in addition to normal plumbing losses. It is shown that the array space factors associated with the individual beams must be such that they are mutually orthogonal over a period of the space-factor pattern.

INTRODUCTION

THE current interest in array-type antennas has led to consideration of array feeds which are capable of forming multiple, simultaneous, independent beams in space in such a manner that essentially the full gain of the antenna is realized in each beam, aside from any transmission losses.

In addition to the use of lenses with multiple feeds for forming multiple beams, transmission line feeds using directional couplers have recently been developed to perform the same function, when used with linear antenna arrays.

Fig. 1 shows a serial feed arrangement,¹ while Fig. 2 shows a parallel-fed beam-forming matrix^{2,3} using hybrid devices having the 90° phase-shift property of, for example, branch-line directional couplers. The same device is realizable with couplers exhibiting the sum and difference property,⁴ as shown in Fig. 3.

The purpose of this discussion is to point out a theoretical limitation on the shape of the space factors⁵ that can be formed losslessly with such an array feed, subject to the assumption that the feed matrix is a reciprocal device, and that the array consists of equispaced radiators.

* Received by the PGAP, October 3, 1960; revised manuscript received, December 16, 1960.

† Lincoln Lab., Mass. Inst. of Tech., Lexington, Mass.

¹ J. Blass, "The multidirectional antenna: A new approach to stacked beams," 1960 IRE INTERNATIONAL CONVENTION RECORD, pt. 1, pp. 48–50.

² J. Butler, "Multiple Beam Antenna," Sanders Associates, Nashua, N. H., Internal Memo. RF-3849; January 8, 1960.

³ J. P. Shelton, S. R. Perrino, and A. B. Davis, "Scanning Techniques for Large Flat Communication Antenna Arrays," Aero Geo Astro Corp., Alexandria, Va., Sci. Rept. No. 1; April 15, 1960.

⁴ J. L. Allen, *et al.*, "Phased Array Studies: July 1, 1959 to July 1, 1960," Lincoln Lab., Mass. Inst. Tech., Tech. Rept. No. 228; August 12, 1960.

⁵ In this discussion, the term "space factor" is used to designate the complex far field of an array of isotropic radiators (after A. S. Schelkunoff, "A mathematical theory of linear arrays," *Bell Sys. Tech. J.*, vol. 22, pp. 80–107; January, 1943).

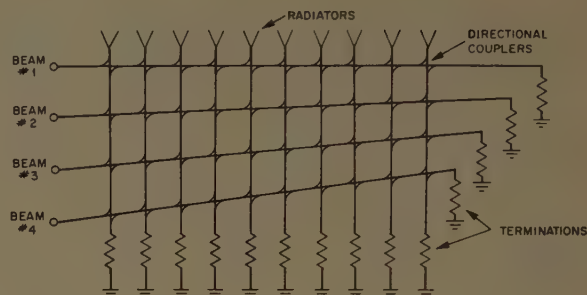


Fig. 1—A serial method of multiple-beam forming (after Blass¹).

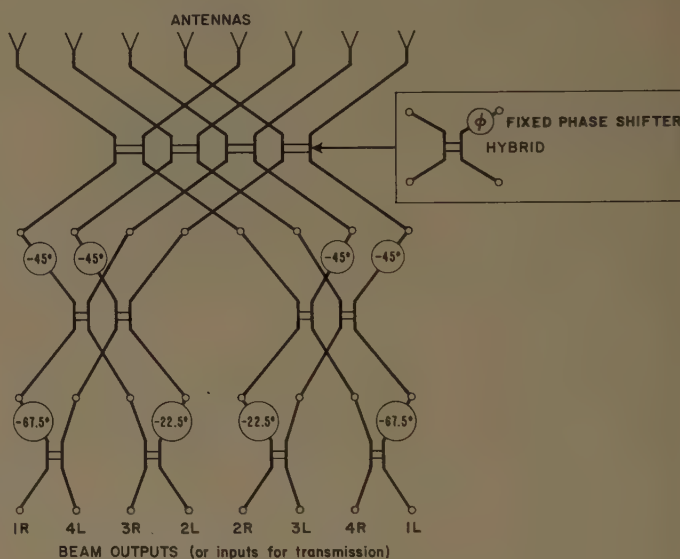


Fig. 2—8×8 beam-forming matrix (after Butler²).

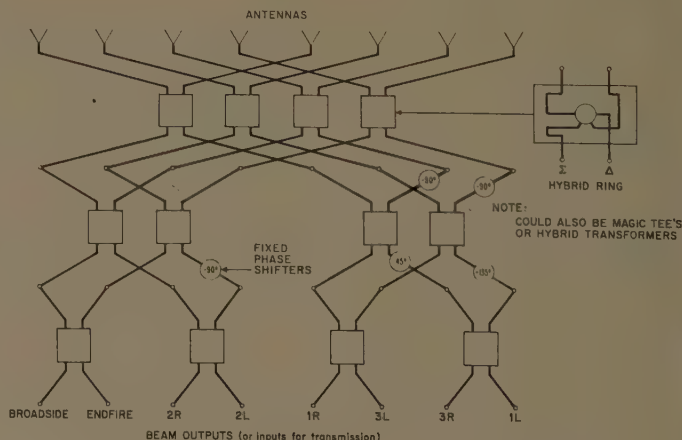


Fig. 3—8×8 beam-forming matrix using sum and difference devices.

ANALYSIS

An $M \times N$ passive beam-forming matrix can be abstracted as a "black box" containing M inputs (considered from the transmitting standpoint) and N outputs, as shown in Fig. 4 (next page). Under the assumption that the device is reciprocal, the point of interest is the limitation on the form of the outputs that arises from the desire that the device be theoretically lossless. The analysis that follows is an extension of that of Shelton, *et al.*³

From the scattering matrix viewpoint,⁶

$$b_j = [S]a_i,$$

where a_i is the complex amplitude of the electric field incident on the i th terminal, and b_j is the complex amplitude of the reflected electric field at the j th terminal. It is desired that when an input is present at the i th terminal only ($i=1, 2, \dots, M$), there be no output from the other input terminals, and no reflection from the i th terminal. Hence, it is required that all the elements of the scattering matrix relating the a_i 's and b_j 's for $i=1, 2, \dots, M$, and $j=1, 2, \dots, M$, be zero. The scattering matrix then takes the form

$$[S] = \begin{bmatrix} 0 & 0 & \cdots & 0 \\ 0 & 0 & \cdots & 0 \\ \vdots & \vdots & \ddots & \vdots \\ \vdots & \vdots & \ddots & \vdots \\ 0 & 0 & \cdots & 0 \\ \hline S_{M+1,1} & S_{M+1,2} & \cdots & S_{M+1,M} \\ S_{M+2,1} & S_{M+2,2} & \cdots & S_{M+2,M} \\ \vdots & \vdots & \ddots & \vdots \\ \vdots & \vdots & \ddots & \vdots \\ S_{M+N,1} & S_{M+N,2} & \cdots & S_{M+N,M} \end{bmatrix} \begin{bmatrix} S_{1,M+1} & S_{1,M+2} & \cdots & S_{1,M+N} \\ S_{2,M+1} & S_{2,M+2} & \cdots & S_{2,M+N} \\ \vdots & \vdots & \ddots & \vdots \\ \vdots & \vdots & \ddots & \vdots \\ S_{M,M+1} & S_{M,M+2} & \cdots & S_{M,M+N} \\ \hline S_{M+1,M+1} & S_{M+1,M+2} & \cdots & S_{M+1,M+N} \\ S_{M+2,M+1} & S_{M+2,M+2} & \cdots & S_{M+2,M+N} \\ \vdots & \vdots & \ddots & \vdots \\ \vdots & \vdots & \ddots & \vdots \\ S_{M+N,M+1} & S_{M+N,M+2} & \cdots & S_{M+N,M+N} \end{bmatrix}.$$

Since the network is reciprocal by assumption, the matrix is symmetrical: *i.e.*, $S_{ij} = S_{ji}$.

The requirement that the device be lossless imposes the unitary condition on the matrix:

$$[S][S]^+ = [1],$$

where $[S]^+$ represents the Hermitian conjugate of $[S]$.

The unitary condition can be equivalently stated⁷ for a symmetrical matrix as

$$\sum_{i=1}^{M+N} S_{li} S_{ki}^* = \delta_{lk}, \quad (1)$$

where the asterisk denotes the complex conjugate, and δ_{lk} is the Kronecker delta ($\delta_{lk}=1$, if $l=k$, and zero if $l \neq k$).

Let us consider the implications of (1) on the space factor of a linear array of equispaced antennas fed by the "black box" of Fig. 4. If an input a_k is supplied to the k th input terminal ($1 \leq k \leq M$), the illumination of an array of isotropic radiators will be

$$g(n) = a_k S_{k,M+n},$$

assuming the outputs of the "black box" of Fig. 4 to be sequentially numbered according to the antenna to which the particular output is connected. For the geometry of Fig. 5, the space factor produced by the k th input to the matrix will be of the form

$$H_k(v) = a_k \sum_{n=1}^N S_{k,M+n} e^{jnDv},$$

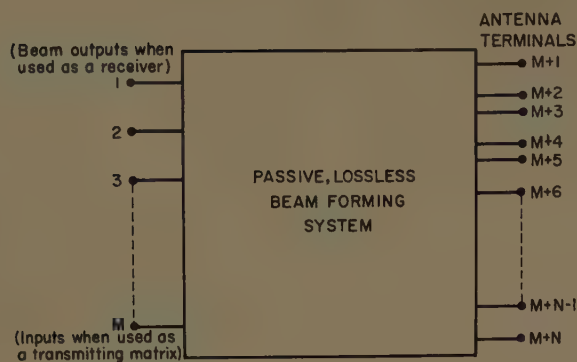
where $v = 2\pi/\lambda \sin \xi$ for $-2\pi/\lambda \leq v < 2\pi/\lambda$ (the "visible range" of angle). Similarly, if the l th input is driven with a wave of complex magnitude a_l , a space factor will be produced of the form

$$H_l(v) = a_l \sum_{n=1}^N S_{l,M+n} e^{jnDv}.$$

The conjugate product of the two factors is

⁶ C. G. Montgomery, R. H. Dicke, and E. M. Purcell, "Principles of Microwave Circuits," Mass. Inst. Tech. Rad. Lab. Series, McGraw-Hill Book Co., Inc., New York, N. Y., vol. 8, pp. 146-149; 1948.

⁷ N. Marcuvitz, "Waveguide Handbook," Mass. Inst. Tech. Rad. Lab. Series, McGraw-Hill Book Co., Inc., New York, N. Y., vol. 10, p. 108; 1951.

Fig. 4—Abstraction of $M \times N$ multiple-beam-forming system.

$$H_l(v)H_k^*(v) = a_l a_k^* \sum_p \sum_n S_{l,M+p} S_{k,M+n}^* e^{j(p-n)Dv}.$$

If the result is now averaged over one period of the pattern from $v = -\pi/D$ to $+\pi/D$, it is found that

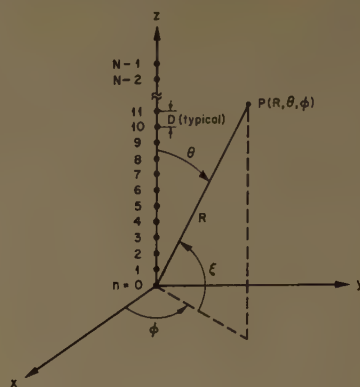
$$\begin{aligned} & \frac{1}{2\pi} \int_{-\pi/D}^{\pi/D} H_l(v)H_k^*(v)dv \\ &= a_l a_k^* \sum_p \sum_n S_{l,M+p} S_{k,M+n}^* \left[\frac{1}{2\pi} \int_{-\pi/D}^{\pi/D} e^{j(p-n)Dv} dv \right]. \end{aligned}$$

The quantity inside the brackets is seen to be unity if $p=n$, and zero otherwise. Hence, we have

$$\frac{1}{2\pi} \int_{-\pi/D}^{\pi/D} H_l(v)H_k^*(v)dv = a_l a_k^* \sum_n S_{l,M+n} S_{k,M+n}^*.$$

Making use of (1), the following result is obtained:

$$\int_{-\pi/D}^{\pi/D} H_l(v)H_k^*(v)dv = \frac{2\pi}{D} |a_l|^2 \delta_{lk}.$$

Fig. 5— N -element linear array geometry.

Thus it is seen that to form simultaneous multiple beams in a lossless manner, it is required that the space factors must be orthogonal over a period (or any integral number of periods) of the pattern thus formed.

DISCUSSION

It has been shown that for a passive, reciprocal matrix to form simultaneous, independent beams in a lossless manner, the shapes must be such that their space factors are orthogonal over the interval of a period of the antenna pattern for the array type assumed; *i.e.*, linear, with equispaced radiators.

Further interpretation of this orthogonality criterion is possible by application of the sampling theorem (or Woodward synthesis technique⁸) to array far fields. Some work on this topic is reported elsewhere,⁴ and it is shown that, for practical applications, the orthogonality criterion appears to limit rather severely the choice of beam shapes.

An investigation is now under way to determine the losses involved in certain departures from the orthogonality criterion.

⁸ P. M. Woodward and J. D. Lawson, "The theoretical precision with which an arbitrary radiation pattern may be obtained from a source of finite size," *J. AIEE*, vol. 95, pt. III, pp. 362-370; September, 1948.

A General Analysis of Nonplanar, Two-Dimensional Luneberg Lenses*

S. ADACHI†, MEMBER, IRE, R. C. RUDDUCK‡, MEMBER, IRE, AND
C. H. WALTER‡, SENIOR MEMBER, IRE

Summary—A class of two-dimensional, nonplanar, modified Luneberg lenses is developed which generalizes the properties of many of the previously developed lenses. By this development the radiated beam can have an arbitrary direction relative to the plane of the lens as compared to previously developed designs in which the beam must lie in the plane of the lens. The lenses are of arbitrary contour; however, only the spherical and the planar contours are considered in detail.

INTRODUCTION

LUNEBERG¹ derived the variation of the index of refraction of a radially symmetric lens which has the optical property that rays from one external focal point are focussed to another external focal point.

Morgan² extended Luneberg's analysis to a lens with an outer shell of arbitrary index where one focus is external and the other focus is either external or internal. The rays of these types of lenses all lie in the plane of the lens.

The analysis presented here is an extension of Morgan's work to a radially symmetric lens of arbitrary contour which focuses rays from an internal point into a collimated beam in a direction diametrically opposite the focus and at an angle β with respect to the plane of the lens (see Fig. 1). The index of refraction is radially symmetric and is arbitrary in an outer annulus, $\alpha \leq r \leq 1$, containing the focus. In the central portion the index depends on the lens contour, the angle β , the index of the outer annulus, and the radius of the focus.

An equation implicitly containing the index is derived for a general lens contour from which the index can be solved when the contour is specified. The index is solved explicitly for the case where the contour is a spherical surface. This special case, denoted as the spherical cap lens, reduces to the planar lens when the cap radius becomes infinite.

ANALYSIS

As seen from Fig. 1, the path length of a ray from the rim of the lens to infinity is

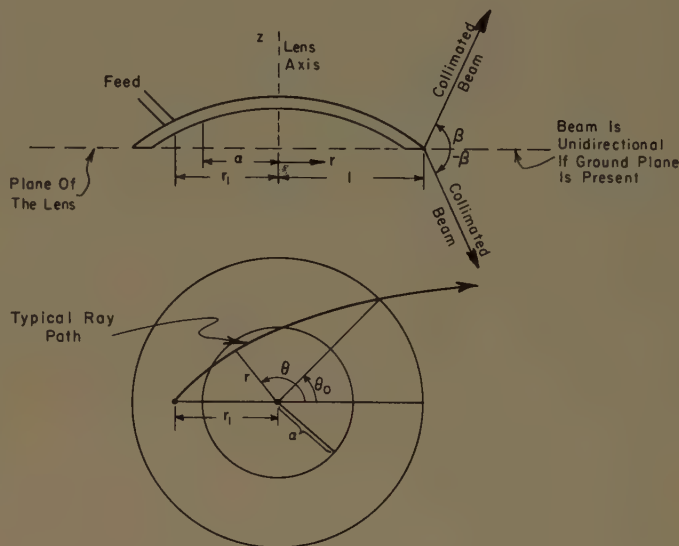


Fig. 1—Nonplanar two-dimensional lens.

$$L = \int n dl = \int_0^{\theta_0} \cos \beta \sqrt{r^2 + \left(\frac{dr}{d\theta}\right)^2} d\theta$$

$$= \int_0^{\theta_0} f_1\left(\beta, r, \frac{dr}{d\theta}\right) d\theta. \quad (1)$$

By Fermat's principle the path L is a path of least time. From the calculus of variations one obtains for a region of radial symmetry an Euler equation of the form

$$f - \frac{dr}{d\theta} \frac{\partial f}{\partial \left(\frac{dr}{d\theta}\right)} = K = nr \sin \phi \quad (2)$$

where ϕ is the angle between the ray path and the radius vector, and K corresponds to an individual ray path.¹

From (1) and (2),

$$K = \frac{r^2 \cos \beta}{\sqrt{r^2 + \left(\frac{dr}{d\theta}\right)^2}}. \quad (3)$$

Solving (3) with respect to $d\theta/dr$ and integrating from the rim of the lens to infinity gives

$$\theta_0 = \frac{K}{\cos \beta} \int_1^\infty \frac{dr}{r \sqrt{r^2 - (K/\cos \beta)^2}} = \sin^{-1} \frac{K}{\cos \beta}. \quad (4)$$

* Received by the PGAP, November 14, 1960; revised manuscript received, January 23, 1961. This work was sponsored, in part, by the Wright Air Dev. Div., Air Res. and Dev. Command, USAF.

† Elec. Communications Dept., Tohoku University, Sendai, Japan.

‡ Elec. Engrg. Dept., The Antenna Lab., The Ohio State University, Columbus, Ohio.

¹ R. K. Luneberg, "Mathematical Theory of Optics," Brown University Press, Providence, R. I., pp. 189–213.

² S. P. Morgan, "General solution to the Luneberg lens problem," *J. Appl. Phys.*, vol. 29, pp. 1358–1368; September, 1958.

From (4) it can be seen that the angle traversed by the ray inside the lens is $\pi - \sin^{-1} K / \cos \beta$. Eq. (4) satisfies the condition that the optical distance from the source to a plane making an angle of $90^\circ - \beta$ with the plane of the lens is the same for all rays.

Inside the lens the path length is given by

$$L = \int f_2 \left(r, \frac{dr}{d\theta}, \dot{z} \right) d\theta \\ = \int n(r) \sqrt{r^2 + (1 + \dot{z}^2) \left(\frac{dr}{d\theta} \right)^2} d\theta \quad (5)$$

where \dot{z} is a function of radius which determines the lens configuration. The function $f_2(r, dr/d\theta, \dot{z})$ also must satisfy (2), giving

$$K = \frac{nr^2}{\sqrt{r^2 + [1 + \dot{z}^2] \left(\frac{dr}{d\theta} \right)^2}} \quad (6)$$

where

$$\dot{z} = dz/dr.$$

Solving for $d\theta/dr$ and integrating from the focus to the rim gives

$$K \int_{r_0}^{r_1} \frac{\sqrt{1 + \dot{z}^2}}{r \sqrt{\rho^2 - K^2}} dr + K \int_{r_0}^1 \frac{\sqrt{1 + \dot{z}^2}}{r \sqrt{\rho^2 - K^2}} dr \\ = \pi - \theta_0 \quad (7)$$

where

$$\rho = n(r)r, \quad (8)$$

and

r_0 = minimum radius of ray path corresponding to a value K ,
 r_1 = radius of internal focal point.

The index of the outer annulus is arbitrary subject to the condition

$$\rho(r) = P(r) \geq \cos \beta, \quad \alpha \leq r \leq 1. \quad (9)$$

Combining (4) and (7),

$$2K \int_{r_0}^{\alpha} \frac{\sqrt{1 + \dot{z}^2}}{r \sqrt{\rho^2 - K^2}} dr \\ = \pi - \sin^{-1} \frac{K}{\cos \beta} - 2K \int_{\alpha}^{r_1} \frac{\sqrt{1 + \dot{z}^2}}{r \sqrt{P^2(r) - K^2}} dr \\ - K \int_{r_0}^1 \frac{\sqrt{1 + \dot{z}^2}}{r \sqrt{P^2(r) - K^2}} dr. \quad (10)$$

An additional condition on $P(r)$ is obtained from (10) by requiring that the ray corresponding to $K = \cos \beta$ not

be refracted through so great an angle that it cannot leave the lens at $\theta = \theta_0$. That is,

$$\frac{\pi}{2} \geq 2 \cos \beta \int_{\alpha}^{r_1} \frac{\sqrt{1 + \dot{z}^2}}{r \sqrt{P^2(r) - \cos^2 \beta}} dr \\ + \cos \beta \int_{r_1}^1 \frac{\sqrt{1 + \dot{z}^2}}{r \sqrt{P^2(r) - \cos^2 \beta}} dr. \quad (11)$$

To solve (10) for n , let

$$G'(\rho) d\rho = -\sqrt{1 + \dot{z}^2} \frac{dr}{r}; \quad (12)$$

thus (10) becomes

$$2K \int_{\cos \beta}^K \frac{G'(\rho) d\rho}{\sqrt{\rho^2 - K^2}} \\ = \pi - \sin^{-1} \frac{K}{\cos \beta} - 2K \int_{\alpha}^{r_1} \frac{\sqrt{1 + \dot{z}^2}}{r \sqrt{P^2(r) - K^2}} dr \\ - K \int_{r_1}^1 \frac{\sqrt{1 + \dot{z}^2}}{r \sqrt{P^2(r) - K^2}} dr. \quad (13)$$

Replacing ρ by σ , multiplying both sides of (13) by $[K^2 - \rho^2]^{-1/2}$, and integrating with respect to K from $K = \rho$ to $K = \cos \beta$, gives

$$\int_{\rho}^{\cos \beta} \left[\int_{\cos \beta}^K \frac{KG'(\sigma)}{\sqrt{(\sigma^2 - K^2)(K^2 - \rho^2)}} d\sigma \right] dK \\ = \frac{\pi}{2} \int_{\rho}^{\cos \beta} \frac{dK}{\sqrt{K^2 - \rho^2}} - \frac{1}{2} \int_{\rho}^{\cos \beta} \frac{\sin^{-1} \frac{K}{\cos \beta}}{\sqrt{K^2 - \rho^2}} dK \\ - \int_{\rho}^{\cos \beta} \left[\int_{\alpha}^{r_1} \frac{K \sqrt{1 + \dot{z}^2}}{\sqrt{P^2(r) - K^2}} \frac{dr}{r} \right] \frac{dK}{\sqrt{K^2 - \rho^2}} \\ - \frac{1}{2} \int_{\rho}^{\cos \beta} \left[\int_{r_1}^1 \frac{K \sqrt{1 + \dot{z}^2}}{\sqrt{P^2(r) - K^2}} \frac{dr}{r} \right] \frac{dK}{\sqrt{K^2 - \rho^2}}. \quad (14)$$

Letting $K/\cos \beta = g$, $dK = \cos \beta dg$ and using the integral defined by Luneberg¹ as

$$\omega(\rho, s) = \frac{1}{\pi} \int_{\rho}^1 \frac{\sin^{-1} \frac{K}{s}}{\sqrt{K^2 - \rho^2}} dK, \quad 0 \leq \rho \leq 1, s \geq 1 \quad (15)$$

and numerically evaluated by Morgan², then

$$\frac{1}{\pi} \int_{\rho}^{\cos \beta} \frac{\sin^{-1} \frac{K}{\cos \beta}}{\sqrt{K^2 - \rho^2}} dK \\ = \frac{1}{\pi} \int_{\rho/\cos \beta}^1 \frac{\sin^{-1} g}{\sqrt{g^2 - \left(\frac{\rho}{\cos \beta} \right)^2}} dg = \omega \left(\frac{\rho}{\cos \beta}, 1 \right) \\ = \frac{1}{2} \ln \left[1 + \sqrt{1 - \left(\frac{\rho}{\cos \beta} \right)^2} \right]. \quad (16)$$

Let

$$\Omega(\rho) = \frac{2}{\pi} \int_{\rho}^{\cos \beta} \left[\int_{\alpha}^{r_1} \frac{K\sqrt{1+\dot{z}^2}}{\sqrt{P^2(r) - K^2}} \frac{dr}{r} \right] \frac{dK}{\sqrt{K^2 - \rho^2}} \\ + \frac{1}{\pi} \int_{\rho}^{\cos \beta} \left[\int_{r_1}^1 \frac{K\sqrt{1+\dot{z}^2}}{\sqrt{P^2(r) - K^2}} \frac{dr}{r} \right] \frac{dK}{\sqrt{K^2 - \rho^2}}. \quad (17)$$

The first integral on the right side of (14) is evaluated as

$$\int_{\rho}^{\cos \beta} \frac{dK}{\sqrt{K^2 - \rho^2}} = \ln \frac{\cos \beta + \sqrt{\cos^2 \beta - \rho^2}}{\rho}. \quad (18)$$

Changing the order of integration on the left side of (14) gives

$$\int_{\rho}^{\cos \beta} \int_{\cos \beta}^K \frac{KG'(\sigma)}{\sqrt{(\sigma^2 - K^2)(K^2 - \rho^2)}} d\sigma dK \\ = \int_{\cos \beta}^{\rho} \int_{\rho}^{\sigma} \frac{KdK}{\sqrt{(\sigma^2 - K^2)(K^2 - \rho^2)}} G'(\sigma) d\sigma. \quad (19)$$

$$n = \frac{\cos \beta (\cos \beta + \sqrt{\cos^2 \beta - \rho^2}) (a + \sqrt{a^2 - \alpha^2})^2 + \rho^2 \alpha^2 e^{2\Omega(\rho)}}{2a\alpha \sqrt{\cos \beta (\cos \beta + \sqrt{\cos^2 \beta - \rho^2})}^{1/2} (a + \sqrt{a^2 - \alpha^2}) e^{\Omega(\rho)}} \quad (27)$$

From standard integral tables it can be shown that

$$\int_{\rho}^{\sigma} \frac{KdK}{\sqrt{(\sigma^2 - K^2)(K^2 - \rho^2)}} = \frac{\pi}{2}. \quad (20)$$

Thus, (14) becomes

$$G(\rho) - G(\cos \beta) \\ = \ln \frac{[\cos^2 \beta + \cos \beta \sqrt{\cos^2 \beta - \rho^2}]^{1/2}}{\rho} - \Omega(\rho). \quad (21)$$

From (12),

$$G(\rho) = \int_r^1 \sqrt{1 + \dot{z}^2} \frac{dr}{r} \quad (22)$$

where the upper limit is chosen for convenience.

The lens design procedure may be summarized as follows: upon specification of $z(r)$ for a given lens contour, $G(\rho)$ is found from (22). After specification of $P(r)$ subject to conditions of (9) and (11), $\Omega(\rho)$ can be evaluated from (17). Eq. (21) can then be solved for the index in terms of ρ by replacing r by ρ/n . Then, using $\rho = nr$, the radius corresponding to index n is found.

SPHERICAL CAP LENS

For a spherical cap lens³ with a cap radius of a , the surface is specified by

$$z = \pm \sqrt{a^2 - r^2} \quad (23)$$

and

$$\dot{z} = \frac{dz}{dr} = \frac{\mp r}{\sqrt{a^2 - r^2}}. \quad (24)$$

Then (22) gives

$$G(\rho) = \int_r^1 \frac{adr}{r\sqrt{a^2 - r^2}} = \left[\ln \frac{r}{a + \sqrt{a^2 - r^2}} \right]_r^1 \\ = \ln \frac{a + \sqrt{a^2 - r^2}}{r(a + \sqrt{a^2 - 1})}, \quad (25)$$

and from (21)

$$\ln \frac{\alpha(a + \sqrt{a^2 - r^2})}{r(a + \sqrt{a^2 - \alpha^2})} \\ = \ln \frac{[\cos^2 \beta + \cos \beta \sqrt{\cos^2 \beta - \rho^2}]^{1/2}}{\rho} - \Omega(\rho). \quad (26)$$

Solving for $n(\rho)$,

where (17) and (24) give

$$\Omega(\rho) = \frac{2}{\pi} \int_{\alpha}^{r_1} \tan^{-1} \left[\frac{\cos^2 \beta - \rho^2}{P^2(r) - \cos^2 \beta} \right]^{1/2} \frac{adr}{r\sqrt{a^2 - r^2}} \\ + \frac{1}{\pi} \int_{r_1}^1 \tan^{-1} \left[\frac{\cos^2 \beta - \rho^2}{P^2(r) - \cos^2 \beta} \right]^{1/2} \frac{adr}{r\sqrt{a^2 - r^2}} \quad (28)$$

and $P(r)$ is subject to the conditions in (9) and (11).

To minimize reflections the index should be continuous throughout the lens and have a value of unity at the rim. This establishes

$$P(\alpha) = \cos \beta \quad (29)$$

and

$$P(1) = 1. \quad (30)$$

One function which satisfies these conditions is

$$P(r) = \sqrt{\frac{(r - \alpha)^2}{(1 - \alpha)^2} \sin^2 \beta + \cos^2 \beta}, \quad (31)$$

³ S. Adachi and C. H. Walter, "A Spherical Cap Lens," Antenna Lab., The Ohio State University Research Foundation; Rept. 903-3, April 30, 1959; prepared under Contract AF 33(616)-6211, Wright Air Div., Wright-Patterson AFB, Dayton, Ohio.

then, for $r_1 = \alpha$,

$$\Omega(\rho) = \frac{a}{\pi} \int_{\alpha}^1 \tan^{-1} \frac{(1 - \alpha) \sqrt{\cos^2 \beta - \rho^2}}{(\sin \beta)(r - \alpha)} \frac{dr}{r \sqrt{a^2 - r^2}}. \quad (32)$$

Eq. (32) has been numerically integrated for $\alpha = 0.75$, $\beta = 20^\circ$, and $a = \sqrt{2}$. The resulting index is illustrated in Fig. 2.

PLANAR LENS

The planar lens is the special case of the spherical cap lens for which $a \rightarrow \infty$. Eq. (27) reduces to

$$n = \frac{1}{\alpha} \sqrt{\cos \beta} (\cos \beta + \sqrt{\cos^2 \beta - \rho^2})^{1/2} e^{-\Omega(\rho)} \quad (33)$$

and (28) reduces to

$$\Omega(\rho) = \frac{2}{\pi} \int_{\alpha}^{r_1} \tan^{-1} \left[\frac{\cos^2 \beta - \rho^2}{P^2(r) - \cos^2 \beta} \right]^{1/2} \frac{dr}{r} + \frac{1}{\pi} \int_{r_1}^1 \tan^{-1} \left[\frac{\cos^2 \beta - \rho^2}{P^2(r) - \cos^2 \beta} \right]^{1/2} \frac{dr}{r} \quad (34)$$

where again $P(r)$ is subject to (9) and (11).

The class of planar lenses for which

$$P(r) = Ar^m = \frac{\cos \beta}{\alpha^m} r^m, \quad m \neq 0, \quad (35)$$

will be considered. The coefficient of r^m was chosen such that the index will be continuous at $r = \alpha$.

Evaluating the integrals with respect to r in (17) by setting $x = r^m$ and $dx = mr^{m-1} dr$ gives

$$\int_{\alpha}^{r_1} \frac{K dr}{r \sqrt{A^2 r^{2m} - K^2}} + \frac{1}{2} \int_{r_1}^1 \frac{K dr}{r \sqrt{A^2 r^{2m} - K^2}} = \frac{1}{m} \left[\sin^{-1} \frac{K}{\cos \beta} - \frac{1}{2} \sin^{-1} \frac{K}{r_1 n(r_1)} - \frac{1}{2} \sin^{-1} \frac{K}{n(1)} \right]. \quad (36)$$

Then, using (15),

$$\Omega(\rho) = \frac{1}{m} \left[2\omega \left(\frac{\rho}{\cos \beta}, 1 \right) - \omega \left(\frac{\rho}{\cos \beta}, \frac{r_1 n(r_1)}{\cos \beta} \right) - \omega \left(\frac{\rho}{\cos \beta}, \frac{n(1)}{\cos \beta} \right) \right]. \quad (37)$$

To make the index continuous at $r = 1$, let $n(1) = 1$; then $A = \cos \beta / \alpha^m = 1$ and the inner radius of the outer shell becomes

$$\alpha = (\cos \beta)^{1/m} \quad (38)$$

and

$$\Omega(\rho) = \frac{1}{m} \left[\ln \left(1 + \sqrt{1 - \left(\frac{\rho}{\cos \beta} \right)^2} \right) - \omega \left(\frac{\rho}{\cos \beta}, \frac{r_1 n(r_1)}{\cos \beta} \right) - \omega \left(\frac{\rho}{\cos \beta}, \frac{1}{\cos \beta} \right) \right]. \quad (39)$$

Thus for $P(r) = r^m$ and $\alpha = (\cos \beta)^{1/m}$

$$n = \frac{1}{\alpha} (\cos \beta)^{(m+2)/2m} (\cos \beta + \sqrt{\cos^2 \beta - \rho^2})^{(m-2)/2m} \cdot \exp \left\{ \frac{1}{m} \left[\omega \left(\frac{\rho}{\cos \beta}, \frac{r_1 n(r_1)}{\cos \beta} \right) + \omega \left(\frac{\rho}{\cos \beta}, \frac{1}{\cos \beta} \right) \right] \right\}. \quad (40)$$

For a planar lens with the focus at the rim and no outer shell,

$$r_1 = \alpha = 1$$

$$\Omega(\rho) = 0 \quad (41)$$

and

$$n(r) = (\cos \beta) \sqrt{2 - r^2}. \quad (42)$$

Eq. (42) corresponds to the index of the well-known Luneberg lens for $\beta = 0$. The index is plotted for several values of β in Fig. 3.

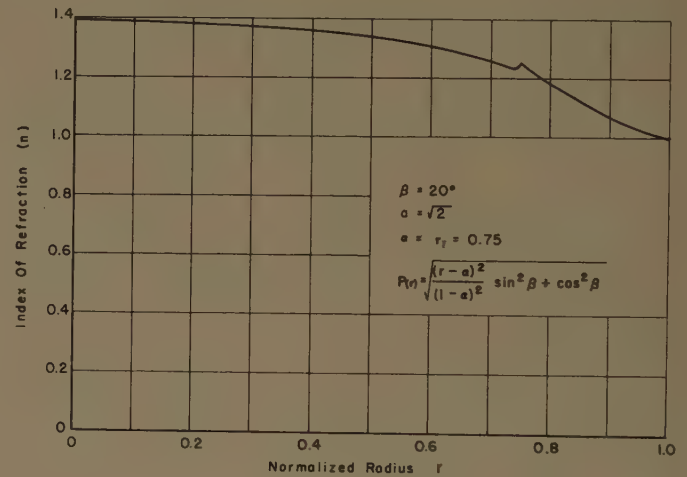


Fig. 2—Variation of index for a spherical cap lens.

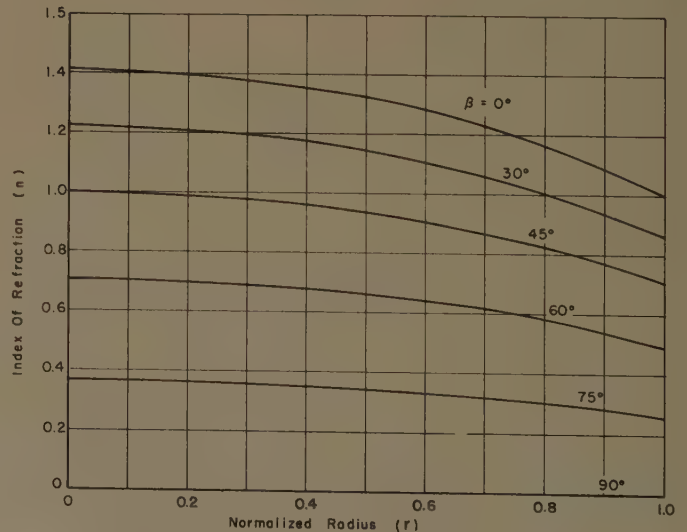


Fig. 3—Index variation for rim-fed planar lenses with no outer shell.

In general, it can be shown that if the index variation of a lens designed for $\beta=0^\circ$ is multiplied by $\cos \beta$, the resulting lens will radiate at an angle β .

DISCUSSION

Although only the cylindrical lens has been considered, the spherical lens having any radial variation of index as derived here for the planar lenses will radiate a conical beam having a cone angle of 2β .

The numerical value of the index or the dielectric constant required becomes less than unity over part or the whole of many of the lenses developed here [for example, see (42)]. This greatly reduces the methods which can be used to obtain these lenses. For a two-dimensional lens a waveguide supporting the TE_{10} mode has an index given by

$$n = \frac{\lambda}{\lambda_g} = \sqrt{\epsilon_r - (\lambda/2d)^2} \quad (43)$$

where

λ = free-space wavelength,

λ_g = guide wavelength,

ϵ_r = relative dielectric constant of material filling guide, and

d = plate spacing.

Thus values of the index less than unity are obtainable. If a three-dimensional lens is desired, plasmas are a possibility for dielectric constants less than unity. The practicability of this suggestion depends on advances in the state of the art of plasmas.

EXPERIMENTAL RESULTS

An 18-inch diameter, X-band, planar lens of the type described by (42) was constructed for TE operation. The index was varied by means of plate spacing. Thus combining (42) and (43) gives

$$d = \frac{\lambda}{2\sqrt{\epsilon_r - \cos^2 \beta(2 - \epsilon_r)}} \quad (44)$$

The lens was designed for $\beta=45^\circ$, $\lambda=3.1$ cm, and ϵ_r was chosen as 1.3. The experimental model is shown in Fig. 4. One side of the dielectric is flat and lies against the ground plane. The other side is contoured in accordance with (44), as is the lower side of the cover plate.

The principal vertical beam pattern shown in Fig. 5 has a half-power beamwidth of 18° . The pattern taken perpendicular to the vertical beam pattern, and at 45° with respect to the ground plane, is also shown in Fig. 5 and has a half-power beamwidth of 5° and a sidelobe level of about -18 db.

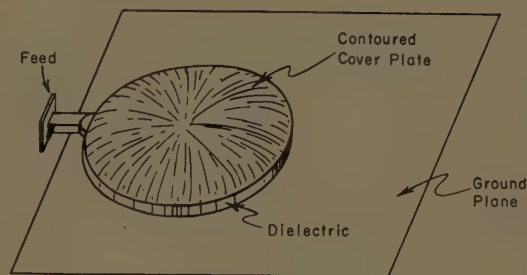


Fig. 4—Planar lens with ground plane.

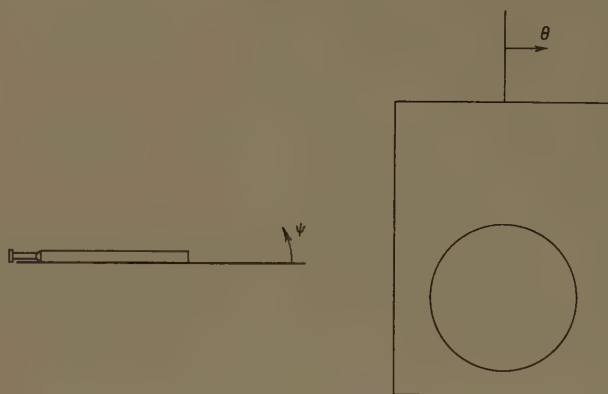
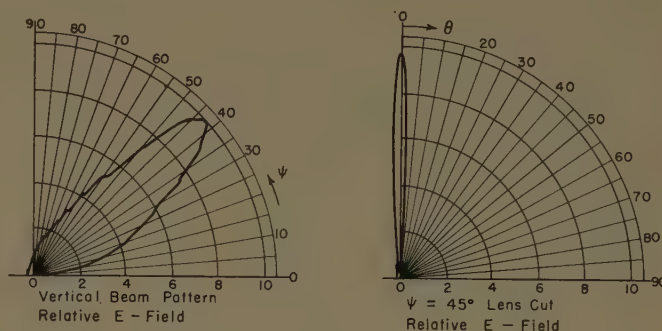


Fig. 5—Planar lens patterns ($\beta=45^\circ$).

CONCLUSIONS

A radially symmetric two-dimensional lens of arbitrary contour has been developed which, fed by a point source, radiates a collimated beam at an angle β with respect to the plane of the lens. In this respect this design is a generalization of many of the previously developed lenses in that they reduce to this design for $dz/dr=0$ and $\beta=0$. As in other analyses the theory is based on optical assumptions and hence nonzero beamwidths result because of diffraction effects.

The feature of arbitrary contour may be beneficial in some situations, such as flush-mounting on aircraft or missiles.

The Numerical Evaluation of Radiation Integrals*

J. H. RICHMOND†, SENIOR MEMBER, IRE

Summary—In the numerical evaluation of radiation integrals, the number of terms required depends on the accuracy desired, the method of integration, the current distribution on the antenna, the length of the antenna, and the observation angle. Simpson's rule and the trapezoidal rule appear to be used almost exclusively at present. A "piecewise linear rule" introduced here is shown to yield greater accuracy for a given calculation time.

INTRODUCTION

THERE are many examples of antenna current distributions (or aperture field distributions) which can be integrated analytically to obtain the far-field patterns. However, the current distribution in many cases is available only in the form of measured data. In this case an analytic integration is not possible until a formula which fits the measured data is derived for the current. Even when a formula is available for the current, a numerical integration may be preferable if the analytic integration cannot readily be performed, or if it leads to a solution which is not convenient for numerical computation.

When numerical integration is to be employed, a choice must be made among the various methods which are available. For a given application, the method which is best for hand calculations may not be best for an electronic computer. Nevertheless, any technique which proves advantageous on the desk calculator is worthy of consideration for automatic electronic computations.

Some data have been reported previously^{1,2} to indicate the results obtained in antenna pattern calculations with the trapezoidal rule,^{3,4} Simpson's rule,^{3,4} and an array of point sources. A "piecewise linear" rule is introduced here and compared with the conventional techniques.

It should be noted that the problem considered here is mathematically the same as that of evaluating Fourier coefficients. The techniques and the discussion

will therefore be found useful in Fourier analysis as well as in antenna problems.

A STATEMENT OF THE PROBLEM

Let $\dot{I}(x)$ represent the current distribution on a line source, or the aperture field of an antenna. The integral which arises in calculating the far-field pattern has the form⁵

$$E = \int_{-a}^a \dot{I}(x) e^{jbx} dx \quad (1)$$

where E is the electric field intensity, b is $\beta \sin \theta$, β is $2\pi/\lambda$, λ is the wavelength, θ is the observation angle, and $2a$ is the length of the antenna as illustrated in Fig. 1. In general $\dot{I}(x)$ is complex, but the complex integral in (1) may be resolved into four real integrals of the forms $\int I(x) \cos bxdx$ and $\int I(x) \sin bxdx$, where I represents the real or imaginary component of the current. Given a table or a graph of $I(x)$, the problem is to evaluate these integrals to a specified degree of accuracy. Usually this must be repeated for many different values of b to provide adequate information on the pattern shape.

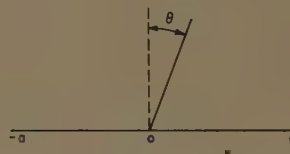


Fig. 1—A line source and the coordinate system.

THE PIECEWISE LINEAR RULE

Let each half of the antenna be divided into N segments of equal length, and let I_n represent the current values at the ends of these segments. If the current $I(x)$ is approximated by a continuous, piecewise linear function on these segments, the following expressions are obtained for the radiation integrals:

$$\begin{aligned} \frac{1}{a} \int_0^a I \cos bxdx &= I_N \left(1 - \frac{\sin ba/N}{ba/N} \right) \frac{\sin ba}{ba} \\ &+ \frac{1}{N} \left(\frac{\sin ba/2N}{ba/2N} \right)^2 \sum_0^N C_n I_n \cos nba/N, \quad (2) \end{aligned}$$

⁵ In some cases a factor such as $\cos \theta$ should appear in front of the integral in (1), but this is immaterial to this study and will be omitted.

* Received by the PGAP, December 18, 1960; revised manuscript received, January 31, 1961. This research was sponsored by the Wright Air Dev. Div. under Contract AF 33(616)-5410.

† Antenna Lab., Dept. Elec. Engrg., The Ohio State University, Columbus.

¹ J. H. Richmond, "Simplified calculation of antenna patterns, with application to radome problems," IRE TRANS. ON MICROWAVE THEORY AND TECHNIQUES, vol. MTT-3, pp. 9-12; July, 1955.

² C. H. Walter, "Surface-Wave Luneberg Lens Antenna," Antenna Lab., The Ohio State University Res. Foundation, Columbus, Rept. 667-32, prepared under Contract AF 33(616)-3353, Wright Air Dev. Div., Wright-Patterson AFB, Dayton, Ohio; May 15, 1957.

³ W. C. Johnson, "Mathematical and Physical Principles of Engineering Analysis," McGraw-Hill Book Co., Inc., New York, N. Y., pp. 76-79; 1944.

⁴ K. S. Kunz, "Numerical Analysis," McGraw-Hill Book Co., Inc., New York, N. Y., p. 146; 1957.

$$\frac{1}{a} \int_0^a I \sin bxdx = \frac{1}{ba} (I_0 - I_N \cos ba) \left(1 - \frac{\sin ba/N}{ba/N} \right) + \frac{1}{N} \left(\frac{\sin ba/2N}{ba/2N} \right)^2 \sum_1^N C_n I_n \sin nba/N, \quad (3)$$

where

$$C_n = \begin{cases} 1/2 & \text{if } n = 0, N \\ 1 & \text{if } n = 1, 2, \dots, N-1 \end{cases} \quad (4)$$

and

$$I_n = I(x_n) = I(na/N). \quad (5)$$

These equations may be derived by assuming that the current is a linear function on each segment of the line source. On the first segment ($0 < x < a/N$), for example, $I = I_0 + x(I_1 - I_0)N/a$. The recursion formula $\cos(n+1)t = 2 \cos nt \cos t - \cos(n-1)t$ and the corresponding one for $\sin(n+1)t$ are also useful in the derivation. These piecewise linear rules yield the exact solutions whenever the current is continuous and piecewise linear. The pattern of a line source having a "gable" current distribution, for example, is given precisely by (2)

for all values of ba if N is unity or greater. The uniform line source is also handled with zero error.

Eq. (2) simplifies considerably if the current goes to zero at the end of the line source. Thus, if $I_N = 0$,

$$\frac{1}{a} \int_0^a I \cos bxdx = \frac{2N}{(ab)^2} (1 - \cos ba/N) \cdot \sum_1^{N-1} C_n I_n \cos nba/N. \quad (6)$$

In this case, the piecewise linear rule (6) requires the same summation that appears in the trapezoidal rule, followed by multiplication by $[(\sin ba/2N)/(ba/2N)]^2$. Once this function has been tabulated, the calculation time will be just slightly greater for the piecewise linear rule than for the trapezoidal rule for the same number of segments $2N$.

Fig. 2 compares the pattern calculations obtained with the trapezoidal, Simpson's, and piecewise linear rules. To permit a fair comparison, N was chosen equal to 5 for the trapezoidal and Simpson's rules, and $N=4$ for the piecewise linear rule. In this way the calculation time was almost the same by each method.

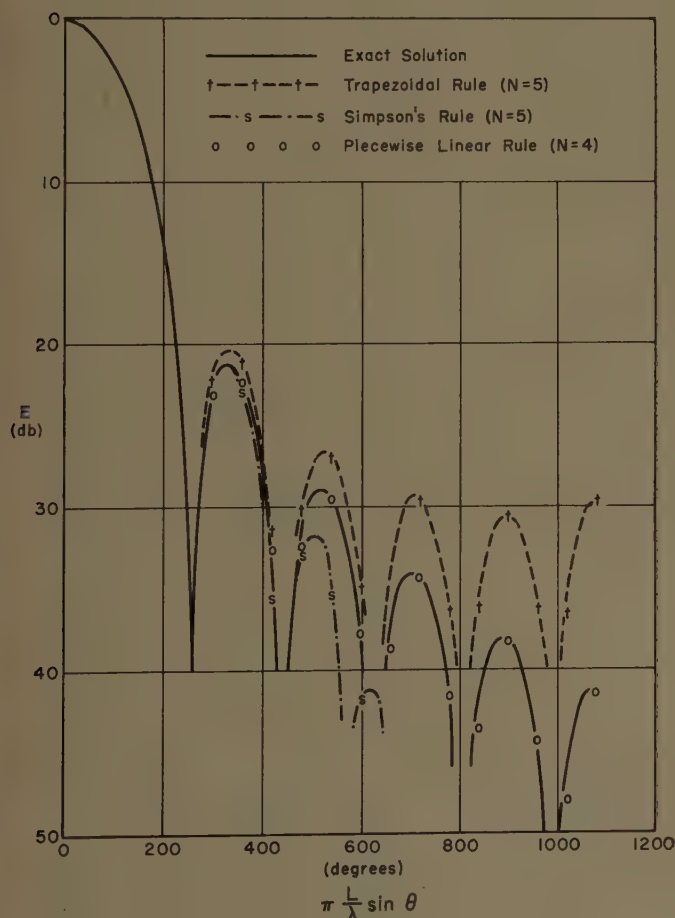


Fig. 2—Trapezoidal, Simpson's, and piecewise linear pattern calculations for a line source with quadratic taper, compared with the exact solution.

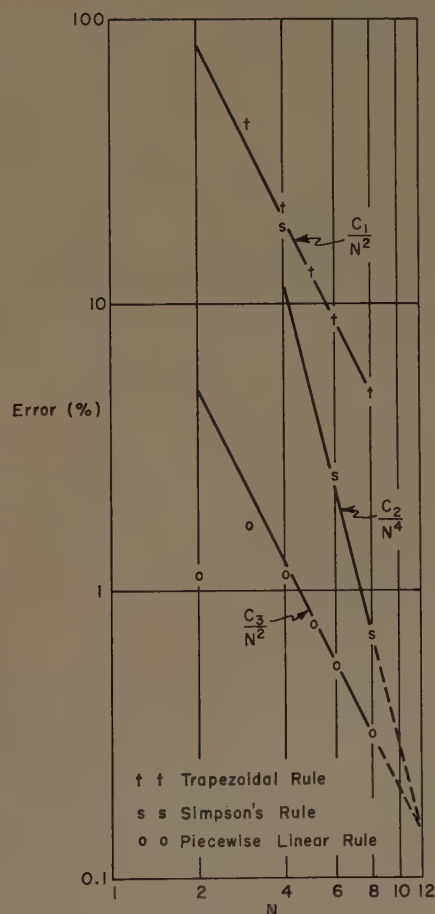


Fig. 3—Error vs N for trapezoidal, Simpson's, and piecewise linear rules applied to a line source with cosine taper.

The far-field pattern expressions obtained from the trapezoidal, Simpson's, and piecewise linear rules are listed below for comparison.

$$E_t = 0.15 + 0.288 \cos ba/5 + .252 \cos 2ba/5 \\ + 0.192 \cos 3ba/5 + 0.108 \cos 4ba/5, \quad (7)$$

$$E_s = 0.20 + 0.192 \cos ba/5 + 0.336 \cos 2ba/5 \\ + 0.128 \cos 3ba/5 + 0.144 \cos 4ba/5, \quad (8)$$

$$E_{p1} = \frac{1 - \cos ba/4}{(ab)^2} (6 + 11.25 \cos ba/4 + 9 \cos 2ba/4 \\ + 5.25 \cos 3ba/4). \quad (9)$$

The current was assumed to have a quadratic taper as given by

$$I(x) = 1 - (x/a)^2. \quad (10)$$

All three methods gave negligible error in the main beam (Fig. 2). Simpson's rule actually gave the best accuracy in the main beam and first sidelobe, but it went wild in the second sidelobe. The trapezoidal rule gave the correct angular positions of all the sidelobes but it yielded large errors in their magnitudes. The piecewise linear rule gave good agreement with the exact solution through the fifth sidelobe.

In the calculations for Fig. 2, it was noted that the trapezoidal and Simpson's rules yielded solutions which are symmetrical about the point $ba = 900^\circ$. This is to be expected since the trigonometric terms in (7) and (8) are harmonically related. Indeed, it can be shown that these two rules yield solutions which are symmetrical about the point $ba = N\pi$ and periodic with a period of $2N\pi$ on ba . Since the correct pattern will not generally have this periodicity or symmetry, the trapezoidal and Simpson's rules must be considered useless when ba exceeds $N\pi$. It follows that the $2N$ segments of the antenna must have lengths l given by

$$l = \frac{L}{2N} < \frac{\lambda}{2 |\sin \theta|}, \quad (11)$$

where $L = 2a$ is the total length of the antenna. Thus, if

calculations are to be made for angles up to 90° , at least one segment is required for each half-wavelength. On the other hand, the piecewise linear rule is nonperiodic and this limitation does not apply.

In these techniques for numerical integration, the error varies in a complicated, irregular manner as a function of N when the segments are longer than the upper bound given by (11). However, when N is reasonably large, the error varies inversely with N^4 in Simpson's rule and inversely with N^2 in the trapezoidal and piecewise linear rules. This is illustrated in Fig. 3 where the error is plotted vs N for calculations at $ba = 360^\circ$ (the center of the first sidelobe). This simple dependence of the error on N makes it easy to estimate the accuracy obtained when calculations have been made using two different values of N .

CONCLUSIONS

Several methods are available for the numerical evaluation of radiation integrals. While the trapezoidal rule and Simpson's rule are probably used most frequently, the piecewise linear rule introduced in this paper appears to be more advantageous.

Because of the periodicity exhibited by the trapezoidal and Simpson's expressions, they require that the antenna be divided into segments no longer than $\lambda/(2 |\sin \theta|)$, where λ is the wavelength and θ is the observation angle. In practice, it is found that the segments must be considerably shorter than this to obtain accurate results. In contrast, the piecewise linear rule is nonperiodic and the above limitation does not apply.

The piecewise linear expression has the correct asymptotic form at large angles: $\lambda/(L \sin \theta)$ if the current is not zero at the ends of the line source, and $\lambda^2/(L \sin \theta)^2$ if the current does go to zero at the ends, whereas the trapezoidal and Simpson's rules yield an incorrect periodic behavior at large angles.

These conclusions are based on comparisons with the exact solutions for a variety of antenna current distributions (cosine, sine, $|\sin|$, exponential, quadratic, uniform, and gable). Applications to antenna pattern synthesis are possible.

An Iris-Excited Slot Radiator in the Narrow Wall of Rectangular Waveguide*

D. G. DUDLEY, JR.†

Summary—The inclined, narrow-wall slot radiator has been used extensively in antenna arrays. The slot is easily machined and handles high power. The inclination of the slot, however, produces an undesirable cross-polarized radiation component. This cross polarization, coupled with the variation of the slot admittance with frequency, causes pattern deterioration and loss in array efficiency. A noninclined, narrow-wall slot radiator has been developed. This slot is excited by two compound irises which produce an inclination of the electric field as it passes the slot. The field inclination replaces the slot inclination, thereby eliminating the cross-polarized component. Although the power handling capability of the slot is limited by the iris structure, the slot has improved conductance characteristics. Variation of slot excitation in both amplitude and phase has been produced by varying the iris dimensions. The iris-excited, narrow-wall slot radiator has application to receiving and to low-power transmitting arrays.

INTRODUCTION

IN modern radar applications, the inclined slot radiator in the narrow wall of rectangular waveguide has been widely used, particularly in large arrays which scan electronically. This slot, commonly called the edge slot, possesses the advantages of relative ease of construction and high power handling. Equally important, since the slot is machined in the narrow rather than the broad wall, neighboring slots in an array can be more closely spaced in order to avoid multiple beams. The edge slot, however, must be inclined to cause excitation and its admittance properties vary rapidly with frequency. Inclination causes a cross-polarized component; admittance variation causes variation in amplitude and phase of the radiated field. Each of these factors can cause pattern deterioration. In the following sections, the cross-polarization and bandwidth variation problems are discussed, and a slot design is presented which solves the former problem and lessens the latter at the expense of the high power handling capability. The designed slot has application to receiving and to low power transmitting arrays.

CROSS POLARIZATION

A theoretical and experimental analysis of the effects of cross polarization in an array of edge slots has been made by Kurtz and Yee.¹ For a two-dimensional 16×16 array employing frequency scan in one plane and phase

scan in the other, the sidelobes were all at least 25 db down from the main beam in the principle *E* plane. However, because of cross polarization, second-order beams were experimentally measured only 12 db down from the main beam. These second-order beams have often been overlooked because, in two-dimensional arrays, they can occur in positions other than the planes in which patterns are normally measured. Several methods have been used to overcome this difficulty. First, each slot can feed an auxiliary waveguide which in turn radiates the energy from an open end. Second, rows of slots in an array can be fitted with external baffles to suppress the unwanted polarization component.² Third, in a one-dimensional array, the row of slots can excite a parallel plate region which radiates the energy from an open end. All of these methods suffer from the same difficulty: they require hardware external to the slot. Apart from the mechanical bulk and structure problems which can arise because of the external hardware, electrical admittance matching of the slot to the suppressing element is sometimes necessary. This matching can cause further bandwidth problems. Therefore, in the slot design considered herein, attention was focused on utilizing a noninclined slot (a slot which would normally be nonexcited) and on means of exciting it internally. Since the radiated electric field from such a slot is entirely horizontal or vertical, depending on the orientation of the array, there is no cross-polarized component.

BANDWIDTH

The bandwidth of a circuit component is usually defined as follows:

$$\%BW = \frac{f_H - f_L}{\frac{f_H + f_L}{2}} \times 100, \quad (1)$$

where f_H and f_L are the high and low extremities of the frequency band, respectively. In low-frequency tuned circuits, f_H and f_L are usually defined as the frequencies at which the magnitude of the circuit voltage gain K is down 3 db from the resonant value K_R ; that is,

$$\frac{K}{K_R} = \sqrt{\frac{1}{2}}. \quad (2)$$

* Received by the PGAP, November 25, 1960.

† Ground Systems Group, Hughes Aircraft Co., Fullerton, Calif.

¹ L. A. Kurtz and J. S. Yee, "Second-order beams of two-dimensional slot arrays," IRE TRANS. ON ANTENNAS AND PROPAGATION, vol. AP-5, pp. 356-363; October, 1957.

² *Ibid.*, p. 361, Fig. 12.

For single-tuned, class A pentodes, the gain K is proportional to the impedance Z of the tuned circuit so that

$$\frac{Z}{Z_R} = \sqrt{\frac{1}{2}} \quad (3)$$

at the 3-db points. Because slots in both the broad and narrow walls of rectangular waveguide exhibit resonance characteristics similar to low-frequency RLC tuned circuits, slot bandwidth has often been characterized by frequency width between 3-db points.³ However, where emphasis in low-frequency circuits is on coupling between stages or coupling to an output load, considerations in slot bandwidth, particularly as applicable to antenna arrays, are more complex. Here, the emphasis is not only on coupling between stages (in this case, the stages are slots) but also on the radiation from each stage. In an end-fed traveling-wave array, for example, if the slot conductances decrease with frequency, both the amplitude distribution and the per cent power in the dummy load change. The amplitude distribution change causes a change in the antenna pattern while the power-into-the-load change causes a loss in over-all antenna efficiency. If the slot susceptances change, phase errors are introduced which, when analyzed into odd and even functions about the array center, produce beam-pointing error and pattern degradation, respectively. Therefore, the conclusion is that a simple definition of slot bandwidth as borrowed from low-frequency concepts is an oversimplification when applied to slots in arrays. It is proposed to consider slot bandwidth as a dual phenomenon which manifests itself differently in the conductance and susceptance variations.

SELECTION OF THE METHOD OF SLOT EXCITATION

If a vertical slot in the narrow wall is to be used to prevent cross polarization, a method of excitation internal to the waveguide structure is necessary. The method of excitation chosen herein is suggested by an experimental investigation of iris-excited, longitudinal slots in the broad wall performed by Tang⁴ of Hughes Aircraft Company. Tang considered the case of the centerline longitudinal slot, a slot which normally is non-excited. He placed a compound iris across the waveguide cross section (Fig. 1) with the position of the iris adjustable in the transverse direction. The amount of asymmetry in the two inductive portions of the iris (the $e:f$ ratio) determined the magnitude of the slot excitation. A correspondence was discovered by Tang between this ratio and the distance from the centerline of the

more usual off-set longitudinal slot. In his results, there is an indication of nearly constant conductance over a broad range of frequencies.

To adapt Tang's concept to the narrow wall required a reconsideration of the role of the exciting iris. In Tang's method, the purpose of the iris was to introduce an effective displacement of the slot off centerline. However, in the narrow wall, the result desired is an effective tilt of the slot rather than a displacement. This effect is realized by tilting the transverse currents in the narrow wall as they pass the plane of the slot rather than tilting the slot itself (Fig. 2). To produce this tilt, a compound iris is placed on each side of the slot, one with the capacitive portion against the top broad wall, the other with the capacitive portion against the bottom broad wall (Fig. 3). It is then proposed to vary the amount of coupling by varying any of three parameters: first, the iris separation c ; second, the iris capacitive height d ; third, the slot length.

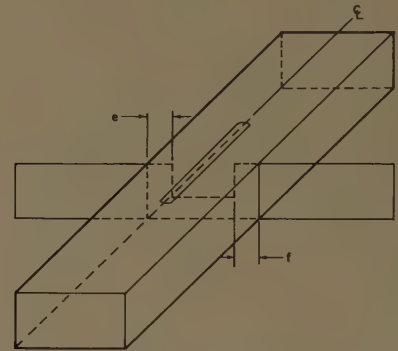


Fig. 1—Iris-excited longitudinal slot in the broad wall.

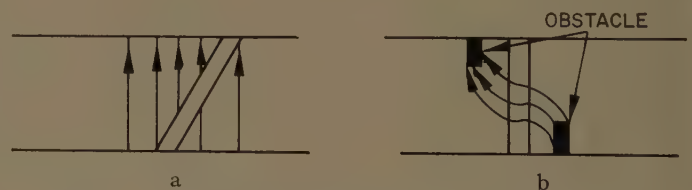


Fig. 2—Exciting the narrow-wall slot. (a) Tilting the slot. (b) Tilting the transverse currents.

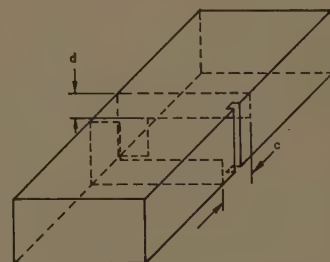


Fig. 3—Iris-excited slot in the narrow wall.

³ I. P. Kaminow and R. J. Stegen, "Waveguide Slot Array Design," Hughes Aircraft Co., Culver City, Calif., Tech. Memo. No. 348; July 1, 1954. See p. 33.

⁴ R. Tang, "A slot with variable coupling and its application to a linear array," IRE TRANS. ON ANTENNAS AND PROPAGATION, vol. AP-8, pp. 97-102; January, 1960.

EXPERIMENTAL RESULTS

The experimental program was accomplished at X band using a X-13B Klystron oscillator driving a set-up capable of measuring admittance by the sliding short δx method.⁵ Gages with an accuracy of ± 0.001 inch were used on both the slotted line and the sliding short. The slotted line, the test piece, the sliding short, and the sliding short gage were all mounted on a solid base and boresighted to minimize error throughout the travel of the plunger on the sliding short. Oscillator drift was checked by making periodic wavelength checks and repeat measurements.

In order to establish a standard for comparison, measurements were taken on a conventional inclined slot in the narrow wall. The slot chosen was a 20° inclined slot with an 0.138-inch cutback into the broad face. (This cutback is necessary in standard height waveguide in order to make the slot resonant in the usable frequency band of the waveguide.) The conductance curve (Fig. 4) resembles the resonance curve of a series RLC circuit. The susceptance curve also resembles the RLC susceptance curve except for the region between 9.00 and 9.45 kMc. (It is postulated that the behavior of the susceptance in this region is caused by the cutback of the slot in the broad wall. Since it is not possible to shorten the slot to eliminate this cutback without forcing the resonant frequency into the TE_{20} mode region, investigation of this postulate is difficult. A possible method would be to increase the narrow wall dimensions rather than to shorten the slot. This method would invite propagation of the TE_{01} mode as well as the desired TE_{10} mode, but excitation of the unwanted mode in this case might be controlled.)

To produce an iris-excited slot, compound irises were designed using the curves for zero-thickness obstacles taken from Marcuvitz.⁶ The objective was to produce an iris with an inductive portion and a capacitive portion which would cancel each other at the resonant frequency. The two exciting irises were placed 0.25 inch apart equidistant to either side of the slot. The resulting data (Fig. 5) showed a remarkably flat conductance characteristic throughout the range of measurement. The susceptance curve, however, varied slightly from the susceptance curve of the irises alone, relative to the terminal plane of the slot. It was postulated that this difference was caused by coupling between the two irises. This postulate was verified by changing the iris spacing while keeping slot length and iris dimensions constant. A range in resonant frequency from 8.4 to 8.92 kMc (Fig. 6) was obtained by varying the spacing from 0.063 to 0.25 inch.

Design data for iris-excited slots are given in Fig. 7 for a resonant frequency of 8.92 kMc and an iris separation of 0.25 inch. For a given height of the capacitive portion of the iris (d/b) the resonant conductance and the width of the inductive portion of the iris (c/a) to cause resonance at 8920 megacycles are determinable. For the test pieces measured, a range of conductance from 0.02 to 0.18 was obtained. Lower conductances should be possible although it was not possible to make measurements accurately below 0.02 because of mechanical imperfections in the sliding short. However,

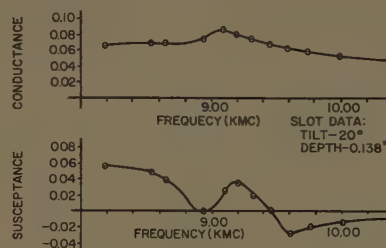


Fig. 4—Slot admittance, normally excited edge slot.

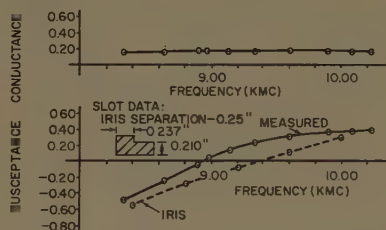


Fig. 5—Slot admittance, iris-excited edge slot.

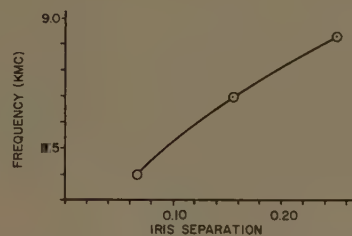


Fig. 6—Slot resonant frequency vs. iris separation.

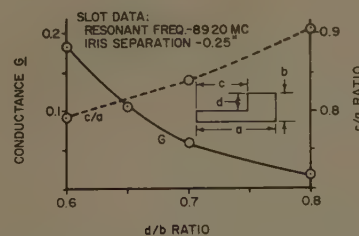


Fig. 7—Resonant conductance and inductive width of iris vs. capacitive width of iris.

⁵ Kaminow and Stegen, *op. cit.*, p. 14.

⁶ N. Marcuvitz, "Waveguide Handbook," McGraw-Hill Book Co., Inc., New York, N. Y., p. 218; 1951.

such measurements are possible using other methods.⁷ Higher conductances should also be possible but are unusual except in arrays with small numbers of elements.

CONCLUSIONS

The iris-excited slot radiator offers a means of radiating power from an array with no component of cross polarization without resorting to external baffles or other cross-polarization suppressing structures. The constant character of the conductance offers an opportunity to control the amplitude distribution over a larger frequency band than with conventional inclined slots. The susceptance, however, varies more rapidly with frequency than with the susceptance of the inclined

slots, but closely follows the susceptance of the exciting irises. In some array applications, this variation could cause troublesome phase errors unless care is taken in the design to assure that phase variations for all elements are similar. Some control is possible in this respect since identical conductance values can be obtained with different size irises by adjusting the iris spacing.

ACKNOWLEDGMENT

A portion of this work was accomplished in partial satisfaction of the requirements for the M.S.E. degree at the University of California at Los Angeles where the guidance of R. S. Elliott is gratefully acknowledged. The author also wishes to acknowledge the cooperation of N. Yaru and the encouragement of L. A. Kurtz who did much to pioneer slot investigations.

⁷ Kaminow and Stegen, *op. cit.*, p. 17.

Reflection of Electromagnetic Waves from a Stratified Inhomogeneity*

R. YAMADA†

Summary—This paper deals with the partial reflection of electromagnetic waves from a stratified inhomogeneity. When the refractive index profile is an analytic function and the wave number is large, the reflection coefficient is calculated by the use of the Volterra integral equation and the relation between the WKB approximation and the internal reflection is examined. The reflection coefficient in this case is calculated also by the WKB method using the connection formula around the turning point which lies in the complex plane. When the index profile is discontinuous, the reflection coefficients are calculated for simple models. The reflection coefficients of the above two cases are compared. The reflected field from randomly distributed multi-layers is discussed using the above results.

I. INTRODUCTION

THE ANALYSIS of the partial reflection of electromagnetic waves from an inhomogeneous medium, whose refractive index varies with height, has been studied by many investigators.¹⁻³ Also, the problem concerning the WKB approximation and the

partial reflection has been long discussed.⁴ The former studies may be classified into two groups: 1) the study of reflection from an inhomogeneity whose refractive index profile is expressed by an analytic function such as the Epstein layer, and 2) the study of reflection from inhomogeneity whose index profile or its derivative is discontinuous, such as in the bilinear model.

To analyze the reflection from an inhomogeneity whose refractive index profile is expressed by an analytic function and to discuss the problem concerning the WKB approximation and the internal reflection, we evaluate the effect of the inhomogeneity on the reflection by the following procedure:⁵ We transform $y'' + f(z)y = 0$ to the Volterra integral equation and solve it by successive substitutions. The integral in the result is evaluated by the method of steepest descents. By this procedure, we examine the effect of the internal reflection on the partial reflection and evaluate the reflection coefficient if this exists. The reflection coefficient is calculated also by the WKB method using the connection formula around the turning point which lies in the complex plane.

* Received by the PGAP, April 12, 1960; revised manuscript received, August 1, 1960.

† Dept. Elect., Faculty of Engineering, Shizuoka University, Hamamatsu-City, Japan.

¹ T. J. Carrol and R. M. Ring, "Normal Tropospheric Propagation of Short Radio Waves Well Beyond the Horizon," M.I.T. Lincoln Lab., Lexington, Mass., Tech. Rept. no. 38; February 12, 1954.

² A. L. Friend, "Theory and practice of tropospheric sounding by radar," PROC. IRE, vol. 37, pp. 116-138; February, 1949.

³ J. R. Wait, "Reflection of electromagnetic waves obliquely from an inhomogeneous medium," *J. Appl. Phys.*, vol. 23, p. 1403; December, 1952.

⁴ S. A. Schelkunoff, "Remarks concerning wave propagation in stratified media," in "Theory of Electromagnetic Waves," Interscience Publishers, Inc., New York, N. Y., pp. 117-128; 1951.

⁵ A. Erdelyi, "Asymptotic Expansions," Dover Publications, Inc., New York, N. Y., pp. 78-107; 1956.

To evaluate the reflection coefficient from an inhomogeneity whose refractive index profile is discontinuous and to discuss the relation between the reflection coefficient and the degree of discontinuity, we calculate the reflection coefficients from the discontinuous layers with simple models; when the profile itself or its first derivative is discontinuous, the models are composed of linear segments [Fig. 1(a) and 1(b)]; when the profile and the first derivative are continuous but the second derivative is discontinuous, the models are composed of linear segments and parabolic arcs [Fig. 1(c) and 1(d)]. We compare these results with those of the Epstein layers of monotonic transition and symmetric deviation. The reflection coefficients from the corresponding layers coincide with each other when the layer thickness is smaller than a certain value; and if the layer thickness becomes larger than this value, the reflection coefficients decrease in different manner.

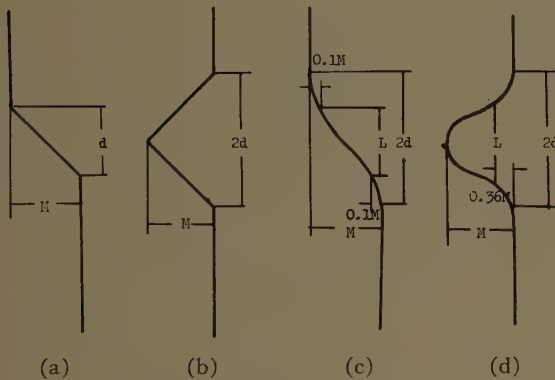


Fig. 1—Permittivity profile.

II. PARTIAL REFLECTION FROM AN INHOMOGENEITY WITH SMOOTH INDEX PROFILE

The problem of the radio wave propagation in a stratified inhomogeneity is solved by appropriate solutions of the equation

$$\frac{d^2 v}{dz^2} + (k^2 N_{\text{eff}}^2(z) - \kappa^2)v = 0, \quad (1)$$

where

- v is the height gain function, or a component of the electric (magnetic) field,
- k is the wave number in vacuo,
- N_{eff} is the effective refractive index,⁶
- κ is the transverse wave number and is equal to $k \cdot N_{\text{eff}}(z) \cos \alpha(z)$ for the ray with angle of incidence $\alpha(z)$.

In this section, we restrict our attention to the case in which $k^2 N_{\text{eff}}^2(z) - \kappa^2$ is an analytic function and is real

and positive large for real z . In this case, the downward total reflection in view of Snell's law is impossible.

We rewrite (1) as

$$\frac{d^2 v}{dz^2} + f(z)v = 0. \quad (2)$$

Following the procedure of the WKB approximation, we introduce the variables t and u defined by

$$t = \int^z f^{1/2}(z) dz, \quad v = u f^{-1/4}. \quad (3)$$

Then (2) becomes

$$\frac{d^2 u}{dt^2} + u = r(t)u, \quad (4)$$

where

$$r(t) = \left(\frac{d^2(f^{1/4})}{dt^2} \right) / f^{1/4} = \frac{1}{4} f^{-2} \left(\frac{d^2 f}{dz^2} \right) - \frac{5}{16} f^{-3} \left(\frac{df}{dz} \right)^2. \quad (5)$$

We solve this equation by the method of variation of parameters, and the solution, which tends to $\exp(it)$ as $t \rightarrow +\infty$, satisfies the Volterra integral equation

$$u(t) = e^{it} + i \frac{1}{2} \int_t^\infty r(s) (e^{i(t-s)} - e^{-i(t-s)}) u(s) ds. \quad (6)$$

The solution of (6) can be obtained by successive substitutions under a certain condition such as $\int_t^\infty |r(s)| ds < 1$. The first approximation of $u(t)$ is

$$u_1(t) = e^{it} + i \frac{1}{2} e^{it} \int_t^\infty r(s) ds - i \frac{1}{2} e^{-it} \int_t^\infty r(s) e^{2is} ds. \quad (7)$$

We can obtain another solution of (2) by the similar method as shown above.

We evaluate the integral in the third term of (7), writing

$$\int r(s) e^{2is} ds = \int e^{\phi(s)} ds, \quad (8)$$

where

$$\phi(t) \equiv 2it + \log r(t), \quad (9)$$

by the method of steepest descents; the integral is along the equiphase lines of e^ϕ from t (corresponding to z) to $+\infty$. The saddle points of this integrand are determined from

$$\frac{d\phi}{dt} = 2i + \left(\frac{dr}{dt} \right) / r(t) = 0. \quad (10)$$

If the saddle point lies on the integral contour, the major contribution to the value of the integral along this contour arises from the vicinity of this point, and

⁶ H. Bremmer, "Encyclopedia of Physics," Springer-Verlag, Berlin, vol. 16, pp. 552-557; 1958.

this contribution can be written in the form

$$-i\frac{1}{2}e^{-it} \int r(s)e^{2is}ds = Ae^{-it}. \quad (11)$$

This result expresses the partial reflection whose reflection coefficient is A .

If the saddle point does not lie on the integral contour and the integrand has its maximum at t , the integral is evaluated as

$$\begin{aligned} & -i\frac{1}{2}e^{-it} \int e^{\phi} ds \\ &= -i\frac{1}{2}e^{-it} \int \exp(\phi(t) + (d\phi/dt)_t(s-t) + \dots) ds \\ &\sim i\frac{1}{2}e^{it}r(t) \left/ \left(\frac{d\phi}{dt} \right)_t \right. \quad k \rightarrow \infty. \end{aligned} \quad (12)$$

This form of integral appears in the problem of diffraction of waves by the screen; formally, this result does not represent the reflection, but gives the correction term to the refracted wave.

If we carry on the above procedure, we can obtain higher-order approximation of the solution.

By this procedure, we evaluate the effects of the internal reflection and add the correction terms to the WKB approximation. We apply the procedure to some special refractive index functions as follows:

A. The case, $f(z) = m + z^2/4$ and $m \gg 1$

If we write $z = h\sqrt{2kb}$, $m = (k^2 - \kappa^2)/2kb$, (2) becomes $d^2v/dh^2 + (k^2(1+b^2h^2) - \kappa^2)v = 0$. This corresponds to the equation for the parabolic profile, and the results are compared with Weber's function $D_{im-1/2}(i^{-1/2}z)$.^{7,8} In this case,

$$\begin{aligned} t &= \int_0^z f^{1/2}(z) dz \\ &= \frac{z}{4} \sqrt{z^2 + 4m} + m \log \frac{z + \sqrt{z^2 + 4m}}{\sqrt{4m}}, \end{aligned} \quad (13)$$

$$r(t) = \frac{8m - 3z^2}{(z^2 + 4m)^3}, \quad (14)$$

and the second term of (7) becomes

$$i\frac{1}{2}e^{it} \int_t^\infty r(s)ds = \frac{i}{48m} \frac{\sqrt{z^2 + 4m}^3 - z^3 - 24mz}{\sqrt{z^2 + 4m}^3} e^{it}. \quad (15)$$

⁷ S. O. Rice, "Diffraction of plane radio waves by a parabolic cylinder. Calculation of shadow behind the hills," *Bell Sys. Tech. J.*, vol. 33, pp. 417-504; March, 1954.

⁸ R. Yamada, "On the radio wave propagation in a stratified atmosphere," *J. Phys. Soc. Japan*, vol. 10, pp. 71-77; January, 1955.

The saddle points of the integrand of the third term of (7) are determined by

$$\frac{d\phi}{dt} = 2i - \frac{24z(z^2 - 6m)}{(z^2 + 4m)^{3/2}(3z^2 - 8m)} = 0. \quad (16)$$

We evaluate the integral in the third term of (7) for the extreme case $m \rightarrow \infty$. In this case, the saddle points lie near the poles of (16),

$$\begin{aligned} z_{01} &= i\sqrt{4m} - i\frac{(18)^{1/3}}{2m^{1/6}} \\ z_{02,3} &= \pm \left(\frac{8m}{3}\right)^{1/2} + i\left(\frac{3}{20m}\right)^{1/2}. \end{aligned} \quad (17)$$

The equiphaser lines for this case are shown in Fig. 2. From this figure, we see that there is no saddle point on the contours from positive z to $\infty i^{1/2}$ and from negative z to $\infty i^{3/2}$, except z lies in the neighborhood of $\pm\sqrt{8m/3}$.

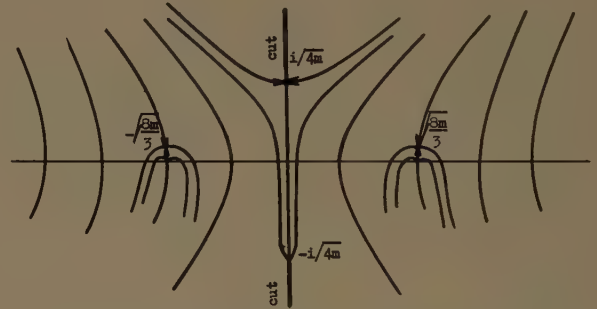


Fig. 2—The equiphaser lines of e^{ϕ} , in the case $f(z) = m + z^2/4$ $m \rightarrow \infty$.

The integral along these paths is evaluated by (12) and becomes

$$\begin{aligned} -i\frac{1}{2}e^{-it} \int_t^\infty r(s)e^{2is}ds &\sim e^{it} \left(\frac{8m - 3z^2}{4(z^2 + 4m)^3} \right. \\ &\quad \left. - i\frac{3z(z^2 - 6m)}{(z^2 + 4m)^{9/2}} + \dots \right) \quad m \rightarrow \infty. \end{aligned} \quad (18)$$

When z lies near $\pm\sqrt{8m/3}$, the saddle point z_{02} or z_{03} lies on the integral contour. But these points lie very near the poles of ϕ , we evaluate this integral by (12), instead of calculating by the usual steepest descents method. The result is the same as given by (18).

When z is negative, the integral contour from $\infty i^{3/2}$ to $\infty i^{1/2}$ passes the saddle point z_{01} . This saddle point lies very near the pole of $r(t)$. We consider the integral in the t -plane. The pole t_0 (corresponding to $i\sqrt{4m}$) is $im\pi/2$ and the saddle point t_{01} (corresponding to z_{01}) approaches $t_0 - i$ as $m \rightarrow \infty$. And the power series expansion of $\phi(t)$ in $(t - t_{01})$ is

$$\phi(t) \rightarrow \phi(t_{01}) - 2 \left(\frac{1}{2} (t - t_{01})^2 + \dots + \frac{(-1)^n}{n} (t - t_{01})^n + \dots \right) \quad m \rightarrow \infty. \quad (19)$$

Therefore, the usual steepest descents method is not applicable. We evaluate this integral by the numerical integration along the steepest path in the t -plane. The result is⁹

$$-i\frac{1}{2}e^{-it} \int r(s)e^{2is}ds = (0.87 + 0(m^{-2/3}))e^{-it-m\pi-i(\pi/2)}. \quad m \rightarrow \infty. \quad (20)$$

Using these results, we can write v_1 as

$$v_1(z) \sim \frac{\sqrt{2}}{\sqrt[4]{z^2 + 4m}} \cdot \left(\exp i \left(\frac{z}{4} \sqrt{z^2 + 4m} + m \log \frac{z + \sqrt{z^2 + 4m}}{\sqrt{4m}} \right) \left(1 + \frac{i}{48m} \frac{\sqrt{z^2 + 4m^3} - z^3 - 24mz}{\sqrt{z^2 + 4m^3}} + \dots \right) \right), \quad (21)$$

if z is positive.

$$\frac{d\phi}{dt} = 2i + \left(\frac{\mu}{k} \right) \frac{4x^4 - (8 + 10d)x^3 - (24 + 24d - d^2)x^2 - 2(1 + d)(4 - d)x + 4(1 + d)^2}{L^{1/2}(4(1 + d) + xd - 4x^2)(1 + x)^{1/2}(1 + d + x)^{3/2}} = 0. \quad (25)$$

$$v_1(z) \sim \frac{\sqrt{2}}{\sqrt[4]{z^2 + 4m}} \cdot \left(\exp i \left(\frac{z}{4} \sqrt{z^2 + 4m} + m \log \frac{z + \sqrt{z^2 + 4m}}{\sqrt{4m}} \right) \cdot \left(1 + \frac{i}{48m} \frac{\sqrt{z^2 + 4m^3} - z^3 - 24mz}{\sqrt{z^2 + 4m^3}} + \dots \right) - i(0.87 + 0(m^{-2/3}))e^{-m\pi} \exp -i \left(\frac{z}{4} \sqrt{z^2 + 4m} + m \log \frac{z + \sqrt{z^2 + 4m}}{\sqrt{4m}} \right) \right), \quad (22)$$

if z is negative, and the second term in the bracket of (22) represents the reflected wave. The reflection coefficient is, therefore, $0.87 \exp -m\pi$, while the reflection

⁹After submission of this paper, I found that (20) can be written as

$$-i\frac{1}{2}e^{-it} \int \frac{-5}{36} \frac{e^{-2it_0-2i(t-t_0)}}{(t-t_0)^2} dt = \frac{-5}{36} e^{-it} \frac{2ie^{-m\pi}}{\Gamma(2)} = -i0.87e^{-it-m\pi}.$$

coefficient calculated by the recurrence formula of Weber's function is $\exp -m\pi$ if m is large. As is seen from Fig. 2, the reflection arises from the point $z=0$. Eq. (21) coincides with the asymptotic expansion of $D_{im-1/2}(i^{-1/2}z)$ when $z^2 + 4m \gg 1$. If we calculate the second approximation of (6), the reflection coefficient becomes $0.93 \exp -m\pi$.

B. The case, $f(z) = k^2(1 + M_0 - Ne^{\mu z}/(1 + e^{\mu z}))$

This corresponds to the monotonic layer calculated by Epstein, and the solution is expressed by the hypergeometric series.²

In this case, writing $e^{\mu z} = x$, $1 + M_0 - N = L$ and $N/L = d$,

$$t = \int_0^z f^{1/2}(z) dz = \frac{k\sqrt{L}}{\mu} \log \left((\sqrt{\frac{1}{2}(1+x)} + \sqrt{\frac{1}{2}(1+d+x)})^2 / (4+d) \right) - \frac{k\sqrt{L+N}}{\mu} \cdot \log \left(\frac{(\sqrt{\frac{1}{2}(1+d)(1+x)} + \sqrt{\frac{1}{2}(1+d+x)})^2}{x(4+d)\sqrt{1+d}} \right), \quad (23)$$

$$r(t) = \left(\frac{\mu}{k} \right)^2 \frac{xd(4x^2 - xd - 4(1+d))}{16L(1+x)(1+d+x)^3}. \quad (24)$$

The saddle points of the integrand of the third term of (7) are determined by

We consider the extreme case $(k/\mu) \rightarrow \infty$, and evaluate the third term of (7) which gives the partial reflection term. In this case, the saddle points lie near the poles of (25). The poles are

$$x_1 = -1, \quad x_2 = -1 - d, \\ x_3 \doteq 1 + \frac{5d}{8} \quad \text{and} \quad x_4 \doteq -1 - \frac{3d}{8}.$$

The equiphase lines for this case are shown in Fig. 3. From this figure we see that there is no saddle point on the integral contour from positive z to $+\infty$ and from negative z to $-\infty$, unless z lies in the neighborhood of x_3 . The contribution of the integral along these paths does not give the reflection term, as in the case of (18). When z is negative, the integral contour passes the saddle point near the pole x_2 of $r(t)$. Here also the saddle point approaches the pole as $(k/\mu) \rightarrow \infty$; we evaluate this integral by the numerical integration along the steepest path in the t -plane as in the case of (20). From this result we obtain the reflection coefficient

$$|R| = 0.87 \exp\left(-2\pi \frac{k\sqrt{1+M_0-N}}{\mu}\right), \quad (26)$$

while the reflection coefficient calculated from the rigorous solution is²

$$|R| = \frac{\sinh\left(\pi \frac{k}{\mu} (\sqrt{1+M_0} - \sqrt{1+M_0-N})\right)}{\sinh\left(\pi \frac{k}{\mu} (\sqrt{1+M_0} + \sqrt{1+M_0-N})\right)} \quad (27)$$

$$= \exp\left(-2\pi \frac{k\sqrt{1+M_0-N}}{\mu}\right) \quad \text{if } \left(\frac{k}{\mu}\right) \text{ is large.} \quad (27')$$

The contribution of the integral in the vicinity of the saddle point near x_3 is evaluated by the method similar to that employed in (18), and this result does not represent the reflection.

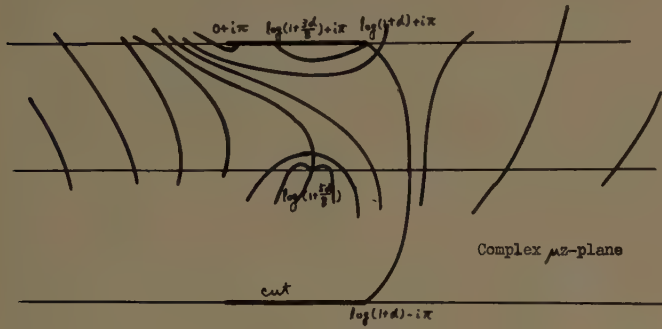


Fig. 3—The equiphasic lines, in the case $f(z) = k^2(1+M_0 - Ne^{\mu z}/(1+e^{\mu z}))$ and $k/\mu \rightarrow \infty$. The lower half is not given, because the end points of these lines vary to the value of k/μ .

C. The cases, $f(z) = z$ (the linear profile), $f(z) = k^2(a + be^{nz})$ (the exponential profile) and $f(z) = k^2(1+M_0 - Me^{\mu z}/(1+e^{\mu z}))$ (the symmetrical layer)

In the case of the linear profile, this method is applicable only when z is positive large, because $r(t)$ becomes infinity at $z=0$. When z is positive, there is no saddle point on the integral contour. The integrals in (7) are evaluated by the methods similar to those employed in (15) and (18), and the result coincides with the asymptotic expansion of the modified Hankel function of order one-third for positive z .¹⁰ In the case of the exponential profile, the result is compared with the Hankel function whose order and argument are $(2/n)k(-a)^{1/2}$ and $(2/n)k(b)^{1/2} \exp(nz/2)$, respectively.³ Finally, in the case of the symmetrical layer, the result is compared with the hypergeometric series.²

¹⁰ D. E. Kerr, "Propagation of Short Radio Waves," M.I.T. Rad. Lab. Series, McGraw-Hill Book Co., Inc., New York, N. Y., p. 87 ff; 1951.

When the condition that $k^2 N_{\text{eff}}^2(z) - \kappa^2$ is positive and large is not fulfilled and $f(z)$ vanishes at real z , $r(t)$ becomes infinite at this point. In this case, the above procedure is not applicable without some modification.¹¹

The reflection coefficient can be calculated also by the WKB method using the connection formula around the turning point. In our case, $k^2 N_{\text{eff}}^2(z) - \kappa^2$ is positive and large for real z ; the turning points at which $f(z)$ vanishes are complex. If we construct the WKB approximation valid in the vicinity of the appropriate turning point, we can obtain the reflection coefficient by the connection formula around this point.¹² In this case, we see that the reflection arises at the point at which the Stokes line intersects the real axis. By this method, the relation between the WKB approximation and the internal reflection is not clear.

Applying this method to the case of the parabolic profile, we obtain the reflection coefficient by the connection formula around the turning point $z = i\sqrt{4m}$,

$$|R| = e^{-m\pi}. \quad (28)$$

In the case of the monotonic layer, we obtain the reflection coefficient by the connection formula around the turning point $z = (\log(1+d) + i\pi)/\mu$,

$$|R| = \exp\left(-2\pi \frac{k\sqrt{1+M_0-N}}{\mu}\right). \quad (29)$$

Considering the above results, we may obtain the better approximation for large wave number if we combine the above two methods; the method using the integral equation and the method using the connection formula.

III. REFLECTION COEFFICIENTS FROM THE DISCONTINUOUS INHOMOGENEITIES

To evaluate the reflection coefficients from various inhomogeneous layers and to discuss the relations between the reflection coefficient and the shape of the index profile and between the reflection coefficient and the degree of discontinuity, we use the simple models whose index profiles are shown in Fig. 1. These profiles are divided into two groups; the one consists of profiles shown in Fig. 1(a) and 1(c) (of the monotonic layer), the other consists of profiles shown in Fig. 1(b) and 1(d) (of the symmetrical layer).

In the cases of Fig. 1(c) and 1(d), we approximate the monotonic layer and the symmetrical layer with two linear segments and parabolic arcs, whose gradients are continuous at their boundaries. In these cases, we cal-

¹¹ D. S. Saxon, "Modified WKB methods for the propagation and scattering of electromagnetic waves," IRE TRANS. ON ANTENNAS AND PROPAGATION, vol. AP-7, Special Supplement, pp. S320-S324; December, 1959.

¹² R. E. Langer, "On the connection formulas and the solutions of the wave equation," Phys. Rev., vol. 51, pp. 669-676; April, 1937.

culate the reflection coefficients using the asymptotic expansions of Weber's functions up to the third term, because the reflection coefficients are of the order of this term.

$$D_{im-1/2}(i^{-1/2}x) \sim \frac{i\Gamma(im - \frac{1}{2})}{\sqrt{2x} \cosh w} \exp\left(\frac{3\pi(m - i\frac{1}{2})}{4} + \frac{ix^2}{4} \left(\cosh w + \frac{1}{2} \sinh^2 w - \left(\sinh^2 w - \frac{2i}{x^2}\right) \log(x \sinh^2 \frac{1}{2}w)\right)\right) \\ \cdot \left(1 + \frac{i}{24x^2} \frac{8\cosh^2 w + 11\cosh w + 5}{\cosh^3 w \cdot \sinh \frac{1}{2}w} - \frac{1}{288x^4} \frac{64 \cosh^4 w - 536 \cosh^3 w + 1281 \cosh^2 w - 1190 \cosh w + 385}{(\cosh w - 1)^2 \cosh^2 w} + \dots\right), \quad (30)$$

where

$$(x^2/4) \cdot \sinh^2 w = m + i\frac{1}{2},$$

and the corresponding expansion of $D_{-im-1/2}(i^{1/2}x)$.

The results are:

$$|R| = \frac{M}{8kd \sin^3 \alpha} \left| 1 - \frac{\sin^3 \alpha}{(\sin^2 \alpha + M)^{3/2}} \cdot \exp i \frac{4kd}{3M} ((\sin^2 \alpha + M)^{3/2} - \sin^3 \alpha) \right|, \quad \text{for Fig. 1(a),} \quad (31)$$

$$= \frac{M}{4 \sin^2 \alpha} \frac{\sin(kd \sin \alpha)}{kd \sin \alpha}, \quad \text{if } M \ll \sin^2 \alpha. \quad (31')$$

$$R = \frac{M}{4kd} \left[\frac{1}{\sin^3 \alpha} - \frac{1}{(\sin^2 \alpha + M)^{3/2}} \cdot \cos \frac{4kd}{3M} ((\sin^2 \alpha + M)^{3/2} - \sin^3 \alpha) \right], \quad \text{for Fig. 1(b),} \quad (32)$$

$$= \frac{M}{2 \sin^2 \alpha} \frac{\sin^2(kd \sin \alpha)}{kd \sin \alpha}, \quad \text{if } M \ll \sin^2 \alpha. \quad (32')$$

$$R = \frac{M}{4 \sin^2 \alpha} \left(1 + \frac{1}{8} \left(\frac{kdM}{2 \sin \alpha} \right)^4 \right), \quad \text{if } M \cdot kd / \sin \alpha < 1, \quad \text{for Fig. 1(c),} \quad (33)$$

$$= \frac{M}{4 \sin^2 \alpha} \frac{\sin^2(kd \sin \alpha)}{k^2 d^2 \sin^2 \alpha}, \quad \text{if } M \ll \sin^2 \alpha. \quad (33')$$

$$|R| = \frac{kd \cdot M}{2 \sin \alpha} \left(1 - \frac{2}{3} \left(\frac{kd \sin \alpha}{2} \right)^2 \right) \quad \text{if } kd \sin \alpha \ll 1, \quad \text{for Fig. 1(d),} \quad (34)$$

$$= \frac{2M}{\sin^2 \alpha} \frac{\sin^2(\frac{1}{2}kd \sin \alpha) \cdot \sin(kd \sin \alpha)}{k^2 d^2 \sin^2 \alpha}, \quad \text{if } M \ll \sin^2 \alpha. \quad (34')$$

For the cases of Fig. 1(a) and 1(c), the reflection coefficients are shown in Fig. 4 with the coefficient of the monotonic layer for oblique incidence ($\sin^2 \alpha = 5 \times 10^{-4}$). The layer thickness L is defined by Friend,² and the relation between L and d is estimated as $L = 1.15d$. The reflection coefficients for the cases of Fig. 1(b) and 1(d) are shown in Fig. 5 with that of the symmetrical layer.

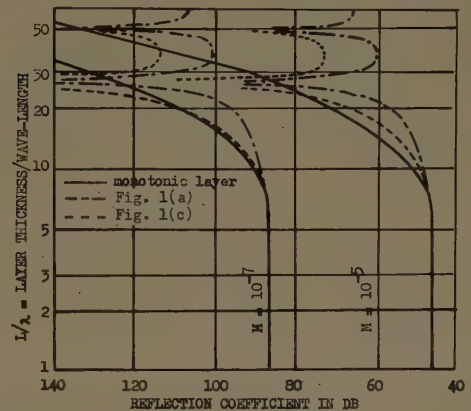


Fig. 4—Reflection coefficients from inhomogeneous media ($\sin^2 \alpha = 5 \times 10^{-4}$), where L is the layer thickness defined by Friend.²

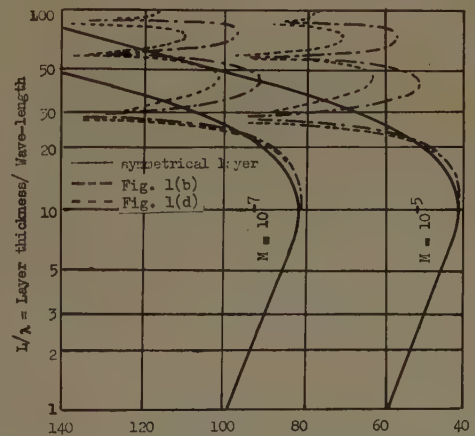


Fig. 5—Reflection coefficients from inhomogeneous media ($\sin^2 \alpha = 5 \times 10^{-4}$), where L is the layer thickness defined by Friend.²

From these figures we see that when $kd \sin \alpha < \pi/2$, the reflection coefficients from the corresponding layers coincide with each other. When $kd \sin \alpha = \pi/2$, the reflection coefficients of the symmetrical layers have their maxima about $(M/3) \sin^2 \alpha$. When $kd \sin \alpha > \pi/2$, the reflection coefficients decrease proportionally to $1/k$ in the case of discontinuity of the gradient, proportionally to $1/k^2$ in the case of discontinuity of the second derivative, and exponentially in the case of an analytic function. In the cases of discontinuities, the coefficients oscillate.

From the above results, we may deduce that when the layer thickness is smaller than a certain value, the reflection coefficient from an inhomogeneity with smooth profile is almost equal to that from an approximate discontinuous layer and the coefficient may be estimated by that from the approximate model. When the layer thickness becomes much larger than this value, the reflection coefficient may be calculated by the WKB method.

IV. CONCLUSION

In Section II, we deal with the problem concerning the WKB approximation, the internal reflection and the partial reflection, and explain the relation between the internal reflection and the partial reflection using the integral equation (6). According to the result, there is

no partial reflection, if there is no saddle point on the equiphase lines of the integrand of the third term of (7) from z to $+\infty$. This is the case of the propagation of radio waves over the earth when the atmosphere is standard.

If we apply the method of Section II to the case, $f(z) = k^2(\sqrt{1+M_0} - Ne^{\mu z}/2(1+e^{\mu z})\sqrt{1+M_0})^2$ which is an approximate formula of the case (b) in Section II when $N/(1+M_0) \ll 1$ and z is real, we obtain the reflection coefficient $|R| = \exp(-2\pi k(1+M_0 - \frac{1}{2}N)/\mu\sqrt{1+M_0})$. From this result and that of Section III, we see that the reflection coefficients depend on the numerical values of index profiles for real z ; the reflection coefficient from a layer with smooth profile almost coincides with that from an approximate layer with simpler and discontinuous profile when the layer thickness is small, and almost equal to that from an approximate layer with smooth profile when the layer thickness becomes large.

Further, we may explain the propagation of short radio waves well beyond the horizon in terms of uncorrelated reflections from the layers mentioned in Section III, instead of the reflections from the discontinuous layers in Friis, Crawford and Hogg's theory.¹³

¹³ H. T. Friis, A. B. Crawford, and D. C. Hogg, "A reflection theory for propagation beyond the horizon," *Bell Sys. Tech. J.*, vol. 36, pp. 627-644; May, 1957.

On Propagating Discontinuities in an Electromagnetic Field*

KENT R. JOHNSON†, MEMBER, IRE

Summary—The propagation of discontinuities of an electromagnetic field is considered for the case of a conducting medium. Conditions relating the values of the discontinuities in the electric and magnetic fields are obtained, and equations governing the transport of the discontinuities through space are derived. Such discontinuity conditions and transport equations are obtained both for the fields and for the n th order partial time derivatives of the fields. Previous derivations have treated the case of a nonconducting medium and have used distribution theory. The present treatment does not use distribution theory.

* Received by the PGAP, June 2, 1960; revised manuscript received, January 17, 1961. The work in this paper was done at Lincoln Laboratory, Mass. Inst. Tech., Lexington, Mass., operated by M.I.T. with support of the U. S. Advanced Research Projects Agency.

† 2114 Sunset Place, Nashville, Tenn.

INTRODUCTION

IN 1951 Kline,¹ using distribution theory, derived a set of conditions relating the values of discontinuities in electric and magnetic fields across a wavefront propagating in a nonconducting medium. He derived "discontinuity conditions" for the fields themselves and for their n th-order partial time derivatives. These conditions were then used to derive equations governing the transport of the discontinuities through

¹ M. Kline, "An asymptotic solution of Maxwell's equations," *Commun. on Pure and Appl. Math.*, vol. 4, pp. 225-262; August, 1951.

space. In a later paper,² Kline used similar methods to treat the corresponding problem for the general linear hyperbolic partial differential equation. Friedlander,³ in a recent book, used distribution theory to derive the zero-order transport equation (*i.e.*, the equation pertaining to the dependent variable itself, rather than to its time derivatives) for the problem of the propagation of sound pulses. Friedlander obtained the higher-order transport equations without distribution theory. Copson⁴ has also used distribution theory to obtain the zero-order transport equations (there are two of them) for the electromagnetic field in a nonconducting medium.

In the present article the discontinuity conditions and transport equations for the electromagnetic field will be derived for the case of a conducting medium. The derivations, which do not make use of distribution theory, illustrate an alternate approach to several problems that have been treated recently by distribution theory.

MAXWELL'S EQUATIONS FOR THE INTEGRATED FIELDS

If S is a fixed surface, with unit normal \bar{n} , and C is its boundary, two of the Maxwell equations are

$$\int_C \bar{E} \cdot d\bar{l} = - \frac{d}{dt} \int_S \bar{B} \cdot \bar{n} ds \quad (1)$$

$$\int_C \bar{H} \cdot d\bar{l} = \int_S \bar{J} \cdot \bar{n} ds + \frac{d}{dt} \int_S \bar{D} \cdot \bar{n} ds. \quad (2)$$

In these equations the integrands, and also the surface integrals of \bar{B} and \bar{D} , may possess finite discontinuities. Integrate both of the above equations with respect to time between the limits t_0 and t , and in the terms

$$\int_{t_0}^t \frac{d}{dt} \int_S \bar{B} \cdot \bar{n} ds dt$$

and

$$\int_{t_0}^t \frac{d}{dt} \int_S \bar{D} \cdot \bar{n} ds dt$$

evaluate the integrals of the derivatives of the possibly discontinuous functions by regarding these functions as actually continuous but rapidly varying. Then the integrals become

$$\int_{t_0}^t d \int_S \bar{B} \cdot \bar{n} ds = \int_S \Delta \bar{B} \cdot \bar{n} ds$$

² M. Kline, "Asymptotic solution of linear hyperbolic partial differential equations," *J. Rat. Mech. and Anal.*, vol. 3, no. 3, pp. 315-342; 1954.

³ F. G. Friedlander, "Sound Pulses," Cambridge University Press, Cambridge, Eng.; 1958.

⁴ E. T. Copson, "The transport of discontinuities in an electromagnetic field," *Commun. on Pure and Appl. Math.*, vol. 4, pp. 427-433; November, 1951.

and

$$\int_{t_0}^t d \int_S \bar{D} \cdot \bar{n} ds = \int_S \Delta \bar{D} \cdot \bar{n} ds,$$

respectively, where $\Delta \bar{B} = \bar{B}(\bar{r}, t) - \bar{B}(\bar{r}, t_0)$, and $\Delta \bar{D} = \bar{D}(\bar{r}, t) - \bar{D}(\bar{r}, t_0)$. Thus there results

$$\int_{t_0}^t \int_C \bar{E} \cdot d\bar{l} dt = - \int_S \Delta \bar{B} \cdot \bar{n} ds$$

and

$$\int_{t_0}^t \int_C \bar{H} \cdot d\bar{l} dt = \int_{t_0}^t \int_S \bar{J} \cdot \bar{n} ds dt + \int_S \Delta \bar{D} \cdot \bar{n} ds.$$

Interchanging the order of integration in the double integrals above yields

$$\int_C \bar{E}_i \cdot d\bar{l} = - \int_S \Delta \bar{B} \cdot \bar{n} ds$$

and

$$\int_C \bar{H}_i \cdot d\bar{l} = \int_S \bar{J}_i \cdot \bar{n} ds + \int_S \Delta \bar{D} \cdot \bar{n} ds, \quad (3)$$

where $\bar{E}_i = \int_{t_0}^t \bar{E} dt$, and similarly for \bar{H}_i and \bar{J}_i .

It will now be assumed that the surface S , and the times t_0 and t , are so chosen that at t_0 the surface bearing the discontinuities has not yet reached any point of S , and that at t the discontinuity surface has passed S completely. Then \bar{E}_i and \bar{H}_i are continuous on S , and have continuous partial derivatives of first order with respect to space and time. Consequently, Stokes' theorem may be used to deduce that

$$\nabla \times \bar{E}_i = - \Delta \bar{B}$$

and

$$\nabla \times \bar{H}_i = \bar{J}_i + \Delta \bar{D} \quad (4)$$

at all points not on the surface carrying the discontinuities.⁵

Now evaluate the left sides of these equations, keeping in mind that \bar{E}_i and \bar{H}_i are the integrals of discontinuous functions. A typical term is

$$\frac{\partial E_{iz}}{\partial y} = \frac{\partial}{\partial y} \int_{t_0}^t E_z(\bar{r}, t') dt'.$$

Let the surface carrying the discontinuities be $t = \tau(\bar{r})$. Assume for simplicity that there is only one such sur-

⁵ A formulation of Maxwell's equations involving time integrals of the fields has been used previously by Luneberg. See R. K. Luneberg, "Mathematical Theory of Optics," Brown University Press, Providence, R. I., ch. 1; 1944.

face, which in the interval (t_0, t) exactly once passes the point at which the derivative is to be evaluated. The above may then be written

$$\frac{\partial E_{iz}}{\partial y} = \frac{\partial}{\partial y} \left[\int_{t_0}^{\tau(\bar{r})} E_z(\bar{r}, t') dt' + \int_{\tau(\bar{r})}^t E_z(\bar{r}, t') dt' \right].$$

Carrying out the differentiation gives

$$\frac{\partial E_{iz}}{\partial y} = - [E_z(\bar{r}, \tau + 0) - E_z(\bar{r}, \tau - 0)] \frac{\partial \tau}{\partial y} + \int_{t_0}^t \frac{\partial E_z(\bar{r}, t')}{\partial y} dt'.$$

In the integral immediately above, $\partial E_z(\bar{r}, t')/\partial y$ is simply a discontinuous function having a finite discontinuity at $t' = \tau(\bar{r})$. The preceding derivative may be written

$$\frac{\partial E_{iz}}{\partial y} = - [E_z]_s \frac{\partial \tau}{\partial y} + \int_{t_0}^t \frac{\partial E_z}{\partial y} dt', \quad (5)$$

where in (5), and in all subsequent equations, the brackets with the subscript s , for saltus, indicate the discontinuity of the bracketed quantity at the surface $t = \tau(\bar{r})$. Calculating the other necessary terms in the manner just described, there results

$$\nabla \times \bar{E}_i = - \nabla \tau \times [\bar{E}]_s + \int_{t_0}^t \nabla \times \bar{E} dt',$$

where $\nabla \times \bar{E}$ is regarded as having a finite discontinuity at $t' = \tau(\bar{r})$.

Using the above expression for $\nabla \times \bar{E}_i$, and the corresponding one for $\nabla \times \bar{H}_i$, equations (4) become

$$\begin{aligned} - \nabla \tau \times [\bar{E}]_s + \int_{t_0}^t \nabla \times \bar{E} dt' &= - \Delta \bar{B} \\ - \nabla \tau \times [\bar{H}]_s + \int_{t_0}^t \nabla \times \bar{H} dt' &= \bar{J}_i + \Delta \bar{D}. \end{aligned} \quad (6)$$

Either (4) or (6) may be taken as the desired reformulation of Maxwell's equations.

THE DISCONTINUITY CONDITIONS

At a point \bar{r} the discontinuity surface passes at time $t = \tau(\bar{r})$. Let $t_0 = \tau - \delta$ and $t = \tau + \delta$, and apply (6). As δ is allowed to become small, the integrals from t_0 to t vanish, \bar{J}_i vanishes, and $\Delta \bar{B}$ and $\Delta \bar{D}$ become $[\mu \bar{H}]_s$ and $[\epsilon \bar{E}]_s$, respectively. There results

$$\begin{aligned} \nabla \tau \times [\bar{E}]_s - [\mu \bar{H}]_s &= 0 \\ \nabla \tau \times [\bar{H}]_s + [\epsilon \bar{E}]_s &= 0. \end{aligned} \quad (7)$$

These are the desired zero-order discontinuity conditions. Notice that (7) implies that $[\mu \bar{H}]_s$ and $[\epsilon \bar{E}]_s$ are tangent to $t = \tau(\bar{r})$.

To obtain the higher-order discontinuity conditions let $t = \tau(\bar{r})$ be the surface on which the discontinuities lie. Then $t = \tau(\bar{r}) \pm \delta$ are surfaces which coincide with the location of the discontinuity surface at the times $t \mp \delta$. At the time t , however, the fields are continuous on these two surfaces, and the usual Maxwell equations are valid on them. If $\rho(\bar{r}) = \tau(\bar{r}) + \delta$, and brackets without the subscript s are used to indicate that the enclosed quantity is evaluated on the surface $t = \rho(\bar{r})$, the following differentiation formula obtains:

$$\frac{\partial [E_z]}{\partial y} = \left[\frac{\partial E_z}{\partial y} \right] + \left[\frac{\partial E_z}{\partial t} \right] \frac{\partial \rho}{\partial y},$$

where $[E_z] = E_z(\bar{r}, \rho(\bar{r}))$. Corresponding formulas apply for differentiation with respect to x and z .

Using the preceding formula and the corresponding formulas for the other necessary derivatives, the following expression is obtained:

$$\nabla \times [\bar{E}] = [\nabla \times \bar{E}] + \nabla \rho \times \left[\frac{\partial \bar{E}}{\partial t} \right]. \quad (8)$$

On the surface $t = \rho(\bar{r})$ Maxwell's equations may be applied in their usual form, and the above equation may be written

$$\nabla \times [\bar{E}] = - [\mu \bar{H}_t] + \nabla \rho \times [\bar{E}_t],$$

where the subscript t indicates the partial derivative with respect to time. If the corresponding relation is written on the other surface, $t = \tau(\bar{r}) - \delta$, and the second equation subtracted from the first, there results, as δ goes to zero,

$$\nabla \tau \times [\bar{E}_t]_s - [\mu \bar{H}_t] = \nabla \times [\bar{E}]_s. \quad (9)$$

Similarly, by starting with the formula for $\nabla \times [\bar{H}]$ that corresponds to (8), it is possible to obtain

$$\nabla \tau \times [\bar{H}_t]_s + [\epsilon \bar{E}_t]_s = \nabla \times [\bar{H}]_s - [\sigma \bar{E}]_s, \quad (10)$$

in which the current density \bar{J} has been evaluated as $\sigma \bar{E}$. To find the higher-order discontinuity conditions, it is only necessary to recognize that on the surfaces $t = \tau(\bar{r}) \pm \delta$, it is possible to differentiate Maxwell's equations with respect to time $n-1$ times. Then using

$$\nabla \times [\bar{E}_{n-1}] = [\nabla \times \bar{E}_{n-1}] + \nabla \rho \times [\bar{E}_n],$$

where the subscript n indicates the n th partial time derivative, the same procedure that was used above yields the n th-order discontinuity conditions,

$$\begin{aligned} \nabla \tau \times [\bar{E}_n]_s - [\mu \bar{H}_n]_s &= \nabla \times [\bar{E}_{n-1}]_s \\ \nabla \tau \times [\bar{H}_n]_s + [\epsilon \bar{E}_n]_s &= \nabla \times [\bar{H}_{n-1}]_s - [\sigma \bar{E}_{n-1}]_s, \end{aligned} \quad n \geq 0. \quad (11)$$

In (11), in order that the equation may apply for $n=0$, it is understood that $[\bar{E}_{-1}]_s = [\bar{H}_{-1}]_s = 0$.

THE TRANSPORT EQUATIONS

There will now be derived a set of equations governing the transport through space of the discontinuities of the \bar{E} and \bar{H} fields, and, in general, of the discontinuities in the n th partial derivatives of these fields with respect to time. These comprise an infinite set of first-order ordinary differential equations, each equation giving the derivative of $[\bar{E}_n]_s$ or $[\bar{H}_n]_s$ in the direction normal to the two dimensional wavefront in x, y, z space on which the discontinuities lie. These derivatives are given in terms of the discontinuities in lower-order time derivatives, so that in principle it is possible to solve the system of equations recursively to determine how all the discontinuities propagate. In Kline's¹ paper the transport equations are derived from the discontinuity conditions by vector manipulation. The present derivation differs from Kline's; however, the basis for the type of derivation that Kline used will be mentioned briefly in the Discussion at the end of this paper.

THE ZERO-ORDER TRANSPORT EQUATION FOR THE ELECTRIC FIELD

The integrated form of Maxwell's equations (4) may be manipulated to give a wave equation in \bar{E}_i :

$$\begin{aligned}\nabla \times \nabla \times \bar{E}_i &= -\mu \nabla \times \Delta \bar{H} = -\mu \Delta (\nabla \times \bar{H}) \\ &= -\mu \Delta (\sigma \bar{E} + \epsilon \bar{E}_t) = -\mu \sigma \Delta \bar{E} \\ &\quad - \mu \epsilon \Delta \bar{E}_t.\end{aligned}\quad (12)$$

In obtaining the second line above, the use of the usual Maxwell equations at the points (r, t_0) and (r, t) is permissible, because these points do not lie on the surface containing the discontinuities in the field. Consider the left side of (12). Assume that the discontinuity surface passes the point of observation just once in the time interval (t_0, t) . Then it has already been shown that

$$\nabla \times \bar{E}_i = \int_{t_0}^t \nabla \times \bar{E} dt - \nabla \tau \times [\bar{E}]_s. \quad (13)$$

Take the curl of each side of (13), using (13) to evaluate the resulting term involving the curl of the integral. This yields

$$\begin{aligned}\nabla \times \nabla \times \bar{E}_i &= \nabla \times \int_{t_0}^t \nabla \times \bar{E} dt - \nabla \times (\nabla \tau \times [\bar{E}]_s) \\ &= \int_{t_0}^t \nabla \times \nabla \times \bar{E} dt - \nabla \tau \times [\nabla \times \bar{E}]_s \\ &\quad - \nabla \times (\nabla \tau \times [\bar{E}]_s).\end{aligned}\quad (14)$$

However, from (8),

$$\nabla \times [\bar{E}] = [\nabla \times \bar{E}] + \nabla \rho \times [\bar{E}]_s.$$

If this equation is written also for the surface $t = \tau(\bar{r}) - \delta$, and the second equation subtracted from the first, the following result is obtained as δ goes to zero:

$$\nabla \times [\bar{E}]_s = [\nabla \times \bar{E}]_s + \nabla \tau \times [\bar{E}]_s. \quad (15)$$

Then, taking the vector product of this equation with $\nabla \tau$,

$$\begin{aligned}\nabla \tau \times [\nabla \times \bar{E}]_s &= \nabla \tau \times (\nabla \times [\bar{E}]_s) - \nabla \tau \times (\nabla \tau \times [\bar{E}]_s) \\ &= \nabla \tau \times (\nabla \times [\bar{E}]_s) - \nabla \tau (\nabla \tau \cdot [\bar{E}]_s) \\ &\quad + |\nabla \tau|^2 [\bar{E}]_s.\end{aligned}$$

Substituting this last result into (14), and expanding the last term of (14), there results

$$\begin{aligned}\nabla \times \nabla \times \bar{E}_i &= \int_{t_0}^t \nabla \times \nabla \times \bar{E} dt - \nabla \tau \times (\nabla \times [\bar{E}]_s) \\ &\quad + \nabla \tau (\nabla \tau \cdot [\bar{E}]_s) - |\nabla \tau|^2 [\bar{E}]_s \\ &\quad - \nabla \tau (\nabla \cdot [\bar{E}]_s) + [\bar{E}]_s \nabla^2 \tau \\ &\quad - ([\bar{E}]_s \cdot \nabla) \nabla \tau + (\nabla \tau \cdot \nabla) [\bar{E}]_s.\end{aligned}\quad (16)$$

However, on the surface $t = \rho(\bar{r}) = \tau(\bar{r}) + \delta$,

$$\nabla \cdot [\bar{E}] = [\nabla \cdot \bar{E}] + [\bar{E}]_s \cdot \nabla \rho. \quad (17)$$

From (17) there follows immediately, in the same way that (15) followed from the equation preceding it,

$$\nabla \cdot [\bar{E}]_s = [\nabla \cdot \bar{E}]_s + [\bar{E}]_s \cdot \nabla \tau. \quad (18)$$

Observe that by the zero-order discontinuity conditions

$$\nabla \tau \cdot [\bar{E}]_s = 0,$$

so

$$\begin{aligned}\nabla (\nabla \tau \cdot [\bar{E}]_s) &= ([\bar{E}]_s \cdot \nabla) \nabla \tau + \nabla \tau \times (\nabla \times [\bar{E}]_s) \\ &\quad + (\nabla \tau \cdot \nabla) [\bar{E}]_s = 0.\end{aligned}\quad (19)$$

If (18) and (19) are substituted into (16), there results

$$\begin{aligned}\nabla \times \nabla \times \bar{E}_i &= \int_{t_0}^t \nabla \times \nabla \times \bar{E} dt + 2(\nabla \tau \cdot \nabla) [\bar{E}]_s \\ &\quad - |\nabla \tau|^2 [\bar{E}]_s - \nabla \tau [\nabla \cdot \bar{E}]_s + \nabla^2 \tau [\bar{E}]_s.\end{aligned}\quad (20)$$

Now substitute (20) into (12) to obtain

$$\begin{aligned}\int_{t_0}^t \nabla \times \nabla \times \bar{E} dt + 2(\nabla \tau \cdot \nabla) [\bar{E}]_s - \nabla \tau [\nabla \cdot \bar{E}]_s + \nabla^2 \tau [\bar{E}]_s \\ + \mu \sigma \Delta \bar{E} + \mu \epsilon \Delta \bar{E}_t - |\nabla \tau|^2 [\bar{E}]_s = 0.\end{aligned}\quad (21)$$

In order to get a transport equation from (21), it is necessary to evaluate $[\nabla \cdot \bar{E}]_s$ in terms of quantities not involving derivatives of \bar{E} . This can be done as follows. Take the divergence of the second of equations (4), giving

$$\nabla \cdot \int_{t_0}^t \sigma \bar{E} dt + \Delta \nabla \cdot \bar{D} = 0,$$

writing $\bar{J} = \sigma \bar{E}$. Using (5) to evaluate the derivatives of the integral, this becomes

$$\int_{t_0}^t \nabla \cdot (\sigma \bar{E}) dt - \sigma [\bar{E}]_s \cdot \nabla \tau + \Delta \nabla \cdot \bar{D} = 0,$$

where, as mentioned in connection with (5), the inte-

grand above is considered everywhere finite. Letting the interval (t_0, t) go to zero in such a way that the discontinuity surface always passes the point of observation during the interval, the integral vanishes, and $\Delta(\nabla \cdot \bar{D})$ becomes $[\nabla \cdot \bar{D}]_s$, yielding

$$-\sigma[\bar{E}]_s \cdot \nabla \tau + [\nabla \cdot \bar{D}]_s = 0.$$

But by the discontinuity conditions (7), the first term above is zero, so $[\nabla \cdot \bar{D}]_s = 0$, or, setting $\bar{D} = \epsilon \bar{E}$,

$$[\nabla \cdot \bar{E}]_s = -\nabla \ln \epsilon \cdot [\bar{E}]_s, \quad (22)$$

which is the desired evaluation of $[\nabla \cdot \bar{E}]_s$. At this point note that

$$|\nabla \tau|^2 = \mu \epsilon. \quad (23)$$

This follows at once from the zero-order discontinuity conditions, which are incompatible unless (23) is met. Eq. (23) is simply the eikonal equation of geometrical optics, so that it is seen that the discontinuity conditions imply that discontinuity surfaces propagate like the wavefronts of geometrical optics. Now substitute (22) and (23) into (21), and let the interval (t_0, t) go to zero in the manner specified just above. Then the integral in (21) vanishes, and, observing that $\Delta \bar{E}$ becomes $[\bar{E}]_s$, and $\Delta \bar{E}_t$ becomes $[\bar{E}_t]_s$, there is obtained the transport equation for discontinuities in the electric field

$$2(\nabla \tau \cdot \nabla)[\bar{E}]_s + \nabla^2 \tau [\bar{E}]_s + \nabla \tau (\nabla \ln \epsilon \cdot [\bar{E}]_s) + \mu \sigma [\bar{E}]_s = 0. \quad (24)$$

The first term on the left is proportional to a directional derivative of $[\bar{E}]_s$ in the direction of the normal to the geometrical optics wavefront $t = \tau(\bar{r})$. Introduce a parameter ν along the normal trajectories to the wavefronts by setting $d/\nu = \nabla \tau \cdot \nabla$. The transport equation becomes.

$$2 \frac{d[\bar{E}]_s}{d\nu} + \nabla^2 \tau [\bar{E}]_s + \nabla \tau (\nabla \ln \epsilon \cdot [\bar{E}]_s) + \mu \sigma [\bar{E}]_s = 0. \quad (25)$$

If the normal trajectories to the surfaces $t = \tau(\bar{r})$ are found by the geometrical optics technique of ray tracing, (25) may be integrated along these trajectories, or rays, to find how the discontinuity $[\bar{E}]_s$ propagates.

The present analysis has considered the permeability of the medium to be constant, but has permitted non-zero conductivity. Kline considered the permeability to vary with position, but took the conductivity to be zero.

HIGHER-ORDER TRANSPORT EQUATIONS FOR THE ELECTRIC FIELD

As in the derivation of the higher-order discontinuity conditions, start with the differentiation formula

$$\nabla \times [\bar{E}] = [\nabla \times \bar{E}] + \nabla \rho \times [\bar{E}_t]. \quad (8)$$

Observe that the following derivation of the first-order, and higher-order, transport equations closely parallels that of the zero-order equation, except that the starting point is now (8), rather than the very similar formula

(13). Take the curl of both sides of (8):

$$\begin{aligned} \nabla \times \nabla \times [\bar{E}] &= [\nabla \times \nabla \times \bar{E}] + \nabla \rho^x \left[\frac{\partial}{\partial t} \nabla \times \bar{E} \right] \\ &\quad + \nabla \times (\nabla \rho \times [\bar{E}_t]) \\ &= [\nabla \times \nabla \times \bar{E}] + \nabla \rho \times [\nabla \times \bar{E}_t] \\ &\quad + \nabla \rho (\nabla \cdot [\bar{E}_t]) - \nabla^2 \rho [\bar{E}_t] \\ &\quad + ([\bar{E}_t] \cdot \nabla) \nabla \rho - (\nabla \rho \cdot \nabla) [\bar{E}_t]. \end{aligned} \quad (26)$$

However,

$$\begin{aligned} \nabla \rho \times [\nabla \times \bar{E}_t] &= \nabla \rho \times (\nabla \times [\bar{E}_t]) - \nabla \rho \times (\nabla \rho \times [\bar{E}_{tt}]) \\ &= \nabla \rho \times (\nabla \times [\bar{E}_t]) - \nabla \rho (\nabla \rho \cdot [\bar{E}_{tt}]) \\ &\quad + |\nabla \rho|^2 [\bar{E}_{tt}], \end{aligned} \quad (27)$$

and

$$\nabla \cdot [\bar{E}_t] = [\nabla \cdot \bar{E}_t] + [\bar{E}_{tt}] \cdot \nabla \rho. \quad (28)$$

Substituting (27) and (28) into (26) gives

$$\begin{aligned} \nabla \times \nabla \times [\bar{E}] &= [\nabla \times \nabla \times \bar{E}] + \nabla \rho \times (\nabla \times [\bar{E}_t]) \\ &\quad + |\nabla \rho|^2 [\bar{E}_{tt}] + \nabla \rho [\nabla \cdot \bar{E}_t] - \nabla^2 \rho [\bar{E}_t] \\ &\quad + ([\bar{E}_t] \cdot \nabla) \nabla \rho - (\nabla \rho \cdot \nabla) [\bar{E}_t]. \end{aligned} \quad (29)$$

But, taking the gradient of the scalar product,

$$\nabla (\nabla \rho \cdot [\bar{E}_t]) = (\nabla \rho \cdot \nabla) [\bar{E}_t] + ([\bar{E}_t] \cdot \nabla) \nabla \rho + \nabla \rho \times (\nabla \times [\bar{E}_t]).$$

Substitution of this expression into (29) yields

$$\begin{aligned} \nabla \times \nabla \times [\bar{E}] &= [\nabla \times \nabla \times \bar{E}] + \nabla (\nabla \rho \cdot [\bar{E}_t]) \\ &\quad + |\nabla \rho|^2 [\bar{E}_{tt}] + \nabla \rho [\nabla \cdot \bar{E}_t] - \nabla^2 \rho [\bar{E}_t] \\ &\quad - 2(\nabla \rho \cdot \nabla) [\bar{E}_t]. \end{aligned} \quad (30)$$

The left side of this equation can be written

$$\nabla \times \nabla \times [\bar{E}] = \nabla (\nabla \cdot [\bar{E}]) - \nabla^2 [\bar{E}],$$

but, again using (17),

$$\nabla \times \nabla \times [\bar{E}] = \nabla [\nabla \cdot \bar{E}] + \nabla (\nabla \rho \cdot [\bar{E}_t]) - \nabla^2 [\bar{E}].$$

Substitute this result on the left side of (30) to obtain

$$\begin{aligned} \nabla [\nabla \cdot \bar{E}] - \nabla^2 [\bar{E}] &= [\nabla \times \nabla \times \bar{E}] + |\nabla \rho|^2 [\bar{E}_{tt}] \\ &\quad + \nabla \rho [\nabla \cdot \bar{E}_t] - \nabla^2 \rho [\bar{E}_t] \\ &\quad - 2(\nabla \rho \cdot \nabla) [\bar{E}_t]. \end{aligned} \quad (31)$$

By Maxwell's equations,

$$\begin{aligned} [\nabla \times \nabla \times \bar{E}] &= [\nabla \times (-\mu \bar{H}_t)] \\ &= -\mu \left[\frac{\partial}{\partial t} (\sigma \bar{E} + \epsilon \bar{E}_t) \right] \\ &= -\mu \sigma [\bar{E}_t] - \mu \epsilon [\bar{E}_{tt}]. \end{aligned}$$

Using this result, and using $|\nabla \rho|^2 = \mu \epsilon$, which is valid because the fact that $\tau(\bar{r})$ satisfies the eikonal equation implies that $\tau(\bar{r}) + \delta$ satisfies it also, (31) becomes

$$\begin{aligned} \nabla [\nabla \cdot \bar{E}] - \nabla^2 [\bar{E}] &= -\mu \sigma [\bar{E}_t] + \nabla \rho [\nabla \cdot \bar{E}_t] - \nabla^2 \rho [\bar{E}_t] \\ &\quad - 2(\nabla \rho \cdot \nabla) [\bar{E}_t]. \end{aligned}$$

If this equation is written also on the surface $t = \tau(\bar{r}) - \delta$, and the second equation subtracted from the first, there is obtained, as δ goes to zero,

$$2(\nabla\tau \cdot \nabla)[\bar{E}_t]_s + \nabla^2\tau[\bar{E}_t]_s - \nabla\tau[\nabla \cdot \bar{E}_t]_s + \mu\sigma[\bar{E}_t]_s = \nabla^2[\bar{E}]_s - \nabla[\nabla \cdot \bar{E}]_s. \quad (32)$$

Just as in the derivation of the zero-order transport equation it was necessary to replace $[\nabla \cdot \bar{E}]_s$ by an expression involving no derivatives of \bar{E} , it is necessary in (32) to replace $[\nabla \cdot \bar{E}_t]_s$ and $[\nabla \cdot \bar{E}]_s$ by expressions involving no derivatives by \bar{E}_t or \bar{E} . In general, in deriving the transport equation for the discontinuity in the n th-order derivative of \bar{E} , the terms $[\nabla \cdot \bar{E}_n]_s$ and $[\nabla \cdot \bar{E}_{n-1}]_s$ will have to be replaced.

To evaluate $[\nabla \cdot \bar{E}_t]_s$ proceed as follows, using one of the Maxwell equations:

$$\nabla \cdot (\nabla \times \bar{H}) = \nabla \cdot (\sigma \bar{E}) + \nabla \cdot (\epsilon \bar{E}_t) = 0.$$

So

$$\nabla \cdot \bar{E}_t = -\nabla \ln \epsilon \cdot \bar{E}_t - \frac{\nabla \sigma}{\epsilon} \cdot \bar{E} - \frac{\sigma}{\epsilon} \nabla \cdot \bar{E}.$$

Writing this equation for points just in front and behind the discontinuity surface, and subtracting the two expressions, there is obtained

$$[\nabla \cdot \bar{E}_t]_s = -\nabla \ln \epsilon \cdot [\bar{E}_t]_s - \frac{\nabla \sigma}{\epsilon} \cdot [\bar{E}]_s - \frac{\sigma}{\epsilon} [\nabla \cdot \bar{E}]_s.$$

Using (22) this becomes

$$[\nabla \cdot \bar{E}_t]_s = -\nabla \ln \epsilon \cdot [\bar{E}_t]_s - \frac{1}{\epsilon} (\nabla \sigma - \sigma \nabla \ln \epsilon) \cdot [\bar{E}]_s.$$

Similarly, for the n th time derivative of \bar{E} , it is not difficult to show that

$$[\nabla \cdot \bar{E}_n]_s = -\left(-\frac{\sigma}{\epsilon}\right)^n \nabla \ln \epsilon \cdot [\bar{E}]_s - \sum_{j=0}^{n-1} (\nabla \ln \epsilon \cdot [\bar{E}_{j+1}]_s + \frac{\nabla \sigma}{\epsilon} \cdot [\bar{E}_j]_s) \left(-\frac{\sigma}{\epsilon}\right)^{n-j-1},$$

where for $n=0$ the summation vanishes. For $\sigma=0$ and $n \neq 0$, the terms for $j=n-1$ is indeterminate. In this case $[\nabla \cdot \bar{E}_n]_s = -\nabla \ln \epsilon \cdot [\bar{E}_n]_s$.

Substituting (22) and the above expression for $[\nabla \cdot \bar{E}_t]_s$ into (32) yields the first-order transport equation for the discontinuity in the electric field:

$$2(\nabla\tau \cdot \nabla)[\bar{E}_t]_s + \nabla^2\tau[\bar{E}_t]_s + \mu\sigma[\bar{E}_t]_s = -\nabla\tau \left(\nabla \ln \epsilon \cdot [\bar{E}_t]_s + \frac{\nabla \sigma}{\epsilon} \cdot [\bar{E}]_s - \frac{\sigma}{\epsilon} \nabla \ln \epsilon \cdot [\bar{E}]_s \right) + \nabla^2[\bar{E}]_s + \nabla(\nabla \ln \epsilon \cdot [\bar{E}]_s). \quad (33)$$

The higher-order transport equations may be obtained in the same way. The general result is

$$2 \frac{d[\bar{E}_n]_s}{d\nu} + \nabla^2\tau[\bar{E}_n]_s + \mu\sigma[\bar{E}_n]_s = \nabla^2[\bar{E}_{n-1}]_s + \nabla\tau[\nabla \cdot \bar{E}_n]_s - \nabla[\nabla \cdot \bar{E}_{n-1}]_s, \quad n \geq 0, \quad (34)$$

where $[\bar{E}_{-1}]_s = 0$, and $\nabla\tau \cdot \nabla$ has been replaced by the derivative with respect to ν . In (34) it is understood that the quantities $[\nabla \cdot \bar{E}_n]_s$ and $[\nabla \cdot \bar{E}_{n-1}]_s$ are to be replaced by means of the expression for $[\nabla \cdot \bar{E}_n]_s$ given above.

THE TRANSPORT EQUATIONS FOR THE MAGNETIC FIELD

The derivation of the transport equations for the \bar{H} field is practically the same as that for the \bar{E} field. Consequently, only the differences in the derivations need be pointed out.

Consider first the zero-order equation. From the integrated Maxwell equations (4),

$$\begin{aligned} \nabla \times \nabla \times \bar{H}_i &= \nabla \times (\sigma \bar{E}_i + \epsilon \Delta \bar{E}) \\ &= \sigma \nabla \times \bar{E}_i + \epsilon \Delta (\nabla \times \bar{E}) + \nabla \sigma \times \bar{E}_i + \nabla \epsilon \times \Delta \bar{E} \\ &= -\mu\sigma \Delta \bar{H} - \mu\epsilon \Delta \bar{H}_t + \nabla \sigma \times \bar{E}_i + \nabla \epsilon \times \Delta \bar{E}. \end{aligned} \quad (35)$$

Except for the last two terms this is exactly the same as (12), which was obtained earlier for \bar{E}_i . Treating the left side of (35) in the same way as the left side of (12), there results, by comparison with (20),

$$\begin{aligned} \nabla \times \nabla \times \bar{H}_i &= \int_{t_0}^t \nabla \times \nabla \times \bar{H} dt + 2(\nabla\tau \cdot \nabla)[\bar{H}]_s \\ &\quad - |\nabla\tau|^2[\bar{H}_t]_s - \nabla\tau[\nabla \cdot \bar{H}]_s \\ &\quad + \nabla^2\tau[\bar{H}]_s. \end{aligned} \quad (36)$$

In (36) the term $[\nabla \cdot \bar{H}]_s$ vanishes, since μ is considered constant and $\nabla \cdot (\mu \bar{H}) = 0$. Remembering that $|\nabla\tau|^2 = \mu\epsilon$, (36) may be substituted into (35), and the interval (t_0, t) allowed to go to zero in such a way that the discontinuity surface always passes the point of observation during the interval. When this is done \bar{E}_i goes to zero, and $\Delta \bar{H}$ and $\Delta \bar{E}$ become $[\bar{H}]_s$ and $[\bar{E}]_s$, respectively. The result is

$$2(\nabla\tau \cdot \nabla)[\bar{H}]_s + \nabla^2\tau[\bar{H}]_s + \mu\sigma[\bar{H}]_s = \nabla \epsilon \times [\bar{E}]_s. \quad (37)$$

From the discontinuity conditions (7),

$$[\bar{E}]_s = -\frac{1}{\epsilon} \nabla\tau \times [\bar{H}]_s,$$

so

$$\nabla \epsilon \times [\bar{E}]_s = -\nabla\tau(\nabla \ln \epsilon \cdot [\bar{H}]_s) + [\bar{H}]_s(\nabla \ln \epsilon \cdot \nabla\tau). \quad (38)$$

Substituting (38) into (37), and letting

$$\begin{aligned} \Delta \epsilon \tau &= \epsilon \left(\left(\frac{\tau_x}{\epsilon} \right)_x + \left(\frac{\tau_y}{\epsilon} \right)_y + \left(\frac{\tau_z}{\epsilon} \right)_z \right) \\ &= \nabla^2\tau - \nabla \ln \epsilon \cdot \nabla\tau, \end{aligned}$$

there results the zero-order transport equation for $[\bar{H}]_s$:

$$2 \frac{d[\bar{H}]_s}{d\nu} + \Delta_e \tau [\bar{H}]_s + \nabla \tau (\nabla \ln \epsilon \cdot [\bar{H}]_s) + \mu \sigma [\bar{H}]_s = 0. \quad (39)$$

The higher-order transport equations for the \bar{H} field can be obtained in the same way as they were for the \bar{E} field. Eq. (31) is valid with \bar{E} replaced by \bar{H} . Making this replacement gives

$$\begin{aligned} \nabla[\nabla \cdot \bar{H}] - \nabla^2[\bar{H}] &= [\nabla \times \nabla \times \bar{H}] + |\nabla \rho|^2 [\bar{H}_t] \\ &+ \nabla \rho [\nabla \cdot \bar{H}_t] - \nabla^2 \rho [\bar{H}_t] \\ &- 2(\nabla \rho \cdot \nabla) [\bar{H}_t]. \end{aligned} \quad (40)$$

But

$$\begin{aligned} [\nabla \times \nabla \times \bar{H}] &= [\nabla \times (\sigma \bar{E} + \epsilon \bar{E}_t)] \\ &= \nabla \sigma \times [\bar{E}] + \sigma [\nabla \times \bar{E}] + \nabla \epsilon \times [\bar{E}_t] \\ &+ \epsilon [\nabla \times \bar{E}_t]. \end{aligned} \quad (41)$$

Now substitute (41) into (40), and set $\nabla \cdot \bar{H} = \nabla \cdot \bar{H}_t = 0$, to yield

$$\begin{aligned} -\nabla^2[\bar{H}] &= -\mu \sigma [\bar{H}_t] + \nabla \sigma \times [\bar{E}] + \nabla \epsilon \times [\bar{E}_t] \\ &- \nabla^2 \rho [\bar{H}_t] - 2(\nabla \rho \cdot \nabla) [\bar{H}_t], \end{aligned} \quad (42)$$

where $|\nabla \rho|^2 = \mu \epsilon$, and Maxwell's equation for $\nabla \times \bar{E}$, have been used. If (42) is rewritten for the surface $t = \tau(\bar{r}) - \delta$, and the second equation subtracted from the first, the result is, as δ goes to zero,

$$\begin{aligned} -\nabla^2[\bar{H}]_s &= -\mu \sigma [\bar{H}_t]_s + \nabla \sigma \times [\bar{E}]_s + \nabla \epsilon \times [\bar{E}_t]_s \\ &- \nabla^2 \tau [\bar{H}_t]_s - 2(\nabla \tau \cdot \nabla) [\bar{H}_t]_s. \end{aligned} \quad (43)$$

From the discontinuity conditions, equations (11),

$$\begin{aligned} \nabla \epsilon \times [\bar{E}_t]_s &= -\frac{1}{\epsilon} \nabla \epsilon \times (\nabla \tau \times [\bar{H}_t]_s - \nabla \times [\bar{H}]_s) \\ &+ \sigma [\bar{E}]_s \\ &= -\nabla \tau (\nabla \ln \epsilon \cdot [\bar{H}_t]_s) + [\bar{H}_t]_s (\nabla \ln \epsilon \cdot \nabla \tau) \\ &+ \nabla \ln \epsilon \times (\nabla \times [\bar{H}]_s) - \sigma \nabla \ln \epsilon \times [\bar{E}]_s. \end{aligned} \quad (44)$$

Substitution of (44) into (43) yields the first-order transport equation

$$\begin{aligned} 2(\nabla \tau \cdot \nabla) [\bar{H}_t]_s + \Delta_e \tau [\bar{H}_t]_s + \nabla \tau (\nabla \ln \epsilon \cdot [\bar{H}_t]_s) + \mu \sigma [\bar{H}_t]_s \\ = \nabla^2 [\bar{H}]_s + \nabla \ln \epsilon \times (\nabla \times [\bar{H}]_s) - \sigma \nabla \ln \epsilon \times [\bar{E}]_s \\ + \nabla \sigma \times [\bar{E}]_s. \end{aligned} \quad (45)$$

The derivation of the n th-order transport equation for the magnetic field is entirely similar to that for (45). The result is, after replacing $\nabla \tau \cdot \nabla$ by $d/d\nu$,

$$\begin{aligned} 2 \frac{d[\bar{H}_n]_s}{d\nu} + \Delta_e \tau [\bar{H}_n]_s + \nabla \tau (\nabla \ln \epsilon \cdot [\bar{H}_n]_s) + \mu \sigma [\bar{H}_n]_s \\ = \nabla^2 [\bar{H}_{n-1}]_s + \nabla \ln \epsilon \times (\nabla \times [\bar{H}_{n-1}]_s) \\ - \sigma \nabla \ln \epsilon \times [\bar{E}_{n-1}]_s + \nabla \sigma \times [\bar{E}_{n-1}]_s, \quad n \geq 0, \end{aligned} \quad (46)$$

where $[\bar{E}_{-1}]_s = [\bar{H}_{-1}]_s = 0$.

Notice that in the n th-order transport equation the quantity $[\bar{E}_{n-1}]_s$ appears. By recursive use of the discontinuity conditions (11), this term in the electric field

could be replaced by terms involving only the magnetic field. Because this procedure results in a rather awkward expression, (46) has been left in terms of $[\bar{E}_{n-1}]_s$.

DISCUSSION

It is interesting to relate the work in this article to the properties of the characteristic surfaces of the Maxwell equations in x, y, z, t space. The properties of such surfaces will be summarized briefly.^{6,7}

The question may be asked, "If the fields \bar{E} and \bar{H} are specified on some 3-dimensional surface S in x, y, z, t space, is it possible, by using Maxwell's equations, to compute the derivatives of \bar{E} and \bar{H} in the direction normal to S ?" The answer is that it is possible unless S belongs to either of the two categories of surfaces listed below, in which case S is referred to as a characteristic surface.

- 1) S is a cylinder with generators parallel to the time axis, or,
- 2) S satisfies the eikonal equation.

In the present article, case 2) has been the one of interest. Notice that discontinuities in solutions of Maxwell's equations can lie only on a characteristic surface, because otherwise Maxwell's equations, by enabling the computation of the derivatives of the fields in the direction normal to the surface, would specify how the fields were to vary as the surface was crossed.

Restricting attention to the surfaces of case 2), note that a 4-vector normal to S is

$$\bar{\lambda} = \left(\frac{\partial \tau}{\partial x}, \frac{\partial \tau}{\partial y}, \frac{\partial \tau}{\partial z}, -1 \right).$$

Thus the space derivatives of quantities evaluated on S , e.g.,

$$\frac{\partial [\bar{E}]}{\partial x} = \left(\frac{\partial \bar{E}}{\partial x} \right) + \frac{\partial \tau}{\partial x} [\bar{E}_t],$$

are directional derivatives in 4-space in directions tangent to S ; i.e., the above derivative is in the direction of the 4-vector

$$\bar{\alpha} = \left(1, 0, 0, \frac{\partial \tau}{\partial x} \right),$$

and $\bar{\alpha}$ is perpendicular to $\bar{\lambda}$, since $\bar{\alpha} \cdot \bar{\lambda} = 0$. A similar calculation can be made for the derivative of a bracketed quantity with respect to y or z .

Eq. (8) and the corresponding equation for the \bar{H} field were used to derive the discontinuity conditions (11) by replacing the derivatives with respect to x, y , and z , that appear in Maxwell's equations in the form $\nabla \times \bar{E}$ and $\nabla \times \bar{H}$, by derivatives tangent to the 3-surface S , and by derivatives with respect to time, which are in

⁶ R. von Mises, "Mathematical Theory of Compressible Fluid Flow," Academic Press, Inc., New York, N. Y., pp. 103-107; 1958.

⁷ A. G. Webster, "Partial Differential Equations of Mathematical Physics," Dover Publications, Inc., New York, N. Y., 2nd ed.: 1955.

a direction having a component along the normal to S . At this point an alternate route to the derivation of the transport equations should be pointed out. The conditions (11) can be regarded as a set of simultaneous algebraic equations involving the six unknowns $[\bar{E}_n]_s$ and $[\bar{H}_n]_s$. It has already been observed that it is necessary that $|\nabla\tau|^2 = \mu\epsilon$, in order for the zero-order discontinuity conditions to be compatible. Hence the determinant of the system of equations for $[\bar{E}_n]_s$ and $[\bar{H}_n]_s$ is zero. Under these conditions, in order for there to be solutions for $[\bar{E}_n]_s$ and $[\bar{H}_n]_s$, it is necessary that the right sides of (11) satisfy certain auxiliary conditions.⁸ These conditions, which can be obtained by vector manipulation of (11), involve $[\bar{E}_{n-1}]_s$ and $[\bar{H}_{n-1}]_s$, and lead to the $(n-1)$ -order transport equations.

Regarding the motivation for the present derivations, consider the first-order discontinuity conditions. The quantity $[\bar{H}_1]_s$ can be eliminated between these two equations, resulting in an equation involving only

⁸ R. Courant and D. Hilbert, "Methods of Mathematical Physics," Interscience Publishers, Inc., New York, N. Y., vol. 1, p. 5; 1953.

$[\bar{E}]_s$ and $[\bar{H}]_s$, and the derivatives of $[\bar{E}]_s$ and $[\bar{H}]_s$ in directions tangent to S . The quantity $[\bar{E}_t]_s$ disappears.⁹ A point on a discontinuity surface propagating in x, y, z space is moving tangent to a characteristic surface in x, y, z, t space. Hence, in searching for information regarding how discontinuities propagate in x, y, z space, it is reasonable to look for equations, such as the one just discussed, involving the derivatives of the discontinuities in directions tangent to the characteristic surfaces in x, y, z, t space. In this manner, it can be anticipated that if (8), and the corresponding equation for \bar{H} , are substituted in Maxwell's equations, or the wave equations obtained from them, and if the equations so obtained are written on each side of a discontinuity surface and subtracted, the resulting equations should lead to information concerning the propagation of discontinuities.

⁹ Upon eliminating $[\bar{H}_t]_s$, the fact that S satisfies the eikonal equation may be used to eliminate the resulting term that is proportional to $[\bar{E}_t]_s$. There remains then a quantity $(\nabla\tau \cdot [\bar{E}_t]_s)$, which may be expressed in terms of $[\bar{E}]_s$ and derivatives of $[\bar{E}]_s$ in directions tangent to S by use of (18) and (22).

Elevated Duct Propagation in the Tradewinds*

D. L. RINGWALT†, MEMBER, IRE, AND F. C. MACDONALD†

Summary—All of the maximum propagation (220 Mc) ranges observed in an elevated duct regime varied from 500 to 1200 miles compared to less than 400 miles observed with the same equipment elsewhere. The measurements were made at the optimum season (November) in a tradewind regime between Brazil and Ascension Island (8° S. latitude). The field strengths above 4000 feet altitude are as much as 40 db larger than those at lower altitudes. From the level at average duct height (6000 feet) the field decreases slowly to 10,000 feet, the maximum altitude investigated. The slow fading rate usually associated with duct propagation is not always observed even on the very long range runs.

An extrapolation to propagation conditions in the month of March via refractive index measurements indicates quite minimal ducting conditions 10 per cent to 20 per cent of the time.

THE TERM "tradewind region" as used here designates the region between the mid-ocean, high-pressure cells and the equatorial doldrums. Statistically, the high-pressure areas occur about 30° north and south of the equator. In the tradewind regions, cool

moist air circulates from east to west at altitudes of roughly less than 6000 feet. Above this is warm dry subsiding air, and the boundary conditions of positive temperature and negative humidity lapse rates are conducive to the formation of radio ducts. For orders of magnitude, 5°C and 50 per cent relative humidity change in 300 feet are large, but not unusual. There is a second duct at the condensation or cloud-base level, and no doubt a third within a few tens of feet of the water surface. The latter, which is too close to the water for aircraft measurements, is not covered by the present measurements.

The meteorological studies made by Katzin¹ and Cunningham² between Brazil and Ascension Island indicated the possibility of year round extended propa-

¹ M. Katzin, B. V-C Koo, J. V. Larson, J. C. Katzin, and H. Pezner, "The Possibility of Transoceanic VHF Propagation through the Trade-Wind Inversions," Electromagnetic Research Corp., Rept. No. CRC 3031-2; December 30, 1958.

² R. M. Cunningham, "Trade-Wind Cloud Forms as Areal Indicators of Duct Strength," presented at URSI Spring Meeting, Washington, D. C.; May 5, 1959.

* Received by the PGAP, August 19, 1960; revised manuscript received, February 14, 1961.

† Wave Propagation Branch, U. S. Naval Res. Lab., Washington, D. C.

gation. Ament³ exhibited duct-like, height-gain curves from a path between Cape Canaveral, Florida, and Nassau in the Bahamas. The latter observations from December, 1956, and May, 1957, were made at 1250 Mc and 9300 Mc.

The subject of this paper is measurement of propagation (220 Mc) and meteorology on the Recife, Brazil-Ascension Island route. During the experiment, the range of propagation was always longer than are average "scatter" ranges. Further, the data also prove that there is a large gain to be obtained by elevating the antenna system to (and perhaps also above) the duct altitude of 6000 feet.

With the proof of extended propagation ranges in hand, whether or not elevated duct propagation is a generally useful increase of range depends upon the unknown seasonal variation. The subject measurements were made in November (1959), which is the seasonal optimum for duct formation. The authors also measured meteorological parameters in March, 1959, (which approaches the period of minimum ducting) and an extrapolation to radio propagation ranges for March is attempted.

It is concluded that as the incidence of days of extreme propagation ranges decreases from November to March the minimum propagation range also decreases from the minimum condition in November which was an extension of about 150 miles to "scatter" ranges. From the vertical gradients of refractive index ($\Delta N/\Delta H$) observed, this minimal condition is predicted to exist 10 per cent to 20 per cent of the time in March.

EXPERIMENTAL PROGRAM

Fig. 1 shows the area in which the measurements were taken. The two terminals of the propagation path, Recife and Ascension Island, are separated by about 1200 nautical miles (n.m.) on a nearly east-west line at about 8° south latitude.

The experimental program was as follows. The transmitter was carried at the inversion altitude by an aircraft which flew a race-track pattern 100 n.m. east of Recife. The receiver was likewise carried at the inversion altitude by another aircraft which flew between Recife and Ascension Island.

The transmitter operated at 220 Mc and had a nominal CW output of 90 watts. The transmitting antenna was a 5-element Yagi (10-db gain) which was mounted in a radome on the underside of the P2V aircraft.

The receiver had a bandwidth of 3 kc and a noise figure of about 4 db. The receiving antenna was also a 5-element Yagi which was mounted in a radome, in this case, on the underside of a WV-2, or Super Constellation aircraft. Both this and the transmitting antenna were

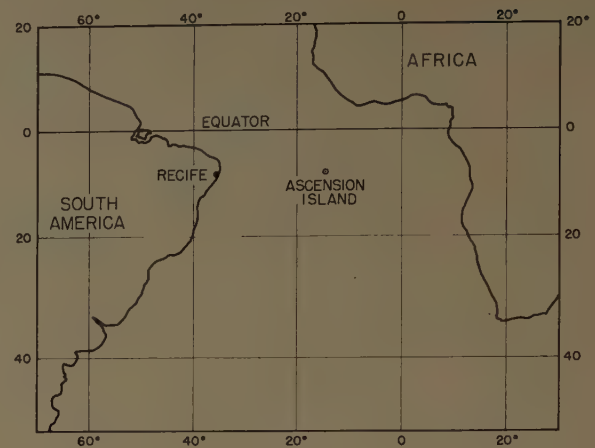


Fig. 1.

azimuth-stabilized from N-1 Compass Systems.

Along with the radio data, the meteorological parameters recorded in the receiving aircraft were pressure, temperature, refractive-index, humidity, wind speed and wind direction as obtained from the APN-66 Doppler Navigator. The meteorological parameters recorded in the transmitting aircraft were pressure, temperature, humidity and refractive index.

The inversion altitude was determined initially by meteorological soundings by both aircraft as they proceeded to the starting point of each run, about 100 n.m. east from Recife. Three times during the transit period of the receiving aircraft, it made meteorological soundings (to insure that it was flying at the inversion altitude) and height-gain measurements between 300 feet and 10,000 feet altitude. Similarly, the transmitting aircraft made three soundings during the transit period of the receiving aircraft.

THE RESULTS

Shortly before the Recife operation, the aircraft made two range runs off the coast of New Jersey in a featureless meteorological structure with both aircraft flying at 4000 feet altitude. These runs gave maximum ranges of 350 and 375 n.m. which compare reasonably well with the work of Ames, *et al.*,⁴ and with the JTAC Report.⁵ Therefore, it is assumed that the 350 to 375 n.m. represents maximum range (for this particular system) by scatter processes.

In all, the receiving aircraft made 14 transits (runs) between the terminals. In Table I are listed the maximum ranges observed; these might be classified as "small," "moderate," or "great" extensions of range over that expected by scatter processes.

⁴ L. A. Ames, P. Newman and T. F. Rogers, "VHF tropospheric overwater measurements far beyond the horizon," *Proc. IRE*, vol. 43, pp. 1369-1373; October, 1955.

⁵ Joint Technical Advisory Committee, "Radio transmission by ionospheric and tropospheric scattering, II. Long range tropospheric transmission," *Proc. IRE*, vol. 48, pp. 30-44; January, 1960.

³ W. S. Ament, "Airborne radiometeorological research," *Proc. IRE*, vol. 47, pp. 756-761; May, 1959.

TABLE I

No. of Flights	First Loss of Signal	Remarks
5	500- 550 miles	
2	550- 600 miles	Intermittent to 850 and 1000 miles
1	750 miles	
4	750- 850 miles	Intermittent beyond 1050 miles
1	950 miles	Terminated by equipment failure
1	1250 miles	

Fig. 2 (next page) is one of the longest range runs observed. The field strength data have been plotted to show the maximum and minimum values during each half-minute interval. Cloud coverage is shown at the top of the figure and wind direction (north upward) is shown just below the clouds. The flight altitudes (vs time or range) are shown second from the bottom for both the transmitting and receiving aircraft and thereby mark the position or time at which the height-gain data and refractive index (N) curves shown above the flight profiles were obtained. On some of the other runs the two aircraft made soundings simultaneously instead of alternately. The range data are plotted through the transmitter soundings but there is a data gap for the receiver soundings.

The qualitative conclusions of the November experiment are simply stated. At least for the time and place of the experiment:

- 1) The long propagation ranges are caused by a strong elevated duct near 6000 feet. The existence of this duct is reasonably well indicated by extensive haze layers and numerous cloud tops at this altitude.
- 2) The elevated duct at the cloud base (2000 feet) plays a minor role in determining the range of radio propagation.
- 3) The radio-signal fluctuation rate is independent of the maximum range of propagation. Usually, but not necessarily, a slow fade rate is associated with long-range propagation.

The Range Dependence

The number of runs on which the signal exceeded a given level is plotted for fixed ranges in Fig. 3. Though it is only at 500 n.m. that all the signals exceed the minimum detectable level, there are sufficient observations at 700 miles to warrant the extrapolation that good reliability could be purchased with very little increase in system sensitivity.

From the maximum ranges observed, a range attenuation rate can be derived by subtracting the horizon

range (180 n.m.) and dividing this into 66 db (the approximate power level change from the horizon to minimum detectable level). For the three classes of runs (short, medium and long), the respective attenuation rates are 13, 9 and 6 db/100 n.m. This rate should be distinguished from the usual scatter rate (approximately 15 db/100 n.m.) which is computed for the signal loss beyond the diffraction zone rather than beyond the horizon.

The above attenuation rates are, in a sense, a poor description of the range function because the signal usually decreases by steps with attenuation rates approaching zero between steps. Extreme examples of these steps appear in Figs. 2 and 4. These steps are attributed to meteorological changes such as rapid changes in duct height or refractive index gradient in the region just passed by the receiver rather than general rearrangements of the meteorology further back toward the transmitter. The argument for this is that fluctuations in the general propagation conditions would have engendered more cases of increase of signal with range (time) than the four that are apparent in the data.

On 9 of the 14 runs, a step occurs near the horizon. The decreases vary from 10 db to 30 db but, to all appearances, do not differ from the 15 other steps at ranges out to 900 miles. These decreases are considered as duct-feeding losses just as would be encountered at the horizon distance beyond a duct discontinuity.

The steps assume importance in predicting propagation from meteorology because continuity, if not reflected in average characteristics of the duct, must be predicted. Duct height will be particularly troublesome because the important changes are localized and small (being of the order of the inversion layer thickness of 300 feet).

The Height Dependence

The signal amplitude is normally much greater (as much as 40 db) near 5000 feet than at low altitudes (e.g., Fig. 2). Certainly the average maximum signal occurs near the duct altitude but the height/gain is variable or slowly decreasing above the duct and the possibility that the duct could be fed with slight loss from altitudes well above 5000 feet is not contradicted. The variation of height/gain with maximum range is not completely specified by the data, being limited by system sensitivity at low altitudes and by the horizon effects at high altitude on the short range runs. On the longer runs the average signal between 6000 and 8000 feet is 25 db stronger than the average between 500 and 2000 feet.

Because of the slow fading rates in the signal, it was impossible to remain at each altitude long enough to obtain a steady average signal, but in two runs there are indications in the height-gain curves that the cloud-base duct located near 2000 feet can carry some energy.

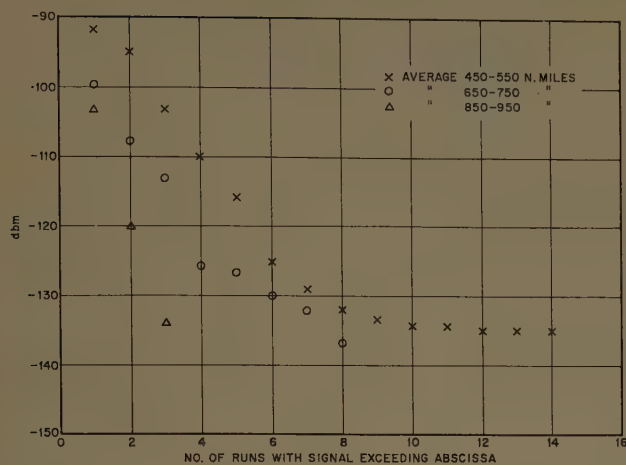


Fig. 3.

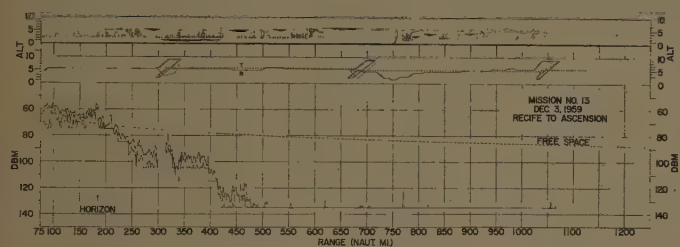


Fig. 4.

The amount of energy is unimportant in the November experiment and is presumed to remain so in March. Average conditions are indicated in Fig. 5 by the relative frequencies of duct occurrence (both the "trade-wind" duct at 6000 feet and the cloud-base duct at 2000 feet) from soundings every 300 miles in November and every 60 miles in March. Herein a duct is defined as a refractive index change (ΔN) greater than 15 at a rate greater than $48N/1000$ feet. From Fig. 5 the maximum cloud-base duct occurrence in March is not greater than that in the western sectors in November and, therefore, is not counted upon as a major contribution to March propagation.

Dependence Upon Meteorological Observations

The gradients of refractive index are greater on the average for the longer runs. A scatter plot of maximum range vs average gradient (includes only complete soundings out to maximum radio range) appears in Fig. 6. Grouping the runs again as short, medium, and long, the average gradients are 50, 70 and 78N units/1000 feet, respectively.

Fig. 7, a plot of refractive-index gradients against radio signal attenuation rate (db/100 n.m.), illustrates that the attenuation rates for $\Delta N/AH > 50$ are small and hence that signal strength does not depend as much on their precise value as upon the large losses due to

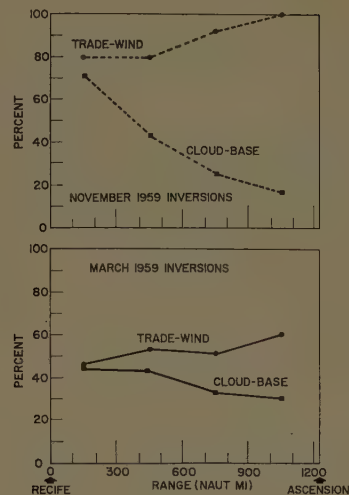


Fig. 5.

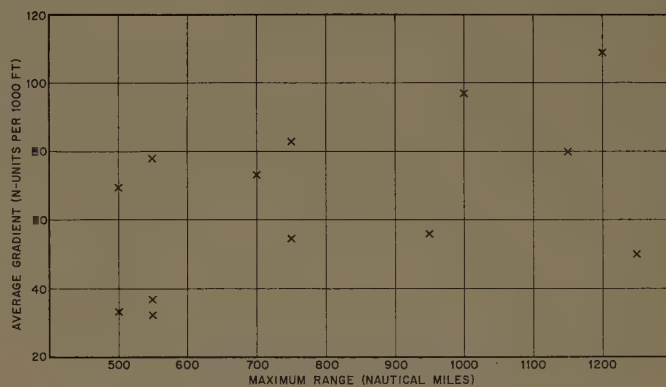


Fig. 6.

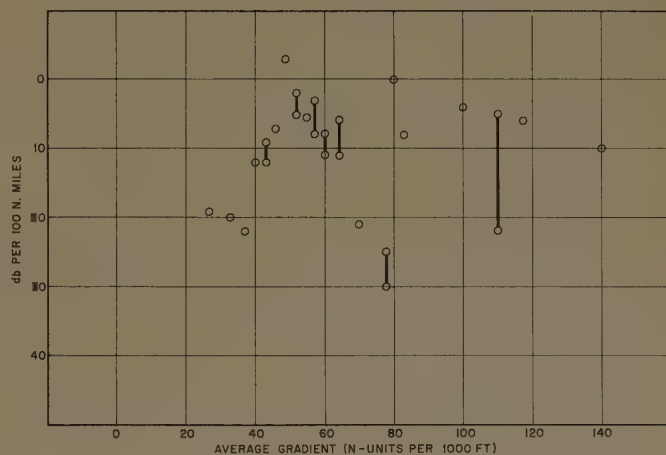


Fig. 7.

duct discontinuities. For example, Fig. 2 shows about 20 db loss from the horizon to 850 miles and 30 db loss in the next 150 miles. The "extended" points in Fig. 7 stem from the multiple choices of attenuation rate presented by the "steps" referred to previously. All the attenuation rates shown are averaged over at least 150 miles in the region where the N measurement was

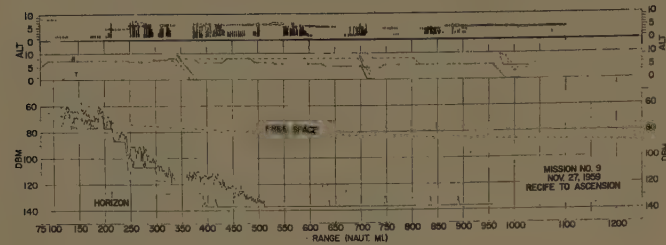


Fig. 8.

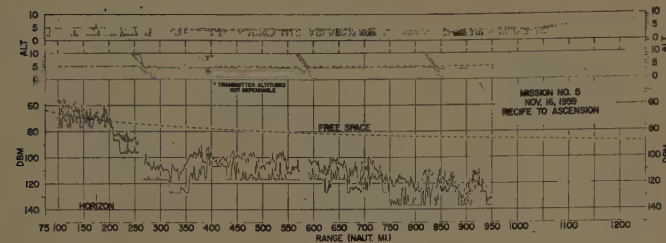


Fig. 9.

made. All of the N -gradients are taken from the higher duct or tradewind level and only a few of the November soundings presented a problem in referring to a single gradient for a single sounding.

Fig. 8 illustrates the average trend in cloud diagrams with convective clouds in the west and increasing incidence of stratus to the east. There is also a general increase of N gradients to the east, hence, the stronger gradients are associated with stratus clouds.

The numerous convective clouds all "topping" at the duct in Fig. 9 are not typical. Noteworthy is that it constitutes the only long range run with a rapidly fluctuating (large separation of $\frac{1}{2}$ -minute maximum and minimum) signal. This is sufficient evidence that such can be the case, but that clouds are a sufficient cause of rapid fluctuations, of course, does not follow necessarily.

Signal Fluctuations

Two types of signal fluctuations are distinguished from the db separation of maximum and minimum signals in $\frac{1}{2}$ -minute intervals. These have been variously referred to as large and small or rapid and slow fluctuations.

The larger separations are normally associated with the shorter maximum ranges (compare Figs. 2 and 8). The relationship is, however, not a necessary one as demonstrated by comparing the separations in the "long" runs of Figs. 9 and 10 and in the "short" runs of Figs. 8 and 11.

In addition to the above, larger separations also appear just beyond (in range) "breaks" in the duct (Fig. 10: 250 and 700 miles) and on many occasions when the transmitting or receiving antenna is below the duct. The fluctuations beyond a break in the duct are presumed to be interference between several signals not all

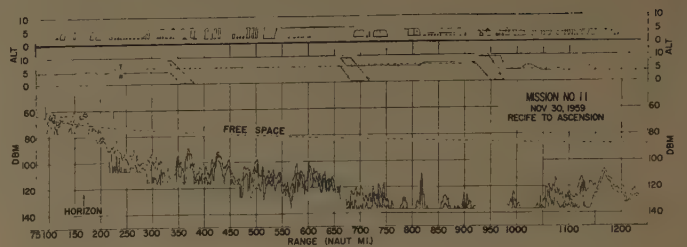


Fig. 10.

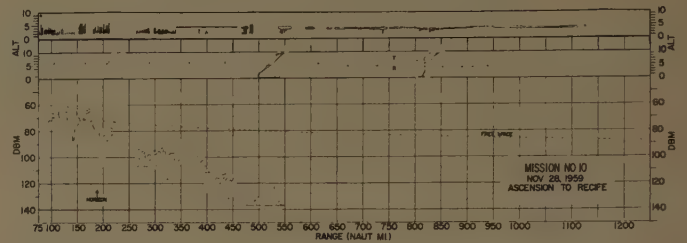


Fig. 11.

of which need be subsequently trapped because of their different angles of travel. Hence, there is the possibility that the larger fluctuations could die out with, say, only a 3 db change of signal amplitude.

The Extrapolation to March

In Table II are the average N gradients for ten⁶ flights of March, 1959, averaged for the same geographic areas as was implied by the radio ranges measured in November (*viz.*, 100–600, 600–900, and 900–1200 miles east of Recife). This table considers only the higher or tradewind duct and averages a gradient for every sounding. No restrictions were placed on the size of the N change (ΔN) or altitude change (ΔH) that could be encountered in the tradewind duct. Actually the values of ΔN ranged mostly between $15N$ and $50N$ while $\Delta N/\Delta H$ usually ranged from 20–100n/1000 feet. Where an obvious choice could not be made in the importance of two layers, both were kept in the average. The usual turbulence in the record resulting from flying through these layers at a slight angle to the horizontal has been smoothed, because it is argued that it represents horizontal and not vertical gradients.

It is inferred from Table II that, with the same radio equipment used in November, five flights would have exhibited ranges of less than 500 miles ($\Delta N/\Delta H$) entries in the first column of less than 49; four flights would have shown radio ranges between 500 and 800 miles (the average of the entries in first two columns lies between 49 and 65); and one flight falls in the third category

⁶ There were two aircraft with different instrumentations involved, and they also made flights to Africa and St. Helena. The table represents the data from one aircraft on the Recife-Ascension route only.

TABLE II

AVERAGE VALUES OF $\Delta N/\Delta H$ (NUMBER OF GRADIENTS IN PARENTHESIS)

Flight	33°-25° W	25°-20° W	20°-14° W
3a	33 (5)	33 (4)	48 (3)
3b	62 (4)	83 (4)	76 (6)
5a	36 (7)	51 (6)	52 (7)
5b	34 (6)	53 (6)	48 (5)
9	56 (9)	53 (6)	85 (5)
17	72 (4)	48 (6)	53 (9)
19a	67 (6)	63 (4)	45 (5)
19b	41 (5)	155 (4)	33 (1)
21a	56 (4)	62 (4)	55 (8)
21b	32 (5)	34 (2)	33 (4)

800-1100 miles with $\Delta N/\Delta H = 74$ averaged along the whole route.

The 10 per cent to 20 per cent mentioned earlier is based on flights 3a and 21b in which increased system sensitivity could not extend propagation to better propagation conditions to the east. Minimal propagation conditions 20 per cent of the time could also be stated of the two eastern sectors from Table II, though two of the observations of small gradient are based on one and two measurements, respectively.

CONCLUSIONS

As observed during the optimum season (November), the tradewind duct between Brazil and Ascension Island always increased propagation ranges by 150 miles as compared to average scatter conditions. Systems with greater sensitivity would have shown greater increases because of the improvements in ducting conditions from west to east in the tradewinds. Meteorological measurements in March show minimal ducting conditions everywhere along this route about 20 per cent of the time.

ACKNOWLEDGMENT

It is impossible to acknowledge all the contributions to this work, but some of the principal ones include: funds from Air Force Cambridge Research Center, Bedford, Mass.; aircraft support from Naval Air Development Unit, South Weymouth, Mass.; instrumentation, P. L. Watkins and J. T. Ransone; meteorology, D. L. Randall and C. G. Purves; and data analysis, R. Shewbridge. Special acknowledgment is due the crew of the NRL aircraft from Naval Air Station, Patuxent River, Md., and LCDR B. R. McClelland, the NRL Project Officer.

Frequency Variations Due to Over-the-Horizon Tropospheric Propagation*

J. H. CHISHOLM†, S. J. GOODMAN‡, MEMBER, IRE, J. M. KENNEDY‡, MEMBER, IRE,
L. B. LAMBERT‡, MEMBER, IRE, L. P. RAINVILLE‡, ASSOCIATE MEMBER, IRE,
AND J. F. ROCHE‡, MEMBER, IRE

Summary—An experiment was performed over a 161-mile path between Alpine, N. J., and Round Hill, Mass., to determine the frequency fluctuations produced by the propagation mechanism on a highly stable signal in an over-the-horizon tropospheric circuit. A signal at 388.0 Mc was transmitted from Alpine using a 10-kw transmitter and a 12° beamwidth antenna. These transmissions were received at Round Hill with a 5° beamwidth antenna and heterodyned to 416.7 Mc using a highly stable local oscillator and retransmitted to Alpine. Using coherent reception techniques, the retransmitted signal was received at Alpine and heterodyned with the signal originally transmitted. The difference frequency was fed to a bank of narrow-bandwidth crystal filters. An analysis of the data obtained from these filters indicated that the standard deviation of the frequency fluctuations of the signal was approximately 0.6 cps when CW transmission was employed.

An additional feature of the experiment was an attempt to measure the variations of the propagation path length as a function of time. It appears that the standard deviation of the path length variations was less than 55 meters when the average path length in $\frac{1}{6}$ -second intervals was measured.

INTRODUCTION

ONE of the problems of current interest to workers in the field of radio propagation is the determination of the perturbations of the frequency of a signal propagated beyond the horizon by means of the troposphere. Many of the previous efforts in this area have been concerned with the characteristics of the fading envelope of the signal; that is, fading rates of the envelope fluctuations were measured,¹⁻³ or autocorrelation functions of the fading envelopes were plotted and transformed to obtain spectral densities,⁴ or the fading envelopes were amplitude detected and the spectra of the detected outputs were studied with spectrum analyzers.⁵ This paper describes an experiment in which the frequency characteristics

of a UHF signal propagated beyond the horizon were measured directly after heterodyning the received signal to a low intermediate frequency. The carrier signal was integrated (at the intermediate frequency) for $\frac{1}{6}$ of a second, and the frequency content of this integrated signal was measured using a bank of crystal filters, each filter having a 3-db bandwidth of 6 cps. This measurement was repeated once every second during each of many transmission samples. Variations of the measured frequency of the integrated signal as a function of time were determined and analyzed. The results indicated that the frequency of the integrated signal exhibited fluctuations within the one-second sampling intervals. The standard deviation of the frequency fluctuations of the samples integrated over $\frac{1}{6}$ of a second for a ten-minute data sampling period was approximately 0.6 cps. It is possible, of course, that there might have been larger but more rapid frequency fluctuations which were smoothed out by the $\frac{1}{6}$ -second integration. The data analysis technique that was employed did not measure such rapid fluctuations, which would appear as additional energy in the received sidebands for each transmission. The result stated above implies that this type of propagation will not begin to seriously degrade the performance of transmitted signals until their frequency stabilities are of the order of five parts in 10^9 or better, at least in the vicinity of 400 Mc and over the path length used in this experiment. This information may be of importance in the design of high-resolution radar and navigation systems.

An additional feature of the experiment was an attempt to measure the variations of the propagation path length as a function of time. It appears that the standard deviation of the path length variations was less than 55 meters when the average path length in $\frac{1}{6}$ -second intervals was measured.

SYSTEM GEOMETRY

The experiment was performed over the 161-mile path shown in Fig. 1, between Columbia University's Armstrong Field Laboratory at Alpine, N. J., and the Lincoln Laboratory Round Hill Field Station at South Dartmouth, Mass. The path runs over Long Island Sound and along the Connecticut coast. Earlier work on this path has been described in the literature.⁶

* Received by the PGAP, August 29, 1960; revised manuscript received, December 5, 1960. This work was performed by the Electronics Res. Labs., Columbia University, and the M.I.T. Lincoln Lab. with the joint support of the U.S. Army, Navy, and Air Force.

† Lincoln Lab., Mass. Inst. Tech., Cambridge, Mass.
‡ Electronics Res. Labs., School of Engrg., Columbia University, New York, N. Y.

¹ K. A. Norton, P. L. Rice, H. B. Janes, and A. P. Barsis, "The rate of fading in propagation through a turbulent atmosphere," *Proc. IRE*, vol. 43, pp. 1341-1353; October, 1955.

² L. G. Trolese, "Characteristics of tropospheric scattered fields," *Proc. IRE*, vol. 43, pp. 1300-1305; October, 1955.

³ A. B. Crawford, D. C. Hogg, and W. H. Kummer, "Studies in tropospheric propagation beyond the horizon," *Bell Sys. Tech. J.*, vol. 38, pp. 1067-1178; September, 1959.

⁴ N. R. Ortwein, R. V. F. Hopkins, and J. E. Pohl, "Properties of tropospheric scattered fields," *Proc. IRE*, vol. 49, pp. 788-802; April, 1961.

⁵ J. H. Chapman, W. J. Heikkila, and J. E. Hogarth, "A new technique for the study of scatter propagation in the troposphere," *Canad. J. Phys.*, vol. 35, pp. 823-830; August, 1957.

⁶ J. H. Chisholm, J. T. De Bettencourt, P. A. Portmann, and J. F. Roche, "Investigations of angular scattering and multipath properties of tropospheric propagation of short radio waves beyond the horizon," *Proc. IRE*, vol. 43, pp. 1317-1335; October, 1955.

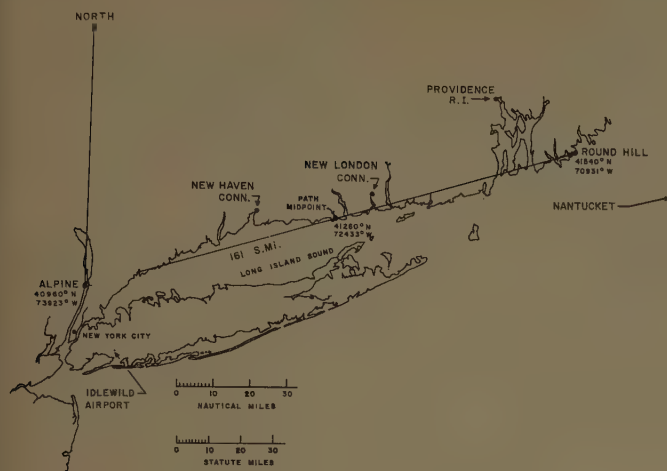


Fig. 1—Map showing Alpine-Round Hill transhorizon path.

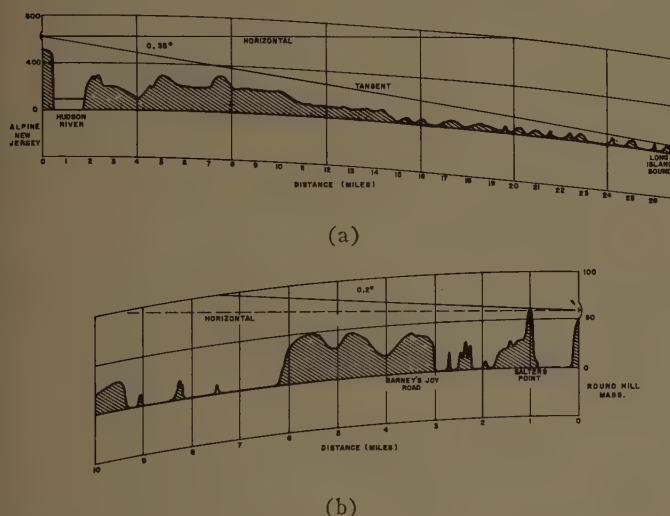


Fig. 2—Path foreground profiles. (a) Profile of the foreground at the Armstrong Laboratories, Alpine, N. J., on a true bearing of 74.6° toward Round Hill, Mass. (b) Profile of the foreground at Round Hill, Mass., on a true bearing of 256.5° toward Alpine, N. J.

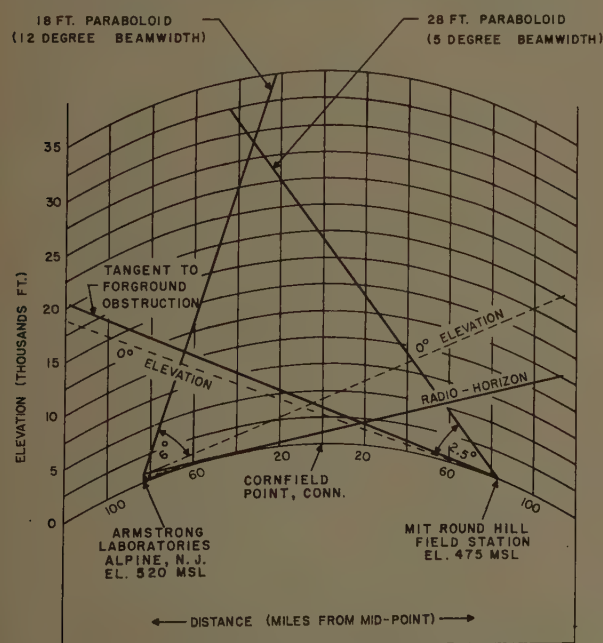


Fig. 3—Path profile and antenna geometry.

Fig. 2 shows the foreground profiles at the Alpine and Round Hill sites.

Fig. 3 shows the path profile and the beam geometry for the entire path. The Alpine site contained a pair of 18-foot paraboloidal antennas rigidly attached together, one being used for transmitting, the other for receiving. A single 28-foot-diameter paraboloidal antenna was used at Round Hill for reception and retransmission in conjunction with a diplexer. The Alpine antennas each had a 3-db beamwidth of 12°, while the Round Hill antenna had a 3-db beamwidth of 5°.

SYSTEM OPERATION

Fig. 4 shows a highly simplified block diagram of the system. A stable signal was transmitted from Alpine using a 10-kw transmitter at 388.0 Mc, in the form of $\frac{1}{6}$ -second pulses repeated every half second. The frequency stability of the transmitted signal was better than one part in 10^8 . The signal was received at Round Hill and was heterodyned to 416.7 Mc using a local oscillator whose frequency stability was also better than one part in 10^8 . The heterodyned signal was amplified and then transmitted back to Alpine. The maximum output of the signal from Round Hill was less than 200 watts. The output varied, of course, with the fading of the signal received from Alpine.

The retransmitted signal was received at Alpine and heterodyned with the original transmitter signal source of 388.0 Mc in order to remove the transmitter frequency instability (of period greater than the 2-msec round-trip delay time) from the observed signal. The difference frequency now consisted of only the frequency of the local oscillator at Round Hill (28.7 Mc) plus any perturbations induced by the two-way transmission path. This signal was then fed into a series of IF and heterodyne stages to beat it down to 30.5 kc, where it was fed into a bank of crystal filters. All the local oscillator signals in the receiver except the last stage were derived from the basic oscillator of the transmitter. A variable oscillator was required for the last local oscillator in order to center the received signal in the filter bank. The frequency of this oscillator was monitored during the experiment. Its total variation was approximately 0.5 cps over a ten-minute interval.

The filter bank was used to determine the frequency of the received signal. It consisted of four crystal filters whose frequency characteristics are shown in Fig. 5(a). These filters had a resonance characteristic with a 3-db bandwidth of 6 cps. The filters were separated by 6 cps in resonant frequency. The frequency of the received signal was determined by considering the ratio of the outputs of the two middle filters on the display. If the frequency was halfway between the resonant frequencies of these filters, then the ratio of the outputs would be unity. If the frequency was closer to the second filter than to the third filter, then the output of the second filter would be greater than the output of the third, and

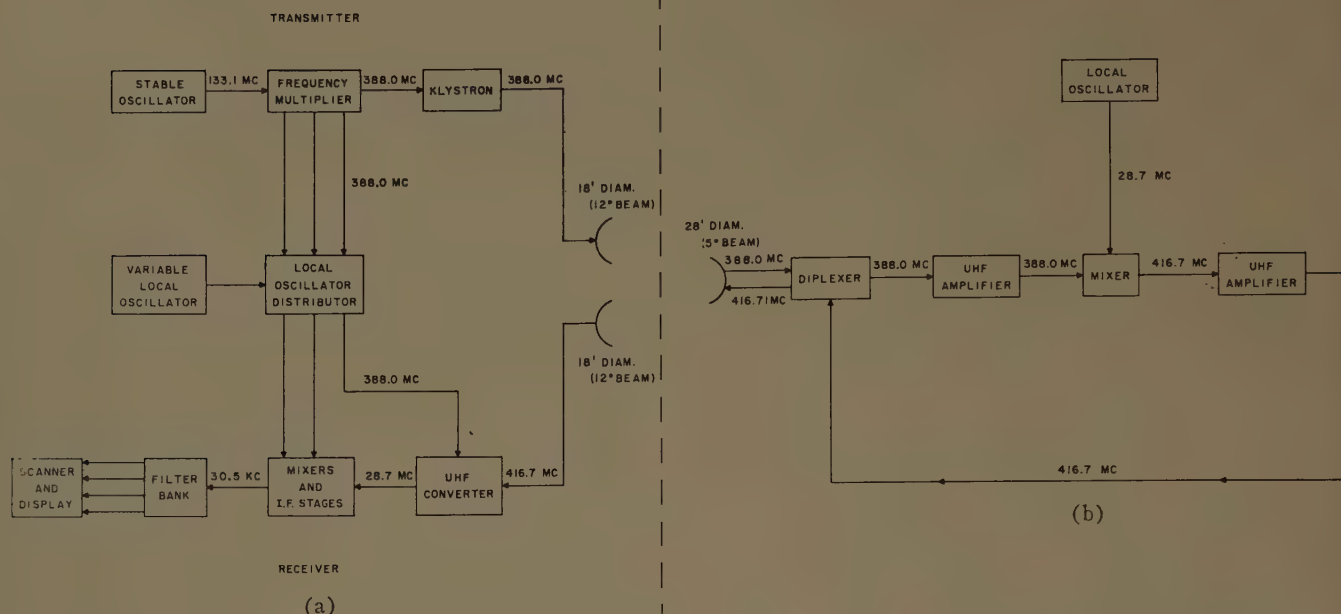


Fig. 4—System block diagram. (a) System at Alpine. (b) System at Round Hill.

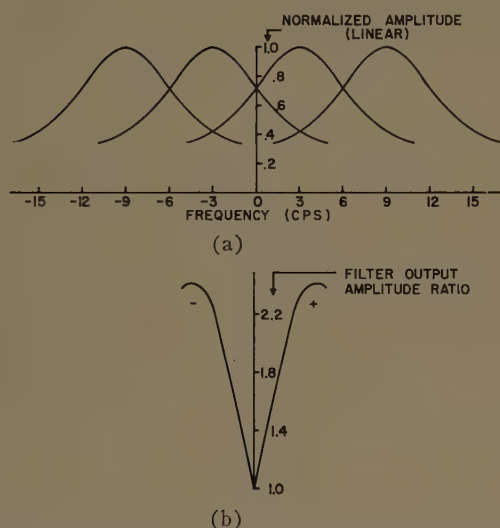


Fig. 5—Characteristics of filter bank. (a) Filter bank frequency response. (b) Frequency calibration curve.

the ratio would be different from unity. A plot of the filter output ratio as a function of applied frequency (monochromatic) is shown in Fig. 5(b) below the filter frequency characteristics of Fig. 5(a). The ratios are shown to be always greater than unity. Therefore, plus and minus signs have been arbitrarily assigned as shown to tell whether the measured frequency is to the right or the left of the center of the filter bank. This curve provides a calibration so that a study of successive filter outputs will provide information on the fluctuation of the received signal frequency with time. The successive filter outputs provide sufficient information to determine the amplitude as well as the frequency of the received signal.

In the experimental transmission between Alpine and Round Hill, the outputs of these filters were scanned

every half second, after integrating for $\frac{1}{8}$ of a second, and displayed on an oscilloscope. Alternate displays were photographed, thus providing data points spaced approximately one second apart. The filter output display appeared as shown in Fig. 6. Each group of four bars above the baseline represents one photograph of the output display of the four filters. These photographs were taken one second apart so that the horizontal axis is an intermittent time axis running from left to right. The height of the bars above the baseline shows the relative amplitude (on a linear scale) of the filter outputs, each bar representing the output of one of the four filters.

PATH LENGTH MEASUREMENTS

In order to measure path length variations, the Alpine transmitter was modified to permit frequency modulation with a linear ramp waveform as shown in Fig. 7. The carrier frequency was increased linearly from 388.0 Mc to 388.4 Mc in $\frac{1}{8}$ of a second. This pattern was repeated every half-second. The signal returned to Alpine from Round Hill would vary linearly from 416.7 Mc to 417.1 Mc, in the absence of perturbations caused by propagation conditions. If there is no path delay, the returned signal will appear as dashed line *A* and the difference frequency will be Δf (28.7 Mc). If there is a round-trip delay T , the return signal will appear as straight line *B* and the difference frequency ($\Delta f'$) will be less than the case of no delay (Δf) by an amount proportional to the path delay. Therefore, by measuring the amount of the change of frequency ($\Delta f - \Delta f'$), it is possible to determine the propagation path delay or the apparent path length, as smoothed by a $\frac{1}{8}$ -second integration time. By making a sequence of such measurements, it is possible to determine the apparent varia-

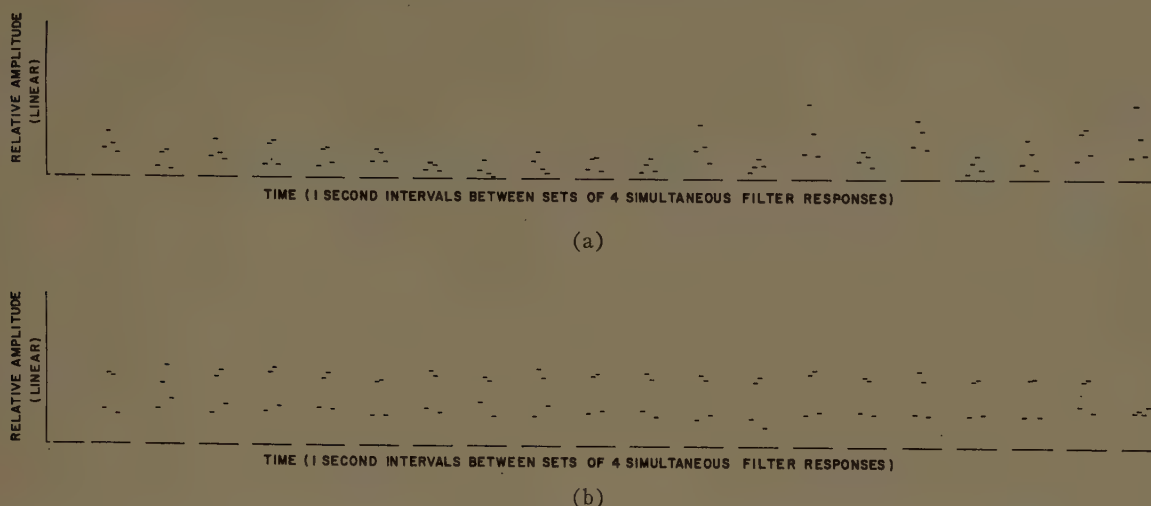


Fig. 6—Filter output display. (a) Typical tropospheric scatter conditions. (b) Enhanced conditions.

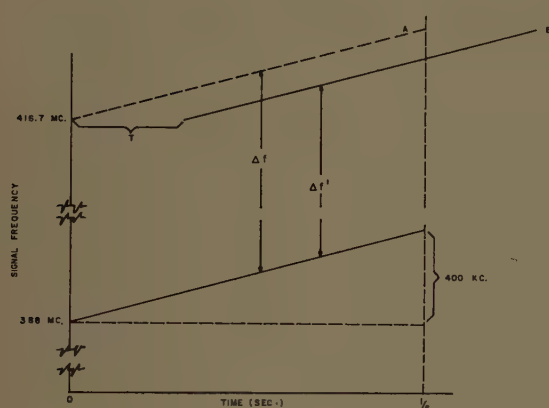


Fig. 7—Frequency modulation pattern.

tion of the propagation path length. Variations in the system oscillators and Doppler shifts acquired during the transmission will contribute to the measured frequency variation. These parameters are determined independently by the CW transmission measurements. The difference frequency corresponding to the Alpine-Round Hill round-trip path shifts the frequency of the signal returned to Alpine while modulating by about 4.2 kc from the frequency of the returned signal when transmitting CW. In order to keep the received signal centered in the filter bank during both modes of operation, the variable local oscillator referred to earlier is employed.

EXPERIMENTAL CONDITIONS

The experiment extended over the 24-hour period from about 10:20 A.M. on June 9 to about 9:40 A.M. on June 10, 1959. Data samples were recorded over a 20-minute interval every hour. The data consisted of photographs of filter output displays spaced one second apart. Each data sample consisted of 500 photographs (about ten minutes) taken during CW transmission followed by 500 photographs taken during modulated transmission.

The transmissions which occurred before about 9:30 P.M. of the first day appeared to be typical tropospheric scatter propagation with rapid amplitude fluctuations. After 9:30 P.M. on June 9, the amplitude fluctuations diminished greatly and the signal level increased by about 16 db, indicating enhanced propagation conditions. Although no meteorological measurements were available for locations precisely along the path between Alpine and Round Hill, there were available some refractive index data from soundings at Nantucket and Idlewild which lie along a line about 40 miles south of the Alpine-Round Hill path. The Nantucket soundings at 7:00 P.M. on June 9 and 7:00 A.M. on June 10 indicated refractive index profiles capable of superrefraction. These same conditions may also have extended to the Alpine-Round Hill path to account for the steady enhanced signals. The data collected during these enhanced conditions were used to determine the over-all frequency variability of the system equipment. The top row of Fig. 6 shows data taken during typical tropospheric scatter propagation at one-second intervals. The bottom row shows data taken during enhanced conditions, also at one-second intervals.

DATA REDUCTION AND ANALYSIS

The data were reduced from film to IBM punched cards and were later processed using an IBM 650 digital computer. Eight consecutive hourly data samples which were obtained under typical scatter conditions were processed in this manner. Two consecutive hourly data samples which were obtained under enhanced conditions were similarly processed. Fig. 8 shows a comparison between data obtained during typical tropospheric scatter conditions and data obtained during enhanced conditions for CW transmission. The modulated transmissions showed essentially the same characteristics. The curves in this figure illustrate the variations of the samples (each integrated for $\frac{1}{6}$ of a second) which were separated by a one-second sampling period and they are not intended to represent continuous functions. Figs.

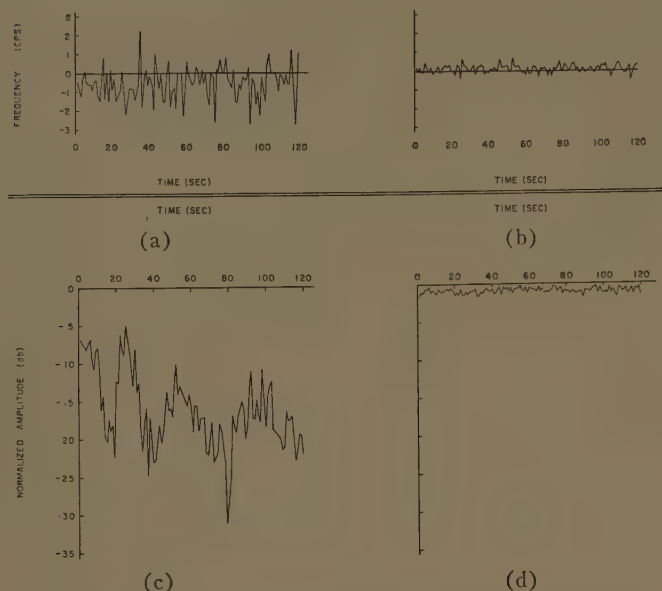


Fig. 8—Frequency and amplitude data. (a) Typical tropospheric scatter condition. (b) Enhanced propagation condition. (c) Typical tropospheric scatter condition. (d) Enhanced propagation condition.

8(a) and 8(b) show the fluctuation of the received signal frequency with time about a reference frequency at the center of the filter bank. Figs. 8(c) and 8(d) show the fluctuation of the received signal amplitude over the same period of time. The data in Figs. 8(a) and 8(c) were taken at about 11:30 A.M. on June 9 during typical tropospheric scatter conditions, while the data in Figs. 8(b) and 8(d) were taken at about 3:30 A.M. on June 10 during enhanced conditions. The signal levels differed by about 16 db in these two samples, which are each two minutes long. These figures illustrate that the frequency, as well as the amplitude, is considerably more stable during the enhanced propagation conditions.

Fig. 9 shows a density function of the frequency variation for each of two ten-minute CW data samples (the data in Fig. 8 were obtained from the same two data samples). Fig. 9(a) shows the typical tropospheric scatter condition while Fig. 9(b) shows the enhanced condition. The apparent frequency variation is approximately four times greater for the typical tropospheric scatter condition.

Fig. 10 shows the cumulative distribution functions for the same two ten-minute CW data samples. Fig. 10(a) shows the typical tropospheric scatter condition, while Fig. 10(b) shows the enhanced condition.

The standard deviation of the frequency fluctuation for each data sample is shown in Fig. 11. Fig. 11(a) shows the results for the CW transmissions while Fig. 11(b) shows the results for the modulated transmissions. Each point shows the results for one of the ten-minute data samples. These plots include the results of all the data samples which have been reduced. In each figure, the eight ten-minute data samples on the left were obtained during typical tropospheric scatter conditions, while the two data samples on the right were obtained during enhanced conditions.

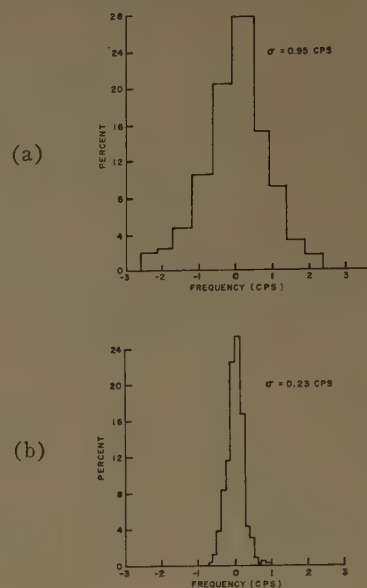


Fig. 9—Typical density functions. (a) Typical tropospheric scatter condition. (b) Enhanced propagation condition.

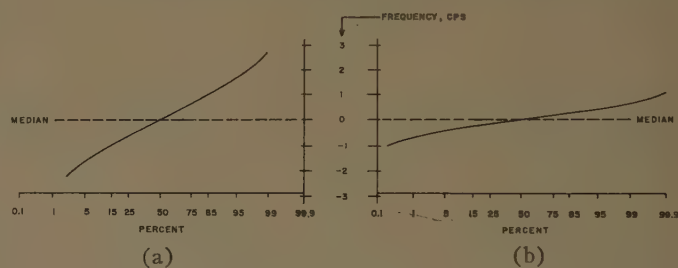


Fig. 10—Typical cumulative distribution functions. (a) Typical tropospheric scatter condition. (b) Enhanced propagation condition.

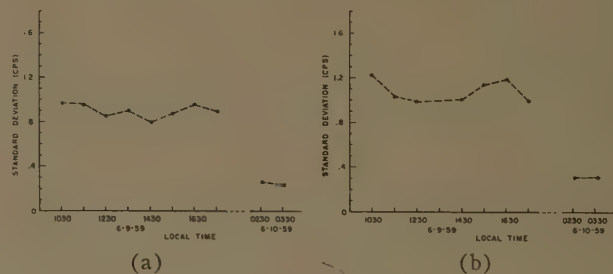


Fig. 11—Standard deviation of the frequency fluctuation. (a) CW transmission. (b) Modulated transmission.

RESULTS OF DATA ANALYSIS: FREQUENCY VARIATIONS

Fig. 11(a) shows that the standard deviation of the data obtained on the round-trip path for CW transmission during normal tropospheric conditions was about 0.9 cps. During enhanced conditions, the standard deviation was about 0.25 cps. It was assumed that the latter results could be used as a measure of the over-all frequency instability of the system equipment plus the errors in recording and reducing the data. If some atmospheric contribution to the frequency instability is present under this quasi-stable tropospheric propagation condition, then the system and data reduction contributions to the frequency are certainly less than indicated by this assumption.

If the atmospheric contribution to the total standard deviation, measured during normal tropospheric scatter conditions, was statistically independent of the system contribution and the data reduction contribution, and if the total of the latter contributions was the observed value during enhanced conditions, then

$$\sigma_t^2 = \sigma_a^2 + \sigma_s^2 + \sigma_d^2 = \sigma_a^2 + \sigma_m^2, \quad (1)$$

where

$\sigma_t = 0.9$ = the total measured standard deviation with CW transmission,

σ_a = the atmospheric contribution,

σ_s = the system contribution,

σ_d = the data reduction contribution,

$\sigma_m = 0.25$ = measured value during enhanced conditions.

Thus,

$\sigma_a = 0.87$ cps for the typical tropospheric scatter propagation conditions.

Thus we see that under these assumptions, the system contributions are small compared with the scatter propagation contributions to the observed frequency fluctuations.

The value, 0.9 cps, for the standard deviation of frequency was obtained over the two-way path. Since the two one-way transmissions were separated by 30 Mc, they can be considered statistically independent of each other. If atmospheric conditions were stable over the 2-msec interval required for the round-trip transmission, the total variance of the frequency fluctuation was twice the variance for each one-way transmission. Therefore, the standard deviation for each transmission was the total standard deviation divided by $\sqrt{2}$, or about 0.6 cps. This figure should be considered as an upper bound of the standard deviation of the frequency fluctuations due to the propagation mechanism, because any errors introduced by data reduction or by equipment instabilities can only have increased the observed standard deviation.

This value is of the same order of magnitude as the results reported by Crawford, Hogg, and Kummer³ based on measurements of envelope fading rates.

RESULTS OF DATA ANALYSIS: PATH LENGTH VARIATIONS

Fig. 11(b) shows that the standard deviation of the data obtained on the round-trip path for modulated transmission during normal tropospheric conditions was about 1.1 cps, which was somewhat greater than the value for the CW transmission. However, the standard deviation for modulated transmission during apparent superrefractive conditions was about 0.325 cps, which was also greater than the comparable CW case.

These measurements can be used to estimate the apparent path length variations. If equipment instabilities are the same for the modulated and the unmodulated signals and if the several sources of frequency variation

are independent, then, for the two-way path,

$$\begin{aligned} \sigma_t'^2 &= \sigma_a^2 + \sigma_s^2 + \sigma_d^2 + \sigma_p^2 \\ &= \sigma_t^2 + \sigma_p^2, \end{aligned} \quad (2)$$

where

$\sigma_t' = 1.1$ = the total standard deviation of frequency measured with modulated transmission,

σ_p = the standard deviation of frequency caused by the propagation path length variation,

$\sigma_t = 0.9$ = the total measured standard deviation with CW transmission.

Therefore,

$$\sigma_p = 0.63 \text{ cps.}$$

Since the slope of the linear modulation characteristic was

$$\frac{4 \times 10^5 \text{ cps}}{1/6 \text{ second}} = 2.4 \times 10^6 \text{ cps/second,}$$

and since the propagation time was 5.35×10^{-6} seconds per mile, the path length calibration of the system was 0.078 mile/cps. If each one-way transmission could be considered statistically independent of the other, then the standard deviation of the frequency for each transmission would be the total standard deviation divided by $\sqrt{2}$ (as for the CW case), or about 0.45 cps. Therefore, the standard deviation of the equivalent path length variation over a one-way transmission was (0.45 cps) \leftrightarrow (0.078 mile/cps) or 0.035 mile, which is about 55 meters.

CONCLUSIONS

These experiments indicate that for paths of lengths of about 100 miles between radio horizons and at a carrier frequency of about 400 Mc, the standard deviation of the frequency fluctuations induced by the propagation mechanism was approximately 0.6 cps when integrated for $\frac{1}{8}$ of a second in a 6-cps filter. This result, which was derived from data taken within a 24-hour period under typical tropospheric scatter conditions for part of the time and enhanced propagation conditions for part of the time, indicates that a frequency reference can be transmitted over this distance with an accuracy of approximately 0.15 parts in 10^8 . These results also indicate that further measurements over different path lengths, under all seasonal conditions and at widely different frequencies, would be desirable. These results further suggest that radar beacon range measurements utilizing tropospheric scatter propagation beyond the horizon may be made with a precision of a few hundred feet at over-the-horizon distances greater than 100 miles.

ACKNOWLEDGMENT

The authors wish to acknowledge the assistance given by J. Meyer of the Lincoln Laboratory in analyzing the meteorological data and by H. Hoover of the Round Hill Field Station in setting up the equipment at Round Hill.

Simultaneous Scintillation Observations on 1300-Mc and 3000-Mc Signals Received During the Solar Eclipse of October 2, 1959*

J. AARONS†, MEMBER, IRE, AND J. P. CASTELLI†, MEMBER, IRE

Summary—During the total solar eclipse of October 2, 1959, and during a 10-day control period bracketing this date, measurements were made of radio signals received at frequencies of 224 Mc, 1300 Mc, and 3000 Mc. These measurements indicated that point sources on the sun, rather than the total disk, were the constant-energy sources responsible for the scintillations of the received signals. This conclusion is in agreement with the work of Kazes and Steinberg. The fact that, during the period of totality, scintillations were observed at the two higher frequencies indicated that limb sources produced the scintillations.

Interferometric maps of the sun taken during this period showed plage areas at frequencies of 1420 Mc and 3300 Mc; however, at a frequency of 169 Mc, these maps showed only a relatively uniformly bright sun. In line with these findings, the recorded radio data did not show scintillations at the 224-Mc frequency but did show scintillations at the 1300-Mc and 3000-Mc frequencies.

During the control period, the scintillations at 1300 Mc were well correlated in detail with those at 3000 Mc. For this frequency range, it therefore appears that the scintillation oscillations are not frequency dependent. The two sets of data were taken at different antenna apertures. The 1300-Mc data were taken on an 84-foot parabolic antenna, whereas the 3000-Mc readings were made on an 8-foot parabolic antenna, 80 feet distant from the larger unit. Thus, it appears that, for this frequency range, the mechanism is not only independent of frequency but, within the experimental limits, is also not greatly affected by the size of the antenna.

The periods of the scintillations (30 seconds to 2 minutes) show that the shadow pattern is large in extent. Almost all scintillations took place when the sun was below 4° of altitude.

A hypothesis is advanced that the blob structure of the troposphere, possibly at the height of the tropopause, is formed into a curved lens. The focusing of the energy through this concave lens produces the scintillations observed.

INTRODUCTION

DURING the solar eclipse of October 2, 1959, measurements of many types were made at the USAF Cambridge Research Center's radio astronomy site at Hamilton, Massachusetts. The location of the site was close to the terminus of the totality region. The sun rose 80 per cent eclipsed. Ten minutes after sunrise, it was totally eclipsed at an elevation of about 1°.

The complexities of correcting for absorption, refraction, and scintillation in the solar data were quite evident when the information was examined. Refraction effects and antenna-pointing errors were considerably reduced by tracking the sun from sunrise on for a week prior to the eclipse and evolving a program of corrections. Absorption was taken into account by using measurements made on the days preceding the eclipse as a

normal curve and comparing the data taken on the eclipse day with this curve. The scintillation or amplitude fluctuations of the signal produced data which were the most difficult to analyze from the solar point of view, but these were, at the same time, the most interesting atmospheric data obtained. The low altitude at which the totality phase of the eclipse occurred produces a relatively large error in the estimation of the residual energy detected during second and third contact. However, the relative error decreases considerably above 5° of elevation. It has, therefore, been possible to obtain detailed data on the uncovering of point sources on the sun for higher elevation angles.¹

THE SUN DURING THIS PERIOD

Eclipse measurements made since 1947² established the fact that solar radiation in the spectral region between the 3-cm and meter wavelengths originated in the solar chromosphere and corona. The observations were used to establish the existence of point sources on the sun; calcium and hydrogen plage areas were usually found to be well correlated with the radio sources. Analysis of the data for limb brightening or darkening could be made during periods of low sunspot number when there was only a quiet sun to analyze. If plage areas extended beyond the limb of the sun, erroneous conclusions on limb brightening might be reached.

Today, by means of solar interferometers which are available at many frequencies, it is possible to obtain contour maps of the sun at frequencies ranging from 169 to 9300 Mc. Correlation of eclipse data and solar maps may perhaps add to the accuracy of the maps themselves, and will certainly insure the validity of claims for limb brightening and darkening and of point-source intensities.

Fig. 1 is such a map, supplied by Christiansen.³ It was taken at a frequency of 1420 Mc (21-cm wavelength) on October 2, 1959 at 0200 U.T. Another map of solar contours, shown in Fig. 2, was taken at a frequency of 3300 Mc (9.1 cm) on October 1, by Bracewell.⁴ Enhanced regions of radio energy may be seen on these maps.

Interferometric maps taken at 169 Mc during the

* Received by the PGAP, September 13, 1960; revised manuscript received, November 7, 1960.

† Radio Astronomy Section, Propagation Sciences Lab., Electronic Res. Div., AF Cambridge Res. Labs., Bedford, Mass.

¹ R. M. Straka and G. Swarup, "10 CM Total Solar Eclipse Observations," presented at the URSI Spring Conf., Washington, D. C.; May 2-5, 1960.

² B. M. Tchikhatchev, "Survey of Soviet observation of radio emission from the sun during solar eclipses," and the discussion of this paper by J. P. Hagen in "I.A.U. Symposium No. 4 on Radio Astronomy," Cambridge University Press, England; 1957.

³ W. N. Christiansen, personal communication; 1959.

⁴ R. N. Bracewell, personal communication; 1959.

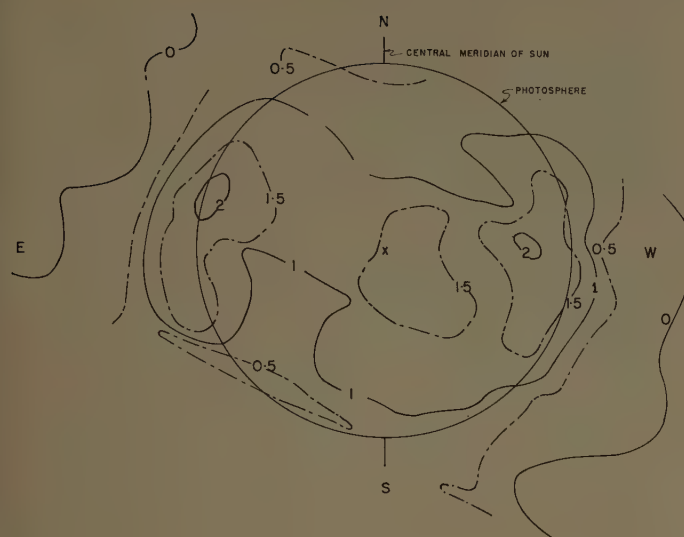


Fig. 1—Interferometric map of the sun at 1420 Mc on October 2, 1959 at 0200 U.T. Contour unit: 10^6 K. (Courtesy of W. N. Christiansen.)

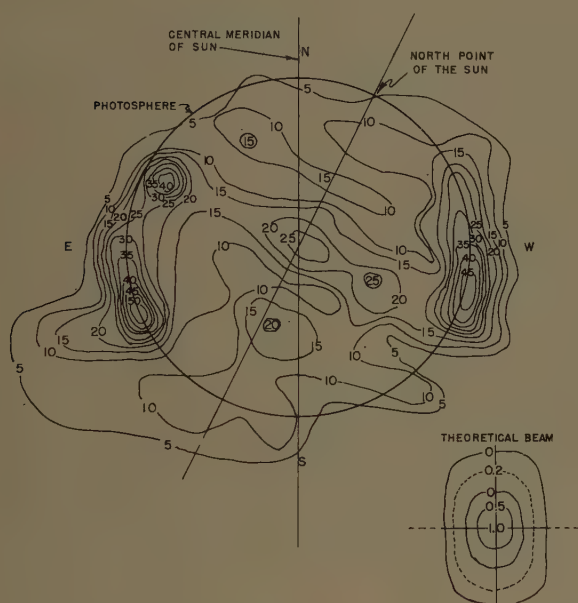


Fig. 2—Interferometric map of the sun at 3300 Mc on October 1, 1959 at 2015–2100 U.T. Contours are in units of $2.1 \times 10^{23} \times$ solar flux in watts/m²/(cps). (Courtesy of R. N. Bracewell.)

control period presented a somewhat different picture. The observatory at Nancay, France⁵ recorded no point sources beyond the disk of the sun at this frequency.

A graphical diagram of the eclipsing of the sun is shown in Fig. 3. At sunrise on the eclipse day at 10 hours 40 minutes U.T. (5 hours 40 minutes E.S.T.), only the west limb of the sun was above the horizon; the sun was 80 per cent eclipsed. Within the next few minutes, the total disk of the sun was above the horizon with only the east limb uneclipsed and, after totality, the west limb again began to appear.

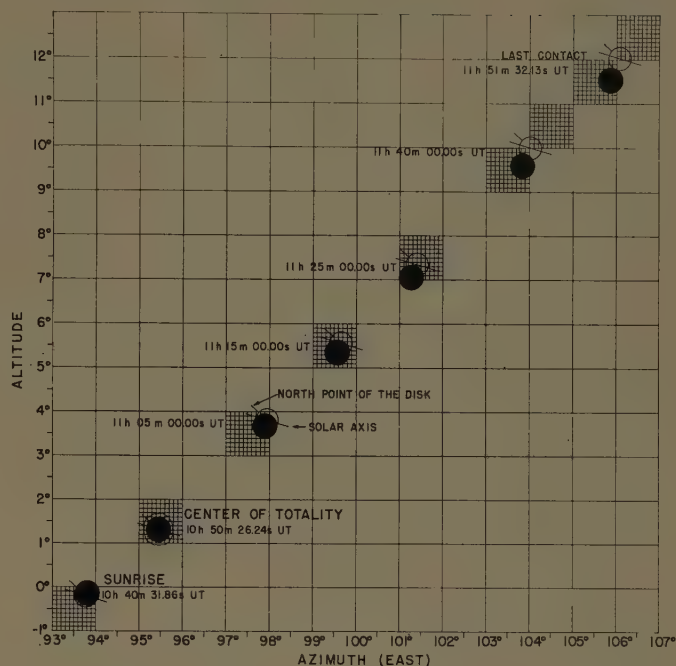


Fig. 3—Graphical diagram of the eclipsing of the sun. The darkened circle represents the moon. The other circle represents the sun with the solar axis oriented in such a way as to make more evident the eclipsing of the three point sources shown in Figs. 1 and 2.

OBSERVATIONS

The solar eclipse data were obtained with three radiometers. Two of these at 224 and 1300 Mc operated from a Jasik feed and an 84-foot equatorially-mounted parabola. The third operating at 3000 Mc from an 8-foot equatorially-mounted parabola was located 80 feet east of the larger antenna.

Throughout the entire control period, only the 1300-Mc and the 3000-Mc signals showed scintillations or amplitude fluctuations at sunrise. For the most part, these fluctuations occurred when the sun was below 4° of altitude. Above this altitude, only infrequent and low-amplitude scintillations were seen.

The mechanism advanced to explain the amplitude fluctuations is that point sources of energy which are constant during the time interval being considered exist on the sun for the 1300-Mc and 3000-Mc frequencies. Irregularities in the atmosphere change the plane wave coming from these sources to a wave front that is corrugated when it arrives at the antenna. These irregularities (or blobs) produce variations in the index of refraction which, in turn, produce an irregular wave front. The signal received at the antenna is characterized by peaks and nulls whose period is dependent on the relative motion of the atmospheric blobs past the antenna. This motion, of course, includes the apparent motion of the source across the atmosphere due to the earth's rotation.

Throughout the entire control period, scintillations were not seen on the 224-Mc records. Since interferometric maps indicate that at 224 Mc there were no distinct high-level sources on the sun during the eclipse and

⁵ J. F. Denisse and P. Simon, personal communication; 1959.

during the control period, the source diameter at this frequency could be considered to be the total diameter of the sun (45 minutes). Other point-source studies made by this group show that sources of this angular diameter do not produce scintillations.

On all days exclusive of the eclipse day, scintillations occurred from the time of sunrise until the sun reached an elevation of about 4° , a time interval of about 20 minutes. Generally, the scintillations were about one minute in duration at low angles, with fade depths of about 15 per cent to 20 per cent of the mean signal level. The amplitude decreased with elevation, but the period remained relatively constant during each sunrise.

Tracings of the recordings taken on the eclipse day are shown in Fig. 4. The large amplitude of the scintillations at 1300 Mc and 3000 Mc during the time between 0542 and 0550 can be noted almost immediately. During the 0542–0550 time period, the east limb was the only visible area. As soon as the west limb appeared at totality, the amplitude of the scintillations decreased. Thus, eclipsing the sources on the west limb and eclipsing the background sun produced a region of high intensity, narrow in angular diameter. This can be considered as a point source capable of producing large-amplitude scintillations similar to those seen when a source such as Cygnus A rises. The large hump or increase in signal at the beginning of the 224-Mc trace is not a scintillation, but is due to ground reflections and appears on all records.

On the control days, such as October 3, plage areas on both the east and west limbs of the sun were visible. Each of these sources produced its own shadow pattern. Since the two patterns of peaks and nulls do not necessarily add up in phase, a lower scintillation amplitude than that of a single source may result.

When these scintillations were studied, the first striking feature observed was the remarkable correlation in detail of the peaks and nulls at the two frequencies, 1300 Mc and 3000 Mc. The similarity can best be seen in Fig. 5. In Fig. 5(a) the two records for October 2 have been placed on the same time scale without regard for the amplitude of the individual signals. The scintillations are essentially independent of frequency. Fig. 5(b), which presents data taken on October 5, also illustrates the pattern observed on all control days, *i.e.*, the correlation in detail of the scintillations. Although the correlation is not perfect, it is remarkably good in view of the following conditions under which the data were taken. The apertures of the two antennas were quite different; the frequencies had a ratio of 2.3 to 1; and the two antennas were separated by 80 feet. This would seem to indicate that the diffractive effects of the atmospheric irregularities were negligible and the refractive effects were the main ones to be considered. If there were no diffraction, the shadow pattern on the ground would simply be a parallel projection of the pattern of irregularities, no matter what the frequency, and complete correlation between scintillations at different frequencies would exist.

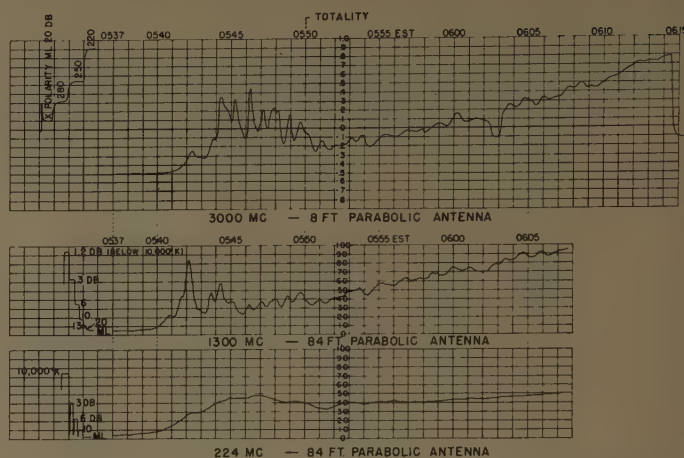


Fig. 4—Tracings of the recordings observed on the eclipse day. Very large amplitude scintillations may be seen on the 3000-Mc and 1300-Mc recordings during the time between 0542 and 0550 when the east limb of the sun was the only visible source.

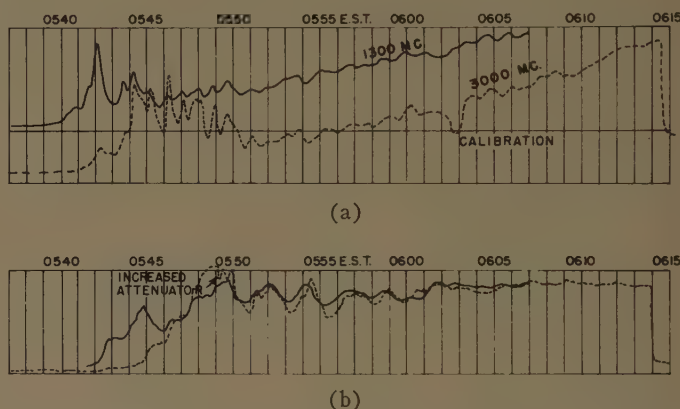


Fig. 5—Tracings of unreduced 1300-Mc records (solid line) and 3000-Mc records (dashed line) for October 2 and October 5, 1959. The two records have been placed on the same time scale without regard for the amplitudes of the individual signals. In general, the peaks and nulls are well correlated; a slight time displacement of the peaks and nulls may be seen in the data for October 5. Other records obtained during the control period show the same good correlation of peaks and nulls. (a) Data for October 2, 1959. (b) Data for October 5, 1959.

A study of the data, therefore, leads to the following conclusions: 1) rather large homogeneous areas in the sky, *i.e.*, the blobs, are responsible for the amplitude fluctuations; 2) the physical mechanism is not frequency sensitive; and 3) in the range from 8 feet to 84 feet, the amplitude of scintillation does not vary with aperture.

COMPARISONS OF THE 1300- AND 3000-Mc SCINTILLATIONS WITH OPTICAL TWINKLING

There is ample evidence that the scintillations of solar signals at 1300 and 3000 Mc are not tied basically to ionospheric parameters, but are more closely related to lower atmosphere winds and structure.

Other radio measurements now in progress by the authors and their collaborators include simultaneous studies at 224 Mc and 1300 Mc of the rise of Cygnus A

and subsequent tracking of this source. Fig. 6, taken at an elevation of 55° , illustrates the high-amplitude scintillations of the 224-Mc trace and the absence of amplitude fluctuations at 1300 Mc. It has been established by many groups⁶ and again in this program that the 224-Mc stellar fluctuations are related to ionospheric parameters.

Studies using the sun as the source made by Kazes and Steinberg⁷ and also by Aarons, *et al.*,⁸ and Castelli, *et al.*,⁹ have indicated that the fluctuations of the solar signals observed at short wavelengths were of tropospheric origin. Since the principal agency responsible for optical star scintillation is also located in the lower atmosphere, comparisons can be made between the short-wavelength scintillations studied here and the amplitude fluctuations recorded by optical telescope.

Some optical measurements using large-aperture telescopes have shown coherent fluctuations at two different wavelengths. Mikesell, *et al.*,¹⁰ using a split-beam photometer attached to the 40-inch reflector at the Naval Observatory in Washington D. C., recorded good correlation between fluctuations observed at two wavelengths, 800 Å apart. Others using smaller-aperture telescopes have observed incoherent fluctuations at two different wavelengths.

A rather clear picture of the dependence of scintillation amplitude upon telescope aperture was observed by Ellison and Seddon.¹¹ Using apertures as large as 100 inches, they found that the amplitude of fluctuation was inversely proportional to the aperture. Thus the large-aperture optical telescopes smooth out the scintillations at a given frequency.

On the other hand, sunrise experiments performed with the 84-foot radio telescope subsequent to the eclipse have shown the same percentage of scintillation amplitude at 1300 Mc and 3000 Mc. The solar-eclipse measurements made with the 84-foot and 8-foot radio telescopes indicated no aperture dependence. On the control days, the amplitude of scintillation referred to a mean amplitude was approximately the same in the case of the 8-foot antenna as in that of the 84-foot parabola. The ratio of antenna areas, however, was 110 to 1.

The periods recorded for optical scintillations are also quite different from those recorded at the radio wavelengths observed. Ellison and Seddon state that, at

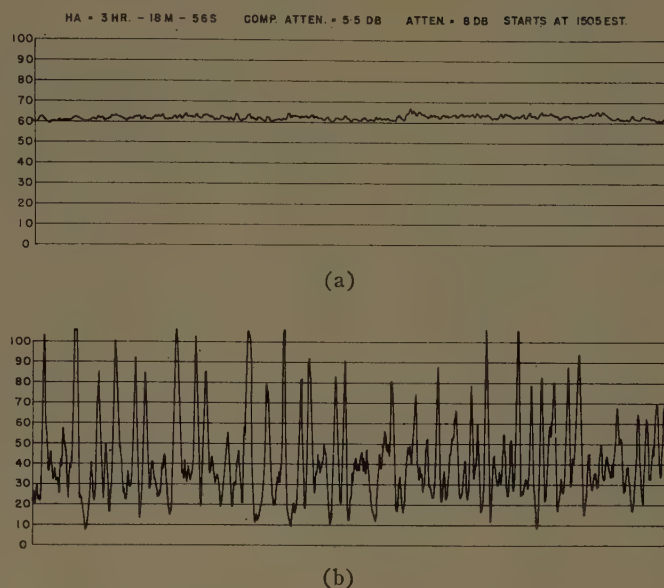


Fig. 6—Simultaneous studies at 224 Mc and 1300 Mc made of Cygnus A at an elevation angle of 55° on January 20, 1960. In this case, high-amplitude scintillations were observed on the 224-Mc measurements. (a) 1300 Mc. (b) 224 Mc.

altitudes below 10° , scintillations with a period of approximately 0.2 second predominate. Shorter scintillation periods are observed at higher altitudes. The periods of the scintillations observed at radio frequencies, however, ranged from 25 to 140 seconds.

DISCUSSION

If the lower atmosphere were homogeneous, a plane wave would be refracted under the rather simple conditions of Snell's law. The earth's curvature leads to only slightly greater mathematical complexity in handling the refraction. Simple refraction of the energy, however, would result in only a slow change in the amplitude of the signal received at the antenna.

The hypothesis advanced here is that, at low elevation angles, the individual blobs, rather than the gross atmosphere, act as lenses. The curvature of the earth focuses the energy refracted by the blob on the antenna. The earth's rotation and atmospheric winds combine to change the position of the blobs with respect to the sources and therefore with respect to the antenna, thus producing the peaks and nulls of the scintillation pattern. This simplified picture accounts for the low-angle prevalence of the scintillations and the lack of frequency dependence of the peaks and nulls.

In order to evaluate the effect of the earth's rotation on the relative position of the blobs with respect to the antenna, it was first assumed that the blobs were stationary and confined to a horizontal layer at the height of the tropopause. The source, and therefore the antenna which is following the source, would move past these blobs as the earth rotated. This motion would cause points in the tropopause in the line of sight to the sun to have a velocity with respect to the antenna which would vary with the elevation angle. The tangential

⁶ H. G. Booker, "The use of radio stars to study irregular refraction of radio waves in the ionosphere," *PROC. IRE*, vol. 46, pp. 298-314; January, 1958.

⁷ I. Kazes and J. L. Steinberg, "Etude de la scintillation du soleil observée avec plusieurs antennes sur la longueur d'onde de 3.2 cm," *Compt. rend. acad. sci. Paris*, vol. 245, pp. 782-785; August, 1957.

⁸ J. Aarons, W. R. Barron, and J. P. Castelli, "Radio astronomy measurements at VHF and microwaves," *PROC. IRE*, vol. 46, pp. 325-333; January, 1958.

⁹ J. P. Castelli, *et al.*, "Absorption refraction and scintillation measurements at 4700 Mc with a traveling-wave tube radiometer," *J. Planet. Space Sci.*, vol. 1, pp. 50-56; 1959.

¹⁰ A. H. Mikesell, A. A. Hoag, and J. S. Hall, "The scintillation of starlight," *J. Opt. Soc. Am.*, vol. 41, pp. 689-695; October, 1951.

¹¹ M. A. Ellison and H. Seddon, "Some experiments on the scintillation of stars and planets," *Monthly Notices Roy. Astron. Soc.*, vol. 112, pp. 73-87; 1952.

velocity of points in the tropopause (assumed to be at a height of 11 km) in line of sight to the sun was therefore computed in terms of the change in elevation angle of the sun with time at the Sagamore Hill site on October 2, 1959. The apparent velocity of such points past the stationary blobs was very high at low angles of elevation, ranging from 337 m/sec at 0° to 80 m/sec at 4° and 18 m/sec at 10° elevation. However, if other than a horizontal distribution of the blobs were to be assumed, the relative speed of the blobs past the antenna would be given by some other component of the tangential velocity. The particular component required would depend upon the type of distribution that had been assumed. If the blobs were also distributed in a vertical layer, the velocity component required would be that component perpendicular to the line of sight, and the velocities computed would be reduced by about one order of magnitude.

Since, for elevation angles of less than 5° , the wind in the tropopause moves much more slowly than the apparent velocity (at these angles) of a point in the tropopause in line of sight to the sun due to the earth's rotation, the latter would be the predominant motion of the atmospheric blobby pattern in the case being considered. The source sweeping across the relatively fixed blob structure in the atmosphere would be focused on the ground and would produce scintillations as its position with respect to the blobs changed.

From the point of view of the antenna, the scintillations can be considered to be time variations of the projection of a shadow pattern on the ground. The observations indicate that the extent of the shadow pattern is at least 80 feet, but a more extensive examination of this problem has been made by Kazes and Steinberg.^{12,7} Two radiometers at 3 cm were used. The cross-correlation function between the two records was calculated as the distance between the two antennas, measured in a direction perpendicular to the line of sight between each antenna and the sun, was varied. In measurements which were made at zenith distances varying between 80° and 85° , the cross-correlation coefficient fell to 0.5 when the perpendicular distance between the two antennas, *i.e.*, the distance between the two rays in space, was 125 meters. At 170 meters the correlation coefficient fell to $1/e$.

Keller, *et al.*,¹³ have obtained data showing that the shadow pattern at optical wavelengths may be regarded as moving horizontally with the velocity of the winds at the level of the turbulent layer of the atmosphere which produces the pattern. However, in the low-angle

case being discussed in the present paper, the earth's rotational velocity is predominant.

To obtain an order of magnitude picture of the physical mechanism involved, we use the simple relationship: rotational velocity \times scintillation period = size of blob in the atmosphere. If the median velocity for the low-angle studies is taken to be 165 m/sec, the value at 2° of elevation, and if the scintillation period is assumed to be 50 seconds, the size of the blob producing the shadow pattern is found to be 8.25 km. This size was calculated on the basis of one particular period, whereas the perpendicular distance obtained from the Kazes-Steinberg cross-correlation curve resulted from the average of a random sample of periods obtained for zenith distances varying from 80° – 85° . The two figures are not directly comparable. We must either know the shape of the cross-correlation curve after it crosses the abscissa (this was not obtained in the cited works) or find the autocorrelation function for one complete period of the 50-second-long sine wave used in our equation and then find the distance represented by the same portion of the autocorrelation function that was used in the cross-correlation function. The latter procedure is roughly equivalent to dividing the 8.25-km distance obtained in our equation by 6. The inhomogeneity size in the atmosphere from this point of view is somewhat over 1.4 km, as compared to a value of 170 meters obtained by Kazes and Steinberg⁷ as the distance between the rays from their two antennas. There are several possible explanations of this disparity. One already mentioned is that the blobs are distributed differently than was assumed; this could lead to an inhomogeneity size of an order of magnitude smaller than that obtained. Another is that the focusing action of the curved blobs at low angles produces on the ground a somewhat fuzzy image of the source. Still another is that the inhomogeneities are located somewhat lower in the atmosphere than the tropopause; a point at this lower altitude would have tangential velocities lower than those found for the 11-km point, and the corresponding blob size would, therefore, be smaller.

Optical-scintillation data utilize representative values of wind velocity of 10 to 25 m/sec¹³ and indicate the altitude of the tropopause as the region responsible for optical scintillation. In the studies reported in this paper, both the size of the blob and the velocities must differ from the optical case.

The work of Kazes and Steinberg and the small displacements in time between the scintillations recorded with the two antennas separated by 80 feet show that, in addition to the apparent rotational velocity of the atmosphere as observed from the earth, there is a wind pattern moving the blob structure through the atmosphere.

The difference between optical and radio scintillation may well be due to the influence of water-vapor pressure on the index of refraction for short radio wave-

¹² I. Kazes, "Contribution a l'etude de l'atmosphere terrestre par l'observation du rayonnement solaire centimetrique," Doctor of Sciences dissertation, University of Paris, France; 1957.

¹³ G. Keller, W. M. Protheroe, P. E. Barnhart, and J. Galli, "Investigation of Stellar Scintillation and the Behavior of Telescopic Images," Ohio State University Res. Foundation, Columbus, and AFRC, Bedford, Mass., Final Rept. on Contract AF10(604)-1409; 1956.

lengths. The dielectric constant and therefore the index of refraction differs in the case of optical wavelengths from that obtained with short radio waves; the partial pressure of water vapor comes into the equation for radio wavelengths.¹⁴

CONCLUSIONS

When the signals received at three different frequencies (224 Mc, 1300 Mc, and 3000 Mc) during the solar eclipse of October 2, 1959 and during a control period were compared with the interferometric maps, it was apparent that scintillations of the signal were recorded for those frequencies for which point sources of energy existed on the sun. The relative motion of the atmospheric irregularities (blobs) past the antenna causes the scintillations of the signal.

During the time before totality on the eclipse day, only one point source, the east limb of the sun, was visible at a very low angle; the west-limb source and the larger part of the solar disk were eclipsed. The resultant low-angle single region of high intensity, narrow in angular diameter, produced scintillations of extremely high amplitude.

¹⁴ E. Vassy, "Physique de L'Atmosphere," Gauthier-Villars, Paris, France, vol. 2, p. 101; 1959.

Throughout the period studied, scintillations at the 1300-Mc and 3000-Mc frequencies were remarkably well correlated in detail. The conclusions drawn were: for this frequency range, the scintillation oscillations are not frequency dependent and are not, at least up to the 84-foot aperture used in this experiment, affected by the size of the antenna.

The periods of the scintillations ranged from 25 seconds to 140 seconds, and large scintillations were received mainly when observations were being made below 4° of altitude. The shadow pattern is therefore large in extent. The analysis and data from other scientific programs indicate an atmosphere blob size of 1.4 km with a ground pattern of 170 meters.

ACKNOWLEDGMENT

The authors would like to thank the following members of the Radio Astronomy Section for assistance in taking the data and performing calculations: W. Kidd, C. Ferioli, R. Straka, W. Barron, and H. Silverman. Mrs. H. Cohen of Wentworth Institute, Boston, Mass., assisted greatly in the data analysis. Professor W. M. Protheroe of the University of Pennsylvania, Philadelphia, was of great help in showing some of his optical scintillation analysis in progress and in making several suggestions.

Studies of Meteor Propagation at 49 and 74 Mc*

J. B. BERRY, JR.†, MEMBER, IRE, J. C. JAMES‡, MEMBER, IRE,
AND M. L. MEEKS†

Summary—The characteristics of meteor propagation were investigated over two nearly parallel paths from Walpole, Mass., to Congaree, S. C. (1250 km) and from Walpole, Mass., to Smyrna, Ga. (1480 km). Simultaneous measurements were made at 49 Mc and 74 Mc. The duty cycle for meteor propagation was measured at both frequencies with separate determination of the contributions from underdense trails, specular overdense trails, and nonspecular trails. As a function of signal amplitude A , the data could be fitted by assuming the duty cycle to be proportional to A^{-k} , where k lies between 0.9 and 1.8 depending on the time of day and types of trail contributing. Roughly half of the duty cycle came from nonspecular overdense trails and only 10 to 20 per cent from underdense trails. Simultaneous measurements with two separate receiving systems

were made at both 49 Mc and 74 Mc in order to determine the effects of antenna height-difference and various lateral antenna-separations. The meteor signals were strongly decorrelated by certain antenna height-differences. Overdense trails produced some decorrelation with lateral antenna-separation, but underdense trails gave well-correlated echoes. No significant differences in meteor echo rate were found between receiving systems in very flat terrain at Congaree, S. C., and hilly terrain at Smyrna, Ga. For the hilly terrain, best signal correlation was found for nearby antennas which were at the same height above sea level.

I. INTRODUCTION

THE scattering of VHF radio signals from meteor trails offers an intermittent mode of propagation which may be used for communication purposes. The operation of meteor communication systems has been described in detail by Canadian workers¹ and by

* Received by the PGAP, October 6, 1960; revised manuscript received, December 19, 1960. This work was supported principally by the Air Force Cambridge Res. Center under Contract No. AF 19(604)-5187, and by the Office of Naval Res. under Contract No. Nonr 991(02). A portion of this work is contained in a thesis submitted by J. B. Berry to the Graduate School, Georgia Inst. Tech., in partial fulfillment of the requirements for the M.S. degree, June, 1960.

† Engrg. Experiment Station, Georgia Inst. of Tech., Atlanta, Ga.
‡ M.I.T. Lincoln Lab., Lexington, Mass. Formerly with Engrg. Experiment Station, Georgia Inst. Tech., Atlanta, Ga.

¹ P. A. Forsyth, E. L. Vogan, D. R. Hansen, and C. O. Hines, "The principles of JANET—a meteor burst communication system," *PROC. IRE*, vol. 45, pp. 1642-1657; December, 1957.

workers² at Stanford Research Institute. Briefly, such systems consist of a transmitter-receiver pair located at each end of a communication path. The flow of information over the path begins when signals exceed some specified threshold on both of the parallel channels. The information flow continues until the signals over one or both of the parallel channels drop below another specified threshold. Thus, information is only transmitted when a closed loop is obtained. The information capacity of a burst communication system then will be directly proportional to the bandwidth of the information channel and the fraction of time that *both* channels satisfy the threshold requirements. Therefore, it is important to know the fraction of time that the meteor signal exists above a given threshold, and the correlation between meteor signals obtained on two parallel paths. There are, furthermore, other considerations in the design of a burst communication system: the choice of frequencies, the influence of terrain and antenna height on system performance, and the variations in meteor echo rates with local time.

The studies reported here have been directed toward a better understanding of some of these problems.

II. DESCRIPTION OF THE EXPERIMENTAL EQUIPMENT AND RELATED MATTERS

The experimental studies which are described in this paper were conducted over two transmission paths. These paths had a common origin at the transmitting site at Walpole, Mass., and they terminated respectively at Congaree, S. C., and at Smyrna, Ga. Transmitters at 49.44 Mc and at 73.82 Mc were maintained and operated by Pickard and Burns, Inc. The transmitting antennas were both five-element Yagis, mounted at 2.82 wavelengths above the ground. With these antenna heights, the centers of the first lobes (assuming perfect reflection from a plane earth) intersected a point at 100 km above the midpoint of the great-circle path from Walpole to Smyrna. These transmitting-antenna orientations were maintained throughout all the experiments performed over both the Smyrna and the Congaree paths. Table I gives a summary of the characteristics of these two paths. The fact that the transmitting antennas were directed toward Smyrna rather than Congaree introduces a small asymmetry, but the difference in bearing of the two receiving sites amounts to only 7° as compared to the half-power beamwidth in azimuth which was 65°.

The terrain in which the antennas were situated is exceptionally flat at Congaree, S. C., on the Atlantic coastal plain. At Walpole, Mass., the terrain is generally flat, although a group of buildings lay in the foreground 0.6 km in front of the antennas. At the Smyrna, Ga.,

site, the terrain is hilly. The maximum height variation of the terrain in the first 49-Mc Fresnel zone of the antennas was determined from contour maps. These variations are as follows: Walpole, 20 feet (excluding building); Congaree, 5 feet; Smyrna, 250 feet.

Two completely separate receiving systems were operated at each of the two frequencies, 49 Mc and 74 Mc. Each receiving system consisted of a five-element Yagi antenna feeding a VHF converter, which in turn gave a 5-Mc input to the receiver. The converters were designed by the Bureau of Standards with cascode input circuits and special negative feedback features to give long-term stability. The receivers are of standard design, and in most of the important measurements their AVC voltages were fed to an Edin six-channel paper recorder. The predetection bandwidth was 3 kc. The equivalent time constant of the Edin recorder was measured and found to be 0.02 second. The chart speed was usually 1 mm/sec, except for 20-minute periods starting at 0600 and 1800 when the speed was increased to 10 mm/sec.

The individual receiving systems were calibrated every four hours by means of a signal generator. In addition, at intervals of one hour a 50-ohm terminating resistor was connected across the input terminals of each of the VHF converters as a means of monitoring drift of the dc amplifiers in the Edin recorder and of checking the performance of the receiving system in general.

TABLE I
CHARACTERISTICS OF THE METEOR-SCATTER PATHS

	Walpole-Smyrna	Walpole-Congaree
Frequency	49.44 Mc 73.82 Mc	49.44 Mc 73.82 Mc
Transmitter Power Output	5 kw on 49.44 Mc 3 kw on 73.82 Mc	5 kw on 49.44 Mc 3 kw on 73.82 Mc
Transmitter Type (49 Mc)	Collins 205G-1	Collins 205G-1
Transmitter Type (74 Mc)	RCA BTF-3B (Modified)	RCA BTF-3B (Modified)
Station Separation	1480 km	1250 km
Path Bearing at Midpoint	51.5° (E of N)	44.1° (E of N)
Path Latitude at Midpoint	38.2° N	38.0° N
Antennas	Five-Element Yagis	Five-Element Yagis
Antenna Beamwidths in Azimuth	65°	65°
Antenna Beamwidths in Elevation	55°	55°
Receiver Types (49 Mc)	Hammarlund Super-Pro SP-200	Hammarlund SP-600-JX
Receiver Types (74 Mc)	Hammarlund Super-Pro BC-778	Hammarlund SP-600-JX

² W. R. Vincent, R. T. Wolfram, B. M. Siffert, W. E. Jaye, and A. M. Peterson, "A meteor-burst system for extended range VHF communication," *PROC. IRE*, vol. 45, pp. 1693-1707; December, 1957.

Throughout most of the experimental studies, the outputs of the four receiving systems were recorded simultaneously on the Edin six-channel recorder. The two remaining channels were used to record the instantaneous differences between the two pairs of receiving systems at each frequency. This system of receivers operated at Congaree, S. C., in all of the experimental studies except those described in Section VI.

The signal at Smyrna, Ga., was recorded on a Meteor-Signal Analyzer (UF/MSA-1) which was designed and constructed at the University of Florida. This equipment was intended to record automatically the number of meteor bursts at two signal levels and the total duration of meteor bursts at four different signal levels. These six quantities were stored internally on capacitors, and the totals could be read out periodically, usually after periods of one hour. Unfortunately, difficulties were experienced in getting this equipment to operate reliably and the data which it provided were comparatively small.

III. SIGNAL CHARACTERISTICS

When recordings of the signals observed at 49 Mc and 74 Mc were compared, two qualitative differences were immediately apparent. First, an ionospheric scatter signal was present throughout almost all of the observations at 49 Mc. This background signal was, of course, stronger during the daylight hours, particularly around noon. In contrast, the observations at 74 Mc failed to show any ionospheric-scatter signals, and the background was dominated by cosmic noise. The second obvious difference was in the appearance of the meteor echoes. At 74 Mc the meteor echoes stood out sharply against the relatively steady background of cosmic noise, while at 49 Mc the echoes had noticeably longer duration but were not so easily distinguishable in the presence of the fluctuating ionospheric-scatter component.

The theory of the scattering of radio waves by meteor trails has been worked out in detail,³⁻⁵ and a strong wavelength dependence is to be expected both for the peak power and for the duration of the echo signal. It is customary to classify meteor trails in the three categories which are described in Table II. Echoes from specular overdense trails give peak echo powers which are proportional to λ^3 , provided that the antenna gains and transmitter powers are held constant. Nonspecular overdense trails give echoes that very roughly follow this relationship. However, the peak echo power from

nonspecular overdense trails is not so well defined, and throughout their lifetime, these echoes are subject to rapid fading which depends on wavelength.

According to the theory, echoes from underdense trails should decay more rapidly for shorter wavelengths, and the decay constant should be proportional to λ^2 . This increasingly rapid decay at shorter wavelengths produces an additional effect. As the wavelength decreases, the peak echo power will decrease more rapidly than λ^3 because the diffusion process which causes the exponential decay will be at work even before the echo maximum is reached. Computations by Loewenthal⁵ show that this additional reduction in echo power for underdense trails, in the present case, should range from about 1.8 to 3.4 db depending on the rate of diffusion, which is in turn a function of trail height.

Echo signals from the same meteor at 49 Mc and 74 Mc were compared to investigate the agreement between our experimental data for the Walpole-Congaree path and the theoretical predictions. The ratio of the peak received power at both frequencies was measured for echoes from 327 underdense meteor trails. The distribution of these ratios, expressed in db, is shown in Fig. 1. The antenna heights at Walpole and Congaree were exactly scaled for the two wavelengths, but the very wide spread of the ratios in Fig. 1 evidently indi-

TABLE II
CLASSIFICATION OF METEOR TRAILS

Category	Description of Echo Signal
Underdense	Rapid rise to a sharp peak followed by roughly exponential decay. Short duration.
Specular Overdense	Rapid rise to a rounded peak, usually followed by rapid fading. Long duration.
Nonspecular Overdense	Comparatively slow rise with rapid fading. Long duration.

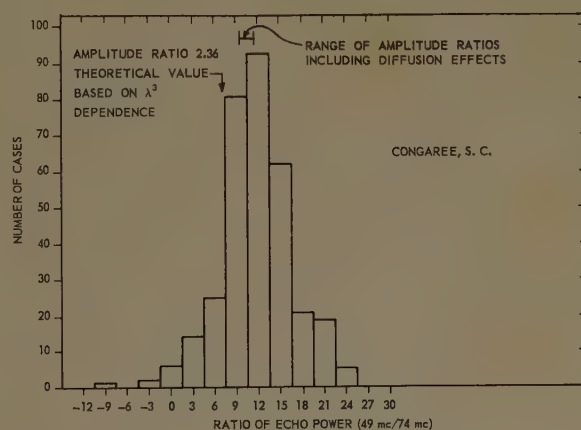


Fig. 1—Distribution of echo amplitude ratios for simultaneous echoes from decay-type meteor trails. The ratios of maximum echo power (49 Mc:74 Mc) are expressed in db. Predicted values for this ratio are shown based on λ^3 -dependence with and without diffusion effects.

³ T. R. Kaiser, "Radio echo studies of meteor ionization," *Phil. Mag. Suppl.*, vol. 2, pp. 495-544; October, 1953.

⁴ V. R. Eshleman and L. A. Manning, "Radio communication by scattering from meteoric ionization," *Proc. IRE*, vol. 42, pp. 530-536; March, 1954.

⁵ M. Loewenthal, "On meteor echoes from underdense trails at with very high frequencies," M.I.T. Lincoln Lab., Lexington, Mass., Tech. Rept. No. 132; December, 1956.

cates that the relative antenna gains varied widely in this group of meteor echoes. The amplitude ratio to be expected on the basis of the λ^3 -dependence is indicated in Fig. 1 by an arrow. The effect of trail diffusion on the peak echo-power further displaces the expected ratio to the range shown on this figure. It may be seen that the most frequently observed value of the echo ratio is in agreement with this theoretical prediction, and that the distribution is roughly symmetrical about this range of values. So it appears that the antenna gains which were encountered most frequently by the meteors in this sample were roughly equal, but over parts of the illuminated region, the gains at these two wavelengths varied widely. Such variations can be explained perhaps by irregularities in the antenna foregrounds, particularly at Walpole.

For communication problems, there is a particularly important quantity associated with the meteoric mode of propagation. This is the so-called duty cycle, which is the fraction of time that the meteoric signals remain above a specified amplitude. This specified amplitude may be thought of as the decision level at which information flow starts in a meteor communication system. It is important for communication purposes to know how the duty cycle depends on decision level and radio frequency, how it varies with time, and what fraction of the duty cycle comes from each of the three meteor categories in Table II. Unfortunately, the duty cycle is not an easy quantity to measure in practice, and so measurements were restricted to periods around 0600 and 1800 EST which coincide roughly with the daily maximum and minimum meteor echo rates, respectively. In order to obtain data suitable for duty cycle measurements we increased the chart speed on the Edin recorder from 1 mm/sec to 10 mm/sec for periods of about 20 minutes around 0600 and 1800. Whenever the echo strengths permitted, the duty cycle was measured at five different levels, and separate measurements were made for echoes in the following categories: 1) specular underdense meteors only, 2) specular underdense and specular overdense only, and 3) all meteors. Fig. 2 (opposite) shows the results of these measurements. The duty cycle D expressed in per cent is plotted against the decision level A in this figure. Logarithmic scales are used for the variables so that distributions of the form $D(A) = (\text{const.})A^{-k}$ will give points falling along a straight line. The various sets of points in Fig. 2 appear to be well described by a distribution of this form. The exponent $-k$ in this type of distribution is equal to the slope of the straight line. Corresponding values of this exponent are given in brackets for each of the straight lines that have been drawn to represent the measured points. Fig. 2(a) and (b) was derived from data taken simultaneously on two separate receiving systems at the same frequency, 49 Mc, with antennas at the same height above ground. The extent of agreement between these two figures gives an indication of the precision of

the measuring procedure. Fig. 2(c) and (d) shows the behavior of the duty cycle from simultaneous records of two receiving systems operating at 74 Mc. The 74-Mc receiving antennas, however, were at different heights, 3.2λ and 1.6λ , as indicated. The 49-Mc data and the 74-Mc data which were used in Fig. 2(a)–(d) were obtained during exactly the same period of time, 0602–0625 EST on April 4, 1958, Fig. 2(e)–(h) is based on data taken on the same day during the period from 1800 to 1822. In this case the receiving antenna heights were 3.2λ and 1.6λ for each frequency. The decorrelation in the signals observed on the same frequency with such different receiving antenna heights makes the records almost independent insofar as the duty cycle measurements are concerned. (A detailed discussion of the decorrelation produced by differences in antenna height is given in Section IV.) The data at 74 Mc have been adjusted in these figures to compensate for the difference in transmitter power. Hence, the duty cycles may be compared directly to examine the effect of frequency on two scaled systems, as if each had a transmitted power of 5 kw.

The extent to which underdense trails contribute to the duty cycle is quite small. The contributions of each trail category in Fig. 2 can be seen in Table III. The fraction of the duty cycle coming from each of the three trail categories (nonspecular overdense, specular overdense and specular underdense) is nearly the same for both frequencies, provided that a distinction is made between relatively high and low decision levels. For high decision levels, the contribution from underdense trails is about twice as great as for low decision levels. Around 1800, as compared to 0600, there is a significantly greater contribution from both nonspecular overdense trails and specular underdense trails. This behavior is to be expected since the meteors in the late afternoon have lower velocities and penetrate deeper into the atmosphere.

TABLE III

THE RELATIVE CONTRIBUTIONS OF VARIOUS METEOR CATEGORIES TO THE DUTY CYCLE

(High and low decision levels are shown separately for the morning and evening observations.)

Decision Level	Period			
	0602–0625 EST		1800–1822 EST	
	Low	High	Low	High
49 Mc				
A (in volts)	0.25	4.00	0.0625	1.0
D (in per cent)	40.0	0.9	7.0	0.8
74 Mc				
A (in volts)	0.1	0.75	0.1	
D (in per cent)	10.0	0.8	2.6	
Composition of D (in per cent)				
Nonspecular Overdense	40	43	65	66*
Specular Overdense	52	41	21	10*
Specular Underdense	8	16	14	24*

* Based on 49-Mc data only.

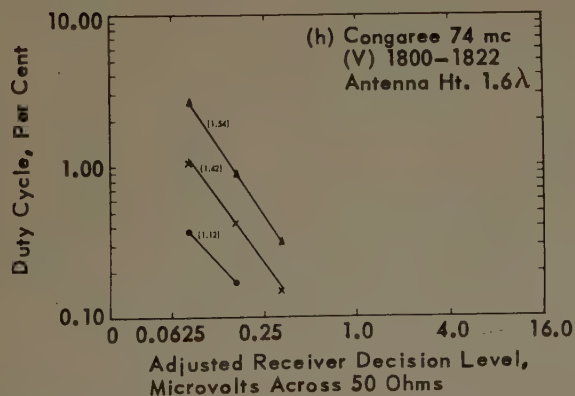
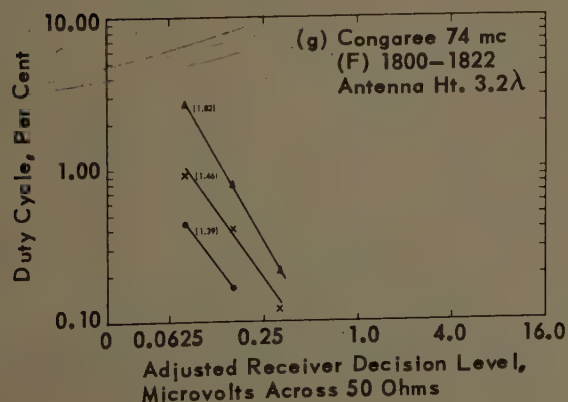
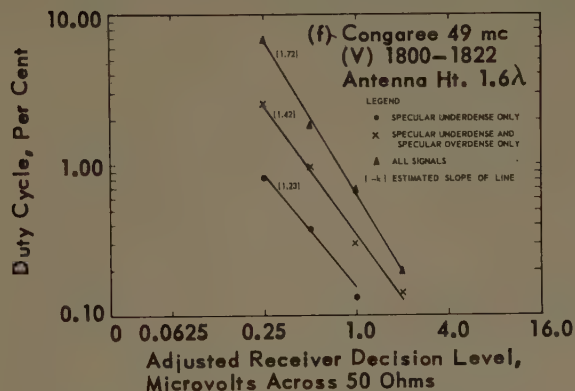
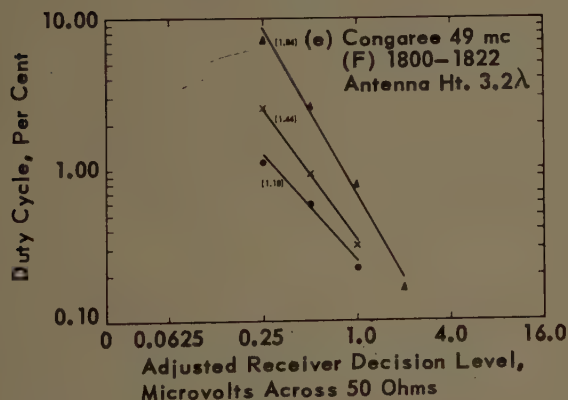
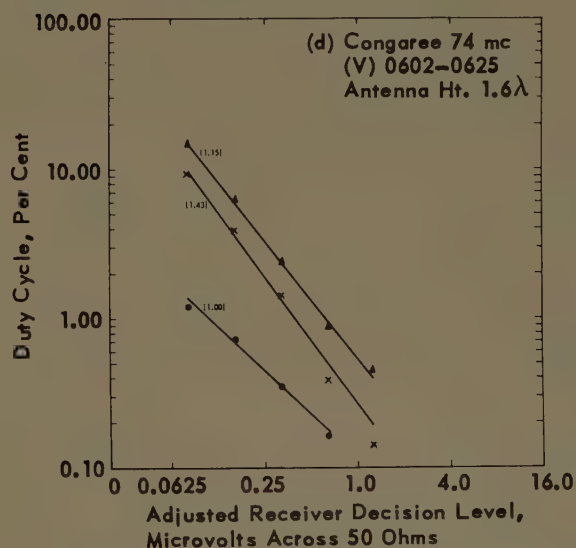
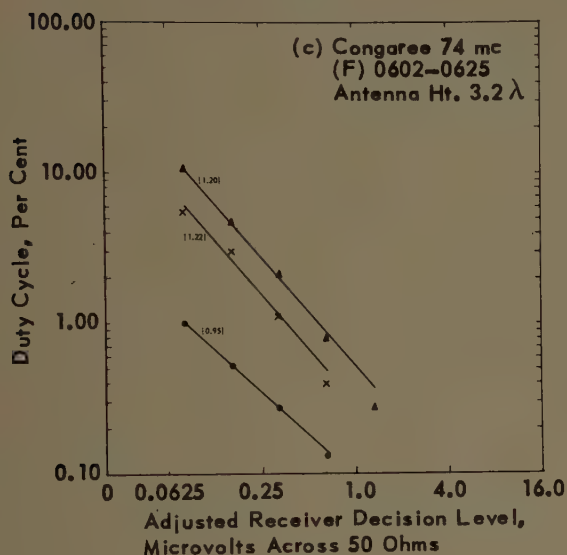
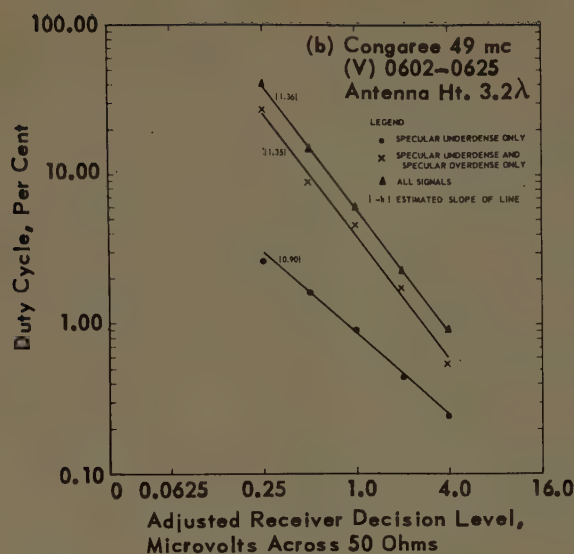
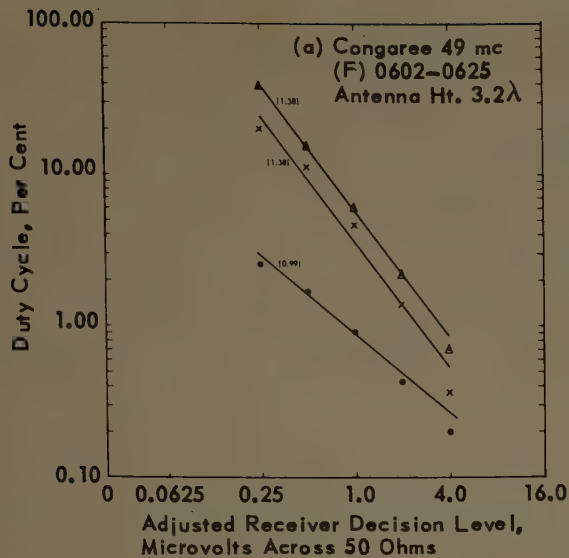


Fig. 2—Observed dependence of duty cycle on receiver decision level. Duty cycle has been determined separately for specular underdense trails, for combined specular underdense and overdense trails, and for all meteor signals combined. (a) through (d) represent early morning observations (0602-0625 EST), (a) and (b) at 49 Mc and (c) and (d) at 74 Mc. (e) through (h) represent late afternoon observations (1800-1822 EST), (e) and (f) at 49 Mc and (g) and (h) at 74 Mc.

IV. VARIABLE ANTENNA-HEIGHT STUDIES

The influence of antenna height above ground on the meteor-signal rate was investigated in a series of tests at the level-terrain site near Congaree, S. C. The experimental procedure in the variable antenna-height studies involved the use of two complete receiving systems on each of the two frequencies. One antenna on each frequency was maintained at a fixed height throughout the study; both of the fixed heights were 3.2 wavelengths above the ground. The other antennas at each frequency were operated at various heights above the ground, and the signals obtained from these four channels were recorded continuously on the multi-channel Edin recorder. The instantaneous differences between the signals from the fixed and variable-height antennas on each frequency were also plotted on the Edin recorder. A telescoping antenna tower was used throughout the study to support one of the antennas so that the height could easily be varied. A continuous range of heights from 22 feet to 92 feet could be obtained with this tower. The other variable-height antenna was mounted on a tower whose height could be varied only by removing or adding 10-foot sections. The difficulties associated with raising or lowering this tower were such that no attempts were made to change the height except during the periods when the transmitter was shut down.

Throughout the period of this study, which extended from February 27, 1958, to May 3, 1958, the transmitter was operated continuously for one 48-hour period each week beginning at noon, Thursday. The transmissions were interrupted for five minutes each hour for identification purposes.

In addition to the usual calibration procedures described in Section I, a special procedure was used with the telescoping antenna tower to insure that the fixed and variable height channels were calibrated with respect to each other. This was accomplished by setting the antenna on the telescoping tower at the same height as the corresponding fixed antenna for about 20 minutes every four hours.

Data taken during the calibration periods show a high degree of correlation between the two channels at the same frequency. As the variable-height antenna was moved slowly from the calibration position, an increasing decorrelation could be observed between these two channels. The extent of the decorrelation in signal power with a change in antenna height is shown in Fig. 3. The distribution of peak-power ratios for 92 meteor echoes observed simultaneously on 49 Mc with equal antenna heights is shown in Fig. 3(a). Very strong correlation is observed in this case. Fig. 3(b) shows the power ratio distribution obtained from 82 meteor echoes observed with the variable-height antenna at 42 feet (2.1λ) and the fixed-height antenna at 64 feet (3.2λ). Here, the ratios show a wide range of values, indicating that the patterns of the two antennas de-

pend on height above ground. This conclusion is confirmed by similar distributions obtained from data for 74 Mc.

It may be concluded, therefore, that whenever flat, uncluttered terrain is used as an antenna site for a burst communication system, the two antennas necessary for closed-loop operation should be placed at the same height. Otherwise, the decorrelation in signal amplitude will reduce the effective duty cycle significantly.

The question of which antenna height, if any, is optimum for the Congaree site was explored in the height-comparison experiments. The evaluation of these experiments was made by counting the number of meteor echoes above the same threshold level from the fixed- and variable-height antennas. This threshold was established during the calibration periods when both antennas were set at the same height. The strong dependence of meteor count on threshold level made the calibration problem particularly important in these experiments. Consequently, data taken using the telescoping antenna tower were considered most reliable. Data were taken on both frequencies with the telescoping tower, and the variable-height antenna was set at heights such that (assuming a smooth conducting earth) various lobes and nulls of the receiving antenna should intersect the first (lowest) lobe of the transmitting antenna at 100 km above the earth.

This series of measurements failed to show any definite advantages of one antenna height over another. This result is supported by computed estimates of the

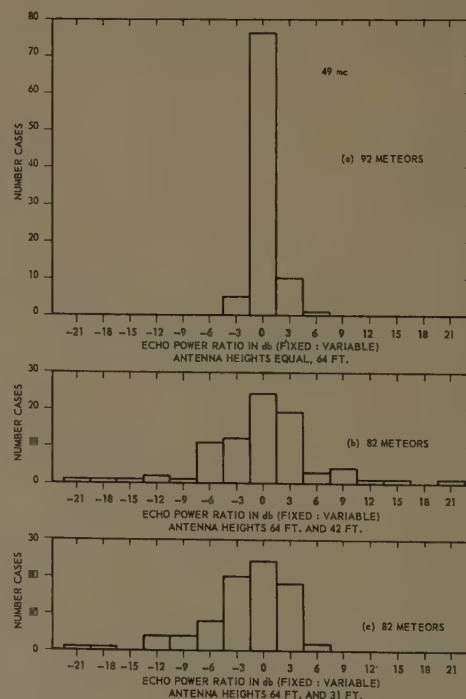


Fig. 3—Distribution of ratios of the maximum echo power observed simultaneously at 49 Mc. (a) Antennas at equal height, 64 feet. (b) Antennas at 64 feet and 42 feet. (c) Antennas at 64 feet and 31 feet.

meteor echo rates based on the three-point-radiant distribution.⁶ No particular height for the receiving antenna appeared to give consistently higher predicted rates throughout the day. Changes in antenna height appeared to redistribute the regions of high combined antenna gain over the meteor zone without appreciably changing the average echo rate.

V. LATERAL SEPARATION STUDIES

The influence of antenna separation on signal correlation at 74 Mc was investigated in a series of tests performed at the Congaree field site. Two receiving antennas were separated along a line perpendicular to the great-circle path joining Walpole and Congaree. The received signals were compared at several separations ranging from 15 feet to 662 feet; these separations were typical of those used in burst communication systems. Two five-element Yagi antennas were used in these tests: a fixed antenna at a height of 21 feet (1.6 λ) above the ground and a movable antenna mounted at equal height on the bed of a truck.

The received signals from the fixed and movable antennas and their instantaneous difference were recorded on the Edin multichannel recorder. Generally, the correlation between meteor bursts was high, and no significant change in the high correlation was found when the separation was changed from 15 to 662 feet. Fig. 4 shows distributions of ratios of the peak echo power from underdense trails measured at two typical separations. The degree of correlation observed here indicates the identity of the antenna patterns for various separations. In particular, the high correlation between echoes from the same meteor does not appear to be affected significantly by the presence of a few trees, a building, and a trailer in front of the antenna for one case of the 340-foot separation (Fig. 4). Hence, these obstacles do not appear to alter the antenna pattern appreciably.

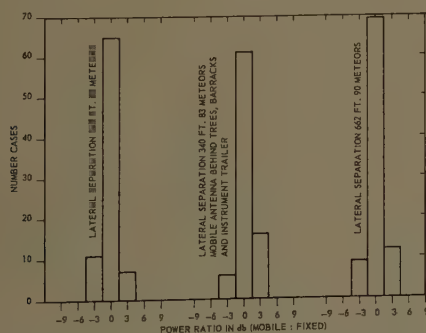


Fig. 4—Distribution of maximum echo-power ratios observed simultaneously with various lateral separations between antennas.

⁶ M. L. Meeks and J. C. James, "Meteor radiant distributions and the radio-echo rates observed by forward scatter," *J. Atmos. Terr. Phys.*, vol. 16, pp. 228-235; 1959. Computations were performed on the ERA 1101 at the Rich Electronic Computer Center, Georgia Inst. Tech., Atlanta.

The echoes from overdense meteor trails frequently showed strong decorrelations. These decorrelations appear to fall into three distinct categories: 1) *echo-overlap decorrelation* produced by the overlap in time of two meteor echoes with different phase relations at the two antennas; 2) *nonspecular overdense echo decorrelations*, produced by the wind distortion of nonspecular overdense trails which produces echo components that combine with different phase relations at the two antennas; 3) *single-trail multipath decorrelation*, produced by wind distortion of a single specular overdense meteor. Decorrelation of 1) was associated with very rapid fluctuations in the meteor signal strength. Some decorrelation of 2) was observed in the echoes from all nonspecular overdense trails. Initially, echoes from overdense trails appeared to be well-correlated, and decorrelation [type 3)] was observed only after the echo intensity began to fluctuate.

VI. TERRAIN STUDIES

The two receiving antenna sites at Congaree and Smyrna differed markedly in the characteristics of the terrain environment. It was therefore desirable to make measurements at both these sites in order to evaluate the effects of terrain on the performance of a meteor-burst communication system. The difference in path length alone might be expected to produce a difference in the counting rate. With equivalent meteor trails, the echo amplitude for the longer path (Walpole-Smyrna) would be less than for the shorter path (Walpole-Congaree). However, this effect will be offset by an increase in the illuminated volume of the meteor-trail zone. No corrections have been made for these effects in the path comparisons which follow.

Two distinct types of comparison were undertaken. 1) The 74-Mc meteor echo rate was measured simultaneously at Congaree and Smyrna to compare the performance of the two paths. 2) Three different antenna sites at Smyrna were used simultaneously to test the echo correlation for various antenna heights in rough terrain.

Of these two investigations, the path comparison 1) could not be carried out with precision because there was no way to eliminate completely all possible measurement factors which had nothing to do with terrain. However, thresholds were set for counting echoes at both sites with signal generators which were checked against each other before and after the experiment was performed. Thus, the receiving systems were calibrated from the terminals of the converters. The meteor echo counts were obtained with the multi-channel recorder in Congaree and the UF/MSA-1 in Smyrna. The results of this experiment are shown in Fig. 5. The Walpole-Smyrna path gave a higher meteor-echo rate from the early morning hours until noon. From noon until midnight, the Walpole-Congaree path gave higher counting rates, except during the two-hour period centered at 1600. Thus, the combined differences in terrain and

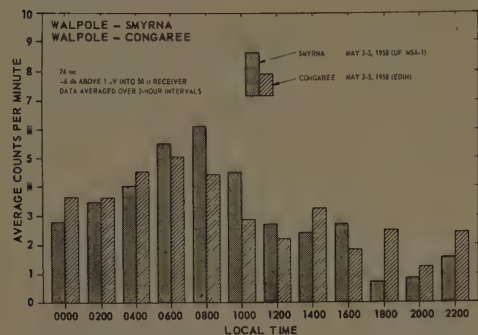


Fig. 5—Echo rates observed simultaneously at Smyrna, Ga., and at Congaree, S. C., at 74 Mc on May 2-3, 1958.

path length do not appear to produce consistently higher rates on either path.

The antenna-height investigation 2) was conducted on rough terrain at Smyrna. Three separate antennas were set up as follows:

- (R) A reference antenna on a 21-foot tower.
- (S) An antenna at the same height above sea level as the reference antenna (R), but mounted on a 12-foot tower.
- (G) An antenna on a 21-foot tower [identical with the tower for (R), but located down the hill so that its height above sea level was 17 feet below that of (R)].

The distance from (R) to (S) was about 85 feet, the distance from (R) to (G) about 160 feet, and the distance from (S) to (G) about 200 feet. The correlations between echo amplitudes obtained from these antennas were measured by determining the distribution of amplitude ratios. Fig. 6 shows these distributions. Clearly, the highest correlation was found between the reference antenna (R) and the antenna (S) at the same height above sea level.

The results of this test indicate that it may be preferable to place the two nearby antennas in a burst communication system at the same height above sea level rather than at the same height above ground in hilly terrain. No very strong preference for level ground appears to be indicated by these experiments.

VII. CONCLUSIONS

For meteor propagation with the equipment parameters described here, most of the duty cycle is contributed by echoes from overdense meteor trails. Roughly half of the duty cycle also comes from nonspecular overdense trails, and only 10 to 20 per cent comes from specular underdense trails. With a meteor burst communication system, one must expect that the parallel propagation paths will show a large amount of uncorrelated fading with the nonspecular echoes. Specular overdense echoes show similar uncorrelated fading after they begin to fluctuate. Specular underdense echoes, however, are well correlated, provided that the same

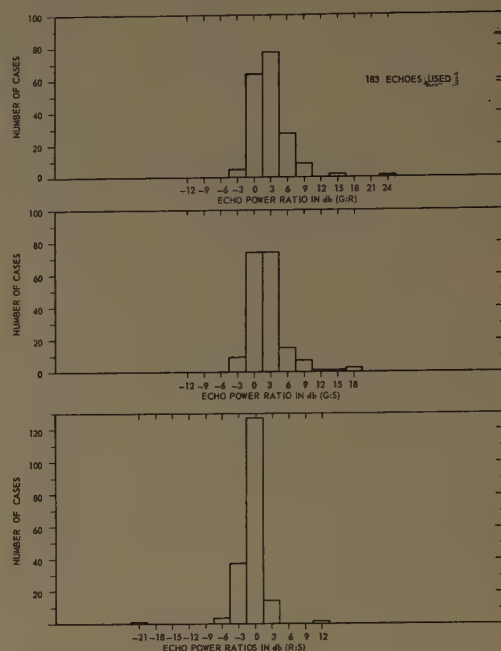


Fig. 6—Distributions of underdense echo-power ratios observed simultaneously at 74 Mc in hilly terrain with three antennas. Antenna R was the reference antenna. Antenna S was at the same height above sea level as R (but on a tower of different height). Antenna G was on a tower with the same height as R (but at a different height above sea level).

areas in the meteor-trail zone are illuminated by the antenna for the parallel paths. Over flat terrain, the antenna illumination was found to depend strongly on antenna height above ground, and consequently in such terrain both the nearby antennas in a meteor communication system should be at equal heights above ground. In hilly terrain, somewhat better correlation was found for antennas at equal heights above sea level. However, no particular antenna heights appeared to give a pronounced improvement in meteor signal. Changing the lateral separation of two nearby antennas on level terrain from 15 feet to 600 feet did not appear to change the degree of correlation of the echoes from underdense meteor trails.

The measured duty cycle D as a function of decision amplitude A can be fit by a curve of the form $D = (\text{const.})A^{-k}$, where the exponent ranges from 0.90 to 1.84. For underdense echoes alone, both 49 Mc and 74 Mc give k approximately equal to unity. Similarly for all specular echoes combined, k lies between 1.2 and 1.4 around 0600 and between 1.4 and 1.5 around 1800. The total duty cycle for all types of meteor echoes gives k in the range 1.2 to 1.4 around 0600 and in the range 1.4 to 1.8 around 1800. The mean rate of information transfer for a meteor communication system I depends on k according to the relation $I = (\text{const.})B^{1-k/2}$. Hence, at both times of day the information rate might be increased by increasing the bandwidth, but the advantage of this procedure appears to be greater at 0600 than at 1800.

The presence of an ionospheric scatter component in the signal at 49 Mc may in some situations appear as noise on a meteor communication system and reduce the advantages of 49 Mc over 74 Mc.⁷ However, the ionospheric scatter signal is not an inherent source of difficulties at lower frequencies. It is always possible to increase the system bandwidth until cosmic noise dominates the mean peak ionospheric scatter component. In this case the ionospheric scatter component will not limit the performance of a meteor communication system.⁸

This state of affairs constitutes an additional advantage for increased bandwidths.

ACKNOWLEDGMENT

The authors wish to acknowledge the contributions of Dr. J. P. Casey (now deceased) of Air Force Cambridge Research Center, who originally proposed some of the experiments reported here. Thanks are also due Dr. J. Taylor for his assistance conducting the experiments, and Miss J. Rice for much of the data processing.

⁷ This problem is discussed in M. L. Meeks and J. C. James, "On the choice of frequencies for meteor burst communication," *PROC. IRE (Correspondence)*, vol. 46, p. 1871; November, 1958.

⁸ The authors wish to thank Dr. Edward Reinhart for pointing out this fact.

A Method for Computing Ionospheric Focusing of Radio Waves, Using Vertical Incidence Ionograms*

E. WARREN† AND D. MULDREW†

Summary—The dependence of the signal strength of radio waves upon ionospheric focusing and spatial attenuation is calculated for a spherical ionosphere in terms of parameters obtainable from the appropriate vertical incidence ionogram. The signal strength at any given distance can be presented as a function of these ionospheric parameters in the form of a contour chart from which the unabsorbed field strength can be obtained easily as a function of frequency. The geometrical optics approximation is used. The limits of the region at the skip distance for which this method fails are estimated by comparing the results of a ray- and a wave-type calculation.

INTRODUCTION

THE EXTENT to which the ionosphere concentrates or disperses the energy of radio waves reflected from it is determined by the curvature and thickness of the ionospheric layers. There are three ways in which radio waves are concentrated by the ionosphere. They are called skip-distance focusing, tangent-ray focusing, and antipodal focusing.

Skip-distance focusing is readily understood in terms of the distance to which radio waves are propagated by one ionospheric reflection.¹ At the transition between high- and low-angle ray propagation, there is a range of angles for which the propagation distance changes relatively little. The power radiated in these elevation

angles is thereby returned to a comparatively small area on the earth's surface causing an increase in power density just beyond the skip distance.

Both tangent-ray focusing and antipodal focusing are due to the curvature of the ionosphere. Tangent-ray focusing (Fig. 1) is a consequence of changes in only the vertical dimension of a ray bundle. Irrespective of the form of the vertical distribution of the ionospheric electron density, a bundle of rays transmitted at zero elevation angle will converge upon returning to earth. Antipodal focusing, however, results from changes in only the horizontal dimension of the ray bundle. Because the earth and ionosphere are concentric spheres, radio waves confined between them are propagated, regardless of the azimuthal angle of transmission, toward the diametrically opposite point on the earth, and they focus there.

The skip-distance and tangent-ray types of focusing were discussed in a paper by Baker and Rice² in 1926. Forsterling and Lassen,³ in 1931, published results of numerical calculations on skip-distance focusing in a plane ionosphere. They also included in their paper a mathematical formula describing the antipodal focusing.

* Received by the PGAP, October 24, 1960; revised manuscript received, January 19, 1961.

† Defence Research Telecommunications Establishment, Ottawa, Canada.

¹ T. L. Eckersley, "Studies in radio transmission," *JIEE*, vol. 71, pp. 405-459; September, 1932.

² W. G. Baker and C. W. Rice, "Abridgment of refraction of short radio waves in the upper atmosphere," *Trans. AIEE*, vol. 45, pp. 302-333; February, 1926.

³ K. Forsterling and H. Lassen, "The ionization of the atmosphere and the spreading of short electric waves (10-100 m) over the earth, III," *Z. Tekh. Phys.*, vol. 12, pp. 502-527; November, 1947.

ing effect. Rawer,⁴⁻⁶ in several publications between 1943 and 1950, published the results of extensive calculations in which all three types of focusing were taken into account for curved parabolic layers. The behavior of the signal strength in the region of the antipodal focus has been described by Furutsu.⁷

In 1950, Lejay and Lepechinsky⁸ realized that for radio waves of a given frequency, it would be useful to represent the apparent points of reflection in the ionosphere as a graph in which the coordinates of distance from the transmitter were plotted against the apparent height. They called this graph "the reflectrix." The example in Fig. 2 is used to show how beams of similar angular width at the transmitter illuminate, on return to the ground, areas of greatly differing size. These authors deduced an expression for the signal strength. This appears to have been the first expression capable of describing, simultaneously, the three types of ionospheric focusing. It may be written in somewhat different form as

$$\frac{2R^2 E^2}{BZ_0} = \frac{\cos^2 K \cos(K + \theta)}{\sin \theta \sin 2\theta \sin K} |\cot \beta - \tan(K + \theta)| \quad (1)$$

where E is the rms value of the amplitude of the electric vector of the radio wave, Z_0 is the impedance of free space, B is the power radiated per unit solid angle, R is the radius of the earth, 2θ is the angle at the center of the earth that measures the separation of the transmitter and the point where the energy returns to earth, K is the elevation angle (Fig. 1), and $\cot \beta$ is the slope of the reflectrix (Fig. 3).

The three types of foci correspond to the three conditions for which the right-hand side of (1) is infinite. The skip-distance focus occurs for a zero value of β , the tangent-ray focus for a zero value of K , and the antipodal focus when 2θ has the value π .

The field strength becomes zero when

$$\cot \beta = \tan(K + \theta), \quad (2)$$

that is, when a ray from the transmitter is tangent to the reflectrix. Since, in general, the ionosphere consists of several layers, the reflectrix, though continuous, usually consists of several segments as illustrated in Fig. 3. It is then possible that the ray tangent to the reflectrix at A can again come in contact with the reflectrix at B . Between this point of contact B and the

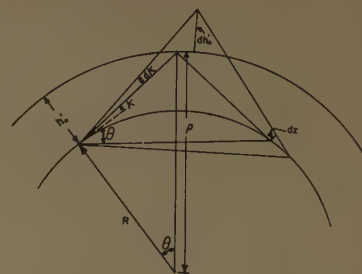


Fig. 1—Geometry of focusing.

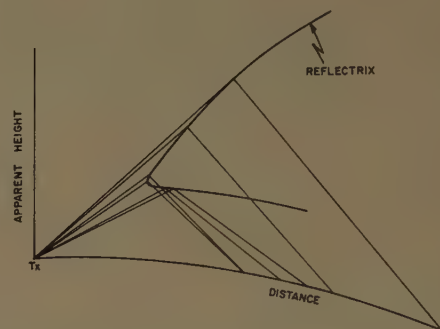


Fig. 2—Focusing and defocusing by the ionosphere.



Fig. 3—Cutoff mechanisms.

point of tangency A , no rays from the transmitter can be reflected at the reflectrix. The obscuring mechanism in the vicinity of these two points, between which reflection cannot occur, are known respectively as "cutoff by a lower layer" (for example, "cutoff by E layer"), and as "cutoff of the Pedersen ray." These are cutoff distance points for a given frequency that have been described; there are also cutoff frequency points for propagation to a given distance.⁹

COMPUTATION OF SINGLE-HOP FOCUSING

When (1) is used for numerical work, a method of computing the slope of the reflectrix is required. The equation of the reflectrix that we will use for a curved ionosphere is

$$f_v(h') \sec \phi(h', \theta) = f = \text{constant}. \quad (3)$$

The function $f_v(h')$ is given by the vertical incidence

⁴ K. Rawer, "Calculations of the field of a space wave," *Rev. Sci. Instr.*, vol. 85, pp. 361-362; April, 1947.

⁵ K. Rawer, "Some important effects in the geometrical optics of the ionosphere," *La Revue Scientifique*, vol. 86, pp. 481-485; May, 1948.

⁶ K. Rawer, "Geometrical optics of ionospheric propagation," *Nature*, vol. 166, p. 316; August, 1950.

⁷ K. Furutsu, "Calculation of Field Intensity about the Antipode of the Transmitting Station," *Rept. of Ionospheric Res. in Japan*, Science Council of Japan, Ueno Park, Tokyo, vol. 5, pp. 159-165; 1951.

⁸ P. Lejay and D. Lepechinsky, "Field intensity at the receiver as a function of distance," *Nature*, vol. 165, pp. 306-307; February, 1950.

⁹ B. Fulton, O. Sandoz and E. Warren, "The lower frequency limits for F-layer radio propagation," *J. Geophys. Res.*, vol. 65, pp. 177-183; January, 1960.

ionogram and f is the frequency of the wave being propagated. Graphs of corrected $\sec \phi(h', \theta)$, plotted as a function of apparent height for a series of discrete θ , are available as a set of transmission sliders.^{10,11} As a result of the failure of the equivalence theorem for a curved ionosphere, any two, but not three, of the variables K , θ , h' can be represented precisely in a single graph of the reflectrix type. When the formula of Lejay and Lepechinsky is used for a curved ionosphere, the approximation is made that the reflectrix $\theta(h')$ has the same form as $\theta(K)$. The latter is the form appropriate to the calculation of the signal strength. The approximation consists in identifying the height of the intersection, h'_0 , obtained by extending the straight-line parts of the ray path, with the apparent height of reflection at vertical incidence, h' , for the frequency reflected at the same real height.

The slope of the reflectrix, found by differentiating (3), is

$$\cot \beta = \frac{dh'}{\rho d\theta} = - \frac{\left[\frac{\partial}{\rho \partial \theta} (\ln \sec \phi) \right]_{h'}}{\left[\frac{\partial}{\partial h'} (\ln f_v \sec \phi) \right]_{\theta}}, \quad (4)$$

in which ρ is the height of the apparent point of reflection above the center of the earth. The subscript to the square bracket denotes the variable that is held constant.

Now, since

$$\begin{aligned} \frac{d}{\rho d\theta} (\ln \sec \phi) &= \left[\frac{\partial}{\rho \partial \theta} (\ln \sec \phi) \right]_{h'} \\ &+ \left[\frac{\partial}{\partial h'} (\ln \sec \phi) \right]_{\theta} \frac{dh'}{\rho d\theta} \end{aligned} \quad (5)$$

it follows, if θ and h' vary in such a way that $\sec \phi$ is constant, that

$$\begin{aligned} \left[\frac{\partial}{\rho \partial \theta} (\ln \sec \phi) \right]_{h'} \\ = - \left[\frac{\partial h'}{\rho \partial \theta} \right]_{\sec \phi} \left[\frac{\partial}{\partial h'} (\ln \sec \phi) \right]_{\theta}. \end{aligned} \quad (6)$$

Consequently, $\cot \beta$ may be written in the form

$$\cot \beta = \frac{\left[\frac{\partial h'}{\rho \partial \theta} \right]_{\sec \phi}}{\frac{d(\ln f_v)/dh'}{[\partial(\ln \sec \phi)/\partial h']_{\theta}} + 1}. \quad (7)$$

Since $f_v(h')$ is recorded on a logarithmic scale, $dh'/d(\ln f_v)$ is the slope of the trace on the ionogram. Also $[\partial h'/\partial(\ln \sec \phi)]_{\theta}$, which is always negative, is the slope of the transmission slider curve for the distance D equal to $2R\theta$. Since $[\partial h'/\partial D]_{\sec \phi}$ can be found readily from the set of transmission sliders, it is possible to evaluate the numerator in (7) through

$$\left[\frac{\partial h'}{\rho \partial \theta} \right]_{\sec \phi} = \left[\frac{\partial h'}{\partial D} \right]_{\sec \phi} \cdot \frac{2R}{R + h'}. \quad (8)$$

If a quantity H is defined as positive for the Pedersen ray and negative for the direct ray, such that

$$\frac{2R^2 E^2}{BZ_0} = |H|, \quad (9)$$

then (1) may be written in the form

$$\begin{aligned} H &= \frac{\cos^2 K \cos(K + \theta)}{\sin K \sin \theta \sin 2\theta} \\ &\cdot \left(\frac{\left[\frac{\partial h'}{\rho \partial \theta} \right]_{\sec \phi}}{\left[\frac{\partial h'}{\partial(\ln \sec \phi)} \right]_{\theta} + 1} - \tan(K + \theta) \right). \end{aligned} \quad (10)$$

In Figs. 4–7, values of E^2/Z_0 in decibels relative to $B/2R^2$ are shown for the distances 1000, 2000, 3000 and 4000 km, respectively. These values have been computed from (10) and the transmission sliders in the NBS circular.¹⁰ Contours of equal $\log_{10} |H|$ are drawn on coordinates of h' and $dh'/d(\ln f_v)$. To represent the complete range of slopes from negative infinity to positive infinity, a nonlinear (tangent) scale was used for the slope coordinate. The size of the diagrams was reduced with little loss of accuracy by making the negative slope scale one-fifth the size of the positive slope scale.

To find corresponding values of h' and $dh'/d(\ln f_v)$, it is convenient to construct a slider, similar to the one in Fig. 8, consisting of a series of known slopes, $dh'/d(\ln f_v)$, drawn on coordinates having the same scale as those of the ionograms being used. These slopes are brought into tangency with the ionogram trace while keeping the two sets of coordinate axes parallel. The height of tangency on the ionogram scale and the corresponding slope are the ones required to determine H from a diagram of the type in Figs. 4–7 appropriate to the path length D . The frequency corresponding to this value of H is computed in the usual way from the ionogram and the transmission slider for distance D .

The received power-per-unit area perpendicular to the direction of arrival, E^2/Z_0 , can be obtained in watts per square meter from H by expressing R in meters and B in watts per steradian.

The signal strength on a 4000-km circuit, computed from the ionogram sketched in Fig. 9, is shown as a function of frequency in Fig. 10. The F2 Pedersen ray shows an increase in signal strength from the cutoff frequency of the Pedersen ray to the MUF at 27 Mc.

¹⁰ "Ionospheric Radio Propagation," Central Radio Propagation Lab., National Bureau of Standards, Boulder, Colo., NBS Circular 462, p. 72 and p. 74; June, 1948.

¹¹ E. Appleton and W. J. G. Beynon, "The application of ionospheric data to radio communication problems," *Proc. Phys. Soc.*, pts. 1 and 2, vol. 52, pp. 518–533; July, 1940; vol. 59, pp. 58–76; January, 1947.

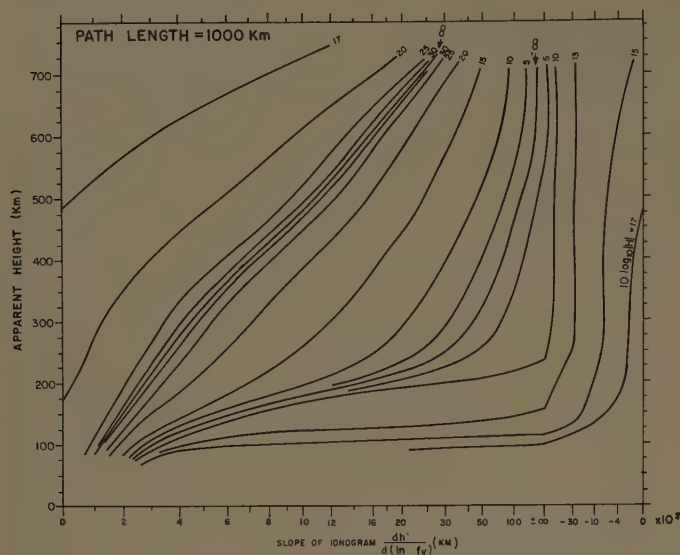


Fig. 4—Computed values of $10 \log_{10} |H|$ for a propagation distance of 1000 km.

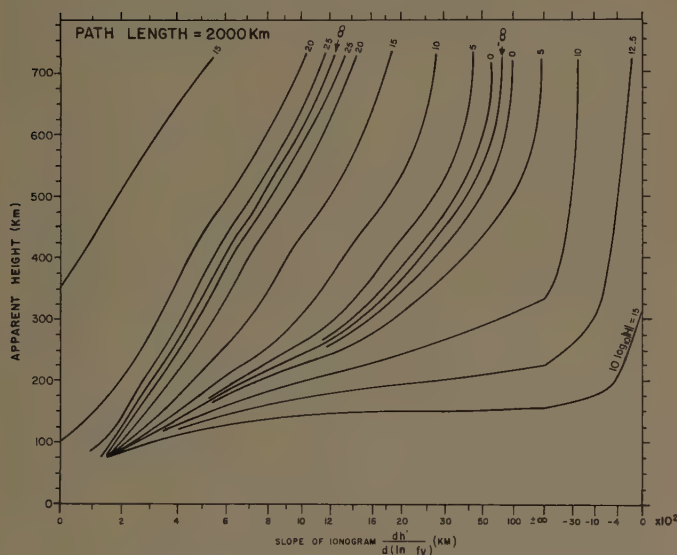


Fig. 5—Computed values of $10 \log_{10} |H|$ for a propagation distance of 2000 km.

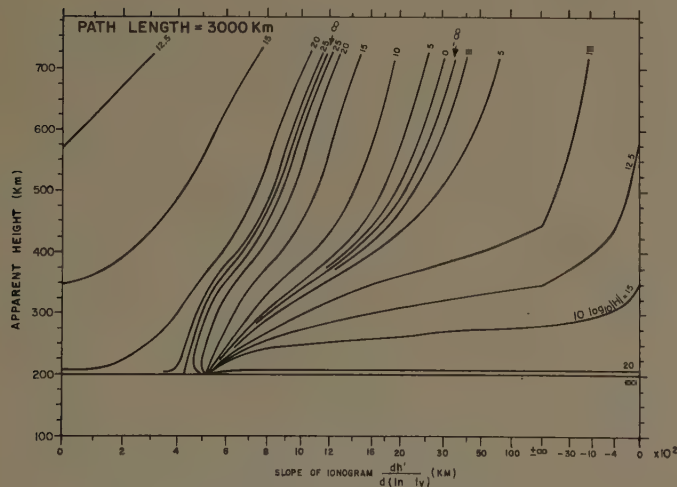


Fig. 6—Computed values of $10 \log_{10} |H|$ for a propagation distance of 3000 km.

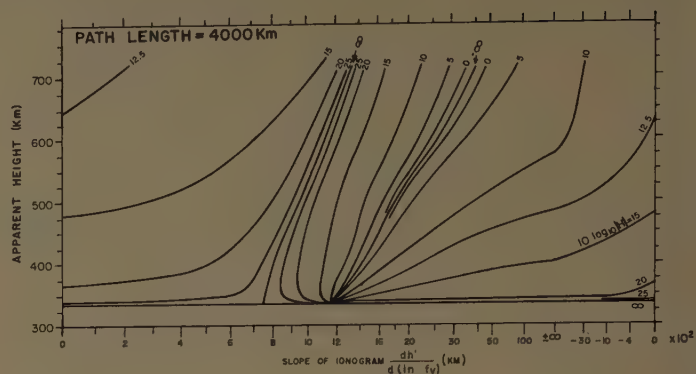


Fig. 7—Computed values of $10 \log_{10} |H|$ for a propagation distance of 4000 km.

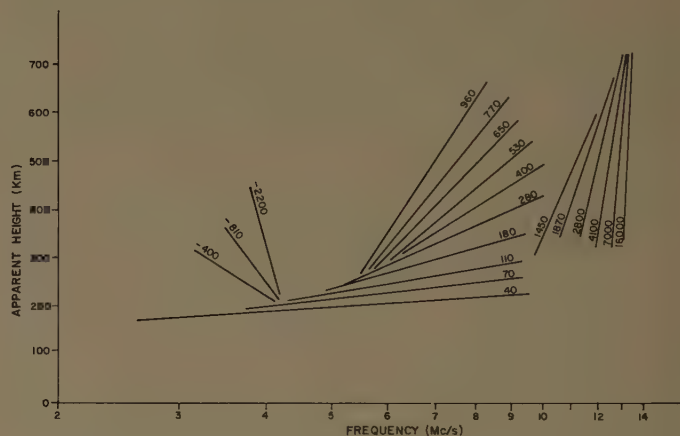


Fig. 8—Slider for determining slopes of ionogram traces.

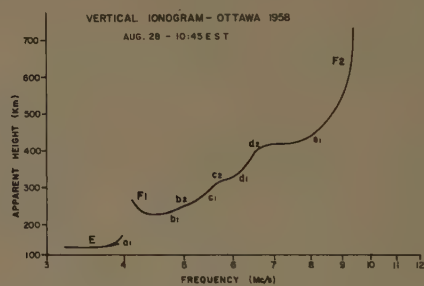


Fig. 9—A vertical incidence sounding record.

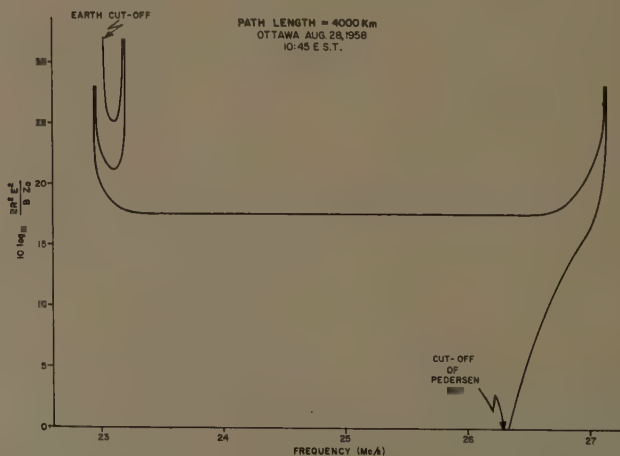


Fig. 10—Computed signal strength for a propagation distance of 4000 km.

The positive infinity at 27 Mc is the ray theory result for skip-distance focusing. The relatively flat part of the curve is for the F2 low-angle ray. The infinity at earth cutoff is due to tangent-ray focusing, while the other two infinities result from skip-distance focusing in a stratification of the F layer.

Calculations of signal strength from the same ionogram for a 2000-kilometer path are shown in Fig. 11(a). The corresponding oblique incidence $p'f$ curve, computed using Breit and Tuve's theorem, is presented in Fig. 11(b) in order to make mode identification easier. This $p'f$ curve looks somewhat unusual in that the stratifications seem very prominent. This impression disappears when it is plotted on the complete frequency scale of an oblique ionogram and account taken of the finite pulse width. The infinities of Figs. 10 and 11, and their corresponding apparent heights of reflection on the vertical ionogram, are labeled by lower case letters. Fig. 12 shows the strength of a 13-Mc signal as a function of distance, also computed from the ionogram of Fig. 9.

RAY-TYPE CALCULATION OF MULTIHOP FOCUSING

The calculation of the signal strength described above is for single-hop propagation only. A similar treatment for multihop propagation is complicated in that the beamwidth of a ray bundle in the vertical plane is dependent on the number and lengths of the individual hops, while the horizontal beamwidth is a function only of the total transmission distance.

The influence of multihop propagation on the signal strength may be deduced from Fig. 13. Two planes separated by an azimuthal angle $d\xi$ intersect along a straight line through the transmitter and the center of the earth. Two rays, one in each of the planes, leave the transmitter at an elevation angle K , and are separated by an angle $d\xi$. It will be seen from the diagram that

$$td\xi/ds = 1, \quad (11)$$

and

$$\frac{d\xi}{d\xi} = \frac{ds}{d\xi t \cos K} = \frac{1}{\cos K}. \quad (12)$$

Consequently, the horizontal separation, dy , of the rays on returning to earth after any number of hops is given by

$$\frac{dy}{d\xi} = p \frac{d\xi}{d\xi} = R \frac{\sin 2\theta}{\cos K}. \quad (13)$$

If rays are confined to elevation angles between K and $K+dK$, between the planes, a rectangular bundle of rays arrives at the receiver. If the beam dimension at the receiver, $2R d\theta \sin K$, perpendicular to the direction of propagation in the vertical plane through the receiver and transmitter, is called dz , then the power passing through the rectangle $dydz$ will have been radiated into the element of solid angle $d\xi dK$. Therefore, on the

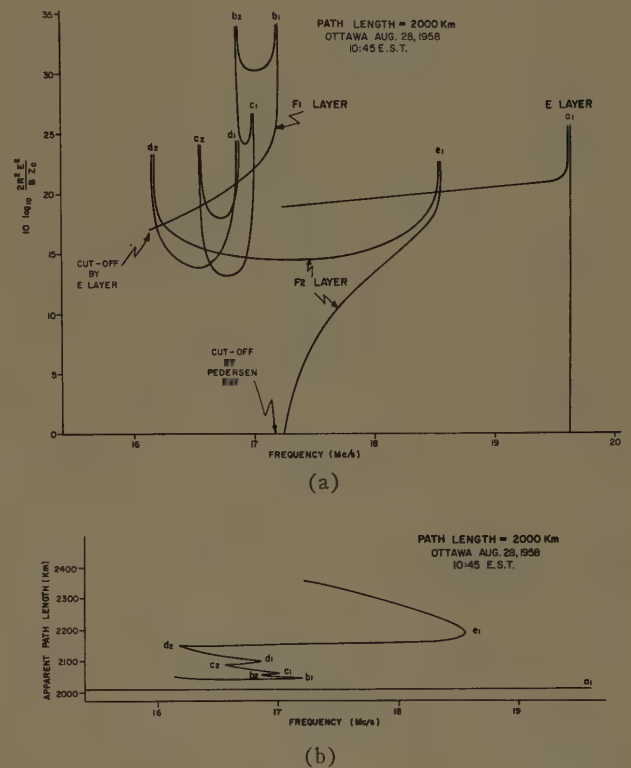


Fig. 11—(a) Computed signal strength for a propagation distance of 2000 km. (b) Computed $p'f$ curve.

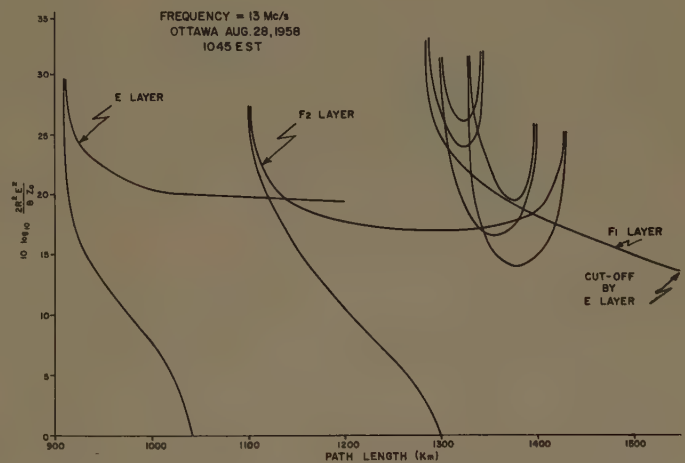


Fig. 12—Computed signal strength for a frequency as a function of distance.

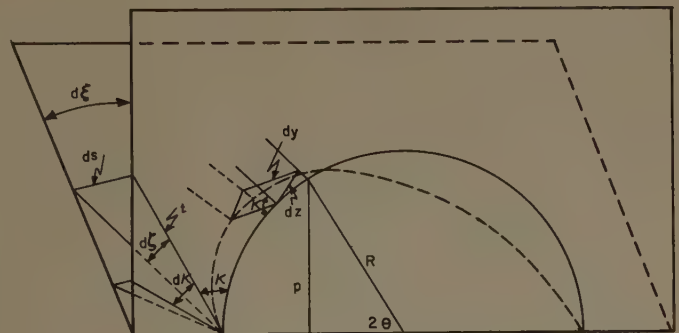


Fig. 13—Geometry describing multihop propagation.

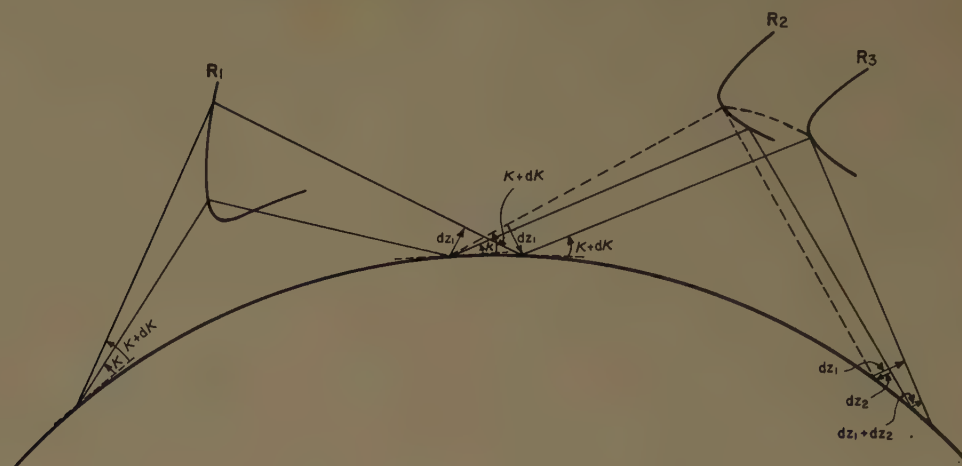


Fig. 14—Geometry of two-hop propagation.

assumption that no energy has been scattered or absorbed from the beam,

$$\frac{E^2}{Z_0 B} = \left| \frac{d\zeta dK}{dy dz} \right| = \frac{|H|}{2R^2}. \quad (14)$$

Since the sign of H is suitable, the combination of (13) and (14) yields

$$H = \frac{2R \cos K}{\sin 2\theta} \frac{dK}{dz}. \quad (15)$$

If horizontal gradients of ionization are neglected over each individual hop, the elevation angle will be the same for successive hops. The range of elevation angles in the beam will also be the same for successive hops, and it may be shown that, if n is the number of hops,

$$\frac{dz}{dK} = \sum_{i=1}^n \frac{dz_i}{dK}. \quad (16)$$

The validity of this equation for a two-hop mode is shown in Fig. 14. The reflectrix R_1 usually differs in shape from reflectrix R_2 ; reflectrices R_2 and R_3 have the same shape since they are separated by a small distance. Eq. (16) follows by induction. If the earth (or sea) is assumed to be perfectly reflecting, it follows from (15) and (16) that

$$\frac{1}{H} = \sin 2\theta \sum_{i=1}^n \frac{1}{H_i \sin 2\theta_i}. \quad (17)$$

The quantity H_i is computed from (10) and from the ionogram appropriate to the distance D_i traveled in the i th hop. The angle θ_i is defined such that

$$D_i = 2R\theta_i. \quad (18)$$

The various D_i can be determined by use of transmission sliders and lines of constant elevation angle all drawn on a single transparent sheet. The n ionograms that describe the conditions at the ionospheric reflec-

tion regions are also superimposed on a single sheet. The scales of the ionograms and transmission sliders must be compatible. A wave frequency is chosen and the set of sliders is moved horizontally over the ionograms, keeping the height scales in agreement until the transmission slider is in the position corresponding to this frequency.¹² That is, any f_o on the ionogram scale is placed directly under the value of $\sec \phi$ on the transmission slider scale that makes the product $f_o \sec \phi$ equal to the chosen frequency. By trial and error, the line of constant K is found that intersects the ordinary wave traces of all the ionograms, in such a way that the distance curves that pass through these points of intersection correspond to distances having a sum equal to the total length of the circuit. These distances are then the required D_i . This process can then be repeated for other frequencies so that H can be found as a function of frequency for n hops. If the K line intersects an ionogram at more than one point, only the intersection that corresponds to the lowest apparent height should be used.

From (17) it can be seen that the condition for the occurrence of a focus on a multihop circuit is

$$\sum_{i=1}^n \frac{1}{H_i \sin 2\theta_i} = 0. \quad (19)$$

From (17) it is also clear that the signal strength of an n -hop mode, in which all the hops are identical, and which covers a total distance D , is

$$10 \log_{10} \frac{n \sin 2\theta}{\sin \frac{2\theta}{n}} \text{ db}$$

below the signal strength of a one-hop mode, at the same frequency, covering the distance D/n .

¹² N. Smith, "The relation of radio sky-wave transmission to ionospheric measurements," *Proc. IRE*, vol. 27, pp. 332-347; May, 1939.

WAVE CALCULATION

To estimate the range of distances near the skip distance for which ray theory is not suitable, a wave calculation was performed assuming a particular density distribution for the ionospheric ionization. The vertical distribution was represented as having a parabolic form with a semithickness and a minimum height each of 150 km. A vertical incidence penetration frequency of 10 Mc was chosen and the wave calculations were performed for the reflection of 20 Mc from this layer using the approximations of plane-earth and plane-ionosphere. Ray path calculations were also carried out for the same model; the results of these calculations are compared in Fig. 15. Since, according to the wave theory for frequencies sufficiently near the MUF, the distinction between the high- and low-angle rays vanishes, the total power predicted by ray theory has been plotted as a function of distance (dashed line). The results obtained for the wave treatment are similar to those of Bremmer.¹³ For the model used, the ray theory yields the average value obtained on wave theory to within about 1 km of the skip distance. For the same ionosphere, this range of distances for the fixed frequency problem corresponds to a frequency range of about 0.02 Mc below the MUF for propagation to a fixed distance when the MUF is 20 Mc.

CONCLUSION

This paper has described a method for calculating, by ray theory, the influence of ionospheric focusing and spatial attenuation upon the signal strength of radio waves. A realistic calculation of the signal strength must, of course, deal with the effects of scattering and of absorption as well. Focusing on multihop circuits is found to be a mechanism very similar to that of "time-

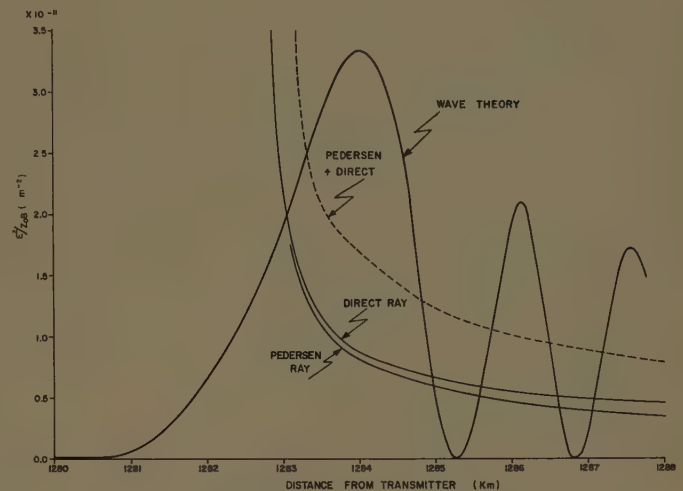


Fig. 15—Comparison of wave- and ray-type calculations of the signal strength.

delay focusing" which has been described for backscatter signals.¹⁴ The ray path approximation may reasonably be expected to yield accurate results for distances as close as a few kilometers to the skip distance. For distances outside of this relatively small skip-distance zone, the error of this method is, therefore, negligible compared with the errors incurred in reading data from the ionograms and in the use of a single set of transmission sliders for all ionospheric ionization density distributions.

ACKNOWLEDGMENT

The authors acknowledge their indebtedness to Dr. J. A. Fejer and to K. Graf for suggestions, and to L. Petrie and R. Maliphant for programming a digital computer for the wave calculation.

¹³ H. Bremmer, "Terrestrial Radio Waves," Elsevier Publishing Co., New York, N. Y.; 1949.

¹⁴ A. M. Petersen, "The mechanism of F-layer propagated backscatter echoes," *J. Geophys. Res.*, vol. 56, pp. 221-237; June, 1951.

CORRECTION

Dr. R. N. Bracewell, whose papers, "The Stanford Microwave Spectroheliograph Antenna, a Microsteradian Pencil Beam Interferometer," "Tolerance Theory of Large Antennas" and "Interferometry and the Spectral Sensitivity Island Diagram" appeared in the January, 1961, issue of the PGAP TRANSACTIONS, has informed the *Editor* of the following corrections:

p. 23, column 2, last line: Insert "pointed" after "are."
p. 25, Table III, column 6, last line: For "10 yagis"

put "10-element yagis."*

p. 25, Table III, column 10, line 3: For "10²⁶" put "10⁻²⁶".

p. 28, column 1, line 9 up: For "0.9" put "09".

p. 51, Fig. 1: For " $\lambda_{1/2}$ " put " $\lambda_1/2$ ".

p. 53, column 2, line 1: For "1/4" put " $\frac{1}{4}$ ".

p. 61, column 1, line 2: For "v" put "V".

p. 61, column 1, line 5: For "U" put "V".

p. 61, column 2, line 3 up: For " $\hat{\epsilon}$ " put " $\hat{\epsilon}_1$ ".

p. 61, column 2, last line: For " $j\hat{\epsilon}_2$ " put " $j\hat{\epsilon}_2$ ".

communications

Graphical Construction of Rays in an Ideal Luneburg Lens*

INTRODUCTION

It has been shown by Eaton¹ and others that the paths followed by the rays in an ideal Luneburg lens lie in planes and have elliptical shapes. For the standard Luneburg lens having one focus on its surface and the other at infinity, the equation of a ray is given by

$$\rho^2 = \frac{\sin^2 \delta}{1 - \cos \delta \cos (2\theta - \delta)}, \quad (1)$$

where ρ and θ are the polar coordinates in the plane containing the ray as defined in Fig. 1. The ray makes the initial angle δ with respect to the axis of the lens, and leaves the lens at E in a direction parallel to the lens axis.

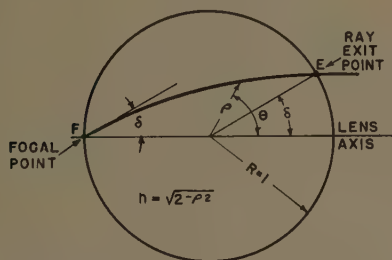


Fig. 1—Typical ray in an ideal Luneburg lens.

A simple graphical construction of these rays is presented, followed by the mathematical derivation.

CONSTRUCTION METHOD

As derived in the following section, the curved ray from the focus F to the exit point

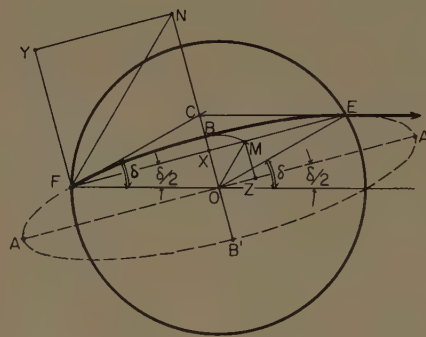


Fig. 2—Construction of ray ellipse in an ideal Luneburg lens.

E is a portion of an ellipse having its major axis along a line through the lens center O parallel to the straight line connecting E with F . This line makes an angle of $\delta/2$ with the lens axis FO , as shown in Fig. 2. The length of the semi-major axis of the ellipse is equal to $\sqrt{2} \cos (\delta/2)$, and the semi-minor axis has a length $\sqrt{2} \sin (\delta/2)$. These principal dimensions of the ray ellipse can be laid out by the following graphical construction, after which the ellipse may be constructed by any of the well-known methods, such as the trammel method.²

- 1) Let the lens radius be normalized, i.e., $FO = 1.00$.
- 2) Starting at the focal point F , draw the line FC in the initial ray direction given by angle δ .
- 3) Construct $OE \parallel FC$ through the lens center; the point E where this line intersects the rim of the lens is the exit point of the ray.
- 4) Complete the rhombus $FCEO$ by constructing $EC \parallel OF$, the lens axis.

- 5) Draw the perpendicular bisectors of the rhombus, FE and CO , which intersect at point X .
- 6) Note that $OX = \sin (\delta/2)$, and lay off $XM = OX$ along XE . The diagonal OM of the small square $OXMZ$ has a length $OM = \sqrt{2} \sin (\delta/2)$, which equals the semiminor axis of the ellipse.
- 7) Using a radius OM and the center O , swing an arc to intersect OC at points B and B' . The line BB' is the minor axis of the desired ellipse.
- 8) Note that $FX = \cos (\delta/2)$, and lay off an equal distance $XN = FX$ along the direction $XC \perp FX$. The diagonal FN of the larger square $FXNY$ has the length of the semimajor axis, i.e., $FN = \sqrt{2} \cos (\delta/2)$.
- 9) Construct a line through O parallel to FE ; lay off the distance FN along this line on both sides of point O to produce points A and A' , which determine the major axis of the ellipse.
- 10) With the major and minor axes of the desired ellipse given by AA' and BB' , respectively, the ellipse can now be constructed by means of standard drafting techniques, as shown dotted in Fig. 2; the segment FBE of this ellipse represents the actual ray path through the Luneburg lens.

MATHEMATICAL DERIVATION

The polar expression for the ray, given by (1), can be readily identified as the equation of a tilted ellipse by starting with the more familiar equation of an ellipse in Cartesian coordinates that is

$$\frac{X^2}{a^2} + \frac{Y^2}{b^2} = 1, \quad (2)$$

where a and b are the lengths of the semi-major and semiminor axes, respectively.

* Received by the PGAP, February 9, 1961.

¹ J. E. Eaton, "An Extension of the Luneburg-type Lenses," Naval Res. Lab., Washington, D. C., Rept. No. 4110, p. 13; February 16, 1953.

² T. E. French, "Engineering Drawing," McGraw-Hill Book Co., Inc., pp. 63-66; 1935.

Using the well-known relations between polar and rectangular coordinates (Fig. 3), namely

$$\begin{aligned} X &= \rho \cos \theta \\ Y &= \rho \sin \theta, \end{aligned} \quad (3)$$

(2) becomes

$$\frac{\rho^2 \cos^2 \theta}{a^2} + \frac{\rho^2 \sin^2 \theta}{b^2} = 1,$$

from which

$$\rho^2 = \frac{a^2 b^2}{b^2 \cos^2 \theta + a^2 \sin^2 \theta}. \quad (4)$$

From trigonometry

$$\cos^2 \theta = \frac{1 + \cos 2\theta}{2}, \text{ and } \sin^2 \theta = \frac{1 - \cos 2\theta}{2},$$

$$\therefore \rho^2 = \frac{a^2 b^2}{\frac{b^2(1 + \cos 2\theta)}{2} + \frac{a^2(1 - \cos 2\theta)}{2}}$$

or

$$\rho^2 = \frac{a^2 b^2}{\frac{(a^2 + b^2)}{2} - \frac{(a^2 - b^2)}{2} \cos 2\theta}. \quad (5)$$

The polar equation of an ellipse whose major axis is inclined at an angle α from the horizontal lens axis can be derived from (5) by using the following relation between angles (see Fig. 4):

$$\begin{aligned} \theta' &= \theta + \alpha \\ \therefore \theta &= \theta' - \alpha. \end{aligned} \quad (6)$$

Substituting (6) into (5) results in the polar equation of the inclined ellipse:

$$\rho^2 = \frac{a^2 b^2}{\left(\frac{a^2 + b^2}{2}\right) - \left(\frac{a^2 - b^2}{2}\right) \cos (2\theta' - 2\alpha)}. \quad (7)$$

Comparing (7) with Eaton's (1) for the ray path, it can be noted that these equations are of the same form and that the following relations between terms are obtained:

$$a^2 b^2 = \sin^2 \delta \quad (8)$$

$$\left(\frac{a^2 + b^2}{2}\right) = 1 \quad (9)$$

$$\left(\frac{a^2 - b^2}{2}\right) = \cos \delta \quad (10)$$

and

$$2\alpha = \delta. \quad (11)$$

From (11) it can be noted that the ray ellipse is tilted at an angle

$$\alpha = \delta/2. \quad (11a)$$

Adding (9) and (10) results in

$$a^2 = 1 + \cos \delta = 2 \cos^2 (\delta/2) \quad (12)$$

or

$$a = \sqrt{2} \cos (\delta/2). \quad (12a)$$

Subtracting (10) from (9) results in

$$b^2 = 1 - \cos \delta = 2 \sin^2 (\delta/2) \quad (13)$$

or

$$b = \sqrt{2} \sin (\delta/2). \quad (13a)$$

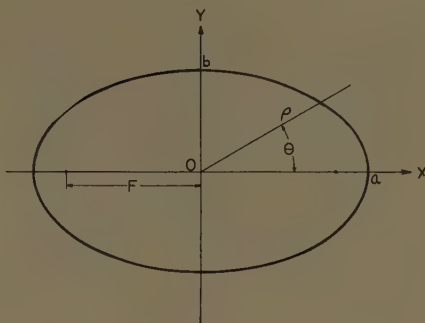


Fig. 3—Ellipse in rectangular coordinates.

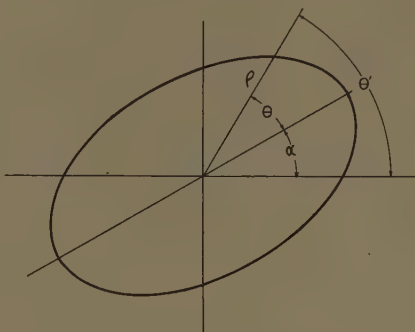


Fig. 4—Inclined ellipse.

Eqs. (12a) and (13a) give the semimajor and semiminor axes of the ray ellipse. Although (8) was not needed in the derivation, it is satisfied by (12) and (13), i.e.,

$$\begin{aligned} a^2 b^2 &= (1 + \cos \delta)(1 - \cos \delta) \\ &= 1 - \cos^2 \delta = \sin^2 \delta. \end{aligned}$$

CONCLUSION

It has been shown that Eaton's equation for a ray in an ideal Luneburg lens represents an ellipse with its major axis inclined at an angle equal to half the initial ray angle δ . The semimajor axis of this ellipse has a length of $a = \sqrt{2} \cos (\delta/2)$, and the semiminor axis is given by $b = \sqrt{2} \sin (\delta/2)$. These expressions lead to a simple graphical method for constructing the principal dimensions of the ray ellipse.

H. E. SCHRANK
Westinghouse Elec. Corp.
Friendship Internatl. Airport
Baltimore 3, Md.

Backscattering From a Finite Cone—Comparison of Theory and Experiment*

The electromagnetic backscattering cross section σ of a perfectly conducting finite

cone was determined by the author¹ by means of the geometrical theory of diffraction. Experimental measurements of σ have been made by Keys and Primich.² Fig. 1(a)–(f) shows both the experimental and theoretical results for cones of various half-angles γ for the case of axial incidence. In the figure the ordinate is $\sigma/\pi a^2$ and the abscissa is ka , where a is the radius of the base of the cone and $k = 2\pi/\lambda$ with λ the incident wavelength. The theoretical curves are based upon (30)¹ which takes account of single and double diffraction by the rear edge of the cone.

Moffatt pointed out the agreement between the curve in the author's¹ article for a cone of half-angle $\gamma = 11.5^\circ$ and the data in Keys and Primich² for a cone with $\gamma = 12^\circ$.

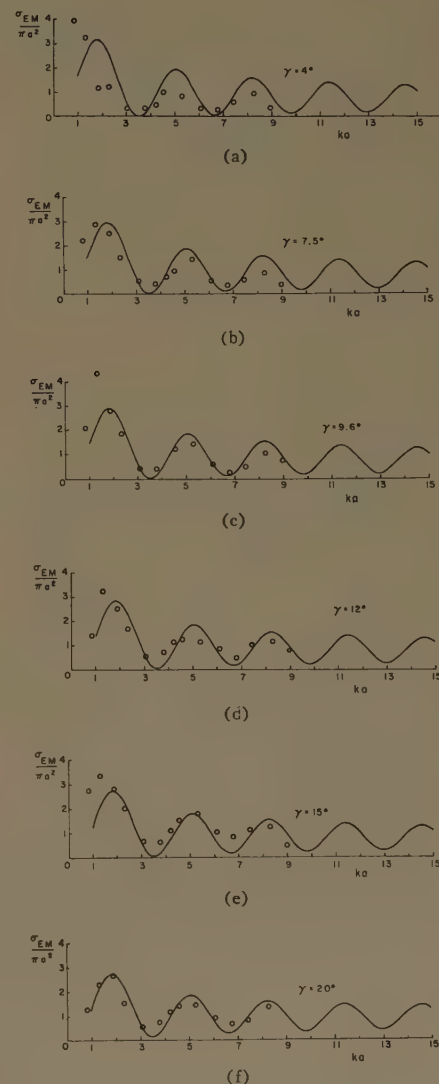


Fig. 1—Experimental and theoretical values of the backscattering cross section σ of a finite cone for axial incidence. The ordinate is $\sigma/\pi a^2$ and the abscissa is ka where a is the radius of the base of the cone and $k = 2\pi/\lambda$. The circles are experimental values and the curves are computed. The half-angle of the cone γ is indicated on each curve.

¹ J. B. Keller, "Backscattering from a finite cone," IRE TRANS. ON ANTENNAS AND PROPAGATION, VOL. AP-8, pp. 175–182; March, 1960.

² J. E. Keys and R. I. Primich, "The Radar Cross-Section of Right Circular Metal Cones," Defense Res. Telecommun. Estab., Ottawa, Can., Rept. No. 1010, ASTIA Doc. No. AD 217–921; May, 1959.

* Received by the PGAP, February 17, 1961. The research in this paper has been sponsored by the AF Cambridge Res. Labs. under Contract No. AF19(604) 5238.

He also observed that in the author's article the two curves in Fig. 4 are mislabeled, the words "solid" and "dashed" having been interchanged.

Safran and Helstrom have pointed out that in the author's article¹ the right sides of (3) and (4) should each be multiplied by a factor of two. This is because the axis is not a caustic of the diffracted rays, as was stated incorrectly before (3). As a consequence, (6)–(8), (11), (17)–(19) all require factors of two on their right sides. The other equations are correct because they were obtained with the aid of (A16),² which is missing a factor of one half. As a result the missing two is cancelled.

In (29)¹ the term $(\cos \pi/n - \cos 3\pi/2n)^{-1}$ was miswritten and should be $(\cos \pi/n - \cos 3\pi/n)^{-1}$.

JOSEPH B. KELLER
Inst. of Math. Sci.
New York University
New York, N. Y.

¹ J. B. Keller, "Diffraction by an aperture," *J. Appl. Phys.*, vol. 28, pp. 426–444; April, 1957.

Focal Length of a Cassegrain Reflector*

In a recent paper, Wilkinson and Appelbaum¹ draw certain conclusions concerning the effective focal length of a Cassegrain reflector system. These conclusions, which are contrary to well-established optical principles, are in error, due to an incorrect definition of the effective focal length. Wilkinson and Appelbaum compute the path length from the point-source feed to the point of final reflection. Their conclusions regarding the properties of this path length are correct, but the path length has no direct relation to the effective focal length.

The effective focal length may be defined as the focal length of a simple lens which achieves the same effect. The situation is as illustrated in Fig. 1. Here we have a parabola at $x=0$, and a hyperbola at

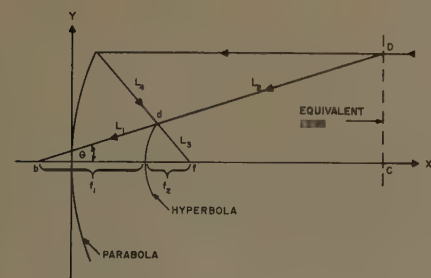


Fig. 1—Cassegrain system.

$x=a$. The two foci of the hyperbola are at $x=f$ (the focus of the parabola) and $x=b$ (b can be either positive or negative). A ray coming in parallel to the x axis is then reflected first from the parabola and then from the hyperbola, being brought to a focus at $x=b$. If we extend the line bd until it intersects the incoming ray at a point D , then a lens placed at this point having a focal length bc will be equivalent to the Cassegrain system. Thus the focal length bc is the effective focal length of the Cassegrain system and can be expressed in terms of the Cassegrain parameters as follows.

From similar triangles we have

$$\frac{d}{D} = \frac{L_1}{L_1 + L_2} \quad (1)$$

and

$$\frac{d}{D} = \frac{L_3}{L_3 + L_4} \quad (2)$$

Solving (1) and (2) for $(L_1 + L_2)$ we have

$$L_1 + L_2 = \frac{L_1(L_3 + L_4)}{L_3} \quad (3)$$

Now as $\theta \rightarrow 0$,

$$\begin{aligned} L_1 + L_2 &\rightarrow f_e \\ L_3 + L_4 &\rightarrow f \\ L_1 &\rightarrow f_1 \\ L_2 &\rightarrow f_2. \end{aligned}$$

Thus,

$$f_e = \frac{f_1 f}{f_2} \quad (4)$$

where

- f_e = effective focal length of Cassegrain system,
- f_1 = distance from feed to vertex of secondary reflector,
- f_2 = distance from the focal point of the parabola to vertex of secondary reflector,
- f = focal length of parabola.

The ratio f_1/f_2 is the magnification of the system and can be expressed as

$$\frac{f_1}{f_2} = m = \frac{e + 1}{e - 1} \quad (5)$$

where

e = eccentricity of the hyperbola.

Eq. (4) can then be expressed as

$$f_e = \frac{e + 1}{e - 1} f, \quad (6)$$

which is identical with (3) of the article by Wilkinson and Appelbaum.

In the case where the feed is located either at the vertex of the parabola or between the parabola and the hyperbola, the effective focal length can vary between 0 and ∞ since

$$\begin{aligned} 0 &\leq f_1/f_2 \leq \infty \\ 1 &\leq e \leq \infty \\ -\infty &\leq e \leq -1. \end{aligned}$$

In the case where the feed is located behind the parabola, the effective length can vary between k and ∞ . The value of k lies be-

tween 0 and ∞ and cannot be zero since, in this case, f_1 is never smaller than the distance between the feed and the vertex of the parabola.

The statement made by Wilkinson and Applebaum that in (6), as $e \rightarrow 1$ the value of $f \rightarrow 0$ is not correct since e and f can be chosen independently of each other.

That the focal length as defined here is the correct value is attested by the facts that:

- 1) It is the correct value for relating lateral displacement of the feed to angular displacement of the resulting beam.
- 2) It is the correct value to use in connection with the aperture diameter to determine the feed angle.
- 3) It is the correct value to use in connection with the aperture diameter to determine coma aberration for small displacement angles.

This last point has been established both analytically and experimentally at this laboratory during the course of a study under a contract sponsored by the Rome Air Development Center.^{2,3} This study also includes an analysis of the Schwarzschild reflector system which is compensated for coma. It is hoped that further details of this study can be published in the near future.

W. D. WHITE
L. K. DESIZE
Airborne Instruments Lab.
A Div. of Cutler-Hammer, Inc.
Deer Park
Long Island, N. Y.

² L. K. DeSize, D. J. Owen, and G. E. Skahill, "Investigation of Multibeam Antennas and Wide-Angle Optics," Airborne Instruments Lab., Deer Park, Long Island, N. Y., Rept. No. 7358-1, under Contract AF 30(602)-1980, Air Res. and Dev. Command, Rome Air Dev. Ctr., Griffiss AFB, Rome, N. Y.; January, 1960.

³ W. D. White, L. J. Kuskowski, and L. K. DeSize, "Investigation of Multifield Antennas and Wide-Angle Optics," Airborne Instruments Lab., Deer Park, Long Island, N. Y., Rept. No. 7358-2, under Contract AF 30(602)-1980, Air Res. and Dev. Command, Rome Air Dev. Ctr., Griffiss AFB, Rome, N. Y.; December, 1960.

Reply to Comments by White and DeSize*

In our previous note¹ we used the increase in distance of a point source feed from the vertex of a parabola as a measure of the reduction in pattern distortion due to off-axis beam positioning in an antenna system employing a secondary hyperbolic reflector. As DeSize and White have pointed out, this distance is not the commonly accepted definition of effective focal length. We recognize

* Received by the PGAP, February 27, 1961.

¹ E. J. Wilkinson and A. J. Appelbaum, "Cassegrain systems," *IRE TRANS. ON ANTENNAS AND PROPAGATION*, vol. AP-9, pp. 119–120; January, 1961.

* Received by the PGAP, March 9, 1961.

¹ E. J. Wilkinson and A. J. Appelbaum, "Cassegrain systems," *IRE TRANS. ON ANTENNAS AND PROPAGATION*, vol. AP-9, pp. 119–120; January, 1961.

and agree with the correctness of their definition in giving quantitative information for situations where the feed is either on the focal axis, or slightly off the focal axis, provided that in the latter case the curvature of the hyperbola is very small. We have not as yet, however, seen any proof that their definition is valid for off-axis feeds when the curvature of the hyperbola becomes large. For use in a qualitative discussion of the wide-angle scanning limitations of Cassegrain systems, which was the intent of our note, we were somewhat reluctant to use a definition which implied off-axis performance approaching that of a parabola of infinite focal length as the curvature of the hyperbola was increased. After studying the rather limited amount of information that was available on this subject, it was our opinion that, over a wide range of angular displacements and hyperbolic curvatures, the off-axis behavior of a Cassegrain was more typically that of a simple parabola having a focal length as defined in our note. Lending some support to our choice of effective focal length is the study² in which curves are presented comparing the coma coefficients of a number of Cassegrain systems with those of simple parabolas. It might be argued that neither definition is accurate for very large beam displacements, but for the purpose for which we have used it, we feel our definition is a more realistic measure of the change in the off-axis performance of the Cassegrain with increasing hyperbolic curvature. It also has the additional advantage of being a length more easily identified with the physical system.

Irrespective of how one defines effective focal length, however, our conclusions regarding the increased size of the feed aperture with increased hyperbolic curvature remain valid, since these follow from the simple geometry of the situation. We continue to feel, therefore, that microwave problems arising from aperture blocking by the feed and from the fact that the feed may no longer appear as a point source to the hyperbola will eventually impose a definite limit on the amount of curvature that can be used in any practical system.

E. J. WILKINSON
A. J. APPELBAUM
Waltham Lab.
Sylvania Electronic Systems
A Div. of Sylvania Electric Products, Inc.
Waltham, Mass.

² W.D. White, L.J. Kuskowski, and C.A. Bergrem, "Investigation of Multifeed Antennas and Wide-Angle Optics," Airborne Instruments Lab., Deer Park, N. Y., Rept. No. 7358-1-5; June, 1960.

Phase Correction by Dielectric Slabs in Sectoral Horn Antennas*

Summary—Beginning with Maxwell's equations, the field components and propagation constants are found inside a plane

aperture *H*-plane sectoral horn antenna containing two dielectrics. The horn is assumed to be fed from a waveguide containing the dominant TE₁₀ mode. Knowing the phase constants in the two dielectrics makes it possible to calculate the dimensions of a triangular-shaped dielectric slab which, when placed in the horn, can alter the curved phase front and produce an approximation to a uniform-plane phase front at the aperture of the horn. This improved phase front results in an improved far field pattern.

INTRODUCTION

The path length of a wave reaching the aperture of a horn antenna at its center is different from the path length of a wave reaching the aperture at the flared side of the horn. This difference in length causes the phase of the field at the plane of the aperture to vary over the horn opening. As long as the difference in path length is a small fraction of a wavelength, the maximum directive gain increases as the aperture and flare angle are increased. However, as the flare angle and aperture increase, the phase of the field at the edge of the aperture changes and can differ sufficiently from the phase of the field reaching the center of the aperture to produce a reduction in the directive gain of the horn. This is an inherent limitation on increasing the gain of conventional horn antennas by means of increasing the flare angle.

To produce a plane phase front, *i.e.*, a plane surface, all points of which have the same phase, at the aperture of a horn antenna requires some corrective device. It is the purpose of this paper to describe a method by which the dimensions of a triangular-shaped dielectric slab can be calculated and used inside an *H*-plane sectoral horn to alter the curved phase front and approximate a uniform phase front at the aperture.

THE FIELDS INSIDE *H*-PLANE SECTORAL HORNS CONTAINING TWO DIELECTRICS

The shape of the sectoral horn and its orientation in a cylindrical coordinate system is shown in Fig. 1. It will be assumed that the horn is excited by a rectangular waveguide containing only the dominant TE₁₀ mode. The metallic walls are assumed to be perfectly conducting, the dielectrics are lossless, all field components vary as $e^{j\omega t}$, and propagation is in the r direction. The sides of the horn are assumed to extend far enough in the r direction that the fields in the region under consideration are not disturbed by end effects.

Beginning with Maxwell's two curl equations,

$$\nabla \times \mathbf{H} = \mathbf{I} + \frac{\partial \mathbf{D}}{\partial t} \quad \text{and} \quad \nabla \times \mathbf{E} = -\frac{\partial \mathbf{B}}{\partial t}, \quad (1)$$

it is possible to write six scalar equations. However, considering the region inside the horn as being conductivity free, and being fed from a waveguide containing only the TE₁₀ mode, these six equations reduce to

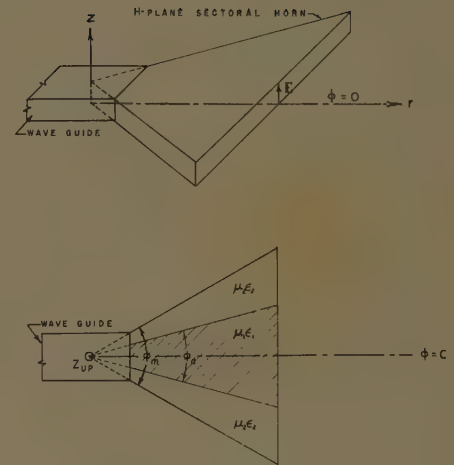


Fig. 1—The sectoral horn and its coordinate system.

$$\begin{aligned} j\omega \epsilon r E_\phi &= \frac{\partial}{\partial r} (r H_\phi) - \frac{\partial H_r}{\partial \phi}, \\ -j\omega \mu r H_r &= \frac{\partial E_\phi}{\partial \phi}, \\ j\omega \mu H_\phi &= \frac{\partial E_r}{\partial r}, \end{aligned}$$

and

$$E_r = E_\phi = H_z = 0. \quad (2)$$

Eliminating H_ϕ and H_r from (2), the following equation is obtained for E_ϕ :

$$\frac{\partial^2 E_\phi}{\partial r^2} + \frac{1}{r} \frac{\partial E_\phi}{\partial r} + \frac{1}{r^2} \frac{\partial^2 E_\phi}{\partial \phi^2} + \omega^2 \mu \epsilon E_\phi = 0. \quad (3)$$

A solution to (3) is well known and can be written as

$$\begin{aligned} E_\phi &= [A \cos(k\phi) + B \sin(k\phi)] [CH_k^{(1)}(\omega\sqrt{\mu\epsilon}r) \\ &\quad + DH_k^{(2)}(\omega\sqrt{\mu\epsilon}r)], \end{aligned} \quad (4)$$

where A , B , C , and D are complex constants, and $H_k^{(1)}(\omega\sqrt{\mu\epsilon}r)$ and $H_k^{(2)}(\omega\sqrt{\mu\epsilon}r)$ are Hankel functions of the first and second kind, respectively. In order to get a central lobe propagating only in the r direction, B and C must be zero.

Using subscript 1 for dielectric 1, and subscript 2 for dielectric 2, the remaining constants can be evaluated from the following boundary conditions:

$$E_{\phi 2} = 0 \quad \text{when} \quad \phi = \pm \frac{\phi_m}{2},$$

$$E_{\phi 1} = E_{\phi 2} \quad \text{when} \quad \phi = \pm \frac{\phi_d}{2},$$

and

$$H_{r1} = H_{r2} \quad \text{when} \quad \phi = \pm \frac{\phi_d}{2}. \quad (5)$$

Assuming the regions inside the horn have the same permeability as free space, *i.e.*, $\mu_1 = \mu_2 = \mu_0$, the field components become, in region 1,

* Received by the PGAP, March 3, 1961.

$$E_{z1} = A_1 \cos\left(\frac{\pi}{\phi_m} \phi\right) H_{\pi/\phi_m}^{(2)}(\omega\sqrt{\mu_0\epsilon_1} r), \quad (6)$$

$$H_{\phi 1} = -jA_1 \sqrt{\frac{\epsilon_1}{\mu_0}} \cdot \cos\left(\frac{\pi}{\phi_m} \phi\right) H_{\pi/\phi_m}^{(2)'}(\omega\sqrt{\mu_0\epsilon_1} r), \quad (7)$$

$$H_{r1} = \frac{-jA_1\pi}{\omega\mu_0\phi_m} \sin\left(\frac{\pi}{\phi_m} \phi\right) H_{\pi/\phi_m}^{(2)}(\omega\sqrt{\mu_0\epsilon_1} r), \quad (8)$$

where $H_{\pi/\phi_m}^{(2)'}$ is the derivative of $H_{\pi/\phi_m}^{(2)}$ with respect to its argument.

In region 2,

$$E_{z2} = A_2 \cos\left(\frac{\pi}{\phi_m} \phi\right) H_{\pi/\phi_m}^{(2)}(\omega\sqrt{\mu_0\epsilon_2} r)$$

$$= \frac{A_1 H_{\pi/\phi_m}^{(2)}(\omega\sqrt{\mu_0\epsilon_1} r)}{H_{\pi/\phi_m}^{(2)}(\omega\sqrt{\mu_0\epsilon_2} r)} \cdot \cos\left(\frac{\pi}{\phi_m} \phi\right) H_{\pi/\phi_m}^{(2)}(\omega\sqrt{\mu_0\epsilon_2} r).$$

Thus,

$$E_{z2} = A_1 \cos\left(\frac{\pi}{\phi_m} \phi\right) H_{\pi/\phi_m}^{(2)}(\omega\sqrt{\mu_0\epsilon_1} r), \quad (9)$$

$$H_{\phi 2} = -jA_1 \sqrt{\frac{\epsilon_2}{\mu_0}} \frac{H_{\pi/\phi_m}^{(2)'}(\omega\sqrt{\mu_0\epsilon_1} r)}{H_{\pi/\phi_m}^{(2)}(\omega\sqrt{\mu_0\epsilon_2} r)} \cdot \cos\left(\frac{\pi}{\phi_m} \phi\right) H_{\pi/\phi_m}^{(2)}(\omega\sqrt{\mu_0\epsilon_2} r), \quad (10)$$

and

$$H_{r2} = \frac{-j\pi A_1}{\omega\mu_0\phi_m} \sin\left(\frac{\pi}{\phi_m} \phi\right) H_{\pi/\phi_m}^{(2)}(\omega\sqrt{\mu_0\epsilon_1} r). \quad (11)$$

PROPAGATION CONSTANTS

The fields inside waveguides are assumed to be exponentially propagated, *i.e.*, $e^{j\omega t - \gamma r}$ where γ is a propagation constant. Following the example set by Barrow and Chu,¹ and assuming this is also true inside the horn, then for region 1,

$$\gamma_1 = \frac{-1}{E_{z1}} \frac{\partial E_{z1}}{\partial r}.$$

Substituting E_{z1} from (6),

$$\gamma_1 = \alpha_1 + j\beta_1$$

$$= -\omega\sqrt{\mu_0\epsilon_1} \frac{H_{\pi/\phi_m}^{(2)' }(\omega\sqrt{\mu_0\epsilon_1} r)}{H_{\pi/\phi_m}^{(2)}(\omega\sqrt{\mu_0\epsilon_1} r)}, \quad (12)$$

where $H_{\pi/\phi_m}^{(2)'}$ is the derivative of $H_{\pi/\phi_m}^{(2)}$ with respect to its argument; α_1 is the attenuation constant in region 1; and β_1 is the phase shift constant in region 1.

Similarly for region 2,

$$\gamma_2 = \alpha_2 + j\beta_2$$

$$= -\omega\sqrt{\mu_0\epsilon_2} \frac{H_{\pi/\phi_m}^{(2)' }(\omega\sqrt{\mu_0\epsilon_2} r)}{H_{\pi/\phi_m}^{(2)}(\omega\sqrt{\mu_0\epsilon_2} r)}. \quad (13)$$

It should be observed that both γ_1 and γ_2 vary with r .

CORRECTION OF THE PHASE FRONT WITH AN OPTIMUM AMOUNT OF DIELECTRIC

It is convenient to define the dielectric having the largest product $\mu\epsilon$ as the hard dielectric, and the other as the soft dielectric. When the hard dielectric is used in the middle of the horn (region 1), the circular wave front of constant phase has a smaller radius in the hard dielectric and a larger radius in the soft dielectric. If the proper amount of hard dielectric is used in region 1, it is possible to reshape the phase front and approximate a uniform phase distribution at the mouth of the horn.

Fig. 2 shows a drawing representing a phase front at the mouth of the horn containing a hard dielectric in region 1. The total phase shift in each region is given by

$$\text{phase shift in region 1} = \int_0^{r_1} \beta_1 dr,$$

and

$$\text{phase shift in region 2} = \int_{r_1}^{r_2} \beta_2 dr.$$

From Fig. 2, it can be seen that the phase shift will be more nearly uniform if the shaded portion is a minimum. Designating the shaded area as A_{sh} ,

$$A_{sh} = 2 \int_{r_1}^{L/\cos\phi} \int_0^{\phi_d/2} r dr d\phi$$

$$+ 2 \int_{L/\cos\phi}^{r_2} \int_{\phi_d/2}^{\phi_m/2} r dr d\phi$$

$$= L^2 \tan^2 \frac{\phi_d}{2} - r_1^2 \frac{\phi_d}{2} + r_2^2 \left(\frac{\phi_m}{2} - \frac{\phi_d}{2} \right)$$

$$- L^2 \left(\tan^2 \frac{\phi_m}{2} - \tan^2 \frac{\phi_d}{2} \right).$$

If the shaded area is to be a minimum, then

$$\frac{d(A_{sh})}{d\phi_d} = 0 = L^2 \sec^2 \frac{\phi_d}{2} - \frac{r_1^2}{2} - \frac{r_2^2}{2}.$$

Solving for the optimum ϕ_d :

$$\text{optimum } \phi_d = 2 \cos^{-1} \frac{L}{\sqrt{\frac{1}{2}(r_1^2 - r_2^2)}}. \quad (14)$$

For a given horn, the length L and radius r_2 are known, but r_1 must be calculated from the relation

$$\int_0^{r_1} \beta_1 dr = \int_0^{r_2} \beta_2 dr.$$

As an example, with $\phi_m = 60^\circ$ and $r_2 = 4.0\lambda$, the wave reaching the aperture at the side of the horn is 0.54λ out of phase with the same wave reaching the center of the aperture. This difference in phase is usually considered too large for an optimum horn.

Fig. 3 shows a plot of the phase constants β_1 and β_2 vs the radial distance from the apex. β is the plot of the imaginary part of (13). Region 1 is assumed to contain a dielectric with relative permittivity $\epsilon_r = 1.22$. The area under the curve up to radius $r_2 = 4.0\lambda$ is found graphically to be

$$\int_0^{r_2} \beta_2 dr = 5155$$

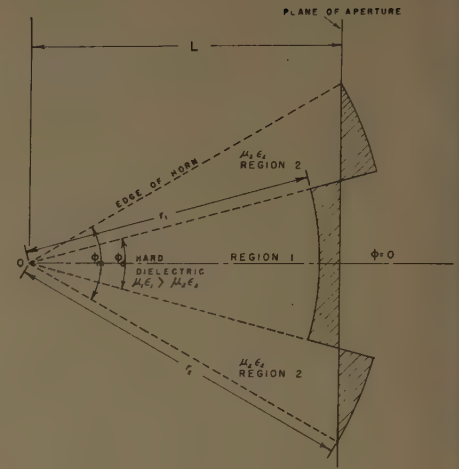


Fig. 2—A phase front at the aperture with two dielectrics in the horn.

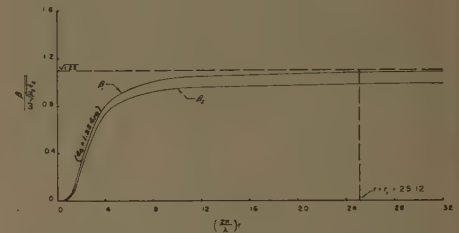


Fig. 3—Phase constants β_1 and β_2 vs radial distance for $\phi_m = 60^\circ$. $\epsilon_{r1} = 1.22$, $\epsilon_{r2} = 1.00$.

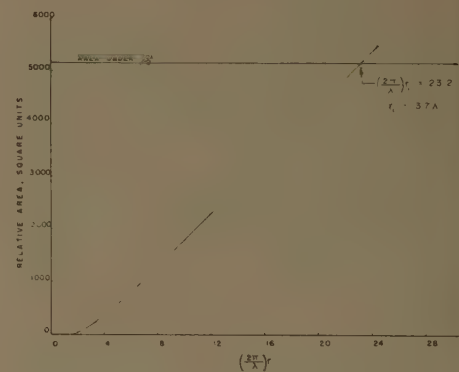


Fig. 4—Area under $\int_0^{r_1} \beta_1 dr$ vs $(2\pi/\lambda)r$.

relative square units. The area under β_1 as a function of r , is plotted in Fig. 4. The radius r_1 , where the area under the two curves is the same, is found graphically to be $r_1 = 3.7\lambda$. Substituting in (14) the optimum ϕ_d becomes $\phi_d = 49^\circ$.

MEASURED DATA

A plot of the relative power at a distance from this horn (example above), with and without the hard dielectric inside, is shown in Fig. 5. Both curves have been normalized to the same relative magnitude: the beamwidth of the main lobe at the 3-db points is reduced from 24° to 20° , and it will be ob-

¹ W. L. Barrow and L. J. Chu, "Theory of the electromagnetic horn," *Proc. IRE*, vol. 27, pp. 51-64; January, 1939.

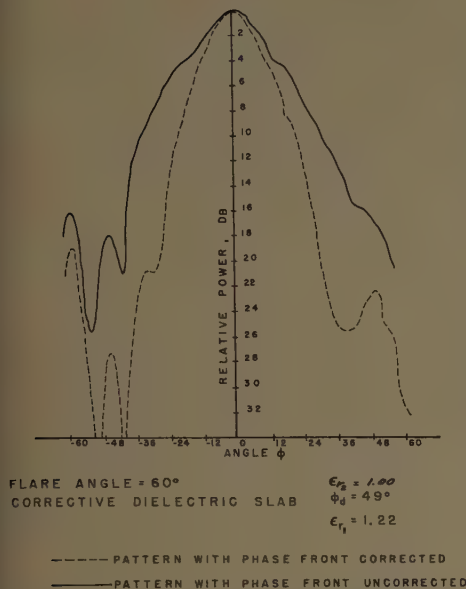


Fig. 5—*H*-plane sectoral horn antenna. Relative power vs azimuth angle ϕ . Dotted line = pattern with phase front corrected; solid line = pattern with phase front uncorrected.

served that the sidelobes are considerably altered.

CONCLUSIONS

The phase front of a wave inside a *H*-plane sectoral horn can be altered by a dielectric inserted inside the horn. An optimum-size hard dielectric can be calculated with a flare angle given by

$$\phi_d = 2 \cos^{-1} \frac{L}{\sqrt{\frac{1}{2}(r_1^2 + r_2^2)}}$$

This correction of phase improves the far field pattern as verified by measurement.

M. A. QUDDUS
Nuclear Engrg. Dept.
Agricultural and Mechanical
College of Texas
College Station, Tex.

J. P. GERMAN
Dept. of Elec. Engrg. and Texas Engrg.
Experiment Station
Agricultural and Mechanical College of
Texas, College Station, Tex.

Comparison of Observed Tropospheric Refraction with Values Computed from the Surface Refractivity*

Summary—Radar elevation-angle errors observed in the Tularosa Basin of New Mexico are compared with values predicted from the surface value of the radio refractive index. Although this method of prediction is not particularly efficacious under the con-

ditions of this experiment, encouraging agreement nevertheless was obtained between predicted and observed: a) mean value of elevation angle error, b) variation of elevation angle error with N_s , and c), the degree of reduction in the uncertainty of prediction gained over the use of a single-standard atmosphere.

INTRODUCTION

A recent article by Anderson, Beyers and Rainey [1] compared computed values of atmospheric refraction obtained from various meteorological data with those obtained experimentally over a 45-mile path at an apparent elevation angle of about one degree. A major conclusion of this study was that the more nearly coincident the measurement of the vertical refractive-index structure in time and space to radio propagation measurements, the better the agreement between observed and calculated values of refraction. It was also found that the use of an exponential model for refractive index vs height, based solely upon the surface value of the refractive index, did not appreciably improve the prediction over that obtained from a fixed standard atmosphere. The purpose of this note is to show the relative agreement between the above measurements and an independent method of predicting the elevation-angle error in terms of the surface value of the refractive index.

REFRACTION THEORY

The angular bending of a radio ray may be well represented by [2], [3]

$$\tau = - \int_{n_1}^{n_2} \cot \theta dn, \quad (1)$$

where n is the refractive index and θ is the apparent elevation angle. Eq. (1) may be evaluated for the total bending of a radio ray passing completely through the atmosphere by integration by parts to obtain

$$\tau = N_s \cdot 10^{-6} \cot \theta_s - \int_{(\cot \theta)_{N=0}}^{\cot \theta_s} N \cdot 10^{-6} d(\cot \theta), \quad (2)$$

where $N \equiv (n-1)10^6$ and the subscript s indicates a value at the earth's surface.

The second term of (2) contributes, at most, only a few per cent of the total for all $\theta_s \geq 10^\circ$ [3], where θ_s is the apparent elevation angle at the earth's surface. This is an important and well-known result at optical frequencies. It has also been shown to hold at radio frequencies [3], [4] sufficiently high (>500 Mc) as to be negligibly affected by the ionospheres. For large initial elevation angles, the bending of a radio ray passing completely through the atmosphere is effectively independent of the vertical refractive-index structure and may be determined from the initial values of the refractive index and elevation angle. Eq. (2) may be written as

$$\tau = - \int_{n_s}^{n_1} \cot \theta dn \cong bN_s + a, \quad (3)$$

where a and b are constants to be determined empirically. Note that for $\Delta h = \infty$, τ is

identical to the elevation angle error ϵ but differs systematically for targets within the earth's atmosphere. Even so, ϵ may be well represented as a linear function of N_s [4].

The elevation-angle error has been evaluated by numerical integration for a large number of refractive-index profiles. These profiles were chosen to represent the range of N profiles likely to be encountered at any location or climate [4]. The values of ϵ and N_s were tabulated. These data, comprising some 77 profiles, then served to determine if ϵ could in fact be represented as a linear function of N_s . This was done by deriving a least-squares regression line of ϵ upon N_s . Thus determinations of the slope b and the intercept a in (3) [modified for ϵ] were obtained in addition to a determination of the scatter of the individual values of ϵ about the regression line. This last value, called the standard error of estimate (SE), allows a quantitative measure of how well variations in ϵ are accounted for by variations of N_s . For example, if all of the variations of ϵ could be attributed to N_s , then $SE(\epsilon) \equiv 0$ or, conversely, if none of the variation in ϵ could be attributed to N_s , then $SE(\epsilon) \equiv s(\epsilon)$, the standard deviation of ϵ , and nothing is gained by the use of N_s .

A measure of the practical usefulness of this approach is the ratio $[SE(\epsilon)/s(\epsilon)] = P_\epsilon$. (This is the same basic measure of improvement used in both references [1] and [4].) P_ϵ is no greater than 0.1 for radio rays passing completely through the atmosphere at $\theta_s \geq 3^\circ$. P_ϵ becomes larger as: 1) the ray traverses as limited height interval of the atmosphere Δh ; or, 2) θ_s becomes smaller. For example, P_ϵ is less than 0.5 if $\Delta h \geq 5$ kM and $\theta_s \geq 1^\circ$, or if $\Delta h \geq 3$ kM and $\theta_s \geq 3^\circ$ [4].

The Anderson, Beyers and Rainey experiment was conducted at $\theta_s \sim 1^\circ$ and $\Delta h \sim 1.7$ kM where P_ϵ would be expected to be about 0.9, and thus constitutes a severe test of this approach to refraction corrections.

COMPARISON OF MEASURED AND PREDICTED ELEVATION-ANGLE ERRORS

Measured and predicted elevation angles vs N_s are compared in Fig. 1. The rather close agreement between the least-squares

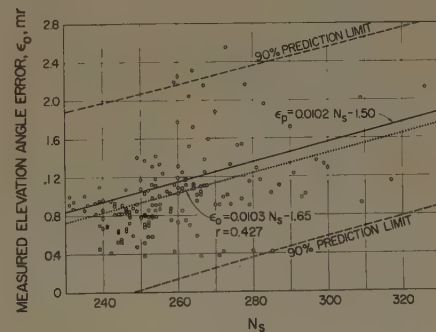


Fig. 1—Comparison of observed, ϵ_0 , and predicted, ϵ_p , elevation-angle error as a linear function of N_s for White Sands Missile Range, Tularosa Basin, N. M. $\theta_s \sim 1^\circ$, $\Delta h = 1.71$ kM.

* Received by the PGAP, March 24, 1961.

regression line determined from the actual data and the predicted line [from (3)] is most striking. In fact, the difference between the two regression lines is not statistically significant. The 90-per cent prediction limits [6] enclose all but about 2 per cent (4 out of 165) of the data points due, presumably, to the prediction process being based upon a wider variation of climatic conditions than occurs in the White Sands area. The reduction in the uncertainty of prediction is about what one would expect for the conditions of this experiment, *i.e.*, 10 per cent or $P_e \sim 0.9$.

CONCLUSIONS

Although the paucity of measured elevation-angle errors prevents any extrapolation, it appears significant that an independent prediction process based solely upon the surface refractive index gave at least for this single case:

- 1) close agreement with the observed mean level of elevation-angle error,
- 2) agreement within 1 per cent between the observed and predicted regression coefficients of elevation-angle error upon N_s ,
- 3) agreement between the observed and predicted reduction in uncertainty of predicting ϵ from N_s alone over use of a single-standard atmosphere value of ϵ .

It is quite evident that the particular method of predicting elevation-angle errors is not highly useful *under the conditions of this experiment*, but the fact that its degree of usefulness was predicted *a priori* augurs well for its utility under more favorable conditions. This last conjecture is particularly reinforced by the close agreement between observed and predicted refraction at $\theta_s \geq 3^\circ$ completely through the atmosphere reported by Marner and Iliff [7].

The author wishes to thank W. L. Anderson, N. J. Beyers, and R. J. Rainey for making their experimental data available for this analysis.

B. R. BEAN
Natl. Bur. of Standards
Boulder, Colo.

BIBLIOGRAPHY

- [1] W. L. Anderson, N. J. Beyers, and R. J. Rainey, "Comparison of experimental and computed refraction," IRE TRANS. ON ANTENNAS AND PROPAGATION, vol. AP-8, pp. 456-461; September, 1960.
- [2] W. M. Smart, "Spherical Astronomy," Cambridge University Press, London, Eng., ch. 3; 1931.
- [3] M. Schulkin, "Average radio-ray refraction in the lower atmosphere," Proc. IRE, vol. 40, pp. 554-561; May, 1952.
- [4] B. R. Bean and B. A. Cahoon, "The use of surface weather observations to predict the total atmospheric bending of radio rays at small elevation angles," Proc. IRE, vol. 45, pp. 1545-1546; November, 1957.
- [5] B. R. Bean, B. A. Cahoon, and G. D. Thayer, "Tables for the Statistical Prediction of Radio Ray Bending and Elevation Angle Error using Surface Values of the Refractive Index," Natl. Bur. Standards, Washington, D. C., NBS Tech. Note 44; March 16, 1960.
- [6] E. L. Crow, F. A. Davis, and M. W. Maxfield, "Statistics Manual," Dover Publications, Inc., New York, N. Y., pp. 161-164; 1960.
- [7] G. R. Marner and W. R. Iliff, "Observed 8.7-mm refraction as a function of surface meteorological conditions," IRE TRANS. ON ANTENNAS AND PROPAGATION, vol. AP-6, p. 308; July, 1958 (Abstract).

The Excitation of a Dielectric-Rod Antenna by a Helix*

The endfire dielectric antenna is a well-known radiator in the field of microwave engineering.¹⁻³ Its operation depends upon the excitation of a surface wave on a solid dielectric rod or a hollow dielectric tube. To excite efficiently any surface-wave structure in a given mode it is, in general, necessary to create a field configuration at the launching point which is as close as possible to that of the desired mode. The useful dominant HE_{11} mode on a dielectric-rod antenna is often excited by the TE_{11} mode in a circular waveguide; however, the HE_{11} mode can also be excited by a probe imbedded in the dielectric rod.² This latter method is more widely used at the larger centimeter wavelengths where a flexible coaxial cable is employed as a transmission line. It is noticed that the field distribution of two orthogonal HE_{11} modes in phase quadrature on the dielectric rod closely resembles that of the -1 space harmonic associated with a tape helix or the -1 mode associated with a sheath-helix.^{2,4} This observation suggests that the helix may be a relatively efficient exciting element for a dielectric-rod antenna.

The phase velocity of the circularly-polarized HE_{11} mode on a dielectric rod, and that of the -1 sheath-helix mode on a helix-wound dielectric rod, can be calculated^{2,5} (some numerical results pertinent to this discussion are shown in Fig. 1) where ka is the circumference in free-space wavelengths, v/c is the ratio of the axial surface wave phase velocity to the free-space phase velocity, and $\epsilon = 2.5$. The field configurations of these two modes are identical if the phase velocities are equal in the two cases, and they resemble each other so long as the deviation between the two phase velocities is small. The helix may be a good launching device for the HE_{11} mode on a polyrod if the -1 mode of the sheath helix carries most of the propagating power. Therefore the helix exciter is expected to function properly in the range of ka , which corresponds to a short rod-supported helix radiating in the axial mode.

The Hansen-Woodyard condition $(\beta - k)l = \pi$ can be easily transformed into the following form

$$\left(\frac{l}{a}\right) \left[\left(\frac{v}{c}\right)^{-1} - 1 \right] = \frac{\pi}{ka},$$

where β is the phase constant of the surface wave, and l is the length of the endfire antenna. Numerical results from this equation also have been plotted in Fig. 1 for $l/a = 81.6$,

* Received by the PGAP, March 24, 1961. This work was sponsored in part by the U. S. Army Engrg. Lab., Fort Monmouth, N. J.

¹ G. E. Mueller and W. A. Tyrrell, "Polyrod antennas," Bell Sys. Tech. J., vol. 26, pp. 837-851; October, 1947.

² D. G. Kiely, "Dielectric Aerials," John Wiley and Sons, Inc., New York, N. Y.; 1952.

³ G. E. Mueller, "End-Fire Dielectric Antennas," Monograph published by The Ohio State Univ. Engrg. Experiment Station, Columbus, Ohio; 1955.

⁴ S. Sensiper, "Electromagnetic Wave Propagation on Helical Conductors," D.Sc. dissertation, M.I.T., Cambridge, Mass.; 1951.

⁵ D. A. Watkins, "Topics in Electromagnetic Theory," John Wiley and Sons, Inc., New York, N. Y.; 1958.

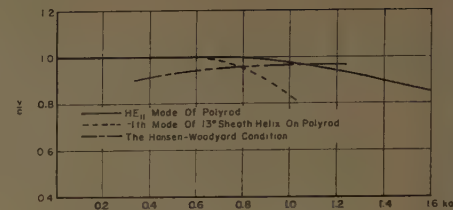


Fig. 1—The surface-wave phase velocities.

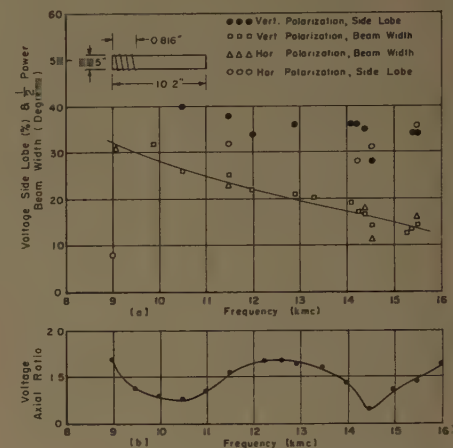


Fig. 2—The performance of a polyrod antenna excited by a 4-turn 13° helix.

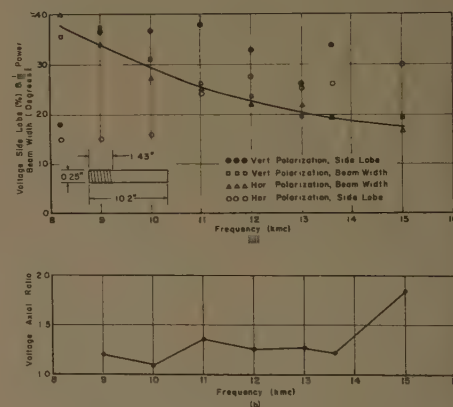


Fig. 3—The performance of a polyrod antenna excited by a 7-turn 13° helix.

which is the ratio of the experimental dielectric rod shown in Figs. 2 and 3. Since the radiation pattern of an endfire antenna deteriorates rapidly when the frequency increases beyond the Hansen-Woodyard condition, it is evident that the helix-excited polyrod antenna has a higher upper frequency limit and is inherently more broadband than the long polyrod-supported helical antenna (the helical exciter is extended to the end of the polyrod).

The patterns and axial ratios of a polyrod antenna excited by a 4-turn end 7-turn 13° helix have been measured over a range of frequencies, and the results are presented in Figs. 2 and 3, respectively. The dimensions of the radiators are also described in

the sketches and the helices have been periphery-fed from a coaxial opening which is located in a square ground plane of 1-inch sidelengths. The beamwidths are about the same as those of the waveguide-fed polyrod antennas. The sidelobe level and the axial ratio are comparable to those of the helices. The 4-turn helix has a wider pattern bandwidth, but a higher axial ratio in its operating band, than the 7-turn helix. Here the pattern bandwidth is defined as the frequency range within which the voltage sidelobe level does not exceed 40 per cent. Measurements also have been carried out for different lengths of polyrods excited by a 4-turn 13° helix. When the polyrod length decreases, the beamwidth increases as one would expect; however, the sidelobe level and the axial ratio remain about the same in

the 1.8:1 bandwidth. If the polyrod dimensions have been selected so that the differential phase shift along the polyrod is less than that required by the Hansen-Woodward condition, the pattern bandwidth as defined above is limited by the characteristics of the helical feed which is certainly more broad-band than the circular waveguide. Experiments indicate that a tapered dielectric sleeve outside the helix can reduce the beamwidth and the sidelobe level at the expense of the bandwidth.

It has been demonstrated that the helix can be a useful exciting element for a dielectric-rod antenna. However, further measurements are still needed to establish the optimum design. This excitation method offers the following advantages over a waveguide type of excitation: a wider bandwidth,

a simpler type of circular polarizer, and a better adaptation of the antenna to coaxial feed. It is obvious from this work that the helix can also be used to excite circularly-polarized surface waves on other types of endfire-dielectric antennas such as the hollow dielectric tube and the dielectric-coated metal rod.⁶

The authors are indebted to Dr. R. G. Kouyoumjian for his valuable comments.

TA-SHING CHU

N. R. KILCOYNE

Antenna Lab.

Dept. Elec. Engrg.

The Ohio State Univ.

Columbus, Ohio

⁶ W. Hersch, "The surface wave aerial," *Proc. IEE*, vol. 107, pt. C, Monograph No. 363 E; February, 1960.

Contributors

Jules Aarons (S'44-A'51-M'58) was born in New York, N. Y., on October 3, 1921. He received the B.S. degree from the College of the City of New York in 1942, the M.A. degree from Boston University, Boston, Mass., in 1949, and the Ph.D. degree from the University of Paris, France, in 1954.



J. AARONS

He served as a radar and radio officer with the U. S. Army Air Force from 1943 to 1946. From 1946 to the present, he has been employed as a physicist with the Air Force Cambridge Research Center, Bedford, Mass., where since 1955 he has been Chief of the Radio Astronomy Section of the Propagation Sciences Laboratory of the Electronics Research Directorate. He has studied low-frequency fluctuations of the earth's magnetic field, solar-terrestrial relationships and their effects on radio communications, and at present is engaged in radio astronomy studies of the earth's atmosphere, the sun, and lunar reflections.

Dr. Aarons is a member of Commission V of URSI, and the AGU, AAS, and RESA.

Saburo Adachi (S'57-M'59), for a photograph and biography please see page 638 of the November, 1960, issue of these TRANSACTIONS.

John L. Allen was born in Estherville, Iowa, on June 13, 1931. He received the B.S. degree in engineering science in 1958 from the Pennsylvania State University, State College, Pa., and is currently pursuing graduate study at the Massachusetts Institute of Technology, Cambridge, Mass., on a part-time basis.



J. L. ALLEN

He served in the U. S. Air Force from 1950 to 1954. He attended the USAF radar school and subsequently was an instructor at that school until 1952, when he was transferred to the M.I.T. Lincoln Laboratory, Lexington, Mass. While there, he was assigned to the data transmission group. Upon discharge from the Air Force, and while attending college, he was employed part-time as an engineer by what is

now HRB-Singer, Inc., State College, Pa. At HRB, he worked on digital computers and various radar studies.

Upon graduation, he returned to the Lincoln Laboratory where he is now assistant leader of the Special Radars Group. His primary interests are in the fields of array antennas and radar systems design.

Mr. Allen is a member of Tau Beta Pi.

Edward E. Altshuler (S'54-M'55) was born in Boston, Mass., on January 10, 1931. He received the B.S. degree in physics from Northeastern University, Boston, Mass., in 1953, and the M.S. degree in physics from Tufts University, Medford, Mass., in 1954. From 1954 to 1957 he attended Harvard University, Cambridge, Mass., on a part time basis. In 1957 he returned to Harvard full-time and received the Ph.D. degree in applied physics in 1960.



E. E. ALTSHULER

From 1954 to 1957 he was employed by Sylvania Electric Products, Inc., Waltham, Mass. He is presently employed by the Electromagnetic Radiation Laboratory of the Air Force Cambridge Research Laboratories, Bedford, Mass.

Dr. Altshuler is a member of Sigma Xi and Sigma Pi Sigma.

John B. Berry, Jr. (M'60) was born in Nashville, Tenn., on July 16, 1928. He received the B.S.E.E. degree from Clemson Agricultural and Mechanical College, Clemson, S. C., in 1949 and the M.S.E.E. from Georgia Institute of Technology, Atlanta, in 1960.



J. B. BERRY, JR.

He joined the faculty of the Georgia Institute of Technology in 1957, as an Instructor in electrical engineering, and was engaged in research on meteor-burst propagation as a Research Associate at the Engineering Experiment Station of Georgia Institute of Technology from 1957 to 1960. He is presently employed by the Southern Bell Tele-

phone and Telegraph Company, Atlanta, Ga., as a Staff Engineer.

Mr. Berry is a member of Tau Beta Pi, Phi Kappa Phi, and the AIEE.

John P. Castelli (A'58-M'58) was born in Lexington, Mass., on November 7, 1916. He received the A.B. and M.A. degrees from Boston College, Chestnut Hill, Mass., in 1938 and 1939, respectively.



J. P. CASTELLI

During World War II, he served in the U. S. Army Air Force as a radar officer. In 1946 he entered the Civil Service at the Air Force Cambridge Research Center, Bedford, Mass., where he has worked on rocket projects and various phases of radar systems. At present, he is engaged in radio astronomy studies of atmospheric absorption, refraction and scintillation and in studies of the variation in lunar temperatures at microwave frequencies.

James H. Chisholm was born in Byron, Ga., on February 8, 1913. He received the B.S.E.E. degree from the Georgia Institute of Technology, Atlanta, in 1934.



J. H. CHISHOLM

He was associated with the Masonite Corp. until his entry into active service with the Signal Corps in 1941. From 1941 to 1946, he served as a signal officer with the U. S. Air Force, where he was engaged in the development and operation of air defense systems.

In 1947, Mr. Chisholm joined the Central Radio Propagation Laboratory of the National Bureau of Standards, Boulder, Colo., where he was engaged in research in tropospheric propagation. In 1951, he joined the Massachusetts Institute of Technology, Lincoln Laboratory, Lexington, Mass., and since 1955 has been group leader of the Radio Propagation Research Group.

Alyce M. Conda (M'57) was born in Leavenworth, Kan., on July 20, 1933. She received the B.S. degree in mathematics

from Southwest Texas State College in 1953.

From 1954 to 1955 Mrs. Conda taught Mathematics at Southwest Texas State College, San Marcos, Tex. She has been briefly associated with the University of Colorado, Boulder, where she taught courses in mathematics.



A. M. CONDA

Since 1956 she has been employed as a mathematician with the Radio Propagation Engineering Division of the National Bureau of Standards, Boulder, Colo.

Mrs. Conda is an associate member of the Boulder Branch of RESA.



Donald G. Dudley, Jr., was born in Bethesda, Md., on October 6, 1931. He received the B.S. degree in 1954 from Virginia Polytechnic Institute, Blacksburg, and the M.S. degree in 1960 from the University of California at Los Angeles, where he is currently working toward the Ph.D. degree.



D. G. DUDLEY, JR.

He joined Hughes Aircraft Company, Field Service and Support Division, Culver City, Calif., in 1956, after serving two years in the U. S. Army specializing in microwave maintenance, and is presently with the Microwave Department, Antenna Design Section, Ground Systems Group, Fullerton, Calif. He is also a teaching associate at UCLA, where he has served as a consultant to the University Extension, concerned with the teaching of microwave measurements, and as lecturer in engineering, particularly in electromagnetic theory.



John D. Dyson (S'49-A'52-M'58) was born in Lemmon, S. D., on August 9, 1918. He received the B.S. degree in economics in 1940 and the B.S.E.E. degree in 1949 from South Dakota State College of Agricultural and Mechanic Arts, Brookings, and the M.S. and the Ph.D. degrees in electrical engineering from the University of Illinois, Urbana, in 1950 and 1957, respectively.



J. D. DYSON

He was employed in 1940 as a statistician, and served in the Army from 1941 to 1946 on active duty. He was part-time instructor at South Dakota State College in 1949, and was on the Research Staff of the Sandia Corporation,

Albuquerque, N. M., in 1951 and 1952. Since October, 1952, he has been on the staff of the Antenna Laboratory of the University of Illinois, Urbana, where he is presently research associate professor.

Dr. Dyson is a member of Sigma Xi, Eta Kappa Nu, Sigma Tau, and Pi Mu Epsilon.



Frank J. Goebels, Jr. (M'60) was born in Brooklyn, N. Y., on June 10, 1933. He received the B.S. degree in physics, *magna cum laude*, from Muhlenberg College, Allentown, Pa., in 1955, and the M.S. degree in physics from the University of California at Los Angeles in 1958. In 1955, he was the recipient of a Howard Hughes M.S. Fellowship.



F. J. GOEBELS, JR.

He has been with the Antenna Department of the Hughes Aircraft Company, Culver City, Calif., for five years and contributed to research in the areas of UHF-VHF antennas, circular aperture antennas, microwave components, breakdown phenomena in waveguides, and solid-state antennas and techniques. He has three patents pending in the field of antennas and solid-state techniques.

Mr. Goebels is a member of the American Institute of Physics.



Stanley J. Goodman (M'55) was born in New York, N. Y., on May 15, 1933. He received the B.E.E. degree from the College of the City of New York in 1955, and the M.S. degree from Columbia University, New York, N. Y., in 1958.



S. J. GOODMAN

Since 1955 he has been a member of the research staff at the Columbia University Electronics Research Laboratories where he has worked on CW radar systems, radar propagation problems, and over-the-horizon tropospheric propagation problems.

Mr. Goodman is a member of Eta Kappa Nu and Tau Beta Pi.



Jesse C. James (S'58-M'59) was born in Florence, Ala., on February 29, 1924. He received the B.S.E.E. degree in 1945 and the B.S. degree in engineering physics in 1946, both from the Alabama Polytechnic Institute, Auburn. In 1950, he received the M.A. degree in physics from the Rice Institute, Houston Texas, and in 1958 he received the Ph.D. degree in electrical engineering at the Georgia Institute of Technology, Atlanta.

From 1946 to 1948 he was with the Southern Research Institute of Birmingham, Ala. as a research assistant; in 1950 he joined



J. C. JAMES

the Navy Mine Defense Laboratory, and in 1951 he was with the Redstone Arsenal, Ala. In 1952, he joined the staff of the Engineering Experiment Station at the Georgia Institute of Technology, and since 1958, he has been with the Lincoln Laboratory, Massachusetts Institute of Technology, Lexington. He has been engaged in various research projects in areas related to nuclear physics and electronics, and more recently, in space communication and radio propagation.

Dr. James is a member of Tau Beta Pi and Sigma Xi.



Kent R. Johnson (S'47-A'55-M'60) was born in Evanston, Ill., on August 26, 1929. He received the B.S.E.E. degree from Vanderbilt University, Nashville, Tenn., in 1950, the M.S.E.E. degree from the Carnegie Institute of Technology, Pittsburgh, Pa., in 1952, and the Ph.D. degree from Northwestern University, Evanston, Ill., in 1954.



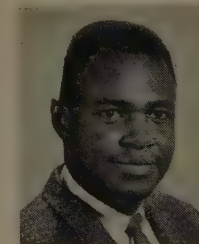
K. R. JOHNSON

From 1954 to 1955 he worked at the Ramo-Woolbridge Corporation, Los Angeles, Calif., on missile guidance. From 1954 to 1955 he was an assistant professor of electrical engineering at the University of Pittsburgh, Pittsburgh, Pa., and from 1956 to 1960 he was a staff member of the Lincoln Laboratory, Massachusetts Institute of Technology, Lexington. At the Lincoln Laboratory he was concerned with radar scattering cross sections and electromagnetic propagation in inhomogeneous media.

Dr. Johnson is a member of the American Physical Society, Tau Beta Pi, and Sigma Xi.



Kenneth C. Kelly (S'53-A'54-M'59) was born in New York, N. Y., on March 6, 1928. After Naval service as an electronics technician, he attended the Polytechnic Institute of Brooklyn, Brooklyn, N. Y., and received the B.S.E.E. degree in 1953.



K. C. KELLY

From 1950 to 1953, he worked part time for the Polytechnic Research and Development Company, Brooklyn, on the production of

microwave signal generators and on the design of waveguide components. Since joining the Hughes Aircraft Company, Culver City, Calif. in 1953, he has been engaged in research and development on slot array techniques, microwave antennas, and microwave components. In his current assignment at Hughes, he heads the Development Section of the Antenna Department.

Mr. Kelly is a member of Tau Beta Pi, Eta Kappa Nu, and RESA.

❖

J. M. Kennedy (M'58) was born in New York, N. Y., on December 3, 1933. He received the A.B. degree in mathematics



J. M. KENNEDY

from Fordham University, Bronx, N. Y., in 1954, and the B.S. degree in electrical engineering from Columbia University, New York, N. Y., in 1956.

Since 1956 he has been employed at the Columbia University Electronics Research Laboratories where he has worked on

CW radar systems, filtering problems and tropospheric scatter transmission.

Mr. Kennedy is a member of Eta Kappa Nu and Tau Beta Pi.

❖

Louis B. Lambert (S'50-A'53-M'59) was born in New York, N. Y., on March 31, 1928. He received the B.E.E. degree *summa cum laude* in 1950



L. B. LAMBERT

from the College of the City of New York and the M.S.E.E. degree in 1951 from the Massachusetts Institute of Technology, Cambridge, Mass., where he was a research assistant engaged in transistor circuits research.

From 1951 to 1955 he was an instructor at the Columbia University, New York, N. Y., Electrical Engineering Department, teaching courses in the graduate school. He was also engaged in semiconductor and pulse techniques research at the Columbia University Electronics Research Laboratories, and in 1955 he became a full time member of the staff at the Research Laboratory.

He is now senior supervisor of the Radar Laboratory. Previous and present research projects in which he has participated include radar system design, radio propagation studies, ultrasonic delay lines, optical filtering techniques, and space communication techniques. He is now a candidate for the D.E.E. degree at Columbia University.

Mr. Lambert is a member of Sigma Xi, Tau Beta Pi and Eta Kappa Nu.

Frank C. Macdonald was born in Bellevue, Pa., on February 2, 1920. He received the B.A. degree in mathematics and the



F. C. MACDONALD

M.A. degree in mathematics from the Catholic University, Washington, D. C., in 1940 and 1946, respectively.

Since 1941 he has worked at the U. S. Naval Research Laboratory, Washington, D. C., in the field of microwave propagation and scattering.

❖

Paul E. Mayes (S'50-A'54-M'59) was born in Frederick, Okla., on December 21, 1928. He received the B.S.E.E. degree from the University of Oklahoma, Norman, in 1950, and the M.S.E.E. and Ph.D. degrees from Northwestern University, Evanston, Ill., in 1952 and 1955, respectively.



P. E. MAYES

He was employed as a graduate assistant and research associate in the Microwave Laboratory at

Northwestern while a graduate student there from 1950 to 1954. Since September, 1954, he has been on the electrical engineering faculty at the University of Illinois, Urbana, where he is now an associate professor. His principal duties include teaching graduate courses in electromagnetic theory and supervising research in the Antenna Laboratory. He has several antenna patents pending.

Dr. Mayes is a member of Sigma Xi, Tau Beta Pi, and Eta Kappa Nu.

❖

M. L. Meeks was born in Gainesville, Ga., on October 1, 1923. He received the B.S. degree from the Georgia Institute of Technology, Atlanta, in 1943. He served in the Navy until 1947, and in 1951 he received the Ph.D. degree in physics from Duke University, Durham, N. C.



M. L. MEEKS

In 1951, Dr. Meeks joined the faculty at the Georgia Institute of Technology, on the staff of the School of Physics and the Engineering Experiment Station. From 1959 to 1960, he was on leave with the Harvard Radio Meteor Project, Harvard College Observatory. He is an associate professor of physics, and has worked in the fields of nuclear physics, operations research, and electromagnetic theory. Currently his interests include radio propagation and radio astronomy.

Dr. Meeks is a member of Sigma Xi, the American Physical Society, the American Astronomical Society, and the American Meteorological Society. He is Consultant to the Radio Astronomy Laboratory and the Radio Meteor Project at Harvard College Observatory.

❖

Donald B. Muldrew was born in Winnipeg, Manitoba, Canada, on October 17, 1934. He received the B.S. degree in physics from the University of Manitoba, Winnipeg, in 1957.



D. B. MULDREW

Since that time, he has been at the Defence Research Telecommunications Establishment, Ottawa, Canada, where he has worked on ionospheric problems, including the spatial distribution of sporadic E, ray tracing and ground backscatter.

❖

Louis P. Rainville (S'56-A'57) was born in Salem Mass., on January 31, 1926. He served in the U. S. Navy from 1944 to 1952 as electronic technician engaged in installation and maintenance of radar and communications systems.

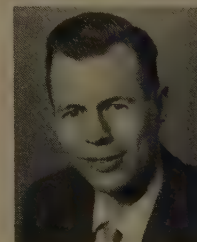


L. P. RAINVILLE

In 1952, Mr. Rainville joined the Massachusetts Institute of Technology, Lincoln Laboratory, Lexington, Mass., and was active in the experimental tropospheric propagation research programs. In 1956 he received the associate degree in electronics from the Lincoln Technical Institute. Since 1957, he has participated as a staff member of the Lincoln Laboratory in the experimental auroral propagation research program.

❖

J. H. Richmond (S'49-M'56-SM'59) was born in Kalispell, Mont., on July 30, 1922. He served in the U. S. Navy as a Chief Electronics Technician from 1940 to 1946 and from 1950 to 1951. In 1950, he graduated *summa cum laude* from Lafayette College, Easton, Pa., with the B.S. degree in electrical engineering. In 1952 he received the M.Sc. degree in electrical engineering at The Ohio State University, Columbus, and in 1955 the Ph.D. degree.



J. H. RICHMOND

Since 1952, Dr. Richmond has been en-

gaged in research on circularly polarized antenna, rotary waveguide phase shifters, and radomes at the Antenna Laboratory of The Ohio State University. He has been an associate professor in the Department of Electrical Engineering since September, 1955.

Dr. Richmond is a member of Tau Beta Pi, Phi Beta Kappa, Sigma Xi, Pi Mu Epsilon, and Eta Kappa Nu.



David L. Ringwalt (A'42-M'52) was born in Oakley, Kan., on July 3, 1920. He received the B.S.E.E. degree from Northwestern University, Evanston, Ill., in 1942, and the M.S.E.E. degree from the University of Michigan, Ann Arbor, in 1946.

Since 1942 he has worked at the U. S. Naval Research Laboratory, Washington, D. C., in the field of microwave propagation. He has been

head of the Wave Propagation Branch, Electronics Division, since 1955.



James F. Roche (M'52) was born in Lynn, Mass., on July 27, 1923. He received the B.S.E.E. degree from the University of Rhode Island, Kingston, in 1943.

From 1943 to 1946, Mr. Roche served with the Signal Corps, primarily with the Radio Propagation Unit. He became a civilian engineer with the Signal Corps in 1946, and was engaged in radio wave propagation studies pertaining to

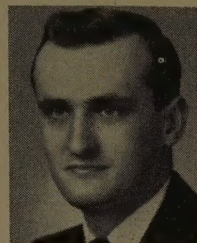
Army communication circuits. In September 1951, he joined Aeronautical Radio Inc., Washington, D. C., as a frequency and radio wave propagation engineer. Since July 1953, he has been a member of the staff of the M.I.T. Lincoln Laboratory, Lexington, Mass., where he is engaged in radio wave propagation research.

Mr. Roche is a registered professional engineer in the District of Columbia.



Roger C. Rudduck (M'60) was born in Dayton, Ohio, on April 28, 1936. He received the B.E.E. degree from the University of

Dayton, Ohio, in 1958, and the M.S. degree from The Ohio State University, Columbus, in 1959, where he is currently a candidate for the Ph.D. degree in electrical engineering.



R. C. RUDDUCK

on radomes and Luneberg lenses.

Mr. Rudduck is a member of Sigma Xi, Pi Mu Epsilon, and Tau Beta Pi.



James R. Wait (SM'56) was born in Ottawa, Canada, on January 23, 1924. He received the B.A.S. and M.A.S. degrees in engineering physics from the University of Toronto, Canada, in 1948 and 1949, respectively. At this time he was employed as a junior research engineer at the Hydro Electric Power Commission of Ontario, Canada. Returning for further graduate work to the University of Toronto, he obtained the Ph.D. degree in electromagnetic theory in 1951.



J. R. WAIT

From 1949 to 1952 he was associated with Newmont Exploration, Ltd., Jerome, Ariz., where he conducted theoretical and experimental research in electrical prospecting. From 1952 to 1955 he was a section leader in the Defence Research Telecommunications Establishment in Ottawa where he was mainly concerned with theoretical problems in radiation. He was associated briefly with McGill University, Montreal, Quebec, during 1954, and with Colorado University, Boulder, in 1955 and 1957 where he taught graduate courses in antennas and propagation. At present he is a consultant to the Director, National Bureau of Standards, Boulder, Colo.

Dr. Wait is a member of the Canadian Association of Physicists, the Society of Exploration Geophysicists, U.S.A., Commissions III and VI of URSI, and is a past president of the Boulder Chapter of RESA.



Carlton H. Walter (S'48-A'51-M'56-SM'59) was born in Willard, Ohio, on July 22, 1924. He received the B.E.E. degree at The Ohio State University, Columbus, in June, 1948, at which time he joined the staff of The Ohio State University Antenna Lab-

oratory. He did graduate work while employed at the Antenna Laboratory, and received the M.S. degree in physics in March, 1951, and the Ph.D. degree in electrical engineering in June, 1957.



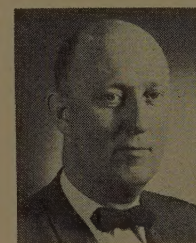
C. H. WALTER

Dr. Walter is now an associate supervisor at The Ohio State University Antenna Laboratory, and an assistant professor in the Electrical Engineering Department.

Dr. Walter is a member of Sigma Xi, Tau Beta Pi, Eta Kappa Nu and Sigma Pi Sigma, and a registered professional engineer (Ohio).



Eldon Warren was born in Digby, N. S., Canada, on August 7, 1922. He received the M.S. degree at Dalhousie University, Halifax, N. S., in 1951, and the Ph.D. degree at Yale University, New Haven, Conn., in 1955. Since 1954 he has been at the Defence Research Telecommunications Establishment, Ottawa, Canada, engaged in ionospheric propagation studies.

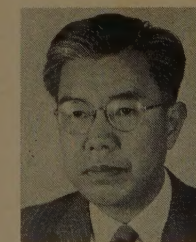


E. WARREN

Dr. Warren is a member of the Canadian Association of Physicists and of the Professional Institute of the Public Service of Canada.



Ryozo Yamada was born in Gifu, Japan, on September 15, 1916. He received the B.S.E.E. degree in 1942, and the D.Sc. in engineering in 1961, both from Tokyo Institute of Technology.



R. YAMADA

In 1943 he joined the Physical Institute of Radio Waves, Ministry of Education, Tokyo, which was reorganized as the Electrical Communication Laboratory, where he was engaged in theoretical and experimental researches on microwave propagation. From 1955 to 1961 he was an assistant professor of electrical engineering at Meijo University, Nagoya, and engaged in the theoretical research on tropospheric propagation. Since 1961 he has been assistant professor at Shizuoka University.

Dr. Yamada is a member of the Physical Society of Japan and the Institute of Electrical Communication Engineers of Japan.

PAPERS TO BE PUBLISHED IN FUTURE ISSUES

Dipole Antennas Coupled Electromagnetically to a Two-Wire Transmission Line.....	<i>K. M. Chen and R. W. P. King</i>
A New Way of Solving Maxwell's Equations.....	<i>V. H. Rumsey</i>
Correlation of Wind Shear with Tropospheric Scatter Signals.....	<i>L. H. Bauer</i>
Optimum Feeds for All Three Modes of a Monopulse Antenna I: Theory.....	<i>P. W. Hannan</i>
Optimum Feeds for All Three Modes of a Monopulse Antenna II: Practice.....	<i>P. W. Hannan</i>
Mutual Coupling Effects in Scanning Dipole Arrays.....	<i>L. A. Kurtz, R. S. Elliott, S. Wehn, and W. Flock</i>
Electromagnetic Propagation in an Exponential Ionization Density.....	<i>L. S. Taylor</i>
Tropospheric Scatter Propagation and Meteorological Conditions in the Caribbean.....	<i>R. E. Gray</i>
Coherent and Incoherent Scattering of Microwaves from the Ocean.....	<i>C. I. Beard</i>
Some Propagation Characteristics of High UHF Signals in the Immediate Vicinity of Trees.....	<i>A. H. LaGrone and C. W. Chapman</i>
Some Remarks on Green's Dyadic for Infinite Space.....	<i>J. Van Bladel</i>
A Reaction Theorem and Its Application to Antenna Impedance Calculations.....	<i>J. H. Richmond</i>
Scattering by a Periodically Apertured Conducting Screen.....	<i>R. B. Kiebertz and A. Ishimaru</i>

INSTITUTIONAL LISTINGS

The IRE Professional Group on Antennas and Propagation is grateful for the assistance given by the firms listed below, and invites application for Institutional Listing from other firms interested in the field of Antennas and Propagation.

AERO GEO ASTRO CORP., 1200 Duke St., Alexandria, Va.
Space Instrumentation; Antennas; Transponders; Command Receivers; Augmenters; Telemetry; Radar

ANDREW CORPORATION, P.O. Box 807, Chicago 42, Ill.
Antennas, Antenna Systems, Transmission Lines, Development and Production

BLAINE ELECTRONETICS, INC., 14757 Keswick St., Van Nuys, Calif.
Antennas, Paraboloids, Scale Models, Antenna Radiation Pattern Measurement Towers

DEVELOPMENTAL ENGINEERING CORP., Leesburg, Va.; Boston, Mass.; Boulder, Colo.; Washington, D.
Antenna Research, Design & Evaluation-Propagation Studies & Communications Systems Engineering

DORNE & MARGOLIN, INC., 29 New York Ave., Westbury, L. I., N. Y.
Research, Development and Manufacture—Antenna and Microwave Technology

FXR, Inc., 25-26 50th St., Woodside 77, N. Y.
Precision Microwave Test Equip., High Power Microwave Electronics, Microwave Components & Instrumentation

HUGHES AIRCRAFT COMPANY, Florence and Teale Sts., Culver City, Calif.
Res., Dev., Mfg.: Radar Systems & Components; Antennas, Tubes, Radomes, Solid-State Devices

MARK PRODUCTS CO., 5439 W. Fargo Ave., Skokie, Ill.
Antennas for Two-Way Communications, Grid Parabolas, Research & Development

SCIENTIFIC-ATLANTA, INC., 2162 Piedmont Rd., N.E., Atlanta 9, Ga.
Antenna Pattern Ranges, R & D, RF Components, Telemetry Tracking Systems,
Fourier Computer & Computations

TECHNICAL APPLIANCE CORP., 1 Taco St., Sherburne, N. Y.
Des., Dev., & Mfg.: Antennas & Antenna Systems for Communications, Telemetry, & Tracking

WEINSCHEL ENGINEERING COMPANY, INC., Kensington, Md.
Antenna Pattern Receivers; Bolometer Amplifiers; Microwave Sources; Insertion Loss Measuring Systems

The charge for Institutional Listing is \$50 for one issue or \$200 for six consecutive issues (one year). Application may be made to the Professional Groups Secretary, The Institute of Radio Engineers, Inc., 1 East 79 Street, New York 21, N. Y.